Rational Design and Development of Nanodelivery Systems and Combination Treatments for Overcoming Chemoresistance in Solid Tumors

by

Hoda Soleymani Abyaneh

A thesis submitted in partial fulfillment of the requirements for the degree of

Doctor of Philosophy

in

Pharmaceutical Sciences

Faculty of Pharmacy and Pharmaceutical Sciences

University of Alberta

Abstract

The long term goal of this research is to develop drug delivery systems and combination treatments that can overcome chemoresistance in breast cancer. Here, we attempted two different approaches: First, we tried development of polymeric micelles capable of enhanced drug delivery to tumor, while avoiding nonspecific drug distribution to healthy organs. Special attention was paid to the effect of core stereoregularity and chemical structure in di- as well as tri-block copolymers in the development of polymeric micellar carriers with enhanced thermodynamic and kinetic stability, high drug loading and slowed drug release. Such nano-carriers are expected to achieve improved accumulation in solid tumors through enhanced permeation and retention (EPR) effect. Synthesis of block copolymers of poly(ethylene oxide)-poly(lactide) (PEO-PLA) with different tacticity in the PLA block was pursued using either bulk or solution polymerization. This was followed by block copolymer self-assembly and micellar characterization. In diblock copolymer micelles, a positive correlation between stereoactivity of the core-forming block and degree of core-crystallinity as well as micellar kinetic and thermodynamic stability was observed. Nonetheless, the improved micellar stability neither translated to a reduced rate of drug release nor increased level of drug loading using nimodipine as a model lipophilic drug. Triblock copolymer micelles with a drug miscible inner core (evidenced by a low Flory Huggins interaction parameter); *i.e.*, poly(ε-caprolactone) (PCL) or poly(α-benzyl carboxylate-ε-caprolactone) (PBCL), and drug immiscible outer core, *i.e.*, PLA, improved nimodipine loading content while inhibiting its burst release from the nano-carrier.

In the second part of this thesis, we investigated application of actively targeted polymeric micelles with and without modulators of relevant mechanisms of hypoxia induced chemoresistance (HICR) to cisplatin to overcome drug resistance in breast cancer at a cellular level. This study was aimed to potentiate cytotoxic effects of free and polymeric micellar cisplatin in MDA-MB-231 cells and its two subpopulations with distinct tumorigenic features. The peptide ligand of epidermal growth factor

receptor (EGFR), GE11 (YHWYGYTPQNVI), was conjugated to the acetal-PEO end of acetal-PEO-Poly(α-carboxyl−ε-caprolactone) (acetal-PEO-PCCL). The polymer then formed a complex with cisplatin through its pendent COOH groups self-assembling to polymeric micelles during the process. GE11-peptide increased cellular uptake of polymeric micellar cisplatin by MDA-MB-231 cells under hypoxic condition, however the cytotoxicity of GE11-cisplatin micelles was not significantly different from plain micellar cisplatin. We then investigated the combination of free and micellar cisplatin with inhibitors of cellular pathways involved in HICR in MDA-MB-231 cells. Our results pointed to a major role for signal transducer and activator of transcription 3 (STAT3) in addition to hypoxia inducing factor-1α (HIF-1α), in the appearance of stem-cell markers and resistance to cisplatin in MDA-MB-231 cells. Hypoxia was also shown to actively convert the low tumorigenic/stem-like subpopulations of MDA-MB-231, separated based on their unresponsiveness to a Sox2 reporter (abbreviated as RU cells), to the more tumorigenic/stem-like subpopulation (abbreviated as RR cells). Evidence for the major role of STAT3 activation as responsible factors for this conversion was also revealed. The use of pharmacological inhibitors of STAT3 and HIF-1α with free, as well as polymeric micellar cisplatin (plain and GE11 modified) substantially enhanced the cisplatin toxicity and showed success in partial reversal of HICR to cisplatin.

Overall, the results of our studies show the chemical structure of block copolymer based nano-carriers has the required flexibility for the development of delivery systems for certain application needs. We have shown this towards development of stable nano-carriers capable of high drug loading and slow drug release by manipulating the stereochemistry and structure of di- as well as triblock copolymer micelles. Nano-delivery systems developed to enhance drug delivery to tumor tissue may not be able to overcome chemoresistance at the cellular level, particularly since they are designed to slow down drug release and have low interaction with cells because of their hydrophilic surfaces. Our results show, the potency of conventional and nano-chemotherapeutics can be enhanced once major cellular and

molecular players of chemoresistance are identified and appropriate inhibitors of the identified pathway are used in combination with the anti-cancer agent. We have shown this through identification of major players in the hypoxia-induced tumorigenic conversion and chemoresistance against cisplatin (STAT3 and HIF-1α) followed by the use of genetic silencers as well as pharmacological inhibitors of the mentioned pathways in combination with free and micellar cisplatin formulations, in MDA-MB-231 cells.

Preface

Section 1.2.1 of Chapter one of this thesis has been published as Soleymani Abyaneh H, Vakili MR, Shafaati A, Lavasanifar A, Block copolymer stereoregularity and its impact on polymeric micellar nano-drug delivery, Molecular Pharmaceutics, in press (2017). I was responsible for the manuscript composition. Vakili MR and Shafaati A contributed to manuscript edits. Lavasanifar A was the supervisory author and was involved with manuscript composition.

Chapter two of this thesis has been published as Soleymani Abyaneh H, Vakili MR, Lavasanifar A, The effect of polymerization method in stereoactive block copolymers on the stability of polymeric micelles and their drug release profile, Pharmaceutical Research, 31(6):1485-500 (2014). I was responsible for the data collection and analysis as well as the manuscript composition. Vakili MR contributed to manuscript edits and was involved with concept formation. Lavasanifar A was the supervisory author and was involved with concept formation and manuscript composition.

Chapter three of this thesis has been published as Soleymani Abyaneh H, Vakili MR, Zhang F, Choi P, Lavasanifar A, Rational design of block copolymer micelles to control burst drug release at a nanoscale dimension, Acta Biomaterialia, 24:127-39 (2015). I was responsible for the data collection and analysis as well as the manuscript composition. Vakili MR contributed to manuscript edits and was involved with concept formation. Zhang F was a summer student under my supervision who assisted with some of the drug release data collection. Choi P assisted with some of the data collection regarding calculation of Flory Huggins interaction parameter and contributed to manuscript edits. Lavasanifar A was the supervisory author and was involved with concept formation and manuscript composition.

Chapter four of this thesis has been submitted as Hoda Soleymani Abyaneh, Nidhi Gupta, Aneta Radziwon-Balicka, Paul Jurasz, John Seubert, Raymond Lai, Afsaneh Lavasanifar, STAT3 instead of HIF-1α is important in mediating hypoxia-induced chemoresistance in MDA-MB-231, a triple negative breast cancer cell line, BMC Cancer (December 2016). I designed the research plan, carried out experiments and wrote the manuscript. Gupta N contributed to data analysis of qRT-PCR experiments. Radziwon-Balicka A and Jurasz P assisted with flow cytometric detection of apoptosis. Seubert J provided intellectual input. Lavasanifar A and Lai R conceived and designed the research plan and were involved with concept formation and manuscript composition.

Chapter five of this thesis will be submitted as Hoda Soleymani Abyaneh, Nidhi Gupta, Keshav Gopal, Raymond Lai, Afsaneh Lavasanifar, Hypoxia induces the acquisition of cancer stem-like phenotype in

triple-negative breast cancer via upregulation and activation of Signal Transducer and Activator of Transcription-3 (STAT3). I designed the research plan, carried out experiments and wrote the manuscript. Gupta N contributed to design and performance of the pull down experiments and data analysis. KG assisted with flow cytometric for RU/RR conversion. Lavasanifar A and Lai R conceived and designed the research plan and were involved with concept formation and manuscript composition.

Chapter six of this thesis will be submitted as Hoda Soleymani Abyaneh, Amir Soleimani, Mohammad Reza Vakili, Rania Soudy, Kamaljit Kaur, Ali Tavassoli, Afsaneh Lavasanifar, Modulation of hypoxia-induced chemoresistance to polymeric micellar cisplatin in MDA-MB-231 cells: The effect of EGFR ligand modification of polymeric micelles and combination therapy with selected chemo-sensitizers. I designed the research plan, carried out experiments and wrote the manuscript. Soleimani A assisted with preparation of micellar formulation, cisplatin measurement using ICP/MS and cytotoxicity studies. Soudy R and Kaur K provided us with GE11 peptide. Tavassoli A provided us with HIF-1α inhibitor peptide. Lavasanifar A conceived and designed the research and was involved with concept formation and manuscript composition.

To my mother and father,

Who

Taught me to find beauty in simplicity and joy in generosity

Showed me how to chase the light in the dark

Taught me to dream with open eyes

and

Gave me wings to fly

Acknowledgements

There are many people who have provided so much guidance, expertise and support over the last several years and they deserve both recognition and appreciation. Without this tremendous amount of inspiration and support, this endeavor would not have been possible.

First and foremost, I would like to extend my heartfelt appreciation to Dr. Afsaneh Lavasanifar who was a constant source of encouragement, optimism and reassurance. As a student I couldn't ask for a more respectful and patient supervisor, and more importantly as a woman I couldn't ask for a better female mentor. I take great pride and great pleasure that I've been able to spend as many years as I have as a member of her lab and am a better person for having done so. Thanks Dr. Lavasanifar for seeing me as an extension of who I want to be, and helping me to become her.

• I sincerely thank my supervising and examining committee members, Dr. Hasan Uludag, for serving on my candidacy and defense committee, for providing me access to his lab and materials, and for his expert advice and all the recommendation letters; Dr. Carlos Velazquez Martinez, for serving on my candidacy and defense committee, for his expert advice and feedback during my seminars, and for all the encouraging talks and the recommendation letters; Dr. John Seubert, for providing me access to his lab and materials, for his expert advice when I was working with hypoxic cells, and for serving on my candidacy and defense committee; Dr. Larry Unsworth, for serving on my candidacy and defense committee; Dr. Mansoor Amiji, for accepting to be my external examiner and serving on my defense committee.

• I sincerely thank Dr. Raymond Lai for providing me access to his lab and materials, and for his expert advice and trainings which made me a better scientist.

• I sincerely thank Dr. Raimar Loebenberg for his advice and support during my tenure as a teaching assistant; Dr. Sharon Marsh for her expert advice and feedback during my seminars and for all the encouraging talks and the recommendation letters.

• I sincerely thank Dr. Farzad Kobarfard, my PharmD supervisor, for always believing in me and instilling a sense of encouragement as well as appreciation for learning. I held and continue to hold his advice close to my heart during my PhD studies to yearn for growth and development rather than solely success.

• I sincerely thank Dr. Mohammad Reza Vakili for training me in polymer chemistry and for all the kind words and encouragement that I received from him during my studies; Dr. Shyam Garg for training me in many lab techniques and for providing me with his unconditional assistance in my experiments, scholarship applications and presentations; Dr. Arash Falamarzian and Dr. Hamidreza Montazeri Aliabadi for assistance with siRNA delivery; Dr. Qi Zhang, Dr. Mostafa Shahin and Dr. Nazila Safaei Nikouei for training and helping me in the lab.

• I sincerely thank Amir Soleimani for his great assistance with cisplatin micelles formulations and in vitro studies; Dr. Nidhi Gupta and Dr. Keshav Gopal for training me in western blotting and flow cytometry; Dr. Rania Soudy for providing me with the GE11 peptides for my cisplatin micellar formulations; Dr. Chris Le and Xiufen Lu for assistance with ICP-MS.

• I sincerely thank Dr. Vishwanatha Somayaji for assistance with LC-MS and NMR analysis; Jingzhou Huang (George) and Dr. Aja Rieger for assistance with flow cytometry; Arlene Oatway for assistance with transmission electron microscopy.

• I sincerely thank Mrs Joyce Johnson for assistance with all the administrative and paper work needed during my studies; Drew Price, James Chaulk and Cory Thorp for maintaining the lab instruments, especially hypoxic chamber, which made sure I finished my work on time.

• I sincerely thank my present lab-mates, Igor, Asma, Nasim, Forugh, Zahra, Hanan, Abdul, Cheng, Winston, Moin and Raheem for creating a friendly environment in the lab. Their feedback and suggestions have helped me greatly during my research; my friends Dr. Ingrit Hamann and Igor Zlobine for helping me with my experiments; Dr. Anastasia Greenberg for helping with my scholarship applications. Their continued love and support is what motivates me to keep aiming higher.

• I sincerely thank the Alberta Cancer Foundation and the Women and Children's Health Research Institute for providing me with financial support during my PhD program. Their support for cancer research made me determined to do better and yearn more to give back to society. I sincerely thank the Faculty of Pharmacy and Pharmaceutical Sciences and the University of Alberta for accepting me into this PhD Program and for supporting me during the course of my PhD program.

Lastly, to the friends who enriched my time here in grad school and to the friends from years past, simply knowing that I've had all of you with me this whole time has been an endless source of comfort and strength.

Table of Contents

List of Tables

List of Figures

List of Abbreviations

2-OG; 2-oxoglutarate

ABC; ATP-binding cassette

Acetal-PEO; Acetal-poly(ethylene oxide

Acetal-PEO-PBCL; Acetal-PEO-α-benzyl carboxylate-ε-caprolactone

Acetal-PEO-PCCL; Acetal-PEO-poly-(α-carboxyl-ε-caprolactone)

Acetal-PEO-PCL; Acetal-PEO-poly-(ε-caprolactone)

Ahr; Aryl hydrocarbon receptor

Ap-1; Activator protein-1

ARD-1; Arrest-defective-1

ARNT; Aryl hydrocarbon-receptor nuclear translocator

ATM; Ataxia teleangiectasia mutated gene

BAK; BCL-2 homologous antagonist/killer

BCL-2; B-cell lymphoma 2

BCRP; Breast cancer resistance protein

BHLH; Basic-helix-loop-helix

BRCA1; Breast cancer susceptibility gene 1

CA; Carbonic anhydrases

CBP; Cyclic adenosine monophosphate (cAMP)-response-element-binding protein (CREB) binding protein

CMC; Critical micellar concentration

COX-2; Cycloxygenase-2

c-PARP; Cleaved Poly (ADP-ribose) polymerase

CSC; Cancer stem cell

DDR; DNA-damage response

DIPEA; N,N diisopropyl ethylamine

DL; Drug loading

DLS; Dynamic light scattering

DMSO; Dimethyl sulfoxide

DNA-PKs; DNA-dependent protein kinases

DSB; DNA double strand break

DSC; Differential scanning calorimetry

EDTA; Ethylenediaminetetraacetic acid

EE; Encapsulation efficiency

EGFR; Epidermal growth factor receptor

Elisa; Enzyme-linked immunosorbent

EPR; Enhanced permeation and retention

FIH-1; Factor inhibiting HIF-1

GAPDH; Glyceraldehyde-3-phosphate dehydrogenase

GLUT1; Glucose transporter 1

GSH; Glutathione

GST; Glutathione-S-transferases

HICR; Hypoxia-induced chemoresistance

HIF-1α; Hypoxia inducing factor-1α

HIF-1β; Hypoxia inducing factor-1β

HRE; Hypoxia response elements

Hsp90; Heat shock protein90

IAP-2; Apoptosis inhibitory protein

IC50; Inhibitory concentration at 50%

ICP-MS; Ion coupled plasma mass

IFP; Interstitial fluid pressure

LDH-A; Lactate dehydrogenase A

LRP; Lung resistance protein

MAPK; Mitogen activated protein kinase

MCT; Monocarboxylate transporter

MD; Molecular dynamic

MDR1; Multidrug resistance 1

MMR; Mismatch repair

Mn; Number average molecular weight

MRAP1; Multidrug-resistance-associated protein 1

mTOR; Mammalian target of rapamycin

mtp53; Mutant p53 protein

MTT; 3-(4,5-dimethylthiazol-2-yl)-2,5-diphenyltetrazolim bromide

NER; Nucleotide excision repair

NF-kB; Nuclear factor-kB

NHE1; Na+/H+ exchanger

NMR; Nuclear magnetic resonance spectroscopy

ODDD; Oxygen-dependent degradation domain

PARP-1; Poly (ADP-ribose) polymerase 1

PBCL; Poly(α-benzyl carboxylate-ε-caprolactone)

PBS; Phosphate buffered saline

PCCL; Poly(a-carboxyl-e-caprolactone)

PCL; Poly(ε-caprolactone)

PD/LLA; Poly(D/L-lactide)

PDK; Pyruvate dehydrogenase kinase

PDLA; Poly(D-lactide)

PDLLA 50–50; Poly(D,L-lactide)

PEG; Poly ethylene glycol

PEO; Poly ethylene oxide

PEO-PLA; Poly(ethylene oxide)-poly(lactide)

PHD; Prolyl hydroxylases

PI; Propidium iodide

PI; Polydispersity index

PI3: Phosphoinositol-3-kinase

PLA; Poly lactide

PLLA; Poly(L-lactide)

pSTAT3; Phospho-STAT3

pVHL; Von Hippel Lindau

qRT-PCR; Quantitative reverse transcription polymerase chain reaction

RAC; Racemic

RES; Reticulo endothelial system

ROP; Ring opening polymerization

ROS; Reactive oxygen species

RR; Reporter responsive

RU; Reporter unresponsive

Scr siRNA; Scrambled SiRNA

SDS; Sodium dodecyl sulfate

shRNAi; Short hairpin RNA interference

siRNA; Small interfering RNA

SnO2; Stannous octoate (tin(II) bis(2-ethylhexanoate))

SRR2; Sox2 regulatory region 2/Sox2 reporter

STAT3; Signal transducer and activator of transcription 3

TAD; Transactivation domains

TCA; Tricarboxylic acid

TEM; Transmission electron microscopy

TFA; Trifluoroacetic acid

THF; Tetrahydrofuran

TNBC; Triple negative breast cancer

UPR; Unfolded protein response

Chapter One

Introduction

The section 1.2.1 of this chapter is published as part of a manuscript titled

Block Copolymer Stereoregularity and its Impact on Polymeric Micellar Nano-Drug Delivery

in

Journal of Molecular Pharmaceutics

1.1 Treatment Failure in Cancer: an Overview

Cancer is one of the leading causes of mortality in the world. It can evolve with time and treatment, often necessitating combination therapy including surgery, radiotherapy, chemotherapy, and immunotherapy. Treatment of many types of cancer has improved dramatically over the past two decades and the cancer death rate has been decreasing steadily. Still, many challenges remain in the pursuit of a cancer cure. One key issue concerns resistance towards chemotherapy. Chemotherapy resistance is the development of a phenotype resistant to a variety of structurally and functionally distinct anticancer drugs which results in treatment failure. Broadly, underlying reasons for most cases of chemotherapy failure can be classified into three categories: inadequate pharmacokinetic properties of the drug, tumor cell intrinsic resistance and tumor microenvironment related factors (2, 3).

Nonselective distribution of the drug between normal and tumor tissue results in inadequate intratumoral drug concentration and distribution. It reduces the exposure of cellular targets to the active form of a drug and increases the impact of dose limiting side effects (4, 5). The therapeutic ratio is further compressed by tumors that display intrinsic or acquired drug resistance. Manifestations of resistance are conventionally referred to as intrinsic or acquired on the basis of the initial response to the first therapy (2, 3). Selection pressures within the tumor microenvironment including abnormal tumor vasculature, hypoxia, decreased pH, increased interstitial fluid pressure, and alterations in the expression of tumor suppressors and oncogenes favor the development of intrinsic drug resistance while the common dose and schedule adjustments that accompany traditional chemotherapy cultivate acquired drug resistance (6).

1.2 Nanotechnology in Cancer Therapy

To overcome pharmacokinetic resistance of a drug, a wide range of nano-scaled drug carriers or nano-carriers have been developed. Being in the nano-scale range gives nano-carriers characteristics different from that of the bulk material due to the large surface area to volume ratio (7-9). This large surface area to volume ratio allows the particles to be held in suspension and also enables extensive surface modification (7-9). For nano-carrier systems that rely on drug encapsulation, the physical and chemical properties of platform material determine the pharmacokinetic profile of the system. These properties easily can be customized to achieve a desired pharmacokinetic profile for a carrier system by manipulation of the size, charge, and surface properties of a nano-carrier. Drugs encapsulated in nano-carriers do not contribute to the pharmacokinetic profile and as long as they retain in the system, they

follow the nano-carrier pharmacokinetic. This approach provides a convenient strategy for altering the drug biodistribution and enhances delivery to tumor site, thereby increasing the treatment efficacy and minimizing the adverse side effects.

Solid tumors are well-known for their leaky vasculature with cell junction gaps ranging between 100 nm to 780 nm and poor functional lymphatic drainage. This is in contrast to normal endothelium (with the exception of kidney and liver) with pores less than 2 nm size and functional lymphatic system (**Figure 1.1**) (10). Drugs loaded in nano-carriers selectively accumulate in tumor sites by taking advantage of the leaky vasculatures and impaired lymphatic drainage. The aberrant fenestration on the blood vessels surrounding tumor tissues causes enhanced permeability of macromolecules of certain size to the tumor microenvironment, and poor lymphatic drainage in the tumor area allows retention of the extravasated nano-carriers. This phenomenon commonly referred to as the enhanced permeability and retention (EPR) effect (11-13).

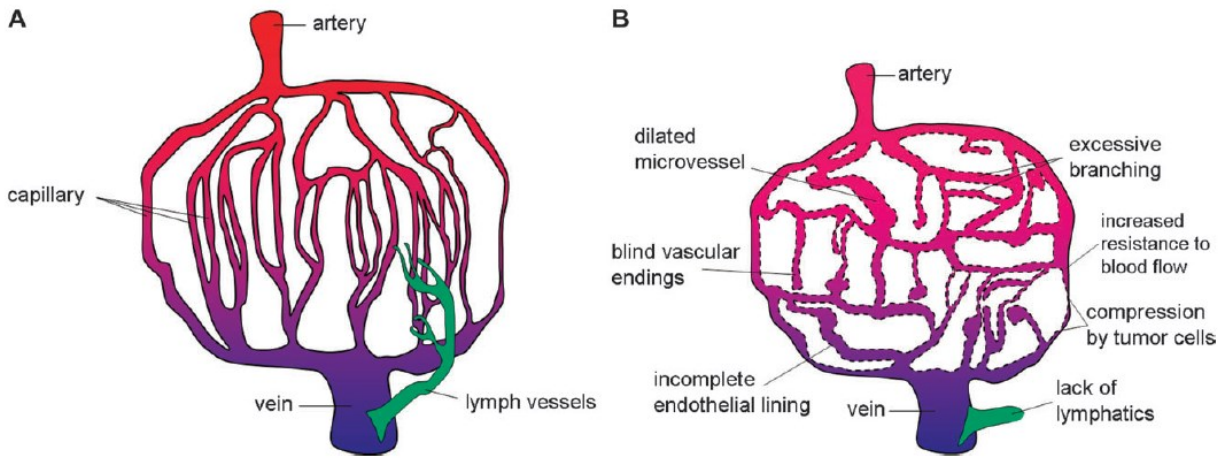

Figure 1.1 Diagrammatic representation of the vascular system. **(a)** Normal tissue. **(b)** Solid tumor. Red represents well-oxygenated arterial blood, blue represents poorly oxygenated venous blood, and green represents lymphatic vessels. Reprinted with permission from Reference (14), Copyright 2007 Nature.

The retained nano-carriers can then act as drug release depots, and release the drug in the tumor microenvironment or they can be internalized within tumor cells over time and release the drug intracellularly. The EPR effect provides means for passive tumor targeting which results in accumulation of nano-carriers in the tumor microenvironment. However, it does not necessarily ensure delivery of the cargo within the tumor cell. For nano-carriers with passive tumor targeting, the cellular internalization

may happen via non-specific endocytosis and therefore will be dependent on spatio-temporal membrane-mediated passive processes (15). To facilitate tumor cell-specific internalization, one of the most promising strategies is incorporation of ligands on the nano-carriers for receptor-mediated endocytosis. Thus, active targeting is achieved through the surface modification of the nano-carriers with targeting moieties for tumor cells. Tumor cells are known to upregulate a variety of receptors on their surface (16). Many of these receptors are 'internalizing' receptors; that is, following ligand binding the ligand–receptor complex is actively endocytosed. Therefore, directing nano-carriers decorated with targeting moieties specific to such receptors into the cell through the receptor-mediated active endocytosis mechanisms. After endocytosis (whether specific or non-specific), it is important for therapeutics to reach their intracellular site of action. For this to occur, endosomal or lysosomal uptake of the drug-loaded nanocarriers is usually followed by intracellular disassembly or degradation of the nano-carriers and release of the drugs in the cytoplasm (6).

To exploit the EPR effect for first passive targeting and then active targeting the nano-carriers must be able to escape systemic recognition by the reticulo endothelial system (RES) such as the kidney, liver, spleen, and lymph nodes. Polyethylene glycol (PEG) modification of nano-carriers increases the circulation time of the nano-carrier by preventing opsonisation and clearance by immune system (17). The stealth effect of the PEG chains is due to the formation of a tightly bound network of water. This will provide a nano-carrier with a hydrophilic surface which masks recognition and interaction of nano-carriers by macrophages to prevent their uptake and clearance. Preventing nano-carriers from clearance by immune system improves the circulation time of the nano-carriers and results in an enhanced tumor accumulation. PEG modification also prevents particle aggregation (18-20).

In summary, the use of nano-carriers leads to enhance treatment efficacy, mostly from reduced drug side effects (Table 1.1). However, despite enhanced tumor tissue concentrations of the drugs and prolonged tumor residence through alterations in drug pharmacokinetic profile, drug delivery by nano-carriers rarely has led to enhanced efficacy of chemotherapeutics. More recent approaches have used internal/external stimuli-activated drug delivery to target sites and/or modification of nano-carriers with ligands for receptors overexpressed on tumor cells. These new approaches are expected to enhance the targeting efficiency of drugs (selectivity) and the therapeutic activity (potency) of anti-cancer drugs (21, 22).

Table 1.1 Clinically-approved intravenous nano-carrier formulations used to treat various cancer types. Reprinted with permission from Reference (23), Copyright 2016 Bioengineering & Translational Medicine, John Wiley and Sons.

Name	Particle type/drug	Approved application/indication	Approval (year)	Investigated application/indication	ClinicalTrials.gov identifier
Cancer Nanoparticle Medicines					
Doxil/Caelyx (Janssen)	Liposomal doxorubicin (PEGylated)	Ovarian cancer (secondary to platinum based therapies) HIV-associated Kaposi's sarcoma (secondary to chemotherapy) Multiple myeloma (secondary)	[a] FDA (1995) [b] EMA (1996)	Various cancers including: solid malignancies, ovarian, breast, leukemia, lymphomas, prostate, metastatic, or liver	166 studies mention Doxil 90 studies mention CAELYX
DaunoXome (Galen)	Liposomal daunorubicin (non-PEGylated)	HIV-associated Kaposi's sarcoma (primary)	FDA (1996)	Various leukemias	32 studies mention DaunoXome
Myocet (Teva UK)	Liposomal doxorubicin (non-PEGylated)	Treatment of metastatic breast cancer (primary)	EMA (2000)	Various cancers including: breast, lymphoma, or ovarian	32 studies mention Myocet
Abraxane (Celgene)	Albumin-particle bound paclitaxel	Advanced nonsmall cell lung cancer (surgery or radiation is not an option) Metastatic breast cancer (secondary) Metastatic pancreatic cancer (primary)	FDA (2005) EMA (2008)	Various cancers including: solid malignancies, breast, lymphomas, bladder, lung, pancreatic, head and neck, prostate, melanoma, or liver	295 studies mention Abraxane
Marqibo (Spectrum)	Liposomal vincristine (non-PEGylated)	Philadelphia chromosome-negative acute lymphoblastic leukemia (tertiary)	FDA (2012)	Various cancers including: lymphoma, brain, leukemia, or melanoma	23 studies mention Marqibo
MEPACT (Millennium)	Liposomal mifamurtide (non-PEGylated)	Treatment for osteosarcoma (primary following surgery)	EMA (2009)	Osteosarcomas	4 studies mention MEPACT: 3 active/recruiting
Onivyde MM-398 (Merrimack)	Liposomal irinotecan (PEGylated)	Metastatic pancreatic cancer (secondary)	FDA (2015)	Various cancers including: solid malignancies, breast, pancreatic, sarcomas, or brain	7 studies mention MM-398/ Onivyde: 6 active/recruiting

[a] Food and Drug Administration (USA).

[b] EMA European Medicines Agency (EMA) in the European Union.

1.2.1 Polymeric Micelles

Polymeric micelles are core–shell nano-structures that are widely used for the solubilisation of poorly water-soluble compounds, development of depots, and targeted drug delivery systems. The introduction of polymeric micelles to the field of cancer therapy was hoped to increase the properties of nano-delivery systems in terms of anti-cancer activity, for two major reasons: first their capacity for incorporation of hydrophobic drugs, and their small size (<100 nm) which was expected to lead to their better tumor accumulation and distribution. Besides, the results of research in this field clearly show that the chemical structure of the polymeric material has a great impact on the physiochemical as well as functional properties of the developed micelles. One of the important structural characteristics of polymers that can affect their properties is their stereochemistry. Stereoactive polymers are composed of repeating units of monomers bearing chiral centers. The type of chiral centers (R or S configuration), their number, and the sequential arrangement of these configurations are important structural features of stereoactive polymers that can affect their physiochemical characteristics (24, 25).

Stereoactive polymers are divided into four main microstructure categories based on the sequential arrangement of their stereo-repeating units (26, 27):

1) isotactic polymers that carry the same chiral centers along the backbone of the polymer.

2) syndiotactic polymers that possess alternative (opposite) chiral centers (R and S) in a sequential arrangement of the backbone.
3) heterotactic polymers that demonstrate alternating opposite pairs of chiral centers (RR and SS) along the backbone.
4) atactic polymers bearing a randomly sequential arrangement of different chiral centers in their backbone.

An example for the structure of isotactic, syndiotactic, heterotactic, and atactic polymers of poly(lactide)(PLA) is shown in **Figure 1.2**. Isotactic , syndiotactic and heterotactic polymers are stereoregular polymers with a higher likelihood of crystallization in the polymer bulk. On the other hand, atactic polymers make polymeric materials with a higher percentage of amorphous structure. The stereoregularity of polymers as building blocks of micelles is suspected to affect the arrangement and compactness of the polymer chains within the micellar structure, hence affecting properties like morphology, stability, drug loading, as well as drug release profile (28-32).

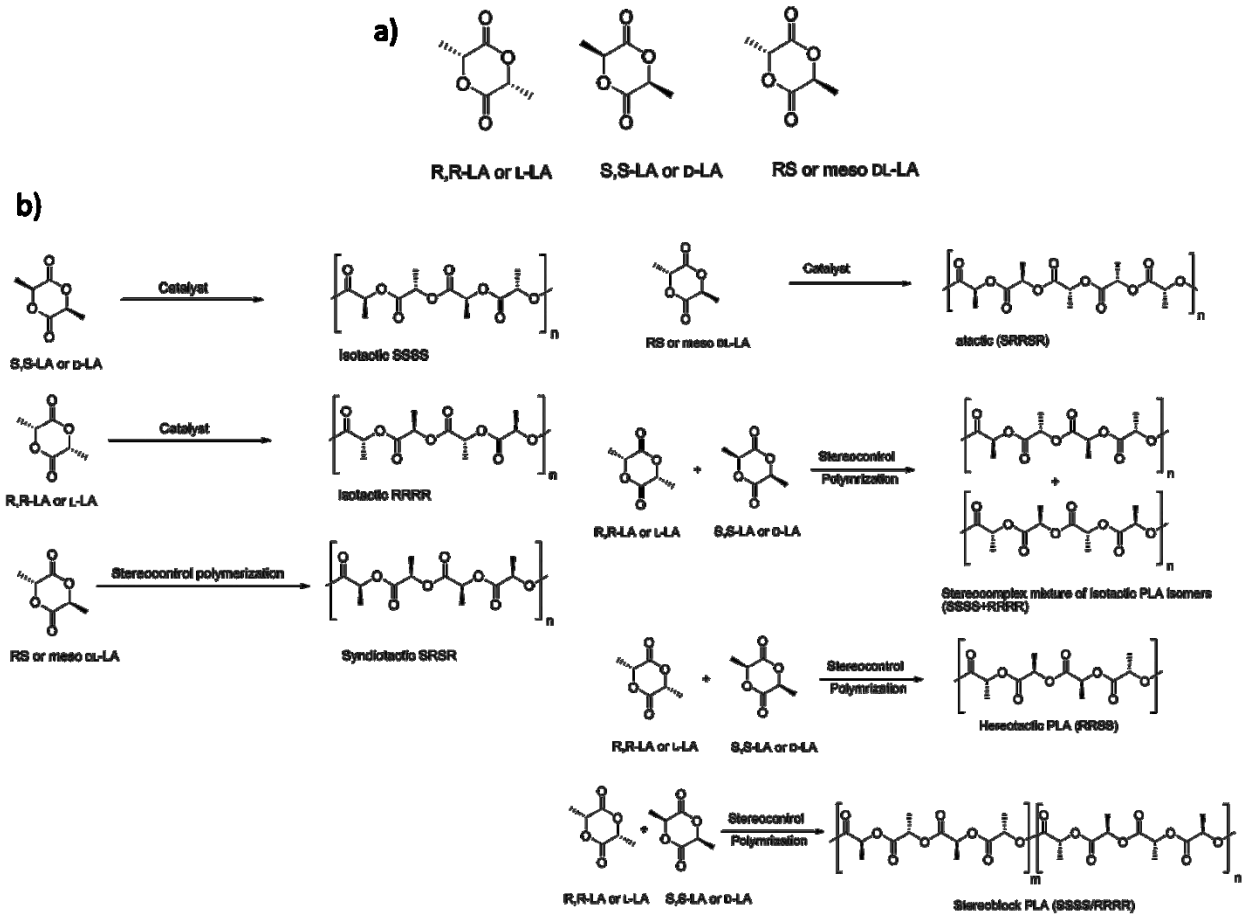

Figure 1.2 (a) Stereoisomers of lactides (LA). **(b)** The schematic model for the structure of isotactic, syndiotactic, heterotactic, atactic and stereoblock polymers of poly(lactide) (PLA). Reprinted with permission from Reference (1), Copyright 2017 American Chemical Society.

The impact of the stereoregularity of the amphiphilic block copolymers, particularly the core-forming segment (**Figure 1.3**), on the functional properties of polymeric micelles has been the subject of several research articles, to date. The results so far, show the stereoregularity of the core-forming block in self-associating block copolymers appears to affect the physiochemical properties of polymeric micelles and their functional behavior both *in vitro* and *in vivo* as illustrated in **Figure 1.4**.

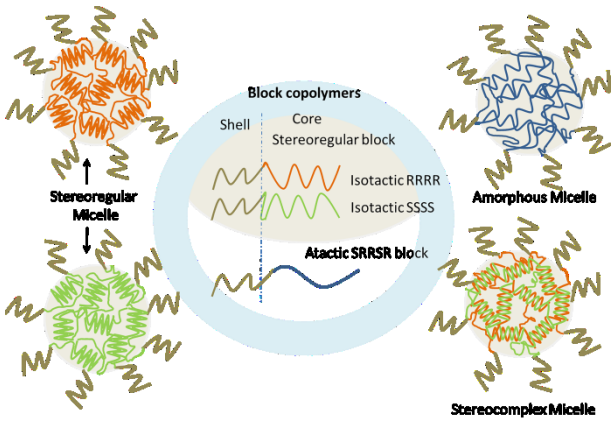

Figure 1.3 Schematic structure of polymeric micelles prepared from block copolymers of different stereoregularity. Micelles composed of stereoregular core-forming blocks, as well as stereocomplex micelles (formed from 1:1 molar ratio of oppositely orientated stereoregular block copolymers) have a higher likelihood of forming semicrystalline core, as opposed to amorphous micelles composed of atactic core-forming block. Reprinted with permission from Reference (1), Copyright 2017 American Chemical Society.

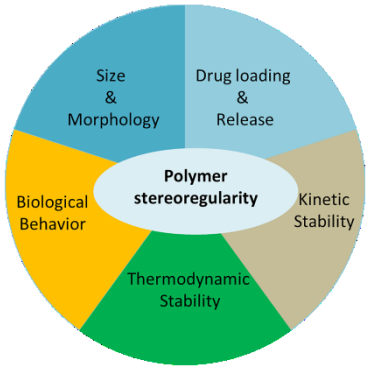

Figure 1.4 Different physicochemical and functional properties of polymeric micelles that are affected by the stereoregularity of the core-forming block in self-assembling block copolymers. Reprinted with permission from Reference (1), Copyright 2017 American Chemical Society.

The direction of the effect on each characteristic is not very well defined and it is still controversial, as summarized in **Table 1.2**. This point by itself indicates a need for the conduction of more systematic studies using appropriate methods and controls that enable the elucidation of other contributing factors and interactive parameters pertaining to structure-activity relationships in this regard. Nevertheless, The results of the conducted studies so far appear to point to a better kinetic stability and tumor

accumulation for block copolymers of higher stereoregularity in the core-forming block (which can form cores of higher crystallinity) compared to those with atactic (or amorphous) cores. Self-assembly of block copolymers containing stereoregular core-forming segments is also shown to lead to formation of cylindrical (micelles) as opposed to spherical ones. In contrast, the effect of introduction of stereoregular core-forming blocks on the direction of the change on micellar thermodynamic stability, drug loading, drug release, and cell interaction has been unpredictable. Most studies conducted so far, also point to higher micellar kinetic stability, slower drug release, higher cellular uptake and enhanced tumor accumulation, for stereocomplex micelles compared to micelles prepared from single type stereoregular block copolymers. However, the direction of the change in micellar thermodynamic stability, drug loading, micellar size and morphology by introduction of stereocomplexes to the core, is still inconclusive.

Table 1.2 The effects of core-forming block stereoregularity on different micellar properties. Reprinted with permission from Reference (1), Copyright 2017 American Chemical Society.

Micellar property	In single type polymeric micelles	Stereocomplex versus single micelles
Thermodynamic stability (CMC)	Stereoregularity ↑ CMC ↑(33-36)	Lower (24, 30, 39-47)
	Stereoregularity ↑ CMC ↓(31, 37, 38)	Equal (48, 49)
Kinetic stability	Stereoregularity ↑ stability ↑(31, 44, 48)(50)	Higher (31, 44, 48, 50)
Morphology	Stereoregularity ↑ cylindrical shape(31, 34, 42, 49, 51, 52)	Cylindrical shape(49)
		Spherical shape (42, 51, 52)
	Coexistence of several shapes(42, 49)	
Size	Stereoregularity ↑ size↓(37, 53)	Smaller (30, 45)
	Independent of stereoregularity(38, 50, 54)	Equal (48)
		Larger (54, 55)
Drug loading	Stereoregularity ↑ loading ↑(36, 44, 49)	Higher (30, 40, 46, 49, 59)
	Stereoregularity ↑ loading ↓(50, 56, 57)	Lower (45)
	Independent of stereoregularity (53, 58)	
Release profile	Stereoregularity ↑ release ↑(31, 36, 53, 57)	Slower (30, 40, 44-46, 49, 59)

	Stereoregularity ↑ release ↓(44, 50)	
Cellular uptake	Stereoregularity ↑ uptake ↑(36)	Higher (59)
	Stereoregularity ↑ uptake ↓(35, 37)	
In vitro toxicity	Stereoregularity ↑ toxicity ↑(36)	Higher (59)
	Stereoregularity ↑ toxicity ↓(35, 37)	Lower (45)
	Independent of stereoregularity (50)	
Tumor accumulation	Stereoregularity ↑ accumulation ↑(50, 60)	Higher (60)
Antitumor efficacy	Stereoregularity ↑efficacy↑ (50)	Comparable to clinical formulation(46)
	Stereoregularity ↑efficacy↓(36)	

1.3 Cisplatin and its Clinical Nano-Delivery Systems in Cancer Treatment

Cisplatin is one of the most widely used anticancer drugs against a broad spectrum of tumors including ovarian, testicular, bladder, colorectal, lung, head and neck and breast cancers (61-63). Cisplatin is a neutral inorganic, square planar complex. The core is a single platinum metal bound to two amino groups and two chlorides that react mostly with DNA (64). Cisplatin is chemically inert until one or both of its cis chloro groups are replaced by water molecules. Once inside the cells, where the chloride concentration is much lower (4–20 mM) than in the bloodstream (100 mM), cisplatin is hydrolyzed yielding monoaqua $[Pt(NH3)_2Cl(H_2O)]^+$ and diaqua complexes $[Pt(NH_3)_2(H_2O)_2]^{2+}$ (**Figure 1.5**)(65, 66). The cytotoxicity of cisplatin is primarily ascribed to interaction of its aquated forms with nucleophilic N7-sites of purine bases in DNA to form DNA–protein and DNA–DNA inter-strand (between strands) and intra-strand (on the same strand of DNA) crosslinks (66, 67). The DNA-platinum adduct is then recognized by over 20 individual candidate proteins, which bind to physical distortions in the DNA that are induced by the platinum adducts (68). The activation of these damage recognition proteins culminates in either repair of the DNA damage and cell survival or activation of the irreversible apoptotic program (69).

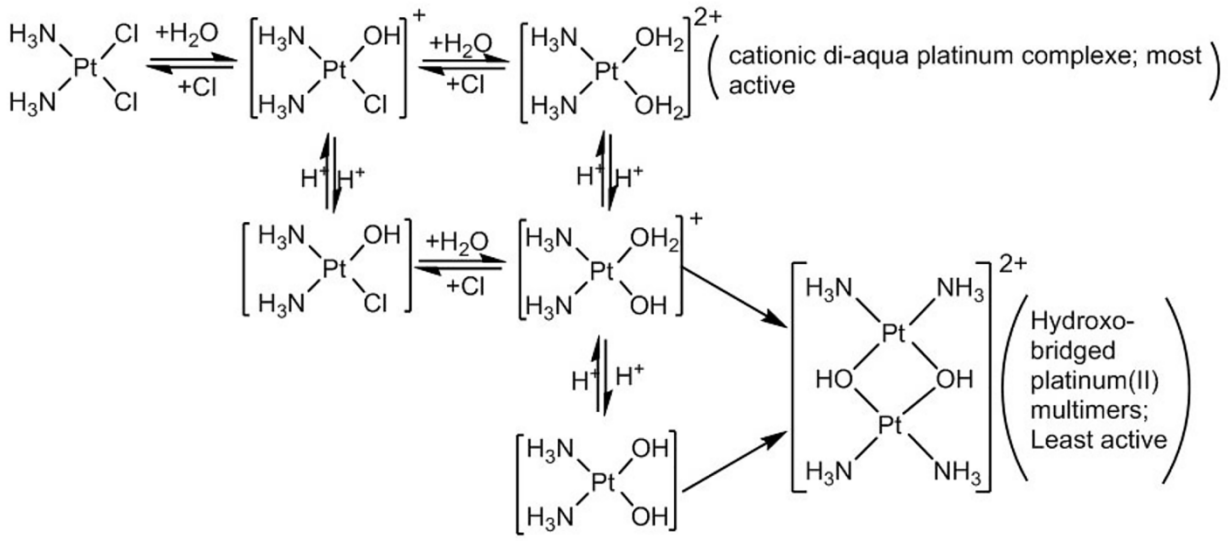

Figure 1.5 Intercellular aquation of cisplatin. Reprinted from Reference (70), Copyright 2016 Biochemical Compounds, Herbert Publications.

The major goal of cancer chemotherapy is to induce tumor cell apoptosis following the exposure of the antitumor agents. Although cisplatin is a very potent inducer of apoptosis (71), resistance and toxicity are two problems associated with its usage in the clinic. Cisplatin therapy is accompanied by severe side effects including renal damage, deafness, and peripheral neuropathy, thus the overall efficacy of the drug cannot be reached due to these side effects. Moreover, many tumors are intrinsically resistant to the platinum drug and fail to undergo apoptosis at clinically relevant drug concentrations. Unfortunately, also for those tumors, which are initially responsive to cisplatin, resistance is likely to develop gradually after initial response. Resistance mechanisms arise as a consequence of intracellular changes that either prevent cisplatin from interacting with DNA, interfere with DNA damage signals from activating the apoptotic machinery, or both. Therefore, the mechanisms of cisplatin resistance can be classified into four categories (72, 73):

1. Pre-target: those interfering with cisplatin transport prior to DNA binding resulting in reduced intracellular drug accumulation (*e.g.*, inactivation of cisplatin transporters, enhanced efflux of cisplatin, and/or increased cisplatin inactivation by endogenous nucleophiles, such as glutathione (GSH), methionine, metallothionein, and protein)

2. On-target: those interfering with generation of an apoptotic signal subsequent to formation of inter- and intra-strand DNA adducts including increased DNA damage repair capacity (e.g. an increase in

nucleotide excision repair (NER)), and/or enhanced tolerance for unrepaired DNA lesions (e.g., loss of DNA mismatch repair (MMR)). The balance of DNA damage and DNA repair dictates death versus survival after cisplatin therapy. Changes in the ability to repair the DNA adduct result in changes in cisplatin sensitivity.

3. Post-target: those interfering with cellular events taking place after DNA platination including defects in initiating or transducing damage signals that normally elicit apoptosis in response to DNA damage (*e.g.*, downregulation of the apoptotic signal through activation of inhibitors of apoptosis) and/or problems with the cell death executioner machinery itself (*e.g.*, dysfunction of tumor-suppressor p53).

4. Off-target: alterations in signaling pathways not directly engaged by cisplatin but interfering with cisplatin induced proapoptotic events including overexpression of human epidermal growth factor receptor 2 (HER-2) and increased activity of phosphoinositol-3-kinase (PI3-K/Akt) pathway.

In general, anti-cancer drug resistance is therefore multifactorial and multiple mechanisms are encountered simultaneously within the same tumor cell, to confer resistance in tumor cells which compounds the difficulty in efforts to circumvent cisplatin resistance as a therapeutic strategy. However, this problem could be overcome by improving and refining the delivery of cisplatin to cancer patients, thus enhancing its activity. Currently, the micellar formulation of a cisplatin (code name NC-6004) is under phase III clinical study (74, 75). In this system, cisplatin was complexed with PEG-poly(L-glutamate) through platinum–carboxylate complex formation, leading to the development of micelles with the size of 30 nm. After systemic administration, cisplatin micelles showed a prolonged circulation and effective tumor accumulation, with reduced side effects. The reversible ligand exchange reaction of platinum (Pt(II)) enables the release of active platinum complexes from the micelles, ensuring their cytotoxic activities (76-78). In summary, these polymeric carriers reduce the toxicity of platinum drugs compared to the free drugs, while their antitumor efficacy was maintained.

In addition to polymeric micelles, liposome-based delivery systems were also examined for cisplatin therapy (Table 1.3). There are three liposomal formulations of cisplatin that entered to the clinical trials. However, only one formulation (lipoplatin) showed very promising efficacy profiles and practical toxicity, while others showed poor performance. For example, SPI-077 was not able to release enough free platinum drugs at certain times to produce the desired anticancer effects. On the other hand, LiPlaCis was withdrawn from trials due to its significant toxicity (70).

Table 1.3 Liposomal formulations of cisplatin in clinical trials. Reprinted from Reference (70), Copyright 2016 Biochemical Compounds, Herbert Publications.

Liposomal formulation	Platinum-based drugs	Liposome	Status	Drug-lipid weight ratio	MTD[a] (mg/m^2)
Lipoplatin	Cisplatin	HSPC[b]/DPPG[c]/DSPE-PEG2000[d]	Phase II/III	1:10	300
SPI-077	Cisplatin	HSPC/cholesterol/DSPE-PEG2000	Phase II	1:70	420
LiPlaCis	Cisplatin	DSPC[e]/DSPG[f]/DSPE-PEG2000	Phase I	--	--

[a] Maximum tolerated dose.

[b] Hydrogenated soy phosphatidylcholine.

[c] DPPG: 1,2-dipalmitoyl-sn-glycero-3-phospho-(1'-rac-glycerol).

[d] DSPE-PEG2000: 1,2-distearoyl-sn-glycero-3-phosphoethanolamine-N-{methoxy(polyethyleneglycol)-2000}.

[e] DSPC: 1,2-distearoyl-sn-glycero-3-phosphocholine.

[f] DSPG: 1,2-distearoyl-sn-glycero-3-phospho-(1'-racglycerol).

1.4 Hypoxia and Cancer

Tumor oxygenation is an important microenvironmental factor in tissue physiology that greatly influences cancer cell biology. Advanced stages of solid tumors contain hypoxic areas which are distributed heterogeneously throughout the tumor mass (79, 80). Hypoxic areas are defined as regions with lower oxygen (O_2) levels than physiological values. Hypoxia happens when the need for oxygen exceeds its supply. In one hand, high consumption rate of rapidly growing tumors lead to decreased amounts of oxygen available locally to the cells. On the other hand, the increase in size of the tumor creates distance between proliferating cells and existing intratumoral blood vessels, thereby progressively increasing the diffusion distance (diffusion-limited hypoxia). Furthermore, the abnormal tumor blood vascular structure results in an insufficient and erratic blood supply so that many tumor regions experience either cycles of acute hypoxia/reoxygenation or chronic hypoxia (perfusion limited hypoxia) (14, 81). Accumulating evidence suggests that the presence of hypoxia within the tumor mass is correlated with poor patient prognosis for various types of cancers (82, 83). Some of these studies demonstrated significantly lower survival for patients with severely hypoxic tumors compared with patients with well-oxygenated tumors. Furthermore, assessment of the oxygenation status of tumors reveals that local recurrences have a higher hypoxic fraction than the respective primary tumors (83). These clinical observations were further supported by experimental studies suggesting a pivotal role of

hypoxia in clonal selection of more tumorigenic (84-86) and chemo and radiant resistant cells (83, 87-90).

1.4.1 Hypoxia and Hypoxia-Inducible Factors

Adaptation of cells under hypoxia happens through the induction of many genes involved in different signaling pathways such as unfolded protein response (UPR), mammalian target of rapamycin (mTOR) and hypoxia-inducing factor (HIF) (91). However, the master regulator of cellular adaptation under hypoxia is believed to be the hypoxia inducible factor (HIF) protein (91-93).

HIFs are heterodimeric transcription factors composed of α (HIF-1α, -2α, and -3α) and β subunits (HIF-1β) (92, 93). HIF-1β is also known as aryl hydrocarbon-receptor nuclear translocator (ARNT), because it was discovered before HIF-1α and was identified as a heterodimeric partner of aryl hydrocarbon receptor (AhR). HIF-1β binds to AhR facilitating its translocation to the nucleus (94).

These two HIF subunits belong to bHLH-PAS protein family, because their structures are related to two nuclear proteins found in Drosophila (Per and Sim, PAS) which have basic-helix-loop-helix (bHLH) motif (95, 96). The bHLH proteins are characterized by having recognizable domains (b, HLH, PAS and TAD). In general, the bHLH-PAS motifs are essential to allow heterodimer formation between HIF-1α and HIF-1β subunits and for binding to the hypoxia response elements (HRE)-DNA sequence on the target genes. Base domains were found to have DNA binding properties required for binding the HRE on the gene, while HLH motifs were found where dimerization with other proteins occurs (**Figure 1.6**).

The HIF-1α subunit has two transactivation domains (TAD): NH_2-terminal (N-TAD) and COOH-terminal (C-TAD). These two domains are responsible for HIF-1α transcriptional activity (97). C-TAD interacts with co-activators such as p300/CBP (cyclic adenosine monophosphate (cAMP)-response-element-binding protein (CREB) binding protein) to modulate gene transcription of HIF-1α under hypoxia. N-TAD is responsible for stabilizing HIF-1α against degradation (98). Moreover, all HIF-α subunits are distinct from HIF-1β in that they all have an oxygen-dependent degradation domain (ODDD) overlapping N-TAD in their structures (**Figure 1.6**). This ODDD domain is important in mediating O_2 regulation stability (99).

Three closely related isoforms of HIF-α have been reported: HIF-1α, HIF-2α, and HIF-3α. HIF-1α and HIF-2α show different pattern of tissue distributions. HIF-1α is ubiquitously expressed in the body, but HIF-2α expression is limited to specific tissues (100). A multitude of HIF-3α isoforms are generated by

alternative splicing and, depending on the particular isoform, may function as an activator or repressor of HIF-dependent transcription (101, 102).

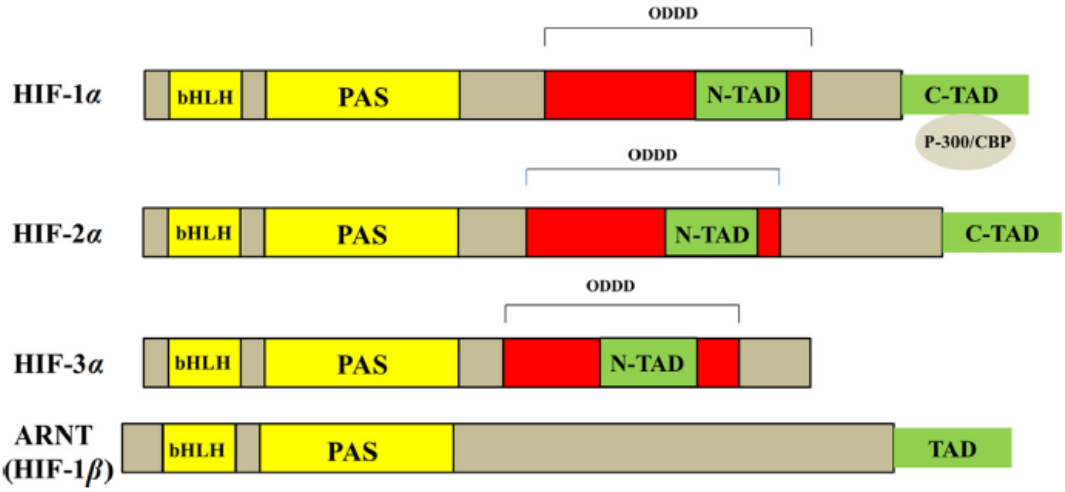

Figure 1.6 Functional domains (bHLH, PAS, TAD) for proteins related to bHLH-PAS family. HIF-1α and HIF-2α share high degree of amino acid sequence similarities and both of them have two distinct TADs (C-TAD and N-TAD). In contrast, HIF-3α only has N-TAD. Reprinted from Reference (103), Copyright 2015 Chinese Pharmaceutical Association and Institute of Materia Medica, Chinese Academy of Medical Sciences.

In contrast to HIF-1β, which is constitutively expressed, the regulation of α-subunits is O_2 dependent and happens post-translationally via prolyl hydroxylases (designated as PHD1, PHD2, PHD3 or PHD4). PHDs are 2-oxoglutarate (2-OG) dependent dioxygenases enzymes which require oxygen for their hydroxylation action, in addition to other co-factors such as iron (Fe(II)) and ascorbate (104). When O_2 is available, PHDs hydroxylate two conserved proline residues (P402/P564) located in the ODDD of HIF-α, which is then recognized by the von Hippel Lindau tumor suppressor protein (pVHL) (92, 104). Moreover, another residue in the ODDD (lysine, K532) could be acetylated by an enzyme called arrest-defective-1 (ARD-1), an acetyl transferase enzyme (105). Although ARD activity does not depend on oxygen availability, the expression of ARD is decreased under hypoxia (105). Consequently, modified HIF-1α subunits with hydroxylated P402/P564 and acetylated K532 moieties are preferably recognized by pVHL. pVHL is a component of an E3 ubiquitin ligase complex, which is responsible for the

ubiquitylation of HIF-α subunits and their subsequent targeting to the 26S proteasome for degradation (**Figure 1.7**).

In addition, a HIF asparaginyl hydroxylase (originally identified as factor inhibiting HIF-1 (FIH-1)) hydroxylates an asparagine residue (N803) located in the C-TAD of HIF-1α, preventing association with the p300/CBP co-activator, thus impairing the proper transcriptional complex formation and eventually reducing its activity (92, 104). A differential in the Km of the PHDs and FIH has been reported suggesting that the PDHs are more readily inactivated by a drop in the oxygen level below normoxic levels than FIH. As tumor cells are progressively distanced from blood vessels the PHD activity will decline leading to accumulation of HIFα but with a lock on the C-TAD due to maintenance of FIH activity at this oxygen level. Thus, if a gene requires only N-TAD activity it will be activated under these conditions and as the oxygen level drops further both PHD and FIH will be inhibited and genes requiring full N-TAD and C-TAD activity will be induced.

In summary, in the presence of oxygen, HIFα is produced, hydroxylated, ubiquitinated and degraded. In contrast, in the absence of oxygen the PHDs that use oxygen in the hydroxylation reaction of HIFα are inactive and consequently HIFα "escapes" hydroxylation, ubiquitination and reaches a higher steady state level. However, stability does not necessarily mean activity. Hydroxylation of HIFα by FIH inhibits its transcriptional activity. Thereby oxygen imposes a double lock on HIFα through control of both stability and activity. Once stabilized, HIFα rapidly translocates to the nucleus and binds its partner HIFβ. Together they bind to target genes through HRE. Finally, the co-activator p300/CBP interacts with the C-TAD of HIFα and transcriptional activity is initiated. Thereby, in the absence of oxygen where the hydroxylases PHD and FIH are inactive, HIF modulates the expression of genes (**Figure 1.7**) (92, 104).

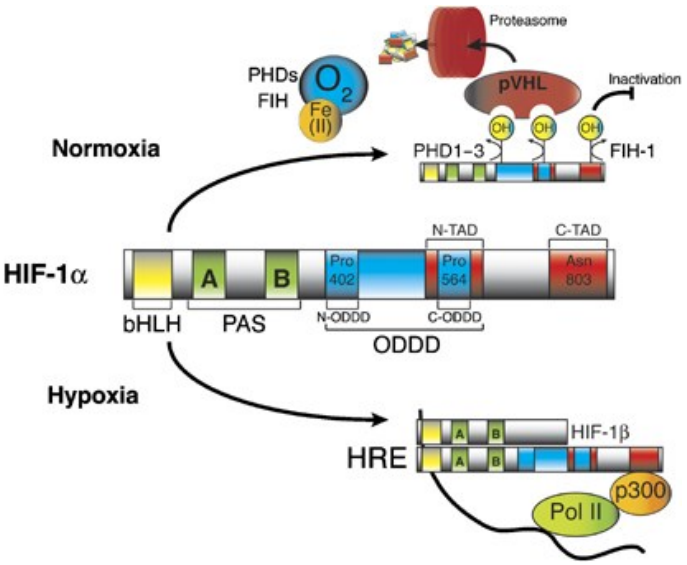

Figure 1.7 Regulation of HIF-1α protein by prolyl hydroxylation and proteasomal degradation. There are three hydroxylation sites in the HIF-1α subunit: two prolyl residues in the oxygen-dependent degradation domain (ODDD) and one asparaginyl residue in the C-terminal transactivation domain (C-TAD). In the presence of oxygen, prolyl hydroxylation is catalyzed by the Fe(II)-, oxygen- and 2-oxoglutarate-dependent PHDs. The hydroxylated prolyl residues allow capture of HIF-1α by the von Hippel–Lindau protein (pVHL), leading to ubiquitination and subsequent proteasomal degradation. Asparaginyl hydroxylation is catalyzed by an enzyme termed as factor-inhibiting HIF (FIH) at a single site in the C-TAD. This hydroxylation prevents cofactor recruitment. In the absence of hydroxylation due to hypoxia or PHD inhibition, HIF-1α translocates to the nucleus, heterodimerizes with HIF-1β and binds to hypoxia-response elements (HREs) in the regulatory regions of target genes. Reprinted with permission from Reference (106), Copyright 2008 Nature.

HIF-1α stabilization can also occur independently of oxygen through growth factors, pro-inflammatory cytokines (*e.g.*, interleukin-1β and tumor necrosis factor-α) (107, 108), other signaling molecules such as Mdm2 (109) and Heat shock protein90 (Hsp90) (110). In non-hypoxic cell, HIF stabilization can also happen via viral proteins (*e.g.*, Hepatitis B and C virus, or Epstein–Barr virus), gain of function of oncogenes, loss of function of tumor suppressor genes and deprivation of metabolic intermediates such as fumarate and succinate (107, 108). Upon activation, HIFs bind to cis-acting DNA sequences (5'–RCGTG-3') of HRE to regulate the expression of target genes, many of which have roles in cancer biology

including: angiogenesis, metabolic reprogramming, genetic instability, senescence, cell survival/apoptosis, cellular pH, and drug resistance (92, 111).

In spite to HIF degradation, HIF-1α synthesis is oxygen independent. The growth factor signaling pathway involving the downstream kinases PI3K/Akt/mTOR represents a major route of HIF-1α translation in human cancer cell lines (112). Synthesis of HIF-1α occurs via PI3K and mitogen activated protein kinase (MAPK) pathways by increasing the rate of translation of HIF-1α mRNA into protein (113).

1.4.2 Hypoxia, HIF-1α and Drug Resistance

The limitations of clinical chemotherapy have been ascribed primarily to mechanisms that mediate drug resistance at the cellular level. Functional gene mutations, gene amplification and epigenetic changes that affect the expression of genes encoding proteins that influence the uptake, metabolism, and export of drugs are important factors contributing to drug resistance. Substantial evidence suggests that tumor microenvironment factors such as hypoxia favor the development of resistance of solid tumors to chemotherapy.

Tumor responsiveness to chemotherapy is influenced both directly and indirectly by the vasculature, which is abnormal both structurally and functionally in solid tumors. Thus, similar to the O_2 scenario, many chemotherapeutic agents have a limited ability to penetrate tumor tissues and cannot reach all layers of tumor cells in a potentially lethal concentration (114-116). In addition, for chemotherapeutic agents that require O_2 to exert their maximum efficacy, oxygen insufficiency is more detrimental. In the presence of oxygen, many anticancer drugs generate free radicals that damage DNA. These drugs accept electrons from biologic sources and then transfer the electrons to oxygen (117). For example, anthracycline drug doxorubicin undergoes chemical reduction to a semiquinone radical, which in turn reduces oxygen to a superoxide that may contribute to cytotoxicity (118). This is supported by the findings that hypoxic cells are significantly more resistant to the agents such as anthracyclines and bleomycins with oxidative damage as their mechanism of action (119, 120). Thus, at low oxygen concentrations the cytotoxicity of the drug whose activity is mediated by free radicals is decreased (121).

While hypoxia can directly limit the efficacy of certain chemotherapeutics, it also upregulates the expression of HIF-1α which regulates the expression of many genes involved in the acquisition of the chemoresistance phenotype of tumor cells (122-133). HIF-1α is causally involved in key aspects of tumor

biology such as angiogenesis, cell survival, resistance to apoptosis, metabolic reprogramming and pH homeostasis (134). Expression of these genes may result in the expansion of populations of cells with altered biochemical pathways that may have a drug-resistant phenotype.

1.4.2.1 HIF-1α Mediated Alterations in Cell Survival and Proliferation

The success of chemotherapy *in vitro* is often measured by the extent of apoptosis triggered in response to cell damage. In the vast majority of cancer cells, HIF-1α functions as a robust suppressor of apoptosis and functional interference with HIF-1α results in enhanced cell death upon treatment with chemotherapeutic agents in tumors of different origins (133, 135-137).

Hypoxia has been shown to promote the emergence of phenotypes resistant to apoptosis through selection for cells that have lost sensitivity to p53-mediated apoptosis. Tumor suppressor p53 protein can bind directly to the ODD domain of HIF-1α, blocking HIF-1α transcriptional activity by competing with HIF-1α for p300 (138). Activation of p53 inhibits HIF-1α protein accumulation by increasing proteosomal degradation, while loss of p53 correlates with increased HIF-1α protein level and increased HIF-1α activity (138). Loss of the tumor suppressor gene p53 enables tumor progression in hypoxic microenvironments, because p53-deficient tumor cells are able to resist hypoxia-induced apoptosis (139, 140).

HIF-1α is also shown to functionally suppress p53 in cell lines and tissues from different origins (111, 140, 141). HIF-1α mediated suppression of intracellular reactive oxygen species (ROS) production served as the molecular mechanism behind reduced p53 stabilization in HIF-1α wild-type cells (111). Functional inactivation of HIF-1α failed to enhance cell death and, hence, chemotherapy efficacy in cells harboring defective p53, raising doubts as to the anti-proliferative efficacy of HIF-1α inhibiting agents in p53-deficient cancer (111, 136).

In breast cancer, p53 is often inactivated because of overexpression of the repressors (*e.g.*, MDM2 and MDMX) (142). Furthermore, almost 50% of breast cancers produce a dysfunctional mutant p53 protein (mtp53) caused by point mutations in the p53 gene which prevent DNA binding, DNA damage-induced cell death and cell cycle regulation (142). Reactivation of p53 through targeting mtp53, MDM2 and MDMX might be suitable strategies in breast cancer treatment, allowing hypoxic cells to be targeted.

Besides apoptosis, the process of autophagy (literally meaning “self-eating”) is increasingly recognized as an important regulator of cellular viability (143). In response to nutrient starvation and metabolic stress, cells are able to produce energy in form of ATP as well as catabolic or anabolic precursors from

internal sources to avoid necrotic or apoptotic cell death through autophagy (144). HIF-1α had primarily been characterized as a central regulator of hypoxia-induced autophagy of mitochondria (mitophagy) during the adaptation of primary cells to hypoxia (145). Later, it was shown that hypoxia induced drug resistance in cancer cells via HIF-1α dependent (122) and independent induction of autophagy (146). Although the precise role of autophagy for tumor formation is still not fully elucidated, it is now widely accepted that autophagy is able to confer failure of anti-proliferative treatment in tumor cells (122, 147-149).

Hypoxia also induces cell cycle arrest which consequently results in slower rate of proliferation of tumor cells with increasing distance from tumor blood vessels (150-152). This effect may be mediated by increase in the levels of cyclin-dependent kinase inhibitor p27 leading to G1/S arrest under hypoxia (153, 154). Most chemotherapeutic drugs that target cell proliferation, are more effective against proliferating than quiescent cells (154). Consequently, slowly proliferating cells at increasing distances from tumor blood vessels are likely to be resistant to therapy. For example, different classes of drugs such as camptothecins, anthracyclines and etoposide (targeting topoisomerases), antimetabolites such as 5-fluorouracil (incorporating into DNA and RNA), vincristine, vinblastine (targeting mitotic spindles through the destabilization of microtubules) or paclitaxel (targeting mitotic spindles through the stabilization of microtubules) are more toxic towards actively proliferating cells.

Cellular senescence is also another mechanism that plays a major role against tumor formation (155). Cellular senescence refers to a naturally irreversible cell-cycle arrest that is induced by signaling from the DNA-damage response (DDR) pathway(156). Many different chemotherapeutic agents show their anti-tumor effect via DDR-induced senescence (123, 157, 158). However, hypoxia is able to counteract drug-induced senescence in a HIF-α dependent manner and ultimately induces drug resistance (123). Furthermore, the role of HIF-1α in suppression of drug-induced senescence was shown under normoxic (111).

It is worthy to note that most primary cells respond to a critical decline of oxygen concentration by inducing cell cycle arrest or apoptosis in a HIF-1α dependent manner (159). However, even within primary cells, there is a great disparity in the response to hypoxia. For example, inflammatory cells such as neutrophils and macrophages need to survive the severely hypoxic conditions of inflamed, infected or wounded areas to function properly. Thus, inflammatory cells have evolved a robust ability to resist hypoxia-initiated apoptosis, achieved largely by HIF-1α mediated stabilization of nuclear factor-kB (NF-kB) and subsequent expression of anti-apoptotic NF-kB target genes (160). It is therefore not surprising

that several pro-apoptotic (e.g. BNIP3, NIX and NOXA) as well as anti-apoptotic factors (e.g. Bak, Bax, Bcl-xL, Bcl-2, Bid, Mcl-1, NF-kB, p53 and survivin) have been identified as regulated by HIF-1α (161-166).

1.4.2.2 HIF-1α Mediated Inhibition of DNA Damage

Genomic instability and DNA damage are hallmarks of cancer (167, 168). Hypoxia in the tumor microenvironment is an accepted driving force of genomic instability. Hypoxia by itself does not inflict any significant DNA damage, however, it interferes significantly with the cellular response to DNA damage (169, 170). The DNA damage response (DDR) pathway aimed at preventing the transmission of damaged DNA, ultimately sustaining integrity of the genome (168). Functional inactivation of DDR and checkpoint genes commonly occurs during cancer progression, resulting in genomic instability and driving malignant progression (171). HIF-1α is at central cross talk with molecules involved in DDR and checkpoint control, such as BRCA1 (breast cancer susceptibility gene 1), DNA-PKs (DNA-dependent protein kinases), ATM (ataxia teleangiectasia mutated gene), and PARP-1 (poly (ADP-ribose) polymerase 1).

BRCA1 has an important role in genome integrity because of its involvement in cell cycle checkpoint control and DNA double strand break (DSB) repair via homologous recombination (172). HIF-1α is able to inhibit BRCA1 activity indirectly, that is, by functionally counteracting c-Myc under hypoxic and normoxic conditions (173). In addition to the process of homologous recombination, DNA DSBs can be repaired via non-homologous end joining. Non-homologous end joining is controlled by the DNA-dependent protein kinase (DNA-PK) complex, three members of which (DNAPKcs, Ku80 and Ku70) have been found to be under transcriptional control by HIF-1α (174).

The DNA damage sensing kinase ATM mediates the primary response to DNA DSBs (168, 175). It was shown that hypoxia results in ATM activation and loss of ATM prevented the stabilization of HIF-1α under hypoxic conditions, establishing ATM as a crucial activator of HIF-1α under hypoxia (176). Akin to ATM, the enzyme PARP-1 functions as a sensor and signal transducer of DNA damage (177) and is central to the process of base excision repair, which reverts more subtle DNA changes, for example, single-strand breaks, oxidative lesions and alkylation products (168, 177). It was shown that PARP-1-dependent activation of HIF-1α relies on the enzymatic activity of PARP-1 and that PARP-1 directly interacts with the HIF-1α protein, ultimately functioning as a transcriptional coactivator under hypoxic conditions (178).

1.4.2.3 HIF-1α Mediated Metabolic Reprogramming

Normal cells convert glucose to pyruvate in cytoplasm and transport it to the mitochondria where it enters the tricarboxylic acid (TCA) cycle (also known as citric acid cycle or Krebs cycle) and then undergoes oxidative phosphorylation. This catabolic pathway yields a high level of ATP but requires oxygen for mitochondrial respiration. However under hypoxia, tumor cells often use the less energy-efficient metabolism. They convert glucose to pyruvate and then into lactate to produce ATP (anaerobic glycolysis) to obtain the energy they need to survive and proliferate. This is similar to metabolic pathway used by muscle tissue when oxygen is low (92, 106). Hypoxic tumor cells in order to obtain enough ATP increase their rate of glycolysis through active HIF-1α that induces the expression of glucose transporters such as glucose transporter 1 (Glut1) and the enzymes involved in glycolysis (92, 106). HIF-1α also induces the expression of pyruvate dehydrogenase kinase (PDK), which inhibits the enzyme pyruvate dehydrogenase by phosphorylation. Thus, pyruvate is not converted into acetylCoA, preventing pyruvate entry into the TCA cycle (179). As a consequence, the mitochondrial oxygen-consumption is downregulated and hypoxic ROS generation is attenuated (180). HIF-1α also drives the reversible conversion of pyruvate to lactate by the HIF-target gene lactate dehydrogenase A (LDH-A) that is up-regulated in cancer cells. The consequence of this cytosolic glucose metabolism is an overload in lactate and CO_2 that contributes to the decrease in the extracellular pH. The lactate produced is excreted from cells through a H^+/lactate cotransporter and the monocarboxylate transporter (MCT), leading to a decrease in the extracellular pH of tumors (181). At least one MCT, MCT4 has been shown to be up-regulated in hypoxia in a HIF-dependent manner (182, 183). In addition, H^+ ions are transported out through the HIF-1α regulated Na^+/H^+ exchanger (NHE1) (**Figure 1.8**). (184).

A parallel increase in the expression of the HIF-induced enzyme the carbonic anhydrases (CA) IX and XII, membrane-bound ectoenzymes that catalyze the reversible conversion of CO_2 to carbonic acid, is also observed. In fact, the expression of the CA IX isoform correlates so well with hypoxia that it is being considered as a marker of hypoxic conditions in certain tumor types. Consequently, substantial interest is also being shown in the immunohistochemical detection of CA IX in tumor sections for prognostic purposes (185). The bicarbonate (HCO_3^-) formed enters cells through the action of the bicarbonate/Cl family of exchangers that re-equilibrate the intracellular pH and contributes further to intracellular alkalinization (92) (**Figure 1.8**).

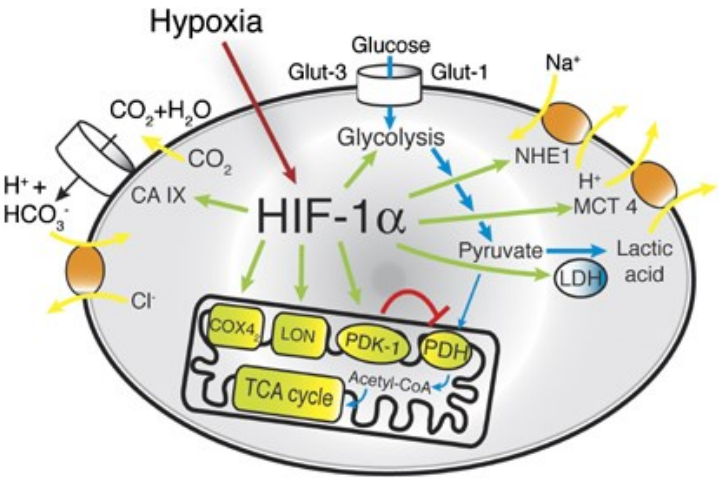

Figure 1.8 HIF-1α controls metabolic and pH-regulating pathways. Cells respond to hypoxia by HIF-1α-mediated upregulation of glucose transporters (Glut-1 and Glut-3) and enzymes of glycolysis. Conversion of pyruvate to lactic acid is facilitated by the induction of lactate dehydrogenase (LDH). HIF-1α also induces pyruvate dehydrogenase kinase-1 (PDK-1), which inhibits the conversion of pyruvate into acetyl-CoA by pyruvate dehydrogenase (PDH), thus preventing entry of pyruvate into the TCA cycle. Furthermore, pH homeostasis is maintained by induction of carbonic anhydrase IX (CAIX) and the monocarboxylate transporter MCT4 and the Na^+/H^+ exchanger NHE1. Reprinted with permission from Reference(106), Copyright 2008 Nature.

The overall consequence of this metabolic reprogramming is that usually tumors have lower extracellular pH (more acidic) than that of normal tissue (6.2-6.8 versus 7.2-7.4) (92). This acidic environment can have a direct impact on the cytotoxicity of anticancer drugs. Uptake of certain drugs occurs through passive diffusion across the cell membrane, which is permitted when these agents are in an uncharged form. However, as a result of the pH gradient established in the tumor microenvironment (*i.e.* low extracellular pH, neutral to slightly alkaline intracellular pH) weakly basic drugs, such as doxorubicin, mitoxantrone, vincristine, and vinblastine become protonated, hindering their passage through the plasma membrane to enter the cell (186, 187). Similarly, active transport of drugs such as methotrexate may also be inhibited by an acidic microenvironment (188).

1.4.2.4 HIF-1α Mediated Regulation of Angiogenesis

Many of the other adaptations that cells undergo in order to survive in the hypoxic environment may also contribute to resistance to chemotherapeutic agents. For example, to stimulate angiogenesis in an

attempt to increase tumor blood flow, HIF-1α induces the expression of vascular endothelial growth factor (VEGF). However, upregulation of VEGF also leads to an increase in vascular permeability (189) and elevated interstitial fluid pressure (IFP) in solid tumors (190).In normal tissues, fluid is removed through a network of lymphatic vessels as well as through the veins. Solid tumors may lack or have fewer functional lymph vessels than normal tissues (191), which contributes to the increased interstitial fluid pressure within them (192-194). Increased interstitial fluid pressure inhibits the distribution of larger molecules by convection (192, 195, 196) and compresses blood vessels such that blood is diverted away from the center of the tumor toward the periphery. Because many tumors have an elevated interstitial fluid pressure and lack a functional lymphatic system, their penetration by most drugs probably relies more on diffusion than convection (195, 197). Convection depends on gradients of pressure (both hydrostatic and osmotic) between the vascular space and the interstitial space; vessel permeability and the surface area for exchange; and the volume and structure of the extracellular matrix. Diffusion of a drug is determined by its concentration gradient in the tumor tissue; by various properties of the drug, including its molecular size and shape and its solubility in water and lipids; by the composition and structure of the extracellular matrix; and by drug consumption, which includes both metabolism and binding of the drug to tissue components (198, 199).

1.4.2.5 HIF-1α Mediated Regulation of Drug Efflux

An additional obstacle for drug accumulation may include hypoxia-induced upregulation of members of the ATP-binding cassette (ABC) transporter protein family, which confer drug resistance through active efflux of a wide range of anticancer agents (200, 201). Multidrug resistance 1 (MDR1/P-gp) is a HIF-1α target gene and a contribution of HIF-1α mediated P-gp expression to hypoxia-induced drug resistance has been observed in a many type of tumor cells including glioma, gastric, breast and colon cancers (131, 202-204). In addition, HIF-1α is known to stimulate expression of breast cancer resistance protein (BCRP/ABCG2) (202, 205). BCRPs are responsible for binding and transporting drug and non-drug substrates such as heme and porphyrins (205). Increased amounts of these molecules can have detrimental effects under hypoxic conditions as elevated intracellular iron content may lead to excessive ROS generation (205, 206). The multidrug-resistance-associated protein 1 (MRP1) constitutes another family of ABC transporter (207) that has been involved in HIF-1α related drug resistance under hypoxic conditions (131, 204, 208). Although the lung resistance protein (LRP) is not an ABC transporter (207), it is also frequently included in discussions of drug resistance, and has been related with HIF-1α mediated drug resistance.

It is worthy to note that ABC transporters have well-established roles in the efflux of GSH-conjugates as well (209). Enzymes such as glutathione-S-transferases (GSTs) contribute to the detoxification of endogenous and exogenous oxidative species, including various chemotherapeutic agents, by conjugating these molecules to GSH to promote their export from the cell (210). Increased levels of the antioxidant GSH is another hypoxia-induced adaptations for protecting tumor cells against oxidative stress and can confer drug resistance to chemotherapeutics such as doxorubicin, cisplatin, melphalan, cytosine arabinoside, and 2-methoxyestradiol, which exert their cytotoxic effects through excessive ROS generation (211-213).

1.4.3 HIF-1α Gene Silencing as a Therapeutic Strategy

Levels of HIF-1α increase in cancerous tissues due to several reasons, the major cause being hypoxic conditions. Other causes of HIF-1α activation can also occur independent of oxygen, for example, via pro-inflammatory cytokines and growth factors, viral proteins, activated oncogenes, loss of tumor suppressor genes and loss of metabolic intermediates of HIF degradation pathway (107, 108). This is shown by the two basic patterns of HIF-1α immunolocalization that are found in human tumors and animal models. In the first pattern, tumor cells distant from blood vessels revealed a heterogeneous pattern of staining for HIF-1α positive cells due to hypoxia-induced HIF-1α stabilization. However, a homogeneous pattern of staining was observed for tumor cells positive for HIF-1α which activation of HIF-1α mediated genetically or virally (214). Whatever be the cause of its activation, HIF-1α has been associated with tumor progression and aggressiveness of tumor. Therefore, there have been great interests in developing inhibitors targeting this pathway.

It is clear that HIF-1α regulation pathway is a highly complex network involving several signaling cascades and overlapping mechanisms, thus development of efficient and, at the same time, well-tolerated drugs that interfere with HIF-1α is the ultimate goal. HIF-1α inhibition can usually be achieved through modulation of one of the following steps: HIF-1α mRNA expression; HIF-1α protein level (protein translation or degradation); HIF-1α/HIF-1β dimerization; HIF-1α-DNA binding (HIF-1α/HRE); or HIF-1α transcriptional activity (CH-1 of p300/C-TAD of HIF-1α) (103) (**Figure 1.9**).

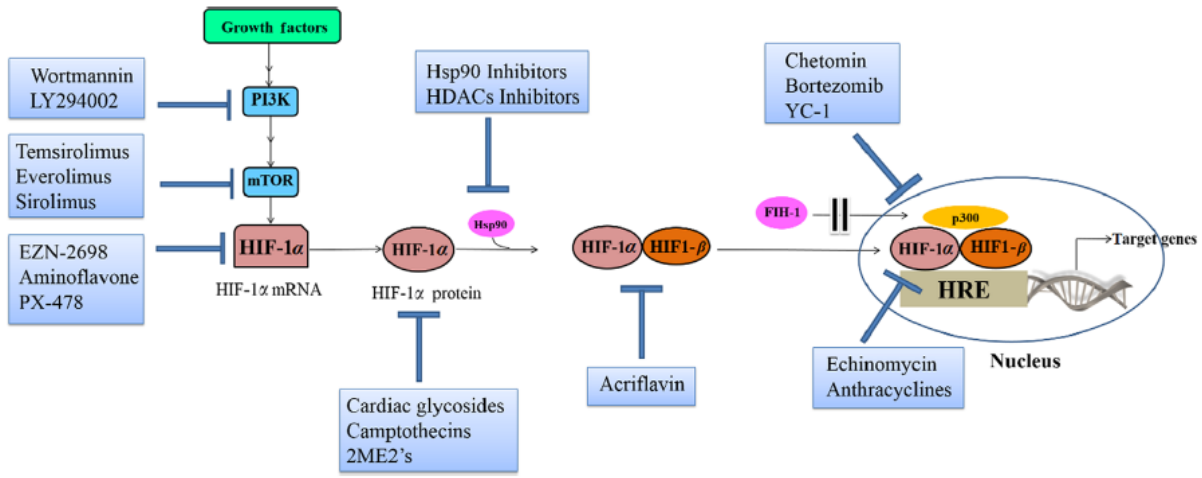

Figure 1.9 HIF-1α inhibitors modulate different level of HIF-1α activation pathway. Reprinted from Reference (103), Copyright 2015 Chinese Pharmaceutical Association and Institute of Materia Medica, Chinese Academy of Medical Sciences.

To date, no selective HIF-1α inhibitor has been clinically approved, partially due to the requirements of targeting protein-protein interactions without affecting other pathways. Nevertheless, there have been several approved drugs that indirectly affect the HIF-1α pathway and could serve as adjuvant therapy for certain types of cancers a long with the existing treatments and some of which are currently being evaluated in phase 1 trials. **Table 1.4** depicts the various small molecules reported as HIF-1α inhibitors in the literature based on their targets, structures and putative mechanisms of action. Most of the reported HIF-1α inhibitors were originally discovered for targeting other endogenous molecules and later their HIF-1α inhibitory activity was recognized through some empirical testing. For this reason, it is uncertain whether the decrease in tumor activity is due to HIF-1α inhibition alone or due the inhibition of other cellular activities. This indicates that these drugs are not very specific in their mode of action. To overcome the problem of non-specificity with HIF inhibitors, HIF silencing by siRNA is another approach which has been carried out *in vitro*, to inhibit the activation of HIF and also study the downstream effects of HIF-1α silencing (123, 127, 130, 131, 215-218).

Table 1.4 Classification of molecules intervening HIF-1α pathway according to their putative mechanism of actions. Reprinted from Reference (103), Copyright 2015 Chinese Pharmaceutical Association and Institute of Materia Medica, Chinese Academy of Medical Sciences.

Mechanism of inhibition	Inhibitor	Target
HIF-1α mRNA expression	EZN-2698 (**1**) Aminoflavone (**2**)	HIF-1α mRNA
HIF-1α translation	*CPTs* (**3**): topotecan (**3a**), EZN-2208 (**3b**), SN38 (**3c**), irinotecan (**3d**)	Topoisomerase I
	Temsirolimus (**4**) Everolimus (**4a**) Sirolimus (**4b**)	mTOR
	LY294002 (**5**) Wortmannin (**6**)	PI3K
	Cardiac glycosides (**7**): digoxin (**7a**), ouabain (**7b**), proscillaridin (**7c**)	HIF-1α protein/HIF-2α mRNA
	2ME2's (**8**): 2ME2 (**8a**), ENDM-1198 (**8b**), ENMD-1200 (**8c**), ENMD-1237 (**8d**)	Microtubules
HIF-1α stabilization	*GAs* (**9**): GA (**9a**), 17-AAG (**9b**), 17AG (**9c**), 17-DMAG (**9d**) Radicicol (**10a**), KF58333 (**10b**) SCH66336 (**11**), Apigenin (**12**)	Hsp90
	Romidepsin (KF228) (**13**) Trichostatin (**14**)	HDAC
	LW6 (**15**)	HDAC/VHL
HIF-1α dimerization	Acriflavin (**16**)	PAS-B
HIF-1/DNA binding	Echinomycin (**17**)	5′-CGTG-3′
	Anthracyclines (**18**): doxorubicin(**18a**), danuorubicin(**18b**)	HRE
HIF-1 transcriptional activity	Chetomin (**19**)	CH1 domain of p300
	Bortezomib (**20**)	C-TAD of HIF-1α and Asn^{803} of FIH
HIF-1α at multiple levels	YC-1 (**21**)	HIF-1&2 protein/FIH
	PX-478 (**22**)	HIF-1&2 protein

In summary, for an effective targeted therapy, including inhibition of HIF activation, two important tasks need to be considered; first, the identification of patient subgroups that are likely to benefit from therapy with targeted drugs; and second, the mechanisms that govern therapy resistance (219). For patient subgroups identification, immunohistochemical determination of nuclear HIF-1α localization should be a suitable method to verify HIF-1α activation in situ. In fact, immunohistochemistry is frequently being applied to analyze HIF-1α activity in human cancer samples (220). To elucidate the mechanisms that govern therapy resistance, characterization of molecular events that could result in diminished anti proliferative efficacy of HIF-1α inhibitors is essential. HIF-1α represents a central pro-tumorigenic factor, and thus HIF-1α inhibition will select for malignant cells with compensatory mechanism for the loss of HIF-1α who has an ability to survive and proliferate in a HIF-1α-independent manner. Support for this idea are the cells with stable functional inactivation of HIF-1α often who do not show any growth defect *in vitro* when compared with the respective wild-type cells. This probably is

due to activation of compensatory mechanisms regulating apoptosis, survival, cell cycle and redox balance upon inactivation of HIF-1α (221, 222).

1.5 Research Proposal

1.5.1 Central Hypothesis

The central hypothesis of this project is that delivering high payload of drug using block copolymer micelles with enhanced physicochemical properties in combination with modulators of chemoresistance can enhance the efficacy of treatment and overcome the problem of chemoresistance.

Two main objectives were set to test this hypothesis:

1) To assess the effect of core/shell modification of polymeric micelles for successful drug delivery to the tumors. For this purpose, the effect of stereoregularity in the core-forming block of polymeric micelles as well as the effect of selection of micellar core segments based on miscibility of drug/core in increasing the physicochemical stability; reducing the rate of drug release; and increasing the content of loaded drug was investigated. Furthermore, the effect of micellar shell modification by covalently conjugating of peptide ligands in active tumor targeting was studied.

2) To expand our understanding of the mechanisms underlying hypoxia-induced chemoresistance (HICR) in a triple negative breast cancer (TNBC) cells and its subpopulations.

3) To assess the effect of ligand modification of polymeric micelles as well as combination treatment with modulators of drug resistance in potentiating the effect of chemotherapy in resistant tumors.

1.5.2 Rationale

Chemoresistance is a multifactorial phenomenon with various underlying mechanisms, such as inadequate pharmacokinetic properties of the drug, tumor microenvironment-related factors, and tumor cell intrinsic resistance (2, 3). Evidence of many different mechanisms of chemoresistance have been reported in the literature, however it remains a great challenge to delineate the pathways involved, and subsequently develop therapies to combat and overcome chemoresistance.

Polymeric micelles are widely used for the delivery of hydrophobic drugs to tumors; however the low stability of these nano-carriers is a major barrier in their success in tumor targeting following systemic administration. Often, premature drug release occurs after systemic administration of these systems because micelles cannot retain their integrity upon introduction to infinite dilution in blood circulation (223). In this thesis, we explored the development of polymeric micelles of high stability, slow release and high drug loading profile to obtain nano-carriers with potentially better passive drug targeting properties to tumor tissues, so that they can overcome the limitations (pharmacokinetics) associated with free drugs, which causes chemoresistance. We also explored combination treatments that can sensitize tumor cells to the effect of chemotherapeutics as means for the modulation of cellular mechanisms of drug resistance in the tumor.

Modification of micellar core-forming block is a popular approach for enhancement of micellar stability (224). The stereoregularity of polymers as building blocks of micelles is believed to affect the arrangement and compactness of the polymer chains within the micellar structure, hence affecting properties like morphology, stability, drug loading, as well as drug release profile(28-32). Stereoregular polymers have a higher likelihood of crystallization in the polymer bulk. On the other hand, atactic polymers make polymeric materials with a higher percentage of amorphous structure. Previous studies have shown an effect of poly(lactide) (PLA) stereoregularity on formation of semicrystalline regions (225). However, the effect of method of synthesis on the preservation of stereoregularity and subsequent micellar stability has not been investigated. Thus, here we studied the effect of polymerization method (bulk versus solution polymerization) on the crystalline structure of the core-forming block in poly(ethylene oxide)-PLA (PEO-PLA) micelles with different stereoregularity of core-forming block and their micellar stability.

Although enhancing the stability of the micellar structure is a crucial step to assure that the encapsulated drug will be kept within the micelles, it is not sufficient. Release of the drug from the micellar carrier must also be controlled to achieve sustained drug release.. In an effort to obtain micelles with enhanced stability, efficient drug encapsulation, and an appropriate drug release profile, we studied the design and development of ABC triblock copolymer micelles by adding of a third block to our AB PEO-PLA diblock copolymer. For the development of this three-layered ABC micelles, the C block was selected from a relatively drug-compatible polymer for efficient solubilisation of our model drug nimodipine. The B block, on the other hand, was selected from a drug-incompatible polymer segment to provide a barrier against drug release (the miscibility of drug/core was predicted by the Flory Huggins

interaction parameter). Thus, poly(α-benzyl-ε-caprolactone) (PBCL) or poly(ε-caprolactone) (PCL), was used as the "C" block to form the micellar inner core because of its excellent solubilisation of nimodipine. PLA, was used as the "B" block to form the micellar outer core acting as a nano-membrane controlling the rate of drug release based on its non-miscibility with the drug (226, 227). With this design in mind, we expected that compatible block at the inner core increased drug loading and encapsulation efficiency while drug incompatible block reduced the initial burst release of drug from the inner core. Furthermore, the effect of stereocomplexation in polymeric micelles (using 1:1 molar blends of oppositely orientated stereoregular block copolymers of PLLA: PDLA) (30, 225) in sustaining the drug release was also assessed.

Hypoxia-induced chemoresistance (HICR) has been observed in a number of human cancer models (228-230). While the mechanism is not well understood, the role of HIF-1α has been highlighted (122-133, 163). Thus, we studied the mechanism underlying HICR to cisplatin in TNBC, MDA-MB-231 cells, since TNBC tumors are known to frequently carry a hypoxic phenotype (231) and cisplatin is a front-line chemotherapeutic agent used to treat TNBC patients (231, 232). In addition, we studied the role of HIF-1α in the generation of intratumoral heterogeneity (conversion of non- tumorigenic cells to tumorigenic cells) under hypoxia (233) using our MDA-MB-231 *in vitro* model to provide a biochemical basis for assumption of tumorigenicity by cells under hypoxia (with chemoresistance being a feature of tumorigenic cells) (234). In this model, a small subset of highly tumorigenic cells can be differentiated from the bulk cell population based on their differential responsiveness to Sox2 reporter (SRR2) with GFP and luciferase as the readouts. Reporter responsive (RR) cells are more tumorigenic as compared to reporter unresponsive (RU) cells (235-237). We exploited the coexistence of hypoxia and high level of epidermal growth factor receptor (EGFR) expression (238-240) to develop EGFR-targeted cisplatin micelles for overcoming HICR to cisplatin. Lastly, we investigated the effect of adding pharmacological inhibitors of key molecules involved in chemoresistance under hypoxic conditions in this cell line, on anti-cancer activity of cisplatin.

1.5.3 Working hypotheses

1) Increasing the stereoregularity of the core-forming block of PEO-PLA block copolymers(which can form cores of higher crystallinity) will increase the thermodynamic and kinetic stability and decrease the rate of dissociation of the generated polymeric micelles when compared with PEO-PLA micelles with atactic (or amorphous) cores.

2) Development of three layered ABC micelles of PEO-PLA-PCL or PEO-PLA-PBCL with drug miscible blocks at the inner core and drug immiscible blocks at the outer core will delay the rate of drug release while providing high amount of drug encapsulated in the polymeric micelles.
3) HIF-1α is a major driver of HICR to cisplatin in MDA-MB-231 cells. Downregulation of HIF-1α can sensitize the cells to cisplatin treatment under hypoxia.
4) HIF-1α is a major driver of intratumoral heterogeneity (conversion of non- tumorigenic cells to tumorigenic cells) under hypoxia in MDA-MB-231 cells. Downregulation of HIF-1α can prevent the generation of tumorigenic cells under hypoxia.
5) Modifying the PEO shell of the cisplatin micelle with the EGFR targeting peptide, GE11 (241), will provide higher uptake in MDA-MB-231 cells when compared with micelles having no modification on the PEO shell. EGFR-targeted cisplatin micelles can be used as a tool to overcome HICR to cisplatin in TNBC.

1.5.4 Specific Objectives

1) To synthesize a library of 6 block copolymers based on PEO-PLA block copolymer with different stereochemistries for core-forming block, L-, meso DL- and racemic-lactides, by two different methods of polymerization (bulk versus solution), and assess the effect of polymerization method on the preservation of core crystallinity; as well as consequent thermodynamic and kinetic stability, size, morphology, drug loading and release of the prepared micelles.
2) To synthesize a library of 12 block copolymers based on PEO-PLA, PEO-PLA-PCL and PEO-PLA-PBCL block copolymers with different stereochemistries for the core-forming block, L-,D-, DL- and racemic-lactides, and assess the effect of stereochemistry of core-forming block, incorporation of third block (PCL or PBCL) and stereocomplexation of oppositely orientated stereoregular block copolymers (PLLA: PDLA containing diblock) on the thermodynamic and kinetic stability, size, morphology, drug loading and release of the prepared micelles.
3) To develop a valid and appropriate experimental model to study HICR in MDA-MB-231 cells and assess the role of HIF-1α protein and other potential pathways in conferring the HICR.
4) To study the effect of hypoxia on the relative proportion, phenotypic and cisplatin resistance characteristics in less tumorigenic RU versus more tumorigenic RR subpopulation of MDA-MB-231 cells and identify the underlying signalling pathways involved in hypoxia induced changes in these two cell subpopulations.
5) To assess: a) the effect of polymeric micellar delivery by plain as well as GE11 modified

polymeric micelles; and/or b) combination treatment with inhibitors of major mediators of drug resistance, identified in previous aims, on the modulation of hypoxia induced drug resistance against cisplatin formulations in MDA-MB-231 cells.

Chapter Two

The Effect of Polymerization Method in Stereo-active Block Copolymers on the Stability of Polymeric Micelles and their Drug Release Profile

A version of this chapter has been published in

Pharmaceutical Research 2014, 31(6):1485-500

2.1 Introduction

Polymeric micelles have been the focus of much interest in research owing to a wide variety of potential applications in pharmaceutical and biomedical field (243-246). In pharmaceutical field, the interest is especially keen on their potential use for solubilization of poorly soluble drugs, sustained drug release following parenteral administration and/or drug targeting (247, 248). For sustained and targeted drug delivery, development of biocompatible and biodegradable polymeric micelles with improved thermodynamic as well as kinetic stability, high capacity for drug solubilization and a slow or delayed rate of drug release are desirable properties.

Although polymeric micelles are superior to their low molecular weight surfactant counterparts in terms of thermodynamic and kinetic stability, their stability profile has yet to present the optimal characteristics (248). Often premature drug release occurs after systemic administration either because the polymeric micellar structure cannot retain their integrity upon introduction to infinite dilution in blood circulation, or because the drug cannot be kept within the micellar carrier (223). Retaining integrity is essential for prolonging the circulation time of polymeric micelles, attaining sustained drug release and/or preferential accumulation of polymeric micelles in the target (*e.g.*, tumor or inflammation) sites. Holding the drug by the micellar carrier, on the other hand, will ensure similar fate and distribution for the encapsulated drug to that of the micellar carrier.

The aim of this study was to assess the effect of polymerization method (bulk versus solution polymerization) on the crystalline structure of the core-forming block in stereoactive block copolymers; and to evaluate the eventual influence of core crystallinity on micellar stability and drug release profile. Polymeric micelles with a poly(lactide) (PLA) segment are suitable candidates for such studies. Lactide has two chiral carbons in its structure and three different enantiomers; *i.e.*, L-lactide, D-lactid and meso-D/L-lactide. Polymerization of either L-, D- or meso D/L- lactide under mild conditions is expected to lead to the production of poly(L-lactide) (PLLA), poly(D-lactide) (PDLA) or poly(D/L-lactide) (PD/LLA), respectively, which are mostly stereoregular (*i.e.*, either isotactic or syndiotactic) (**Figure 2.1**). The stereoregular PLAs can theoretically form semicrystalline core structures in PEO-PLA polymeric micelles. On the other hand, polymerization of a mixture of L- and D-lactide can lead to the production of poly(D, L-lactide) (PDLLA) (**Figure 2.1**) with less or no degree of stereoregularity (*i.e.*, atactic polymers), which are known to form majorly amorphous polymeric micellar cores (249).

Previous studies have shown an effect for the stereoregularity of PLA segment on the kinetic stability (225) and release behavior of assembled polymeric micelles (250). Enhanced resistance against sodium

dodecyl sulfate (SDS) induced dissociation for PEO-PLLA micelles that had stereoregular cores compared to PEO-PDLLA micelles with no stereoregularity in their core has been reported (225). In addition, a lower partition coefficient for pyrene in stereoregular and crystalline cores compared to those with no stereoregularity in the core and amorphous structures has been observed (251). Other studies have indicated an effect for the degree of crystallinity of the PLA block on the rate of drug release from PLA-PEO-PLA micelles, where the release rates of sulindac and tetracaine was shown to be much faster from micelles with semicrystalline PLA cores as compared to those with amorphous ones (250). In this chapter, the effect of polymerization method on the crystallinity of the PLA block in methoxy poly(ethylene oxide)-poly(lactide)(PEO-PLA) block copolymers of different stereoregularity was investigated. The eventual effect of PLA crystallinity on the stability of polymeric micelles and their release profile for a model hydrophobic drug, *i.e.*, nimodipine, at different loading levels was then evaluated. For this purpose, diblock copolymers consisting of methoxy PEO and PLAs of different stereoregularity (**Figure 2.1**) were prepared by either bulk or solution polymerization using stannous octoate as catalyst. This led to the production of block copolymers with different degrees of crystallinity in the PLA block. Nimodipine, a second-generation dihydropyridine calcium antagonist with apparent selectivity for cerebral blood vessels (252) was selected as a model hydrophobic drug for incorporation in polymeric micelles. This choice was made based on the results of our previous study where molecular dynamics (MD) simulation have shown a preferential interaction of nimodipine with the core (rather than the shell) forming block in a series of micelle-forming block copolymers (227). The effect of the degree of PLA crystallinity on the kinetic stability of polymeric micelles and the release profile of nimodipine from the micellar carrier at various drug loading levels was then investigated.

2.2 Materials and Methods

2.2.1 Materials

L-lactide (98%) and meso D/L-lactide (99%) were purchased from Alfa Aesar, Lancashire, UK. D-lactide (98%) was a generous gift from Purac, Schiedam, Netherlands. Methoxy-PEO 5000 (MePEO), sodium dodecyl sulfate (SDS) and tin(II) bis(2-ethylhexanoate) (stannous octoate) were obtained from Sigma, St Louis, MO, USA. Stannous octoate was dried and purified using anhydrous magnesium sulfate, dry toluene and vacuum distillation (253). All other chemicals and reagents used were of analytical grade.

2.2.2 Synthesis of Diblock Copolymers in Bulk

L-lactide, D-lactide, meso D/L lactide and MePEO 5000 were dried in a vacuum oven at 65 °C overnight. Diblock copolymers of MePEO (as the hydrophilic block) and poly(L-lactide) (PLLA), poly(D/L-lactide) (PD/LLA) and poly(D, L- lactide) were prepared using a ring opening polymerization reaction using L-lactide, meso-lactide or a 50-50 racemic mixture of L-lactide and D-lactide. The prepared diblock copolymers are abbreviated as PEO-PLLA, PEO-PD/LLA and PEO-PDLLA 50-50 in the chapter, respectively (**Figure 2.1**). Briefly, MePEO (0.5 g, 0.1 mmol) was reacted with (L-lactide), (D/L-lactide) (0.5 g, 3.4 mmol) or a 50-50 ratio of L-lactide and D-lactide (total weight 0.5 g), in an ampule using 5 mg (0.5% w/w) of stannous octoate as catalyst. The ampule was then sealed and left at 160 °C for 7 h. The obtained product was dissolved in dichloromethane, and precipitated by adding n-hexane, dried at room temperature in a vacuum oven overnight and washed with anhydrous ethyl ether. This was followed by drying in a vacuum oven at room temperature overnight.

2.2.3 Synthesis of Diblock Copolymers in Solution

To prepare diblock copolymers of PEO-PLLA, PEO-PD/LLA and PEO-PDLLA 50-50 in solution, MePEO (0.5 g, 0.1 mmol) was reacted with (L-lactide), (D/L-lactide) (0.5 g, 3.4 mmol) or a 50-50 ratio of L-lactide and D-lactide (total weight 0.5 g), respectively, in 10 mL of dry toluene. Purified stannous octoate (5 mg, 0.5 w % of the weight of reactants) was added to the solution. The reaction mixture was refluxed for 24 h. The synthesized polymers were precipitated in n-hexane, dried at room temperature in a vacuum oven overnight. The copolymers were washed using anhydrous ethyl ether and dried under vacuum at room temperature.

2.2.4 Self-assembly of Prepared Block Copolymers

Preparation of colloidal dispersions from synthesized block copolymers was tried by the co-solvent evaporation method, adding an organic solvent to water. Briefly, the diblock copolymer (20 mg) was dissolved in tetrahydrofuran (THF) (2.5 mL). After sonication for 10 min, this solution was added dropwise to 5 mL deionized water while stirring. The solution was stirred for 24 h under a fume hood to remove the organic solvent by evaporation.

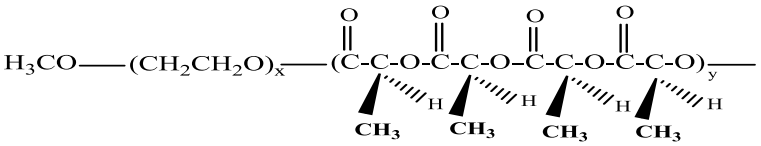

Isotactic PLLA

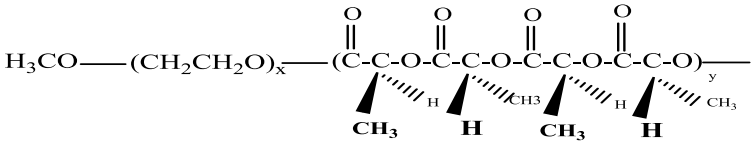

Syndiotactic PD/LLA

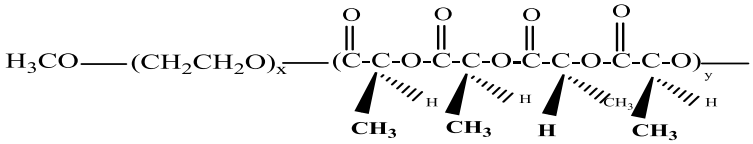

Atactic PDLLA 50-50

Figure 2.1 The schematic model of synthesized diblock copolymers having isotactic PLLA, syndiotactic PD/LLA and atactic PDLLA 50-50 structures.

2.2.5 Characterization of Block Copolymers and their Self-assembled Structures

2.2.5.1 ^{1}H NMR Spectroscopy

^{1}H NMR was performed on a Bruker, ASEND^{TM} 600 MHz spectrometer. Polymers were dissolved in $CDCl_3$ or assembled in D_2O at a concentration range of 1-4 mg/mL. ^{1}H NMR spectra were recorded using $CDCl_3$ as the solvent and dimethyl sulfone as the internal standard, respectively. All integrations were referenced to proton peaks for the internal standard at about δ = 3.0 ppm.

2.2.5.2 Gel Permeation Chromatography (GPC)

The poly dispersity index of the copolymers were determined at room temperature by GPC using a Shimadzu LC-10AD HPLC pump and M302 triple detector array (Viscotek Corp., Houston, TX) connected to a 10 µm Waters Strygel HT3 column. The mobile phase was THF with a flow rate of 1 ml/min. The injection volume of the sample was 20 µL at a polymer concentration of 1 % (w/v). The molecular weights of the polymers were determined relative to polyethylene glycol standards using the universal calibration and OmniSEC 4.7 software (Malvern Instruments Ltd., Malvern, UK).

2.2.5.3 Determination of Thermal Behavior of Copolymers and their Micelles

The melting and crystallization temperatures as well as corresponding enthalpies for block copolymers and polymeric micelles (empty and drug loaded freeze-dried ones) were identified by Differential Scanning Calorimetry (DSC), Q2000-1576, TA Instrument. The heating rate was 2°C/min under nitrogen atmosphere. Samples were weighed (3-5 mg) in Tzero aluminum pans. To determine reproducibility, melting temperatures and enthalpies were measured in three cycles. First cycle was from 8 °C to 170 °C, second cycle was from 170 °C to 8 °C and third cycle was from 8 °C to 170 °C.

2.2.5.4 Determination of Optical Activity of Block Copolymers

Specific rotation, [α], of various diblock copolymers was determined in dimethyl sulfoxide (DMSO) at a concentration of 1 g/dL at room temperature using Perkin-Elmer 241 polarimeter at a center wavelength of 589 nm.

2.2.5.5 Determination of Critical Micellar Concentration (CMC)

The CMC of diblock copolymers was determined using pyrene as the fluorescent probe. From a stock solution of 0.435 mM pyrene in acetone, a 1 µM solution was prepared by serial dilution. Aliquots of this solution (1.8 mL) were transferred to glass vials and the solvent was allowed to evaporate under vacuum while protected from light overnight. A series of polymer solution (0.060 to 125 µg/mL) in deionized water were added to the vials. The final pyrene concentration in each vial was 0.6 µM. The solutions were heated in water bath for 1 h at 65 °C and then cooled overnight. Nitrogen gas was used for deoxygenation of solutions prior to measurements. Excitation fluorescence spectra of pyrene was recorded between 300 to 360 nm, keeping the emission wavelength and excitation slit at 390 and 5 nm, respectively. The ratio of fluorescence intensity of pyrene excitation peak at 337 nm over the one at 334 nm was plotted vs. logarithm of the polymer concentration. The intersection of the two linear graphs in the sigmoidal curve, *i.e.*, the onset of a rise in the excitation fluorescence intensity ratio of pyrene, was defined as the CMC value.

2.2.5.6 Determination of the Size of Self-assembled Structures

The hydrodynamic diameter of assembled structures with or without drug at a polymer concentration of 4 mg/mL was measured using dynamic light scattering (DLS) ZETA-Sizer Nano (Malvern Instruments Ltd., Malvern, UK). The analysis was performed at a scattering angle of 173° at 25 °C at least three times.

2.2.5.7 Determination of the Morphology of Self-assembled Structures

Transmission electron microscopy (TEM) (FEI Morgagni ™ 268, North America NanoPort, Oregon, USA) was used to observe the morphology of self-assembled structures. For TEM measurements, the polymer concentration in micellar solutions was 1 mg/mL. Samples were placed onto copper grid, dried at room temperature, and examined using TEM by negative staining with 4% -uranyl acetate.

2.2.5.8 Assessing the Kinetic Stability of Nanostructures

The micellar solutions (1 mg/mL) were mixed with sodium dodecyl sulfate (SDS) (20 mg/mL) at a 2:1 v/v ratio. Scattered light intensity and polydispersity index (PI) were measured at different incubation time intervals using ZETA-Sizer Nano (Malvern Instruments Ltd., Malvern, UK) at scattering angle of 173° at 25 °C.

2.2.5.9 Encapsulation of Nimodipine in Polymeric Micelles

Drug-loaded polymeric micelles were prepared using the same procedure as described for the self-assembly conditions, except nimodipine (1 or 2 mg) was dissolved along with the block copolymers in THF. After the evaporation of THF, the micelle solution was centrifuged to remove the precipitated drug. To measure the concentration of loaded drug, UV spectroscopy was used. First, micellar solution was diluted with equal volume of methanol. Nimodipine concentration was measured by UV spectroscopy at 357 nm against a calibration curve plotted at 5-120 µg/mL nimodipine concentration in methanol: water 50:50 solution (227). The level of encapsulated nimodipine was calculated by multiplying nimodipine concentration by sample volume while taking the dilution factors into consideration. The encapsulation efficiency (EE) and drug loading (DL) percentages were calculated from the following equations.

$$EE\ (\%) = \frac{the\ amount\ of\ encapsulated\ nimodipine}{the\ total\ feeding\ amount\ of\ nimodipine} \times 100$$

$$DL\ (\%) = \frac{the\ amount\ of\ encapsulated\ nimodipine}{the\ total\ amount\ of\ polymer} \times 100$$

For block copolymers prepared in bulk, encapsulation of nimodipine was also tried by adding water (5 mL) to a solution of nimodipine (1 or 2 mg) and polymer (20 mg) in THF (2.5 mL).

2.2.5.10 Assessing the *in vitro* Drug Release

A dialysis bag (Spectraphor, Mw cutoff 3500 g/mol) containing 5 mL of the drug-loaded micelle solution was placed in 500 mL deionized water at 37 °C in a Julabo SW 22 shaking water bath (Seelbach, Germany). At predetermined time intervals, 200 µL of the dialysis bag content was collected and diluted

with methanol. The 500 mL deionized water in the recipient media was taken out and replaced by fresh water at the same time interval. The concentration of nimodipine that in the dialysis bag, at each time point, was determined by UV spectroscopy (Beckman Coulter DU 730) at 357 nm. The remaining drug concentration was subtracted from the initial concentration of the drug and used to plot the cumulative drug release (%) versus time.

2.2.6 Statistical Analysis

Statistical analysis was performed either using unpaired Student's *t*-test or one way ANOVA with *Tukey* post-test analysis. The significance level (α) was set at 0.05. For non-linear regression analysis, Graphpad prism was used (version 5.00, Graphpad Software Inc., La Jolla, CA, USA). All experiments were conducted in triplicate unless mentioned otherwise in the text, Tables or Graphs.

2.3 Results

2.3.1 Characterization of Synthesized Block Copolymers

2.3.1.1 ^{1}H NMR Spectroscopy

The ^{1}H NMR spectra of synthesized PEO-PLLA, PEO-PD/LLA and PEO-PDLLA 50-50 diblock copolymers prepared by bulk polymerization are shown in **Figure 2.2 a-c**. Similar spectra were obtained for polymers prepared by solution polymerization (**Figure 2.S1 a-c**). Signals at 3.7, 3.4, 5.2 and 1.5 ppm in ^{1}H NMR spectra correspond to protons in CH_2 (b), CH_3 (a), CH (c) and CH_3 (d), respectively. The molecular weight of PLLA, PD/LLA and PDLLA 50-50 segments was determined from the ^{1}H NMR spectra by examining the peak intensity ratio of methine proton of the PLA segment (CO<u>C</u>H(CH_3)O: δ = 5.2 ppm) and the methylene protons of MePEO (OC<u>H</u>$_2$C<u>H</u>$_2$: δ=3.7 ppm). The theoretical and calculated molecular weights for block copolymers were similar for both methods of polymer synthesis (**Table 2.1**).

a

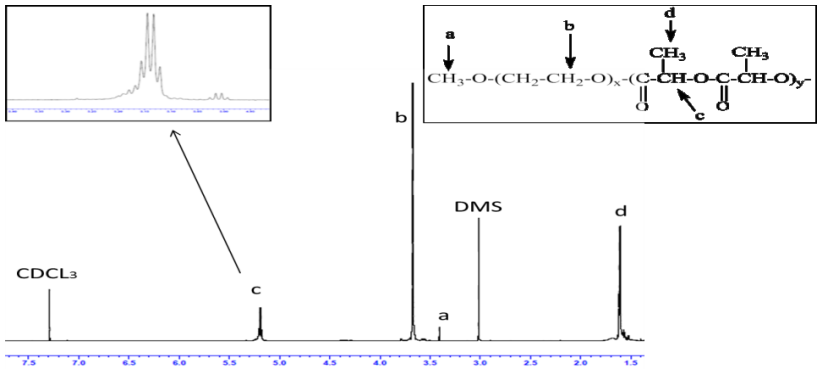

b

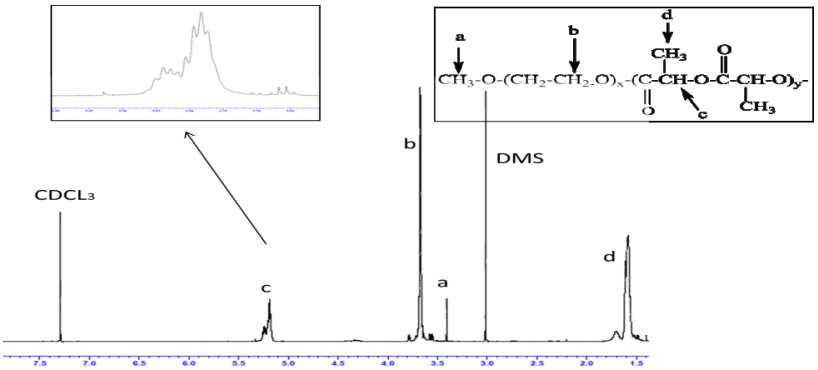

c

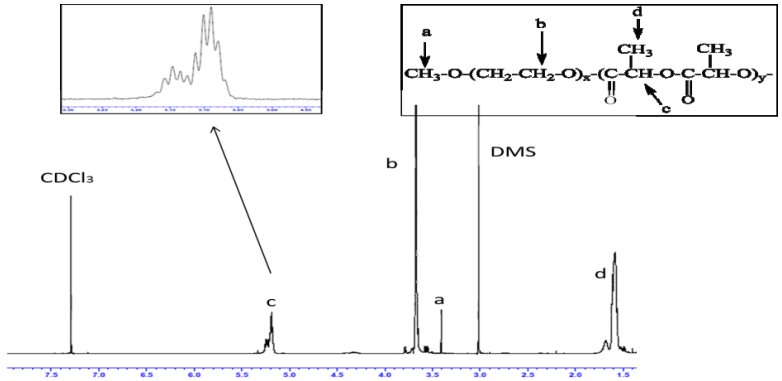

Figure 2.2 ^{1}H NMR spectra and peak assignments for **(a)** PEO-PLLA; **(b)** PEO-PD/LLA; and **(c)** PEO-PDLLA 50-50 block copolymers in $CDCl_3$ with dimethyl sulfone (DMS) as the internal standard.

2.3.1.2 Optical Activity of Copolymers

PEO-PLLA copolymer yielded high optical purity irrespective of the method of polymerization. This was revealed by a high specific rotation in the block copolymer (-53, 38 % of pure PLLA) which was reflective of the corresponding w % of PLA block (42 %) in the block copolymer structure under study (**Table 2.1**), whereas PEO-PD/LLA and PEO-PDLLA 50-50 diblock copolymers were racemized in both methods of polymerization. Optical purity of the PLLA block was significantly higher in the PEO-PLLA copolymer synthesized by solution polymerization compared to PEO-PLLA of bulk polymerization (Student's *t* test, $p<0.05$). Racemization of lactide can occur at high temperatures used in bulk polymerization (249, 254) leading to lower optical activity of PLLA.

Table 2.1 Characteristics of synthesized block copolymers.

Polymer	Polymerization method	Theoretical M.wt. ($g.mol^{-1}$)	M_n ($g.mol^{-1}$) [a]	M_w/M_n ± SD [b]	PLA (w %) [c]	[α] ± SD [d]	[α]/140 (%) [e]
PEO-PLLA	Bulk	9968	8582	1.46 ± 0.06	42	- 53 ± 0.08*	38 ± 0.06
PEO-PD/LLA			8629	1.24 ± 0.05	42	0.64 ± 0.05	0.5 ± 0.01
PEO-PDLLA 50-50			8629	1.30 ± 0.11	42	- 4 ± 0.01	2.0 ± 0.01
PEO-PLLA	Solution		9224	1.52 ± 0.10	46	-59 ± 0.04*	42 ± 0.02
PEO-PD/LLA			7845	1.30 ± 0.13	36	0.97 ± 0.03	0.7 ± 0.01
PEO-PDLLA 50-50			7868	1.34 ± 0.09	36	- 2 ± 0.02	1.4 ± 0.01

[a] Number- average molecular weight measured by ^{1}H NMR

[b] Measured by GPC, relative to polyethylene glycol standard

[c] $\frac{The\ number\ average\ molecular\ weight\ of\ PLA}{The\ number\ average\ molecular\ weight\ of\ polymer\ as\ determined\ by\ H\ NMR}$ ×100

[d] Specific optical rotation of diblock copolymer measured in DMSO

[e] $\frac{Specific\ optical\ rotation\ of\ diblock\ polymer}{Optical\ rotations\ of\ highly\ pure\ polylactide} \times 100$. The reported optical rotations of enantiomerically highly pure PLLA and PDLA typically lie between |140| and |156|(249, 255-257).

* Means optical purity of the PLLA block was significantly higher in the PEO-PLLA copolymer synthesized by solution polymerization compared to PEO-PLLA of bulk polymerization (Student's *t* test, $p<0.05$).

2.3.1.3 Thermal Behavior of Copolymers

Thermal behavior of block copolymers polymerized in bulk and solution were investigated using DSC. To determine reproducibility, melting temperatures and enthalpies were measured at a heating rate of 2 °C/min in three cycles. The thermograms of the second and third cycles are shown in **Figure 2.3a** and **3b** for clarity of presentation. Homo-polymer of PEO showed a melting peak at 63.53 °C. Crystallization of the PEO occurred after slow cooling of the homo-polymers from the melt at 44.78 °C. The enthalpies of melting and crystallization for the PEO homo-polymer were 216 and 189 J/g, respectively. The melting and crystallization temperatures and enthalpies for PEO in the block copolymers were reduced irrespective of the stereochemistry of the PLA block or the method of PLA copolymerization (**Table 2.2**). This indicates a lower degree of PEO crystallinity in the copolymer, possibly due to the interference of the PLA block with the crystallization of MePEO (258). The interference of core forming block in

crystallization of PEO seem to be higher for PLLA than PD/LLA or PDLLA 50-50 (ΔH of crystallization and melting of PEO is lower in PEO-PLLA compared to PEO-PD/LLA and PEO-PDLLA 50-50, irrespective of polymerization method, **Table 2.2**). This may indicate a better interaction between crystalline segments of core forming block (which is higher in PLLA compared to PD/LLA and PDLLA 50-50) and PEO chains leading to interference in the crystalline PEO structure.

Crystallization of the PLA segment was not detected for PEO-PD/LLA or PEO-PDLLA 50-50 block copolymers irrespective of the method of polymerization (**Figure 2.3**). Only PEO-PLLA showed crystallization and melting peaks for the PLA segment. The PLLA related crystallization and melting peaks were observed at 75.1 and 126.9 °C, respectively, for PEO-PLLA copolymers prepared by bulk polymerization. For polymers prepared by solution polymerization, crystallization and melting peaks were observed at 107.5 and 148.0 °C, respectively. The degree of crystallinity in the hydrophobic block is significantly higher for PEO-PLLA block copolymers synthesized through solution polymerization with ΔH crystallization of 16.7 versus 9.5 J/g for solution and bulk polymerized PLLAs, respectively (Student's *t* test, $p<0.05$) (**Table 2.2**).

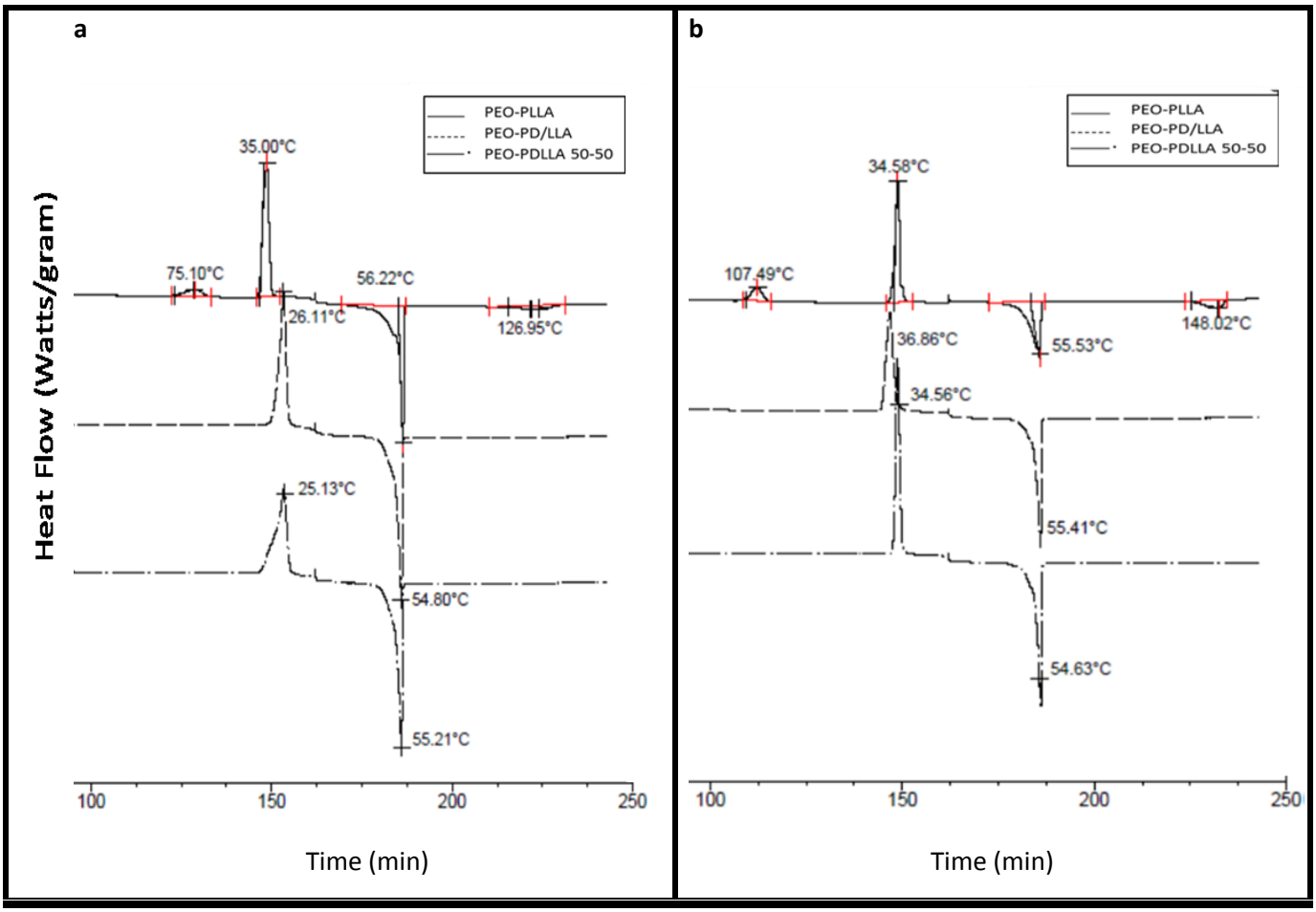

Figure 2.3 DSC thermograms of diblock copolymers polymerized in **(a)** bulk and **(b)** solution.

To determine reproducibility, melting temperatures and enthalpies were measured at a heating rate of 2 °C/min in three cycles. The thermograms of the second and third cycles are shown.

Table 2.2 Thermal properties of the diblock copolymers polymerized in bulk and solution.

Polymerization Method		$T_{m,PEG}$ ± SD (°C) [a]	$\Delta H_{m,PEG}$ ± SD (J/g)	$T_{cr,PEG}$ ± SD (°C) [b]	$\Delta H_{cr,PEG}$ ± SD (J/g)	$T_{m,PLA}$ ± SD (°C)	$\Delta H_{m,PLA}$ ± SD (J/g)	$T_{cr,PLA}$ ± SD (°C)	$\Delta H_{cr,PLA}$ ± SD (J/g)
PEO		63.53 ± 0.15	216.0 ± 0.89	44.78 ± 0.56	189.1 ± 0.10	-	-	-	-
PEO-PLLA	Bulk	56.22 ± 0.13	70.0 ± 1.21	35.00 ± 0.91	66.9 ± 0.97	126.9 ± 1.35	8.3 ± 0.73#	75.1 ± 0.31	9.5 ± 0.34*
PEO-PD/LLA	Bulk	55.02 ± 1.15	80.5 ± 0.79	26.13 ± 0.75	77.9 ± 1.69	-	-	-	-
PEO-PDLLA 50-50	Bulk	54.91 ± 0.78	81.6 ± 1.78	25.44 ± 0.56	79.3 ± 1.01	-	-	-	-
PEO-PLLA	Solution	55.53 ± 0.43	68.5 ± 3.39	34.58 ± 0.89	67.6 ± 0.45	148.0 ± 1.64	16.4 ± 0.86#	107.5 ± 0.42	16.7 ± 0.87*
PEO-PD/LLA	Solution	55.37 ± 1.20	85.7 ± 1.07	39.87 ± 0.64	84.1 ± 1.38	-	-	-	-
PEO-PDLLA 50-50	Solution	55.25 ± 0.96	92.1 ± 1.89	35.30 ± 3.29	90.8 ± 1.66	-	-	-	-

[a] Melting point (T_m)

[b] Crystallization temperature (T_{cr}).

Means $\Delta H_{m,PLA}$ of PEO-PLLA copolymer synthesized by solution polymerization was significantly higher compared to PEO-PLLA of bulk polymerization (Student's *t* test, $p<0.05$).

*Means $\Delta H_{cr,PLA}$ of PEO-PLLA copolymer synthesized by solution polymerization was significantly higher compared to PEO-PLLA of bulk polymerization (Student's *t* test, $p<0.05$).

2.3.2 Characterization of Self-assembled Structures

The characteristics of the self-assembled structures prepared from block copolymers of this study are reported in **Table 2.3**. Irrespective of the method used for the polymerization of block copolymers, the Z average diameter of their self-assembled structures was below 50 nm and with a relatively narrow

polydispersity in micellar size distribution. All block copolymers showed a CMC in µg/mL range. Among different block copolymers prepared by bulk polymerization, PEO-PDLLA 50-50 showed a significantly higher CMC (One way ANOVA, $p<0.05$). This result is in line with previous findings in which stereo-regularity in the hydrophobic block led to decrease in CMC. This observation was attributed to the facilitation of micelle formation by polymeric cores capable of forming semicrystalline structure (20). In line with this explanation, polymers prepared in solution have shown significantly lower CMCs compared to those prepared in bulk (Student's *t* test, $p<0.05$). However, no significant difference in CMC of polymers prepared by solution polymerization was observed irrespective of the stereochemistry of the core forming. This could be due to the low sensitivity of the method of CMC determination used in our study.

Table 2.3 Characteristics of assembled structures from block copolymers under study.

Polymer	Polymerization method	Diameter ± SD[a] (nm)	PI	CMC ± SD (µg/ml)
PEO-PLLA	Bulk	44.9 ± 1.3	0.252 ± 0.061	0.625 ± 0.014[#]
PEO-PD/LLA		28.5 ± 1.0	0.184 ± 0.162	0.606 ± 0.050[#]
PEO-PDLLA 50-50		24.2 ± 3.7	0.129 ± 0.038	0.952 ± 0.014[#]*
PEO-PLLA	Solution	43.9 ± 4.5	0.269 ± 0.078	0.352 ± 0.020
PEO-PD/LLA		39.13 ± 6.2	0.226 ± 0.010	0.335 ± 0.043
PEO-PDLLA 50-50		41.2 ± 2.5	0.293 ± 0.078	0.359 ± 0.024

[a] Z average measured by DLS.

* Means PEO-PDLLA 50-50 copolymer showed a significantly higher CMC among other polymers prepared in bulk polymerization (one way ANOVA with Tukey post-test, $p<0.05$)

[#]Means polymers prepared in bulk have shown significantly higher CMCs compared to those prepared in solution (Student's *t* test, $p<0.05$).

The morphology of empty polymeric micelles from polymers synthesized by bulk polymerization was spherical and uniform in most cases except for the PEO-PDLLA 50-50 where a tendency for micellar aggregation was apparent (**Figure 2.4a**). Moreover, for polymeric micelles from PEO-PLLA polymers

synthesized by solution polymerization in addition to spherical particles, rod and worm-like micelles were also observed (**Figure 2.4b**). Worm micelles from PEO-PLLA polymers prepared in solution were observed in different sections of TEM sample (**Figure S2.3**).

This phenomenon is in line with previous reports on the deviation of crystalline micellar core structure from spherical morphologies, where the micelles assembled with crystalline core took a cylindrical shape whereas those formed by non-crystalline structures adopted a classical spherical shape. It has been assumed that the crystallization of the core-forming blocks is the driving force governing the morphology of micelles in solution and when the core-forming block is a crystalline chain, the energy of crystallization is so large that this block must pack in a folded structure to keep its stability, leading to formation of non-spherical structures(251, 259).

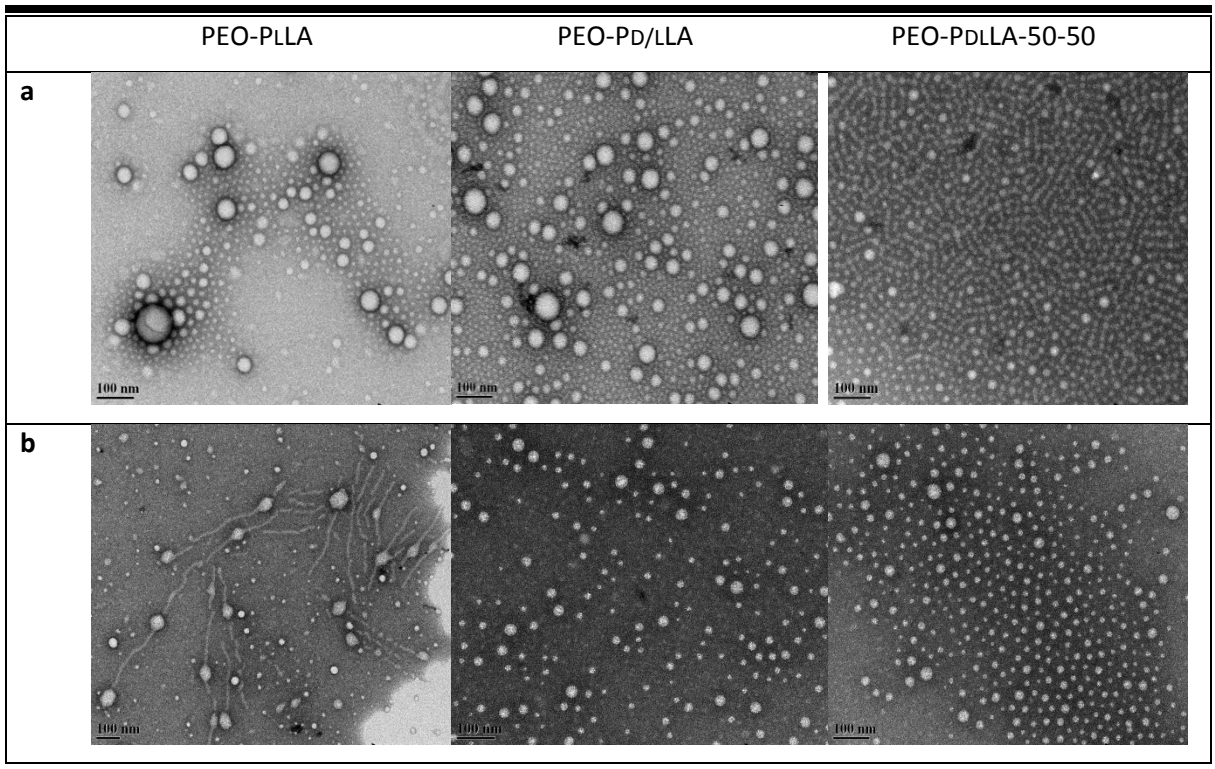

Figure 2.4 TEM images of polymeric micelles from block copolymers synthesized in **(a)** bulk and **(b)** solution**.**

2.3.2.1 Kinetic Stability of Polymeric Micelles

Micelle kinetic stability was studied by DLS in the presence of SDS, which acted as a destabilizing agent. SDS consists of a 12-carbon tail attached to a sulfate group bearing a negative charge, giving the material the amphiphilic properties. When incubating micelles in the presence of SDS, its straight

hydrophobic tail can adsorb onto the hydrophobic segment of the micelles and destabilize them due to electrostatic repulsion between negatively charged head of SDS (260). **Figure 2.5** shows the time dependence in (a) scattered light intensity and (b) polydispersity index (PI) of micelles. SDS-treated PEO-PD/LLA or PEO-PDLLA 50-50 micelles prepared in bulk exhibited a drastic decrease in scattered light intensity and an increase in PI within 2 h. The same trend but at a reduced extent was observed with PEO-PD/LLA or PEO-PDLLA 50-50 micelles where the polymers were prepared using solution polymerization. Micellar structures of PEO-PLLA, particularly those prepared by solution polymerization, showed an enhanced kinetic stability in comparison with other structures when exposed to SDS. In general, these results indicated that the polymeric micelles prepared from copolymers synthesized in solution were more stable compared with their counterparts prepared in bulk. Among different structures under study, PEO-PLLA micelles prepared by solution polymerization were the most stable ones.

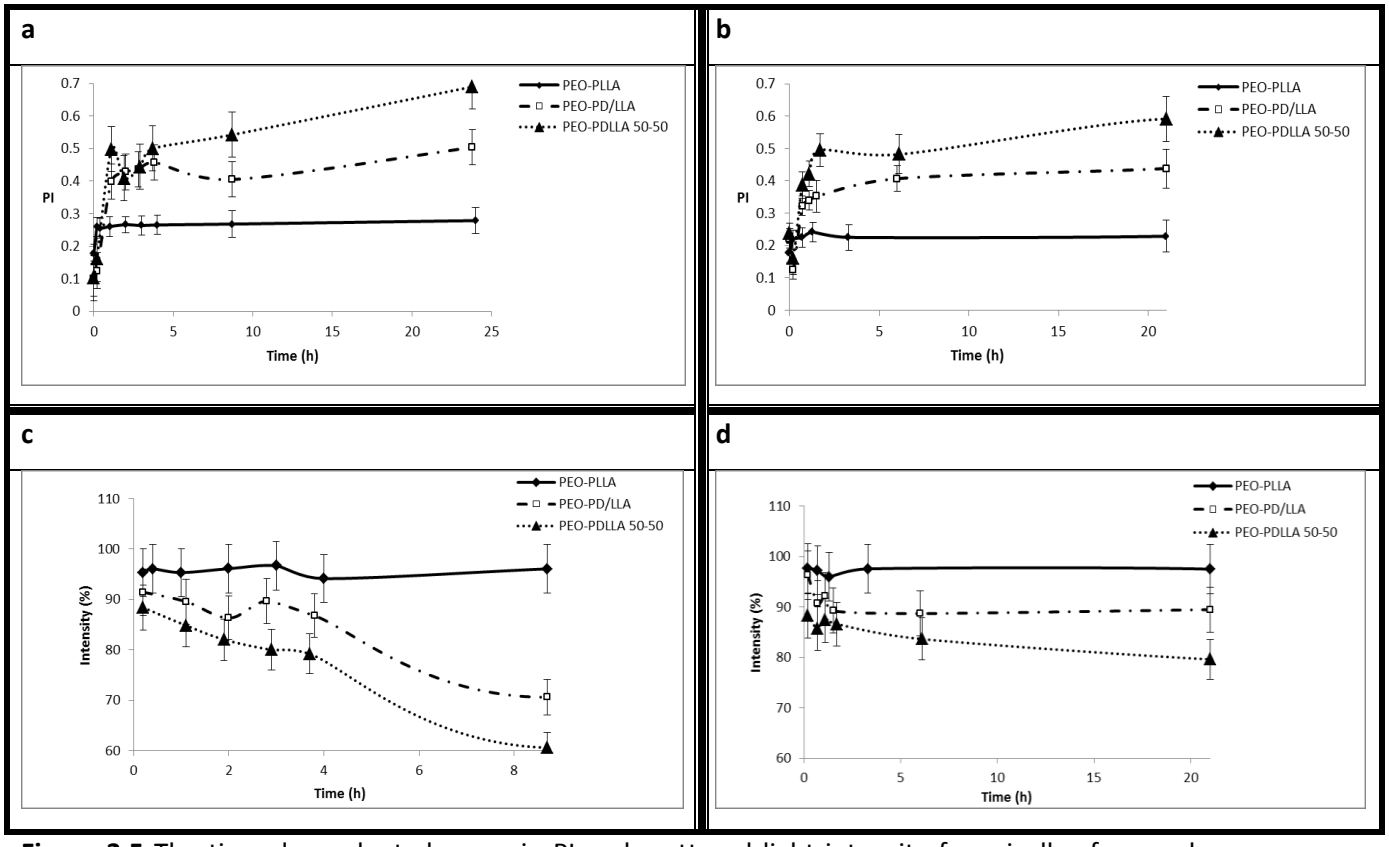

Figure 2.5 The time dependent changes in PI and scattered light intensity for micelles from polymers prepared by either **(a, c)** bulk or **(b, d)** solution polymerization. The data was gathered after addition of SDS solution to micelles at different incubation time points.

2.3.2.2 Thermal Behavior of Freeze-dried Polymeric Micelles

The thermal behavior of freeze-dried polymeric micelles was investigated using DSC. Similar to what was observed for the block copolymers, freeze-dried micelles of PEO-PLLA synthesized in bulk and solution methods were the only structures that exhibited PLA crystallinity in their thermograms. The PLLA related crystallization and melting points for freeze-dried polymeric micelles of bulk polymerized block copolymers were observed at 79.57 and 127.72 °C, respectively (**Figure 2.6a**, **Table 2.4**). For polymeric micelles of block copolymers prepared in solution, these temperatures were 105.83 and 148.28 °C, respectively. The degree of crystallinity in the micellar core is significantly higher for those block copolymers synthesized through solution polymerization with ΔH crystallization of 16.45 versus 8.50 J/g for solution versus bulk prepared PLLAs, respectively (Student's *t* test, $p<0.05$). This data is in good agreement with the thermal behavior of block copolymers in solid form (**Figure 2.3**).

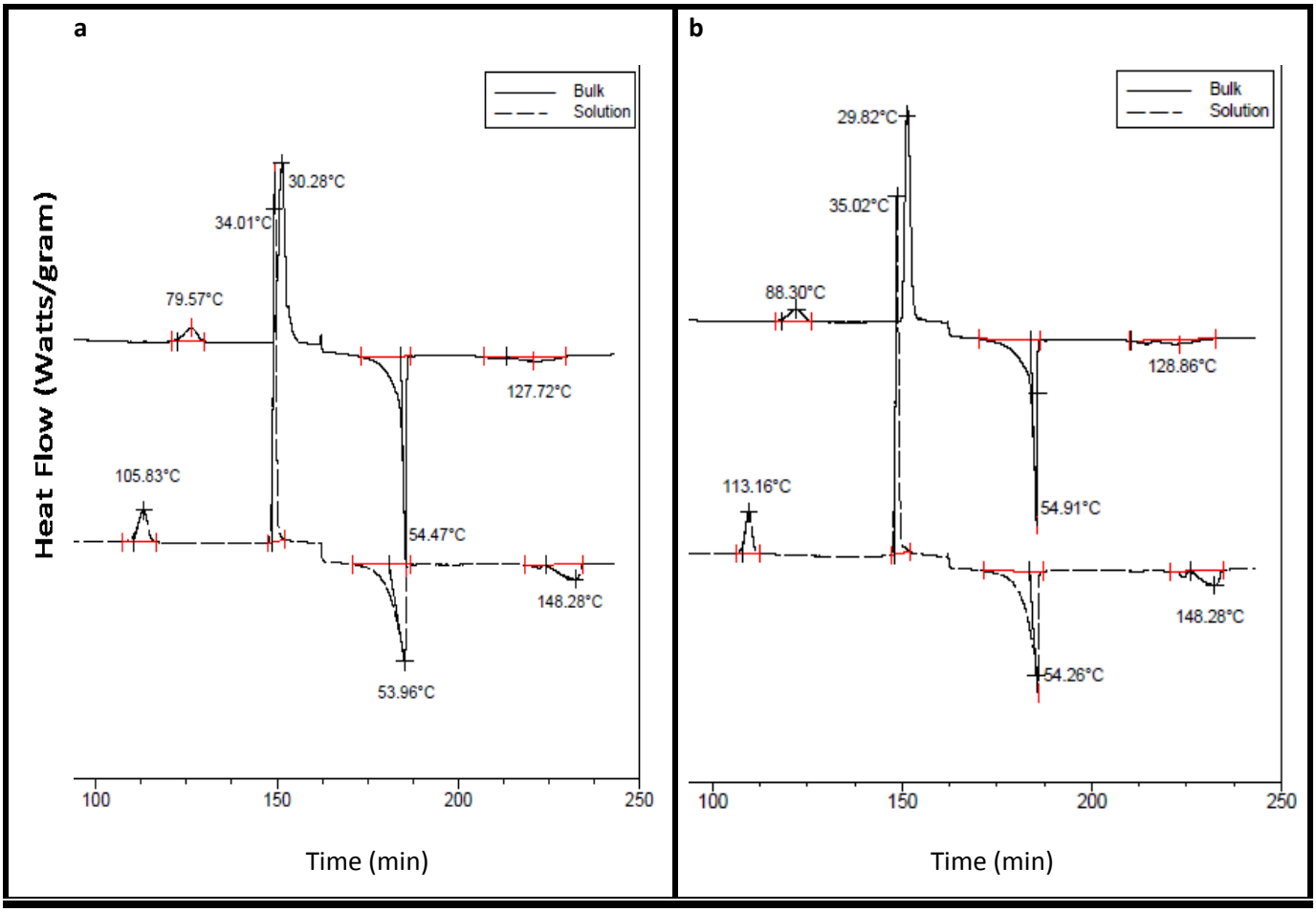

Figure 2.6 DSC thermograms of freeze-dried **(a)** empty and **(b)** nimodipine loaded micelles of PEO-PLLA.

To determine reproducibility, melting temperatures and enthalpies were measured at a heating rate of 2 °C/min in three cycles. The thermograms of the second and third cycles are shown.

Table 2.4 Thermal properties of the freeze-dried empty and nimodipine loaded PEO-PLLA micelles as determined by DSC.

Method of Synth.	Freeze-dried micelles	$T_{m,PEG}$ ± SD °C [a]	$\Delta H_{m,PEG}$ ± SD (J/g)	$T_{cr,PEG}$ ± SD °C [b]	$\Delta H_{cr,PEG}$ ± SD (J/g)	$T_{m,PLA}$ ± SD °C	$\Delta H_{m,PLA}$ ± SD (J/g)	$T_{cr,PLA}$ ± SD °C	$\Delta H_{cr,PLA}$ ± SD (J/g)
Bulk	Empty	54.47 ± 0.65	55.76 ± 1.59	30.28 ± 1.93	54.53 ± 1.56	127.72 ± 0.22	8.18 ± 0.89#	79.57 ± 0.35	8.50 ± 1.05*
Solution		53.96 ± 2.44	60.40 ± 0.98	34.01 ± 1.03	59.97 ± 0.94	148.28 ± 1.14	16.30 ± 1.01#	105.83 ± 0.58	16.45 ± 0.99*
Bulk	Loaded	54.91 ± 0.13	60.67 ± 1.41	29.82 ± 0.85	58.47 ± 1.09	128.86 ± 0.66	9.15 ± 1.12#	88.30 ± 1.50	9.13 ± 0.12*
Solution		54.26 ± 0.19	59.71 ± 1.02	35.02 ± 0.01	59.54 ± 0.98	148.28 ± 1.56	15.31 ± 1.53#	113.16 ± 1.94	15.04 ± 1.31*

[a] Melting point (T_m)

[b] Crystallization temperature (T_{cr}).

Means $\Delta H_{m,PLA}$ of freeze-dried empty and nimodipine loaded PEO-PLLA micelles synthesized by solution polymerization was significantly higher compared to their counterparts of bulk polymerization (Student *t* test, $p<0.05$).

*Means $\Delta H_{cr,PLA}$ of freeze-dried empty and nimodipine loaded PEO-PLLA micelles synthesized by solution polymerization was significantly higher compared to their counterparts of bulk polymerization (Student *t* test, $p<0.05$).

2.3.2.3 Characterization of Nimodipine Loaded Polymeric Micelles

Encapsulation of nimodipine in micelles of block copolymers prepared by bulk polymerization was examined using either the addition of water to polymer/drug THF solution or adding drug/polymer THF solution to water. Characteristics of nimodipine loaded polymeric nano-carriers using addition of water

to THF solution are summarized in **Table 2.5**. Overall, the encapsulation efficiency and loading level of nimodipine in polymeric micelles using addition of water to THF were relatively low.

Table 2.5 Characteristics of nimodipine loaded micelles prepared adding water to organic solvent (n=1).

Polymerization method	Polymer	Drug added (w/w %)	Diameter [a] (nm)	PI	EE%	DL%
Bulk	PEO-PLLA	10	49	0.439	35.61	3.56
	PEO-PD/LLA		36	0.394	18.23	1.82
	PEO-PDLLA 50-50		51	0.479	19.22	1.92

[a]Z average measured by DLS.

Characteristics of nimodipine loaded polymeric micelles using addition of THF to water are summarized in **Table 2.6**. Compared to the previous method of encapsulation (addition of water to THF), yielded micelles were with higher encapsulation efficiency. This observation is in line with our previous data (261). Using addition of THF to water, drug loading was increased for polymers prepared by bulk polymerization when a higher concentration of nimodipine in polymer (10 w/w %) was used in the encapsulation process. The opposite trend was observed for polymers prepared by the solution polymerization; where encapsulation efficiency and drug loading both decreased when a higher amount of drug was used. At high drug loading levels, a comparison of micellar size showed a significantly lower size only for PEO-PLLA micelles prepared from solution versus bulk polymers (Student's *t* test, $p<0.05$). The polymerization method did not appear to significantly affect the average diameter of loaded micelles prepared from PEO-PD/LLA and PEO-PDLLA 50-50 (Student's *t* test, $p>0.05$).

Table 2.6 Characteristics of nimodipine loaded micelles prepared by adding organic solvent to water.

Polymerization method	Polymer	Drug added (w/w %)	n	Diameter ± SD[a] (nm)	PI ± SD	EE%	DL%
Bulk	PEO-PLLA	5	1	72.2	0.160	22.4	1.12
		10	3	62.1 ± 4.7	0.184 ± 0.031	96.8	9.67
	PEO-PD/LLA	5	1	50.3	0.228	21.3	1.06
		10	3	45.2 ± 4.5	0.236 ± 0.011	93.5	9.35
	PEO-PDLA 50-50	5	1	51.4	0.251	22.9	1.14
		10	3	36.2 ± 1.1	0.226 ± 0.053	89.6	8.96
Solution	PEO-PLLA	5	1	49.2	0.232	70.2	3.51
		10	3	41.3 ± 6.0	0.182 ± 0.074	12.4	1.24
	PEO-PD/LLA	5	1	40.4	0.057	101	5.05
		10	3	44.4 ± 7.5	0.222 ± 0.133	11.7	1.17
	PEO-PDLA 50-50	5	1	39.3	0.097	51.2	2.55
		10	3	40.1 ± 9.4	0.200 ± 0.016	11.8	1.18

[a]Z average measured by DLS.

Polymeric micelles prepared by adding THF to water and containing similar drug/polymer level of ~ 1.5 % (w/w) were used for further studies. The thermal behavior of freeze-dried nimodipine loaded polymeric micelles was investigated and compared to that of empty micelles (**Figure 2.6b**, **Table 2.4**). Similar to empty micelles, only PEO-PLLA prepared by bulk and solution methods showed crystallization and melting points for the PLA block. In line with what was observed for empty micelles the degree of crystallinity appeared to be higher for micelles in which the block copolymer was synthesized through solution polymerization. The PLLA melting temperature and enthalpy of melting appeared to be similar for nimodipine loaded versus empty micelles. The PLLA crystallization temperatures and enthalpies; however, slightly increased for loaded versus empty micelles irrespective of the used method of polymerization. This indicates nimodipine loading has facilitated the crystallization of the core-forming block. No extra peak was observed for nimodipine.

The effect of nimodipine loading on kinetic stability of polymeric micelles from different block copolymers under study was then investigated. Similar to empty micelles, nimodipine loaded micellar

structures of PEO-PLLA showed an enhanced kinetic stability in comparison with other structures (**Figure 2.7**). PEO-PDLLA 50-50 loaded with nimodipine showed the lowest resistance toward dissociation by SDS in comparison to other formulations. In line with previous observation for empty micelles, the drug loaded polymeric micelles prepared from copolymers polymerized in solution were more stable than their counterparts prepared in bulk. This was characterized by a smaller decrease in scattered light intensity and a smaller increase in PI index as a function of incubation time with SDS. Interestingly, nimodipine loading enhanced micellar stability irrespective of the method of polymerization (**Figure 2.7** for loaded micelles versus **Figure 2.5** for empty micelles).

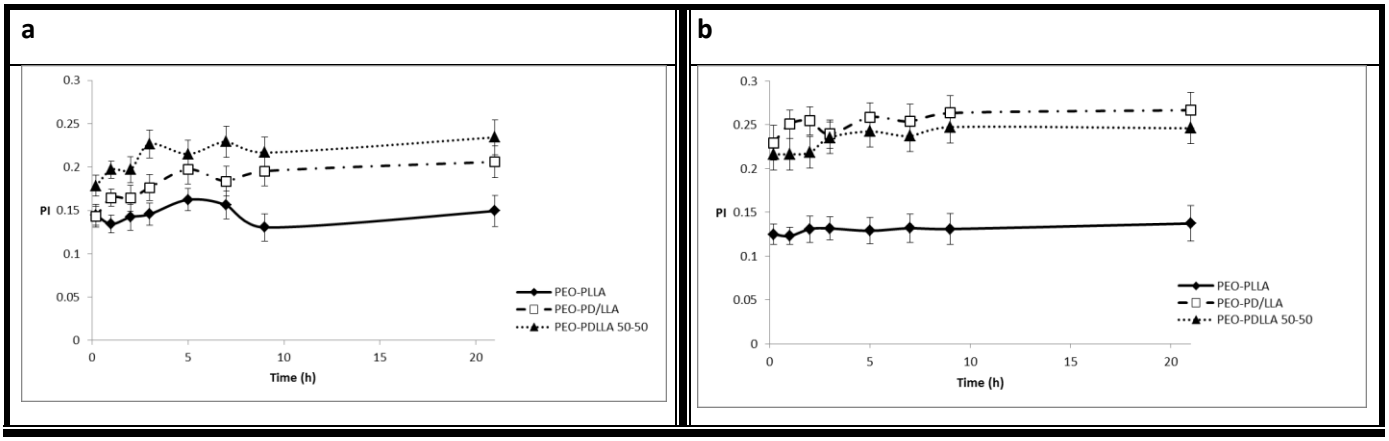

Figure 2.7 The time dependent changes in PI for nimodipine loaded micelles prepared from polymers by either **(a)** bulk or **(b)** solution polymerization. The data was gathered after addition of SDS solution to micelles at different incubation time points.

We have then assessed the effect of different factors on the release profile of nimodipine from polymeric micelles. **Figure 2.8** shows the release profile of nimodipine from polymeric micelles of block copolymers prepared by bulk method using addition of water to THF. Under these conditions, low levels of nimodipine loading were achieved (1-3.5 %). For these micelles, similar (~ 65 %) nimodipine release within 24 hs of study irrespective of the stereochemistry of the block copolymer was seen.

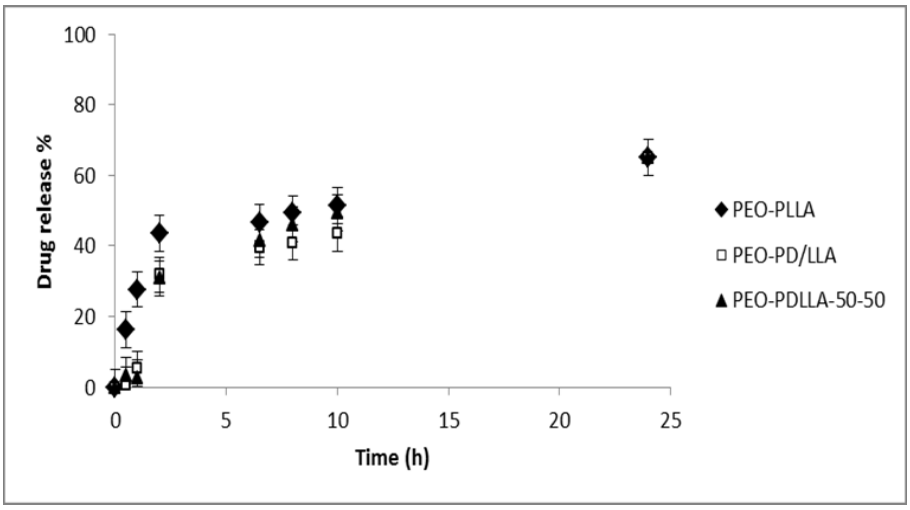

Figure 2.8 The effect of the stereoregularity of the block copolymer structure on the release profile of nimodipine from micelles prepared through addition of water to THF solution. The block copolymers were prepared by bulk polymerization.

Figure 2.9 shows the effect of stereoregularity of the block copolymer on the release profile of nimodipine from polymeric micelles prepared by adding THF to water at two different drug loaded levels. For polymeric micelles with high drug loading ~ 9 % (w/w), maximum accumulative drug release was observed for PEO-PLLA micelles. The lowest rate of drug release was observed for PEO-PDLLA 50-50 micelles (**Figure 2.9a**). In the case of polymeric micelles with low drug loading ~ 1.5 % (w/w), however, no difference was observed between polymeric micelles with various stereochemistries in their core structure (**Figure 2.9b**).

a

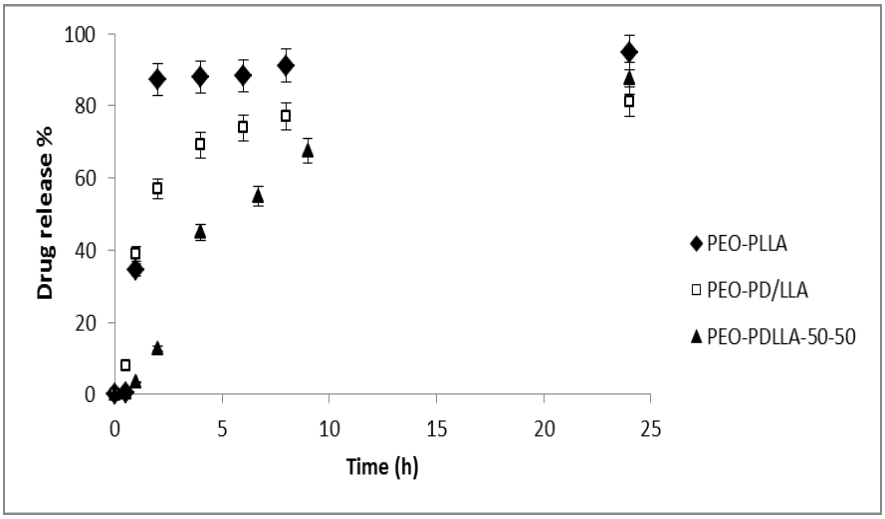

b

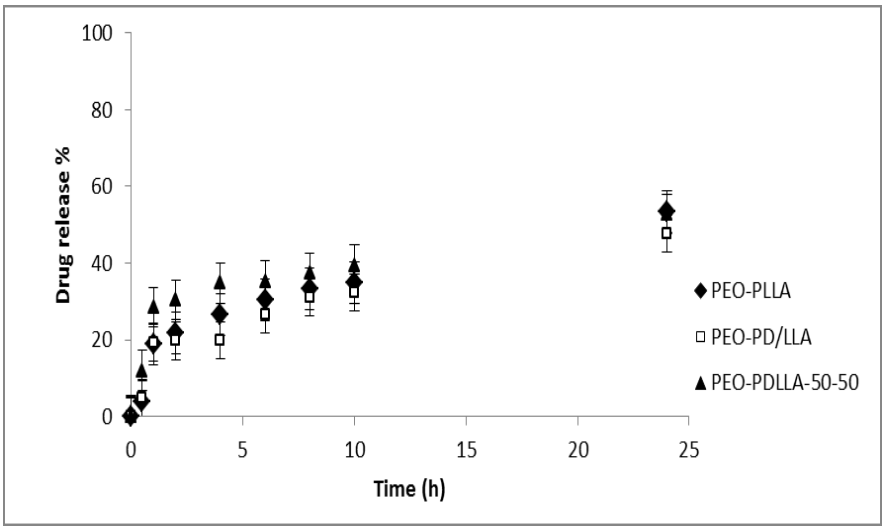

Figure 2.9 The effect of the stereoregularity of block copolymer structure on the release profile of nimodipine from micelles prepared by adding THF to water with **(a)** high drug loading ~ 9 % (w/w); and **(b)** low drug loading ~ 1.5 % (w/w). The block copolymers were prepared by bulk polymerization.

Figure 2.10 shows the effect of polymerization method on the release profile of nimodipine from block copolymer micelles with low level of drug loading (1.5 %). The results showed that method of polymerization did not affect the overall pattern of cumulative drug release at the early time points. Significant differences were only seen at later time points (> 8h) for PEO-PLLA and (>2 h) for PEO-PD/LLA micelles, where the cumulative drug release appeared to be significantly higher in micelles prepared from polymers synthesized by solution polymerization compared to those prepared in bulk (Student's *t* test, $p<0.05$). In PEO-PDLLA 50-50 there was not a significant difference in the cumulative drug release from micelles prepared from polymers synthesized by solution polymerization compared to those prepared in bulk (Student's *t* test, $p>0.05$).

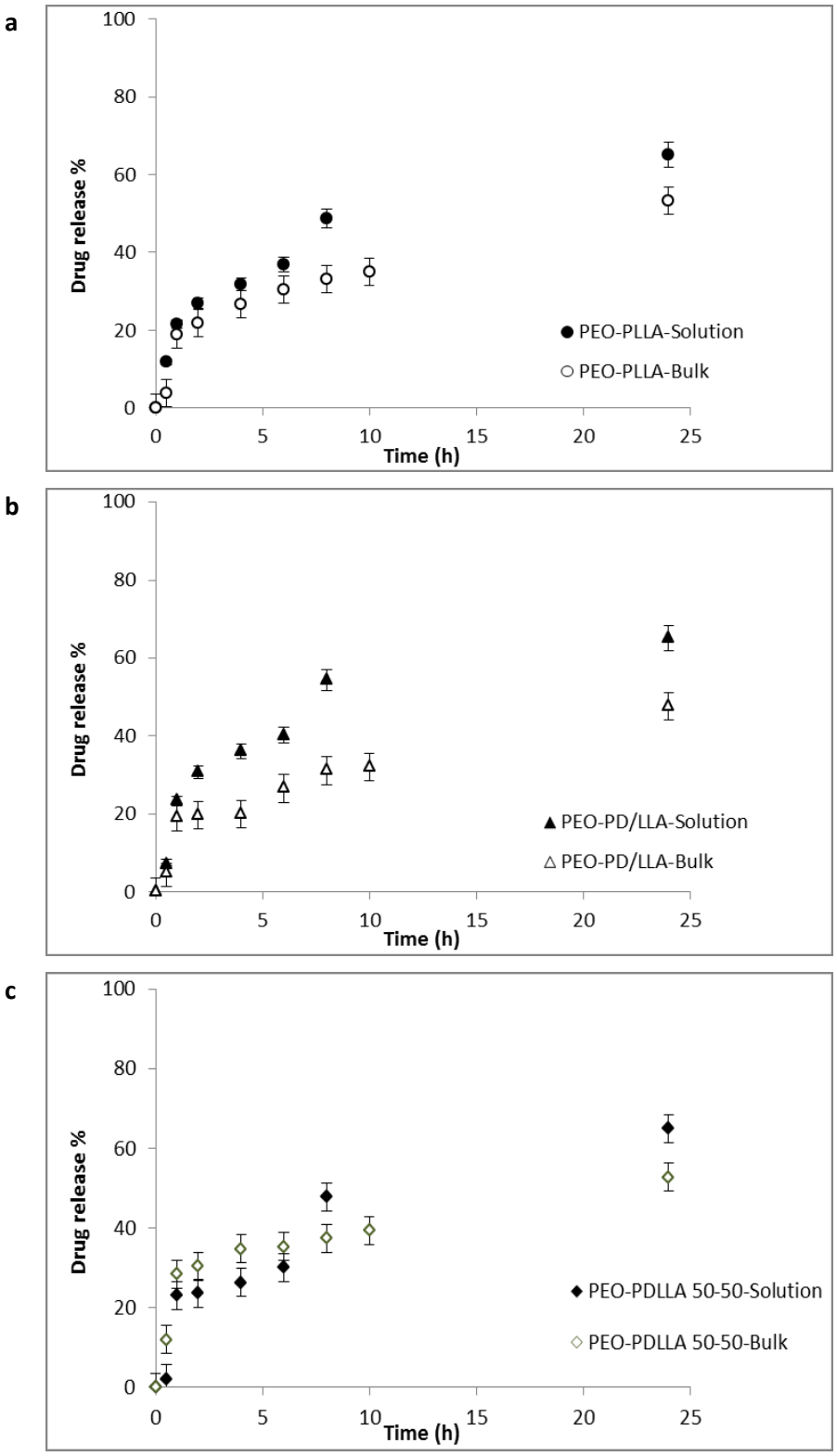

Figure 2.10 Assessing the effect of polymerization method on the release profile of nimodipine from **(a)** PEO-PLLA **(b)** PEO-PD/LLA and **(c)** PEO-PDLLA 50-50 micelles.

2.4 Discussion

For the goal of depot and/or targeted drug delivery, development of stable polymeric micelles that can solubilize high levels of therapeutics and, at the same time, release it in a sustained or even delayed manner is of interest. Achieving this goal has been a challenging task, however. Previous studies have presented a case for the effect of micellar core crystallinity on the stability of micellar structure and their drug release profile. For instance, enhancing core crystallinity has been shown to improve the stability of micellar structure (225), while restricting the partitioning of pyrene into the micellar core, leading to lower loaded pyrene levels (251). The increase in core crystallinity also led to a rapid release of sulindac and tetracaine from polymeric micelles (250). Here we studied the effect of polymerization method on the crystallinity of core-forming block in PEO-PLA block copolymers and its eventual influence on the properties of resulted polymeric micelles. To minimize the detrimental effect of high temperature on stereoregularity and gain more control over stereochemistry of polymer backbone, the method of polymerization was changed from bulk to solution in this study.

Among different structures under study, PEO-PLLA micelles prepared by solution polymerization were the most stable ones, owing to their greater stereoregularity and subsequent higher crystallinity. Higher degree of crystallinity in the core seems to be the main reason behind higher kinetic stability and resistance to micellar dissociation to single chains when incubating with SDS (262). The detrimental effect of temperature on stereoregularity can be avoided by changing the method of polymerization from bulk to solution. Since solution polymerization employs lower temperatures during reaction, the stereoregularity of produced polymers can be preserved better. In the present study, we did not observe a significant difference in the polydispersity index of polymers synthesized by bulk versus solution polymerization. However, the use of solution polymerization led to the production of more stereoregular PLLA.

High temperatures used for polymerization in the bulk method led to racemization, and subsequently, decreased the stereoregularity, therefore the polymer chains cannot stack on top of each other. This results in a lower melting and crystallization. Application of solution polymerization instead of bulk polymerization was shown to favor the crystallization of the PLA segment in PEO-PLLA block copolymers (made from polymerization of L-lactide) and micelles. However, no change in the crystallinity of PEO-PD/LLA and PEO-PDLLA 50-50 block copolymers and micelles was detected when the method of polymerization was switched to solution from bulk. Because the tin-catalyzed ROP of lactide does not differentiate between the monomer enantiomers, it will likely produce random atactic PLA with racemic-lactide (263). The same scenario might have happened to meso-lactide resulting in the non-

selective addition of monomers to polymer chain and production of an atactic polymer with a random distribution of stereo-centers along the polymer backbone (that is amorphous) instead of syndiotactic one with alternating arrangement of stereo-centers in the polymer. Despite the recent development of complexes for the ROP of lactide, relatively few well-defined metal catalysts are capable of achieving high stereo-chemical control in the ROP of meso- or rac-lactide (264).

In line with enhanced crystallinity of the core in PEO-PLLA block copolymers prepared by solution polymerization, PEO-PLLA micelles showed a tendency for the formation of cylindrical and worm like micelles (instead of spherical ones) and demonstrated improved kinetic stability. A slight increase in the kinetic stability of spherical micelles formed from PEO-PD/LLA and PEO-PDLLA 50-50 was also noted.

In the next step, we investigated the effect of core crystallinity, on the stability and release profile of drug loaded polymeric micelles. Nimodipine was used as the model drug for these studies because of its proven preferential interaction with the polyester core structure (227). Similar to empty micelles, drug loaded micelles with semicrystalline cores were shown to be more stable than those with amorphous ones. The application of solution polymerization also enhanced the kinetic stability of prepared micelles. In general, the presence of drug in the micellar core was shown to enhance the stability of polymeric micelles, irrespective of the core crystallinity. An interaction between the drug and the core-forming block is possibly responsible for enhanced kinetic stability of drug loaded polymeric micelles (265).

We then investigated the effect of core crystallinity on the release of nimodipine from PEO-PLA polymeric micelles. Since drug release from polymeric micelles is predominantly governed by diffusion of drug through amorphous regions of the micellar structure, an increase in the crystalline structure of the core was expected to increase the diffusion path and as a result, reduce the rate of drug release from the micellar carrier. This is provided to the localization of the drug in the core of polymeric micelles. Our observations, however, were in contrary to this expectation. When addition of organic solvent to water was used as the method of micellization for polymers prepared by bulk method, at high drug loaded levels ~ 9 % (w/w) , the PEO-PLLA micelles showed more rapid drug release compared to PEO-PD/LLA and PEO-PDLLA 50-50 micelles. When drug-loading levels were low 1.5 % (w/w) drug release from polymeric micelles was similar irrespective of the core crystallinity and structure. A higher release of nimodipine from micelles was observed when PEO-PLLA and PEO-PD/LLA polymers were prepared by solution polymerization compared to those prepared by bulk polymerization.

The observed difference between the release of nimodipine from polymeric micelles of different core crystallinity may in fact reflect the influence of core crystallinity on the localization of drug within the micellar structure rather than the diffusion path of drug from the micellar core. In fact when data from

all sample studied here is considered, a good correlation between drug loading level and the time required to release 50 % of drug (R^2 = 0.8896) is observed. Rapid formation of micellar structure from PEO-PLLA block copolymers that have crystalline PLLA blocks may prevent the uniform dispersion of the drug in the micellar core. In this case, the drug may be squeezed out of the core and eventually accumulate in the surrounding regions of core (core/shell interface or the shell) and released with a rapid rate from micelles particularly at high drug loading levels. In contrast, PEO-PD/LLA and PEO-PDLLA 50-50 copolymers that have less crystalline core forming structure may allow better drug loading within the micellar core (250). Formation of polymeric micelles from block copolymers prepared in solution may also be more rapid, owing to higher stereoregularity, compared to polymers prepared in bulk. In comparison, micelles of diblock copolymers prepared by bulk polymerization can provide a higher chance for drug loading in the micellar core, leading to slower rate of drug release (**Figure 2.11**).

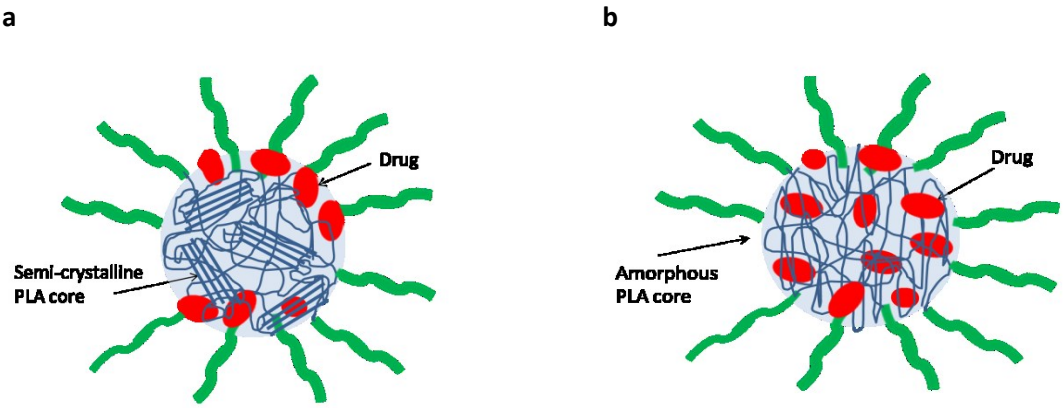

Figure 2.11 Depiction of drugs dispersion in the **(a)** semicrystalline PLA core and **(b)** amorphous PLA core.

With this in mind we have investigated whether a change in the method of micelle preparation by addition of water to polymer/drug solution in THF can slow down the kinetics of micelle formation, leading to better drug encapsulation within micellar core and a slower release profile for nimodipine from PEO-PLLA micelles that have semicrystalline core structure. Our results did not show any benefit for this approach in terms of drug release. Instead, the encapsulation efficiency of nimodipine was drastically reduced.

2.5 Conclusions

The application of solution polymerization led to better preservation of stereoregularity and crystallinity of the PLA block in PEO-PLLA block copolymers compared to polymers made from bulk polymerization. Consequently, polymeric micelles prepared from polymers synthesized by the solution method showed enhanced kinetic stability. Loading of a core-compatible drug, *i.e.*, nimodipine, in PEO-PLA polymeric micelles enhanced the stability of prepared polymeric micelles. Nimodipine loading in polymeric micelles prepared from block copolymers synthesized by solution polymerization was reduced and its release was enhanced compared to those prepared by bulk polymerization. The latter observation may be a reflection of the enhanced kinetics of micelle formation leading to drug loading in the micellar shell or core/shell interface for the more stereoregular PEO-PLAs prepared through solution polymerization.

2.6 Acknowledgments

This study was supported by grants from Natural Sciences and Engineering Research Council of Canada (NSERC). A.L. also acknowledges support from Canadian Foundation for Innovation (CFI) and Alberta Advanced Education and Technology (AAET) for the infrastructure used in the study.

2.7 Supplementary Information

a

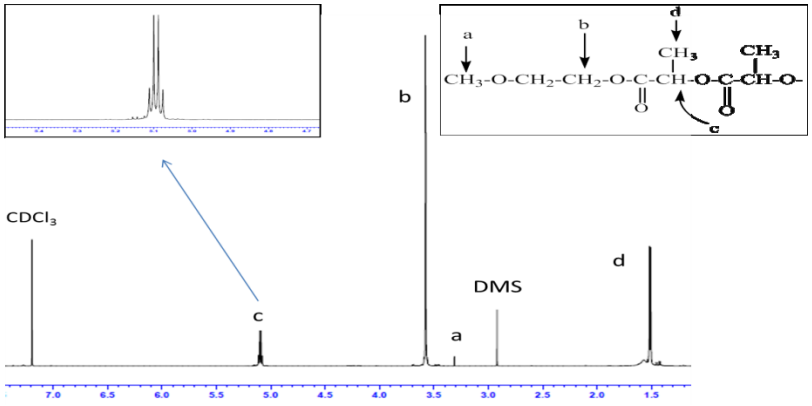

b

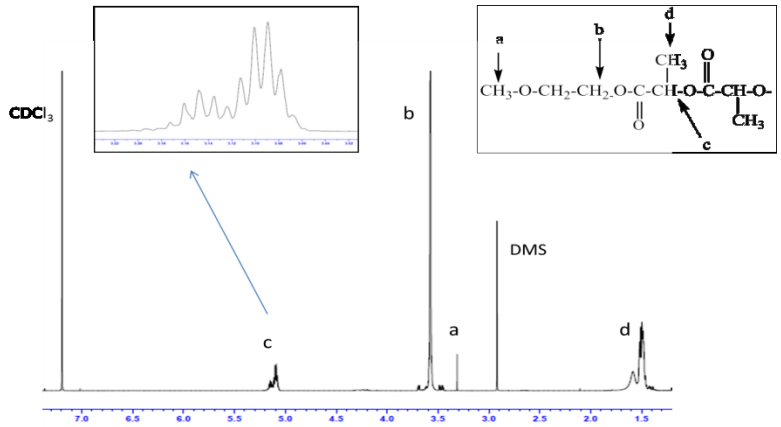

c

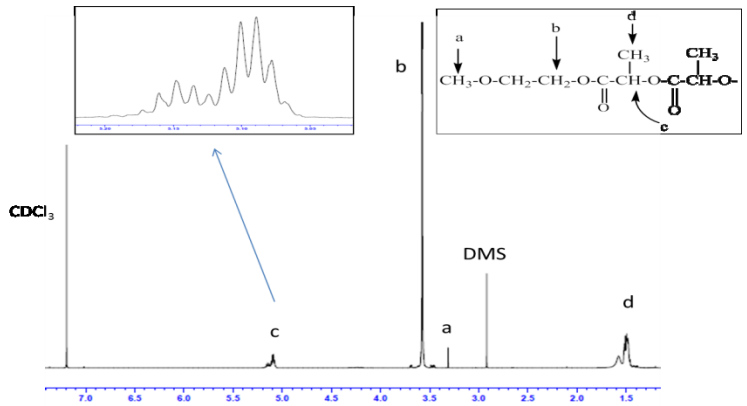

Figure 2.S1 ^{1}H NMR spectra and peak assignments for **(a)** PEO-PLLA; **(b)** PEO-PD/LLA; and **(c)** PEO-PDLLA 50-50 block copolymers prepared by solution method in $CDCl_3$ with dimethyl sulfone (DMS) as internal standard. Signals at 3.7, 3.4, 5.2 and 1.5 ppm in ^{1}H NMR spectra correspond to protons in CH_2 (b), CH_3 (a), CH (c) and CH_3 (d), respectively.

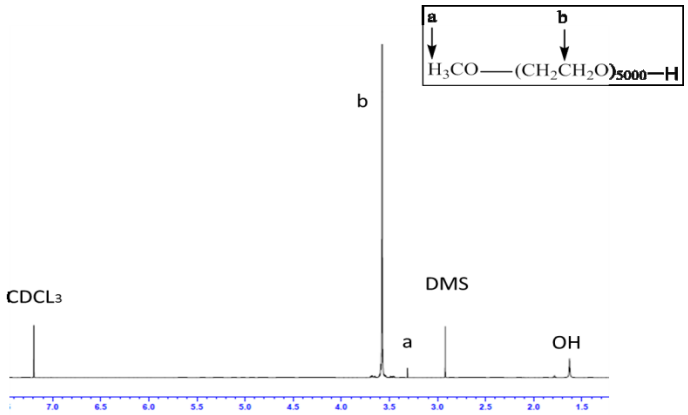

Figure 2.S2 ^{1}H NMR spectra and peak assignments for methoxy poly ethylene oxide in $CDCl_3$ with dimethyl sulfone (DMS) as internal standard. Signals at 3.7, 3.4 ppm in ^{1}H NMR spectra correspond to protons in CH_2 (b) and CH_3 (a), respectively.

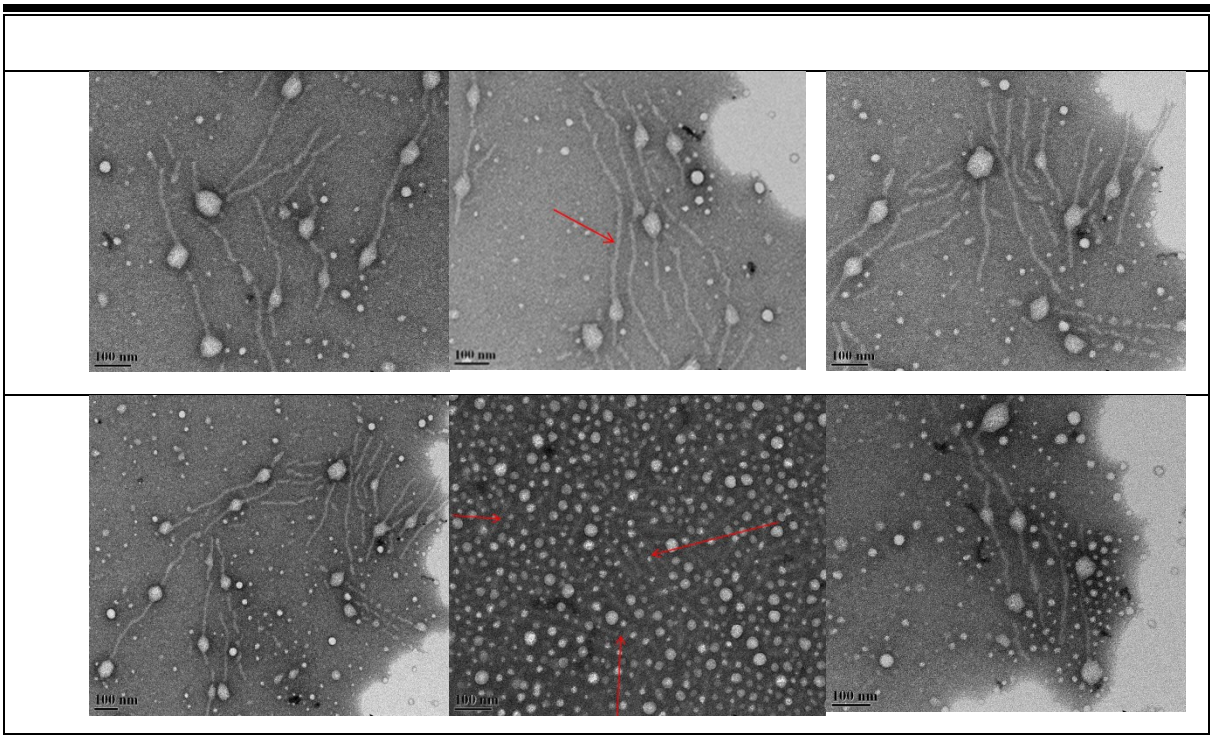

Figure 2.S3 TEM images of PEO-PLLA polymeric micelles from block copolymers synthesized in solution**.** Worm shaped micelles have been shown by red arrows in different sections.

Chapter Three

Rational Design of Block Copolymer Micelles to Control Burst Drug Release at a Nanoscale Dimension

A version of this chapter has been published in

Acta Biomaterialia 2015, 24:127-39

3.1 Introduction

A common problem with the use of polymeric micelles is the premature release of the incorporated drug from these nano-carriers under sink condition (223). Keeping the drug within the micellar carrier is a prerequisite for the successful use of polymeric delivery systems for targeted as well as depot drug delivery applications (247, 248).

Several strategies have been tried to achieve efficient drug solubilization and, at the same time, sustained drug release from polymeric micelles. These strategies include chemical cross-linking of either core or shell segments (224), incorporation of stereoregular polymers in the micellar core leading to core crystallization (250), as well as stereocomplexation of the micellar core through physical interaction of two stereoregular structures of opposite conformation (30). These strategies have been mostly successful in enhancing the stability of polymeric micelles, but are not particularly effective in controlling the burst and premature drug release from the micellar nano-carriers (225). Although enhancing the stability of the micellar structure is a crucial step to ascertain that the encapsulated drug will be kept within the nano-carrier, it is not sufficient. Release of the drug from the micellar carrier must also be controlled to attain sustained drug release and/or insure the same fate for the incorporated drug and the micellar carrier for the purpose of targeted drug delivery.

In an effort to achieve micellar nano-containers with sufficient drug encapsulation, micellar stability and appropriate drug release profile, we exploited the design and development of ABC triblock copolymer micelles, where the C block was selected from a relatively drug compatible polymer for efficient solubilization of the drug of interest. The B block, on the other hand, was selected from a drug incompatible polymer segment to provide a barrier against drug release. The A block was expected to make the micellar shell, interfacing the media.

Our model drug was nimodipine. Poly(α-benzyl-ε-caprolactone) (PBCL) and poly(ε-caprolactone) (PCL), were used as the “C” block to form the micellar inner core because of their excellent solubilization of nimodipine. Poly(lactide) (PLA), was used as the “B” block to form the micellar outer core acting as a nano-membrane controlling the rate of drug release (**Figure 3.1**) based on its non-miscibility with nimodipine as judged by the nimodipine/PLA value of Flory Huggins interaction parameter (χ = 1.35). The effect of this specific structural design as well as the stereochemistry of the B block on the crystallinity of the core in ABC micelles, micellar stability, drug solubilization and release profile was then assessed. Comparisons were made with AB or AC diblock copolymer micelles.

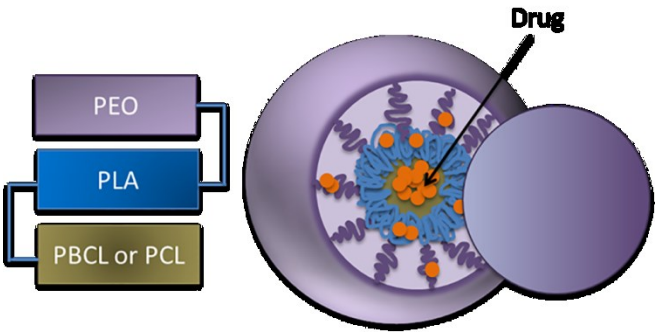

Figure 3.1 Depiction of three layered ABC micelles. Micellar nano-container with the C block (PBCL or PCL) serving as the inner core of micelles acting as a nano-reservoir for the drug of interest; the B block (PLA) providing a barrier against drug release, and the A block (PEO) interfacing the media.

3.2 Experimental Section

3.2.1 Materials and Methods

L-lactide (98%) and meso-D,L-lactide (99%) were purchased from Alfa Aesar, Lancashire, UK. D-lactide (98%) was a generous gift from Purac, Schiedam, Netherlands. Methoxy-PEO 5000 (MePEO), sodium dodecyl sulfate (SDS) and tin(II) bis(2-ethylhexanoate) (stannous octoate) were obtained from Sigma, St Louis, MO, USA. Stannous octoate was dried and purified using anhydrous magnesium sulfate, dry toluene and vacuum distillation (253). α-benzylcarboxylate-ε-caprolactone (BCL) was synthesized by Alberta Research Chemicals Inc. (ARCI, Edmonton, AB, Canada) based on methods published previously by our group (266). All other chemicals and reagents used were of analytical grade.

3.2.2 Synthesis of PEO-PLA Diblock Copolymers

L-lactide, D-lactide, meso-D,L-lactide and methoxy PEO 5000 were dried in a vacuum oven at 65 °C overnight. Diblock copolymers of MePEO (as the hydrophilic block) and poly(L-lactide) (PLLA), poly(D-lactide) (PDLA), poly(D/L-lactide) (PD/LLA) and poly(D,L-lactide) were prepared using ring opening polymerization of either L-lactide, D-lactide, meso-lactide or a 50-50 racemic mixture of L-lactide and D-lactide, respectively (**Figure 3.2a**). The prepared diblock copolymers are abbreviated as PEO-PLLA, PEO-PDLA, PEO-PD/LLA and PEO-PDLLA-50-50 in the chapter, respectively. Briefly, MePEO (0.5 g, 0.1 mmol) was reacted with (L-lactide), (D-lactide), (D/L-lactide) (1 g, 6.8 mmol) or a 50-50 ratio of L-lactide and D-lactide (total weight 1 g), in an ampule using stannous octoate (5 mg) as catalyst. The ampule was then sealed and left at 160 °C for 7 h. The obtained product was dissolved in dichloromethane, and

precipitated by *n*-hexane, dried at room temperature in a vacuum oven overnight and washed with anhydrous ethyl ether. This was followed by drying in a vacuum oven at room temperature overnight.

3.2.3 Synthesis of PEO-PLA-PBCL and PEO-PLA-PCL Triblock Copolymers

α-benzylcarboxylate-ε-caprolactone (BCL) monomer was dried in a vacuum oven at 65 °C overnight. Triblock copolymers of PEO-PLLA-PBCL, PEO-PDLA-PBCL, PEO-PD/LLA-PBCL and PEO-PDLLA-50-50-PBCL were prepared using ring opening polymerization of BCL with corresponding diblock copolymers as initiators, respectively (**Figure 3.2a**). Briefly, diblock copolymers (0.2 g) were incubated with BCL (0.2 g) in an ampule using stannous octoate (8 mg) as catalyst. The ampule was then sealed and left at 142 °C for 8.5 h. The obtained product was dissolved in dichloromethane, and precipitated by *n*-hexane, dried at room temperature in a vacuum oven overnight and washed with anhydrous ethyl ether. This was followed by drying in a vacuum oven at room temperature overnight (**Figure 3.2b**).

Triblock copolymers of PEO-PLLA-PCL, PEO-PDLA-PCL, PEO-PD/LLA-PCL and PEO-PDLLA-50-50-PCL were prepared using ring opening polymerization of ε-caprolactone with the corresponding PEO-PLA diblock copolymers (**Figure 3.2a**). Briefly, diblock copolymers (0.2 g), were reacted with caprolactone monomer (0.2 g) in an ampule in the presence of stannous octoate (8 mg) as catalyst. The ampule was then sealed under vacuum and left at 142 °C for 6 h. The obtained product was dissolved in dichloromethane, and precipitated by *n*-hexane, dried at room temperature in a vacuum oven overnight and washed with anhydrous ethyl ether. This was followed by drying in a vacuum oven at room temperature overnight.

(a)

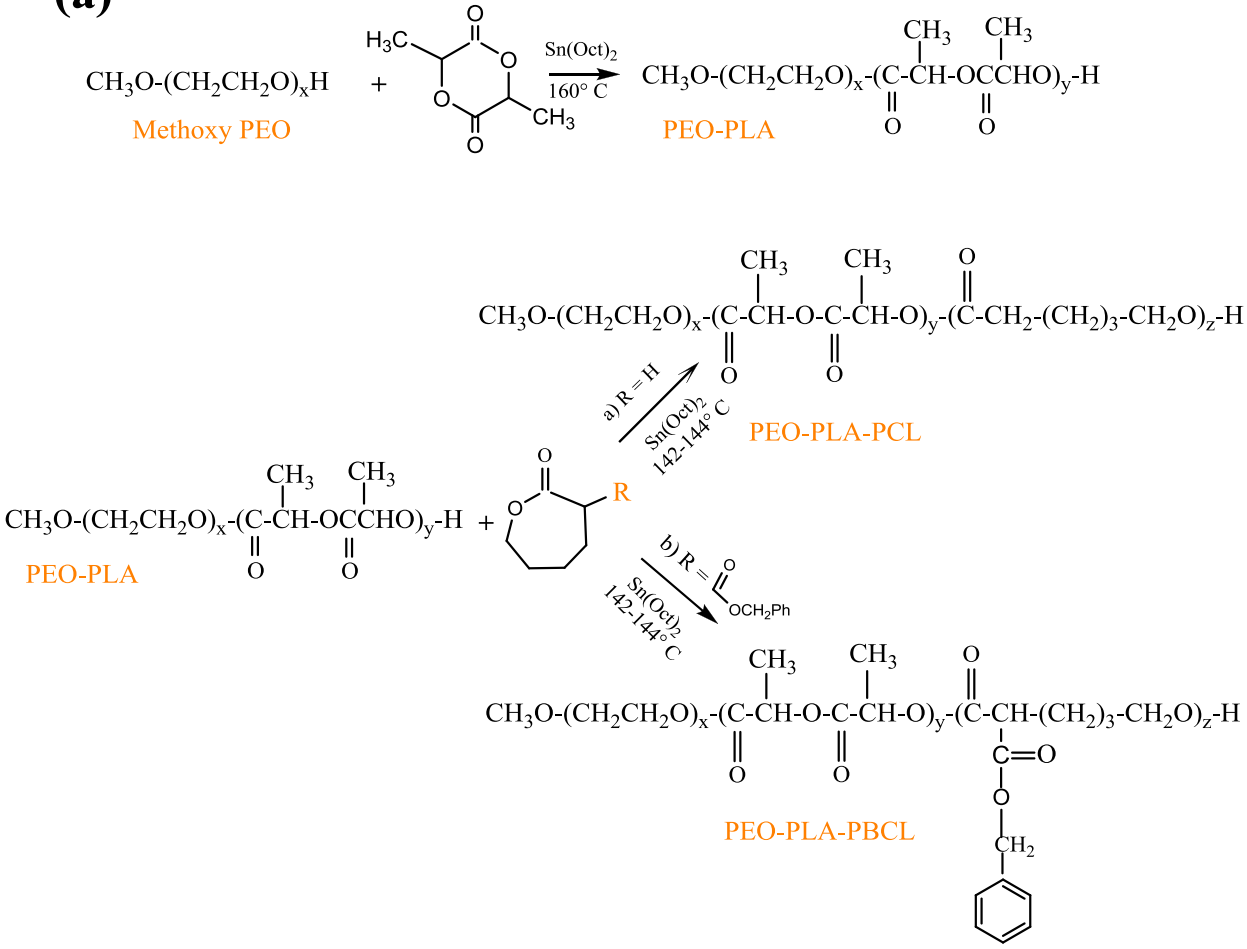
CH3O-(CH2CH2O)xH
Methoxy PEO
Sn(Oct)2
160° C
CH3O-(CH2CH2O)x-(C-CH-OCCHO)y-H
PEO-PLA
CH3O-(CH2CH2O)x-(C-CH-O-C-CH-O)y-(C-CH2-(CH2)3-CH2O)z-H
a) R = H
Sn(Oct)2
142-144° C
PEO-PLA-PCL
PEO-PLA
R
b) R =
OCH2Ph
Sn(Oct)2
142-144° C
PEO-PLA-PBCL

(b)

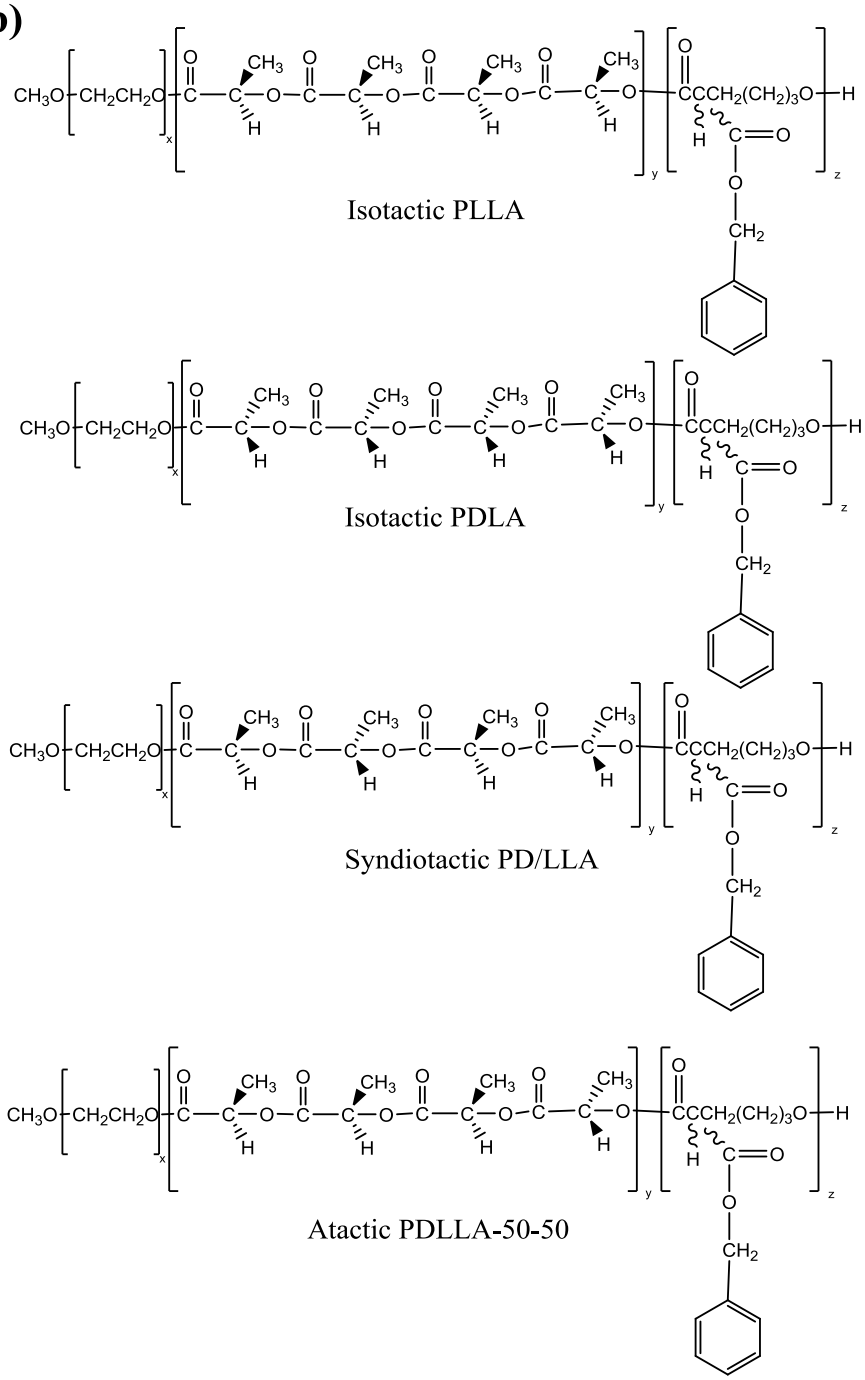

Figure 3.2 (a) General synthesis scheme for the preparation of ABC triblock copolymers of PEO-PLA-PCL and PEO-PLA-PBCL. **(b)** The Schematic Model of Synthesized ABC Triblock Copolymers of PEO-PLA-PBCL having isotactic, syndiotactic and atactic PLA (block B) structures.

3.2.4 Self-assembly of Prepared Block Copolymers

Preparation of colloidal dispersions from synthesized block copolymers was tried by co-solvent evaporation method. Briefly, the di- or triblock copolymers (20 mg) were dissolved in tetrahydrofuran (THF) (2.5 mL). After sonication (10 min) and centrifugation (3000 rpm, 5 min) respectively, this solution was added in a drop-wise manner to deionized water (5 mL) while stirring. The solution was stirred for 24 h under a fume hood to remove the organic solvent by evaporation. Preparation of mixed micelles were attempted using the same procedure as described above by blending 1:1 molar ratio of PEO-PLLA (10 mg) and PEO-PDLA (10 mg) containing di- or triblock copolymers. Similar procedure was also exploited to prepare drug-loaded polymeric micelle, except nimodipine (2 mg) was dissolved along with the block copolymers (20 mg) in THF (2.5 mL).

3.2.5 Characterization of Prepared Polymers and Micelles

3.2.5.1 Polymer Molecular Weight and Polydispersity

^{1}H NMR was performed on a Bruker, ASEND^{TM} 600 MHz spectrometer using $CDCl_3$ as solvent. Polymers were dissolved in $CDCl_3$ at a concentration range of 1-4 mg/mL. ^{1}H NMR spectra were generated using dimethyl sulfone as the internal standard (δ = 3.0 ppm). The ^{1}H NMR spectra of synthesized PEO-PLLA, PEO-PDLA, PEO-PD/LLA and PEO-PDLLA-50–50 diblock copolymers are shown in **Figure 3.S1a–d** in supplementary information. The molecular weight of PLLA, PDLA, PD/LLA and PDLLA-50–50 blocks was determined from ^{1}H NMR spectra by examining the peak intensity ratio of methane protons of the PLA segment ($COC\underline{H}(CH_3)O$: δ = 5.2 ppm) and the methylene protons of MePEO ($OC\underline{H_2}C\underline{H_2}$: δ = 3.7 ppm). The ^{1}H NMR spectra of synthesized PEO-PLLA-PBCL, PEO-PDLA-PBCL, PEO-PD/LLA-PBCL and PEO-PDLLA-50–50-PBCL triblock copolymers are shown in **Figure 3.S2a–d**. The ^{1}H NMR spectra of synthesized PEO-PLLA-PCL, PEO-PDLA-PCL, and PEO-PDLLA-50–50-PCL triblock copolymers are shown in **Figure 3.S3a–c**. The molecular weight of PBCL or PCL segments was determined from ^{1}H NMR spectra by examining the peak intensity ratio of methylene protons of PBCL segment ($COCH(COOCH_2Ph)CH_2CH_2CH_2C\underline{H_2}O$): δ = 4.1 ppm) or PCL segment ($COCH_2CH_2CH_2CH_2C\underline{H_2}O$): δ = 4.1 ppm) and the methylene protons of MePEO ($OC\underline{H_2}C\underline{H_2}$: δ=3.7 ppm). The calculated molecular weights for block copolymers are summarized in **Table 3.1**. The polydispersity index of the copolymers were determined at room temperature by GPC using a Shimadzu LC-10AD HPLC pump and M302 triple detector array (Viscotek Corp., Houston, TX) connected to a 10 µm Waters Strygel HT3 column. The mobile phase was THF with a flow rate of 1 mL/min. The injection volume of the sample was 20 µL at a polymer concentration of 1 % (w/v). The molecular weights of the

polymers were determined relative to polyethylene glycol standards using the universal calibration and OmniSEC 4.7 software (Malvern Instruments Ltd., Malvern, UK).

3.2.5.2 Polarimetry

Specific rotation, [α], of various di and triblock copolymers (1 g/dL) was determined in chloroform ($CHCl_3$) at room temperature using Perkin-Elmer 241 polarimeter at a center wavelength of 589 nm.

3.2.5.3 Thermal Properties of Polymers and Micelles

The melting temperatures for block copolymers and empty freeze-dried polymeric micelles were identified by Differential Scanning Calorimetry (DSC), Q2000-1576, and TA Universal Analysis 2000 software (TA Instruments, New Castle, USA). The heating rate was 2°C/min under nitrogen atmosphere. Samples were weighed (3-5 mg) in Tzero aluminum pans. Melting temperatures were measured in heat-cool-heat cycles. First cycle was from 8°C to 170°C, second cycle was from 170°C to 8°C and third cycle was from 8°C to 240°C. Data were shown for the third cycle.

3.2.5.4 Micelle Size

The hydrodynamic diameter of assembled structures (4 mg/mL) was measured using dynamic light scattering (DLS) ZETA-Sizer Nano (Malvern Instruments Ltd., Malvern, UK). The analysis was performed at a scattering angle of 173° at 25 °C.

3.2.5.5 Micelle Stability

The CMC of di- and triblock copolymers was determined using light scattering measurement with a Varian Cary Eclipse fluorescence spectrophotometer (Mulgrave, Australia), with excitation and emission wavelengths set at 451 nm (267). A series of polymer solutions (0.060 - 125 µg/mL) in deionized water were prepared for all the different copolymers. Excitation and emission was set at 451 nm and the average intensity of scattered light from three measurements was plotted against polymer concentration. The intersection of the two linear graphs in the sigmoidal curve, *i.e.*, the onset of a rise in the intensity of scattered light, was defined as the CMC value. Kinetic stability of nano-structures was measured by preparation of different micellar solutions (0.031 mg/mL) which were mixed with sodium dodecyl sulfate (SDS) (40 mg/mL) at a 2:1 v/v ratio. Scattered light intensity was measured at different incubation time intervals using ZETA-Sizer Nano (Malvern Instruments Ltd., Malvern, UK) at scattering angle of 173° at 25 °C.

3.2.5.6 Micellar Morphology

Transmission electron microscopy (TEM) (FEI MorgagniTM 268, North America NanoPort, Oregon, USA) was used to observe the morphology of self-assembled structures as shown in **Figure 3.S4**. For TEM measurements, the polymer concentration in micellar solutions was 2 mg/mL. Samples were placed onto the copper grid, dried at room temperature, and examined using TEM by negative staining with 4% uranyl acetate.

3.2.6 Calculation of Flory-Huggins Interaction Parameter

Group contribution method (GCM) was used to determine the compatibility of drug/block-copolymer (**Table 3.4**). In particular, the GCM method was utilized to calculate the Hildebrand solubility parameters (δ) of nimodipine and of the hydrophobic block (PBCL and PCL block) of triblock copolymers of PEO-PLA-PBCL and PEO-PLA-PCL and (PLA block) of diblock copolymer of PEO-PLA. The GCM assumes that each substructure within a molecule (or a repeat unit in the case of polymer) such as a methyl group, a hydroxyl group, etc., contributes a certain average amount to the solubility parameter of a material. By adding up various contributions of the constituent groups of a molecule or a repeat unit, one obtains a statistical guess of the solubility parameter of a particular material. The essential assumption of this method is that the intermolecular interactions are linear additive and do not depend on the detailed local architecture of a molecule. Using such δ, the Flory-Huggins interaction parameters (χ) were calculated using the following equation (**Table 3.4**).

$$\chi = \frac{V_R}{RT}(\delta_1 - \delta_2) \qquad (1)$$

where δ_1 and δ_2 are the Hildebrand solubility parameters of the block of interest and of nimodipine; V_R is the reference molar volume at temperature *T*. Usually, the component that has the smaller molar volume (molar volume of a repeat unit in the case of polymer) is taken as the reference volume. *R* is the universal gas constant.

3.2.7 Encapsulation of Nimodipine in Polymeric Micelles

Drug-loaded polymeric micelles were prepared using the same procedure as described for the self-assembly conditions, except nimodipine (2 mg) was dissolved along with the block copolymers in THF (2.5 mL). After the evaporation of THF, the micelle solution was centrifuged to remove the precipitated drug (5 min, 3000 rpm). To measure the concentration of loaded drug, UV spectroscopy was used. First, micellar solution was diluted with equal volume of methanol. Nimodipine concentration was measured by UV spectroscopy at 357 nm against a calibration curve plotted at 5-120 µg/mL nimodipine

concentration in methanol-water 50:50 solution (268). The encapsulation efficiency (EE) and drug loading (DL) percentages were calculated from the Equation (2) and Equation (3), respectively.

$$EE\ (\%) = \frac{the\ amount\ of\ encapsulated\ nimodipine}{the\ total\ feeding\ amount\ of\ nimodipine} \times 100 \quad (2)$$

$$DL\ (\%) = \frac{the\ amount\ of\ encapsulated\ nimodipine}{the\ total\ amount\ of\ polymer} \times 100 \quad (3)$$

3.2.8 In vitro Drug Release

A dialysis bag (Spectraphor, Mw cutoff 3500 g/mol) containing the drug-loaded micelle solution (5 mL) was placed in deionized water (500 mL) at 37 °C in a Julabo SW 22 shaking water bath (Seelbach, Germany). At predetermined time intervals, 200 µL of the dialysis bag content was collected and diluted with methanol. The deionized water (500 mL) in the recipient media was taken out and replaced by fresh water at the same time interval. The concentration of nimodipine remained in the dialysis bag at each time point was determined using UV spectroscopy (Beckman Coulter DU 730) at 357 nm. The remained drug concentration was subtracted from the initial concentration of the drug and used to plot the cumulative drug release (%) versus time. The release profiles were compared using similarity factor, f_2, and the profiles were considered significantly different if f_2 <50 (269). The similarity factor, f_2, was calculated based on Equation (4) (270).

$$f_2 = 50\ \times \log\left(\left[1 + \left(\frac{1}{n}\right)\sum_{j=1}^{n}|Rj - Tj|^2\right]^{-0.5} \times 100\right) \quad (4)$$

where n is the sampling number, R_j and T_j are the percent released of the reference and test formulations at each time point j.

3.2.9 Statistical Analysis

Statistical analysis was performed either using unpaired Student's *t* test or one way ANOVA with *Tukey* post-test analysis. The significance level (α) was set at 0.05. For non-linear regression analysis, Graphpad prism was used (version 5.00, Graphpad Software Inc., La Jolla, CA, USA). All experiments were conducted in triplicate unless mentioned otherwise in the text, Tables or Graphs and the results were represented as mean ± standard deviation (SD).

3.3 Results and Discussion

3.3.1 Characterization of Prepared Polymers

The synthesis scheme and model of produced structures under current study are shown in **Figure 3.2a** and **b**, respectively. The characteristics of prepared polymers are also summarized in **Table 3.1**. Characterization of polymers for their specific rotation showed polymers containing isotactic stereoisomers (*i.e.*, PLLA or PDLA) yielded negative or positive values for their optical activity reflective of the corresponding weight % of PLLA and PDLA blocks, respectively (**Table 3.1**). No optical rotation was obtained for those containing alternate PD/LLA or random PDLLA-50-50 blocks due to their intrinsic optical inactivity. In general, diblock copolymers have shown a better correlation between their specific rotation and weight % of the PLA segment when compared to the triblock copolymers (249, 262). This may be due to minor side reactions during the second ROP performed for the synthesis of triblock copolymers at high temperatures. ^{1}H NMR spectroscopy (600 MHz, $CDCl_3$, δ) as outlined in **Figure 3.S1–3** and gel permeation chromatography (GPC) data revealed a well-defined composition of copolymers with low polydispersities (Mw/Mn) (**Table 3.1**).

Thermal behavior of copolymers as characterized by DSC is shown in **Figure 3.3**. PEO-PLLA and PEO-PDLA contained crystalline domains, as their DSC analysis exhibited the melting peaks arising from PLLA and PDLA domains at 165.4 and 167.3 °C, respectively (**Figure 3.3a**). On the other hand, the PLA block in PEO-PD/LLA (alternate) and PEO-PDLLA-50-50 (random) copolymers were shown to be amorphous as evidenced by the absence of PLA associated melting peaks (264). We also observed a reduction in the melting temperature and enthalpy for PEO (from 63.5 °C and 216 J/g, respectively) in the diblock copolymers irrespective of the stereochemistry of the PLA block. This is possibly due to the interaction of the PLA block with the PEO leading to its interference with PEO crystallization (258).

Figure 3.3b shows the DSC thermograms of PEO-PLA-PBCL triblock copolymers with different PLA stereochemistries. The absence of melting peaks for the PLA segments in the thermograms of the triblock copolymers indicated the absence of PLA crystalline regions. The DSC thermograms for PEO-PLA-PCL triblock copolymers with different PLA stereochemistries are also shown in **Figure 3.3c**. In line with our observation on PEO-PLA-PBCL triblock copolymers, no PLA related melting peak was observed for PEO-PLA-PCL triblock copolymers irrespective of the PLA stereoregularity.

Table 3.1 Characteristics of synthesized block copolymers.

Polymer	PLA Mn[a] (Da)	PBCL or PCL Mn[a] (Da)	polymer Mn[a] (Da)	PDI ± SD[b]	[α][c]	PLA w%[d]	% Iαl/140[e]
PEO[f]-PLLA	9522	-	14522	1.77 ± 0.40	-94.7 ± 0.01	65.5	67.6 ± 0.02
PEO-PDLA	8424	-	13424	1.36 ± 0.18	89.7 ± 0.02	62.7	64.0 ± 0.04
PEO-PD/LLA	8100	-	13100	1.29 ± 0.29	-0.79 ± 0.02	61.8	-
PEO-PDLLA-50-50	8640	-	13640	1.21 ± 0.09	-0.68 ± 0.01	63.3	-
PEO-PLLA-PBCL	1799	6591	13391	1.67 ± 0.07	-13.9 ± 0.08	13.4	9.91 ± 0.07
PEO-PDLA-PBCL	2154	6301	13456	1.59 ± 0.09	14.3 ± 0.04	16.0	10.2 ± 0.08
PEO-PD/LLA-PBCL	2205	6214	13420	1.57 ± 0.09	-0.64 ± 0.06	16.4	-
PEO-PDLLA-50-50-PBCL	2064	6373	13438	1.75 ± 0.02	-0.80 ± 0.01	15.3	-
PEO-PLLA-PCL	2008	5620	12628	1.46 ± 0.26	-20.8 ± 0.07	15.9	14.8 ± 0.06
PEO-PDLA-PCL	1875	5690	12565	1.47 ± 0.70	16.7 ± 0.04	14.9	12.0 ± 0.05
PEO-PDLLA-50-50-PCL	1707	5774	12451	1.46 ± 0.35	-1.03 ± 0.03	13.7	-
PEO-PBCL	-	6696	11696	2.33 ± 0.48	-1.26 ± 0.02	-	-
PEO-PCL	-	4790	9790	1.57 ± 0.78	-	-	-

[a] Number- average molecular weight measured by ^{1}H NMR.

[b] Measured by GPC, relative to polyethylene glycol standards.

[c] Specific optical rotation of copolymers, $[\alpha]_D^{25}$ (*chloroform*) deg cm^3 g^{-1} dm^{-1}.

[d] $\frac{The\ number\ average\ molecular\ weight\ of\ PLA\ as\ determined\ by\ H\ NMR}{The\ number\ average\ molecular\ weight\ of\ polymer\ as\ determined\ by\ H\ NMR}$ ×100.

[e] $\frac{Specific\ optical\ rotation\ of\ block\ copolymer}{Optical\ rotations\ of\ highly\ pure\ optical\ active\ polylactide} \times 100$. The reported optical rotations [α] of enantiomerically highly pure PLLA and PDLA typically lie between |140| and |156| deg dm^{-1}cm^3 g^{-1}(249, 262).

[f] The molecular weight (Mn) of methoxy PEO in all the synthesized block copolymers is 5000 (Da).

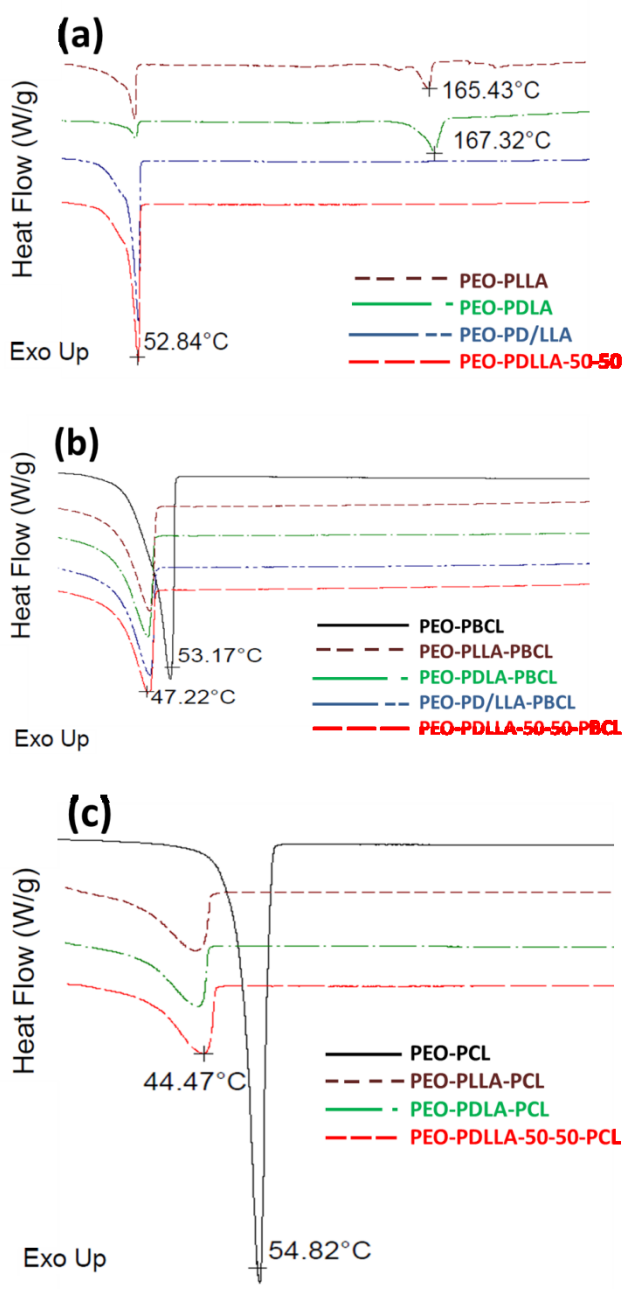

Figure 3.3 (a) DSC thermograms of PEO-PLA diblock copolymers, **(b)** PEO-PLA-PBCL triblock copolymers in comparison to PEO-PBCL, and **(c)** PEO-PLA-PCL triblock copolymers in comparison to PEO-PCL. Melting temperatures were measured for the second heating ramp at a heating rate of 2 °C/min from 8 °C to 240 °C.

3.3.2 The Effect of ABC Design and B block Stereoregularity on the Characteristics of Polymeric Micelles

3.3.2.1 Micelle Size

All block copolymers under study self-assembled to colloidal structures with Z average diameters below 100 nm with a relatively narrow polydispersity (**Table 3.2**). Of note was the effect of core structure on the Z average diameter of polymeric micelles formed from di and triblock copolymers. Despite similar molecular weight of di-versus tri block copolymers used in the study and the bulky nature of the PBCL cores, micelles composed of PEO-PLLA-PBCL, PEO-PDLA-PBCL triblock copolymers revealed smaller sizes compared to their counterparts from diblock PEO-PLLA and PEO-PDLA as well as PEO-PLLA-PCL and PEO-PDLA-PCL copolymers (**Table 3.2**). The exact reason behind this observation is not clear but may be attributed to differences in the aggregation number and/or compactness of the micellar structure.

Table 3.2 Characteristics of assembled structures from block copolymers.

Block copolymer	Diameter ± SD[a] (nm)	PDI ± SD[b]	CMC ± SD[c] (μM)	HLB[d]
PEO-PLLA	92.5 ± 2.13	0.10 ± 0.01	0.26 ± 0.01[†]	195.2
PEO-PDLA	93.1 ± 1.55	0.09 ± 0.02	0.27 ± 0.01[†]	193.7
PEO-PD/LLA	62.0 ± 3.27	0.18 ± 0.01	0.57 ± 0.02	186.5
PEO-PDLLA-50-50	56.0 ± 4.29	0.16 ± 0.03	0.55 ± 0.01	198.1
PEO-PLLA-PBCL	47.1 ± 2.24	0.20 ± 0.01	0.75 ± 0.02	76.40
PEO-PDLA-PBCL	49.6 ± 1.23	0.19 ± 0.04	0.85 ± 0.01	78.84
PEO-PD/LLA-PBCL	47.2 ± 2.20	0.22 ± 0.01	0.83 ± 0.02	78.85
PEO-PDLLA-50-50-PBCL	60.7 ± 5.22	0.23 ± 0.05	0.93 ± 0.03	77.84
PEO-PLLA-PCL	84.0 ± 3.55	0.08 ± 0.02	0.15 ± 0.03[¥]	72.70
PEO-PDLA-PCL	84.8 ± 2.10	0.10 ± 0.07	0.14 ± 0.01[¥]	71.44
PEO-PDLLA-50-50-PCL	98.0 ± 4.55	0.07 ± 0.01	0.18 ± 0.02[¥]	70.00

[a] Z average measured by DLS.

[b] Polydispersity index measured by DLS.

[c] CMC measured by DLS (267).

[d] HLB measured by the effective chain length (ECL) method (271).

(†) means prepared micelles from PEO-PLLA, PEO-PDLA copolymer showed a significantly lower CMC among other diblock copolymers (one way ANOVA with *Tukey* post-test, $p<0.05$).

(¥) means prepared micelles from PEO-PLA-PCL triblock copolymers have shown significantly lower CMCs compared to those from PEO-PLA-PBCL triblock and PEO-PLA diblock copolymers (Student *t* test, $p<0.05$).

3.3.2.2 Micelle Morphology

TEM images showed that empty polymeric micelles of different di and triblock block copolymers adopted a spherical and uniform shape in most cases (**Figure 3.S4**). However, a subpopulation of micelles with irregular or rod/worm morphology was seen in some sections of prepared samples of PEO-PLLA and PEO-PDLA diblock copolymers. As it can be clearly seen from the TEM images, and in agreement with DLS results (**Table 3.2**), the three layered micelles prepared from triblock copolymers of PEO-PLA-PBCL are smaller in size comparing to two layered micelles prepared of diblock copolymers of PEO-PLA at the similar molecular weight.

3.3.2.3 Thermal Behavior

Similar to what was observed for the diblock copolymers, freeze-dried micelles of PEO-PLLA and PEO-PDLA were the only structures that exhibited PLA crystallinity with the melting points of 167.2 and 166.9 °C for PLLA and PDLA segments, respectively (**Figure 3.4a**). No PLA crystallinity was observed for PD/LLA or PDLLA-50-50 blocks in micelles containing such core structures.

In triblock copolymer micelles, the PBCL or PCL block seemed to hinder the crystallization of PLLA or PDLA blocks (**Figure 3.4b** and **4c**), as no melting peak was observed for micelles of PEO-PLLA-PBCL or PEO-PDLA-PBCL, despite stereoregularity of the PLA block. The absence of PLA related melting peaks in the thermograms indicates the absence of crystalline regions even for the micelles containing stereoregular PLA segments. This is perhaps due to the interaction of PBCL or PCL with PLA block hindering an ordered conformation within the micellar core. Similar observation was made in case of solid block copolymers (**Figure 3.3**).

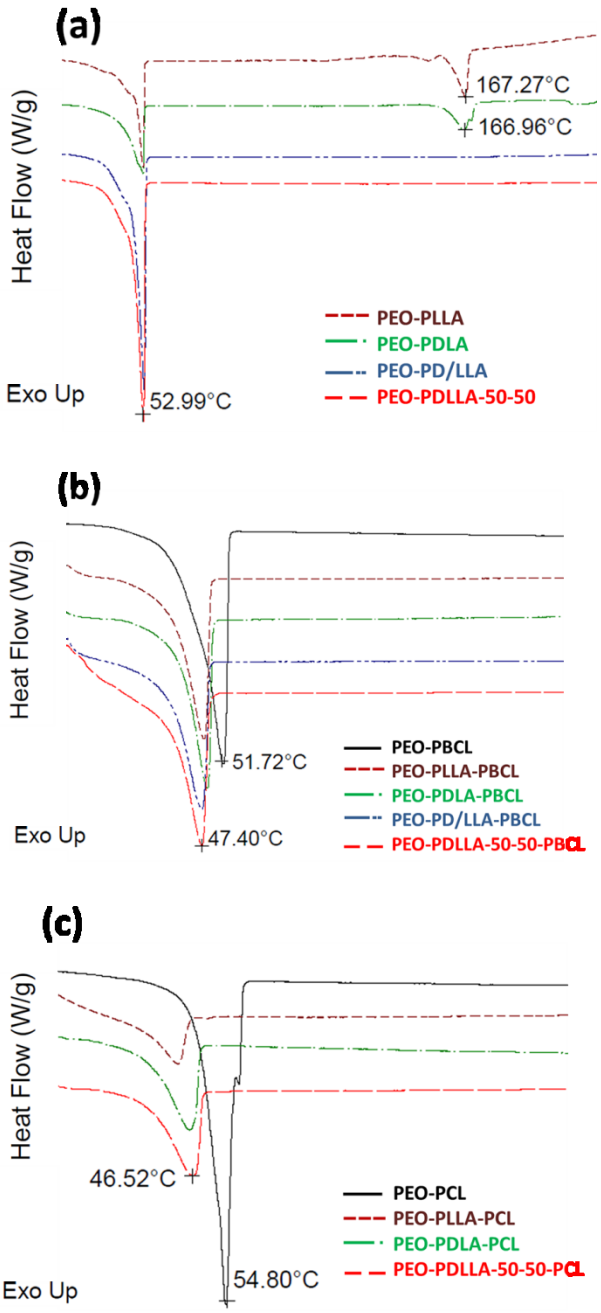

Figure 3.4 (a) DSC thermograms of freeze-dried micelles of PEO-PLLA, PEO-PDLA, PEO-PD/LLA and PEO-PDLLA-50-50, **(b)** freeze-dried micelles of PEO-PLLA-PBCL, PEO-PDLA-PBCL, PEO-PD/LLA-PBCL and PEO-PDLLA-50-50-PBCL in comparison to PEO-PBCL, and **(c)** freeze-dried micelles of PEO-PLLA-PCL, PEO-PDLA-PCL and PEO-PDLLA-50-50-PCL in comparison to PEO-PCL. Melting temperatures were measured for the second heating ramp at a heating rate of 2 °C/min from 8 °C to 240 °C.

3.3.2.4 Critical Micellar Concentration (CMC)

For the determination of CMC, micelle formation was monitored by DLS (267). Compared to the fluorescent spectroscopy techniques, application of DLS is expected to reduce the chance of error in CMC measurement (267), as the measurement of CMC using fluorescent probes such as pyrene, heavily depends on partition equilibrium coefficient (Kv) of the fluorescent probe to the core of micelles solution. The physical state of the micellar core may affect this partition influencing the measured CMC values (251).

All block copolymers under study showed CMC values in the µM range. The following trend in the CMC of di- versus triblock copolymers was observed: PEO-PLA-PBCL > PEO-PLA > PEO-PLA-PCL (**Figure 3.5**). No correlation between the CMC of different block copolymers and their hydrophilic-lipophilic balance (HLB) as calculated by the effective chain length (ECL) method (271) was observed (**Table 3.2**). For instance, despite having relatively similar HLBs, the CMC of PEO-PLA-PCL triblock copolymers were significantly lower than those of PEO-PLA-PBCL (Student's *t* test, $p<0.05$). Also, in contrast to the lower HLB of PEO-PLA-PBCL block copolymers, their CMC was found to be higher than the PEO-PLA diblock copolymers. These observations points to the effect of other structural factors in the core-forming block in addition to block copolymer HLB in defining CMC in polymeric micelles.

As for the effect of stereochemistry in the B block, for diblock copolymers, PEO-PLLA and PEO-PDLA showed a significantly lower CMC compared to PEO-PD/LLA and PEO-DLLA-50-50 diblock copolymers ($p<0.05$, one way ANOVA with *Tukey* post-test). This observation is in line with previous reports (30, 272-274) and is likely caused by stereoregularity of the PLLA and PDLA core-forming structure that promotes micelle formation as a result of core crystallization (as evidenced by the DSC data in **Figure 3.4a**). In contrast, for the PEO-PLA-PBCL and PEO-PLA-PCL triblock copolymers, no significant difference in the CMC of block copolymers with stereoregular PLLA or PDLA segment to irregular ones, *i.e.*, PD/LLA and PDLLA-50-50, was observed, which is again in line with amorphous nature of the core in these structures (as evidenced in **Figure 3.4b** and **c**).

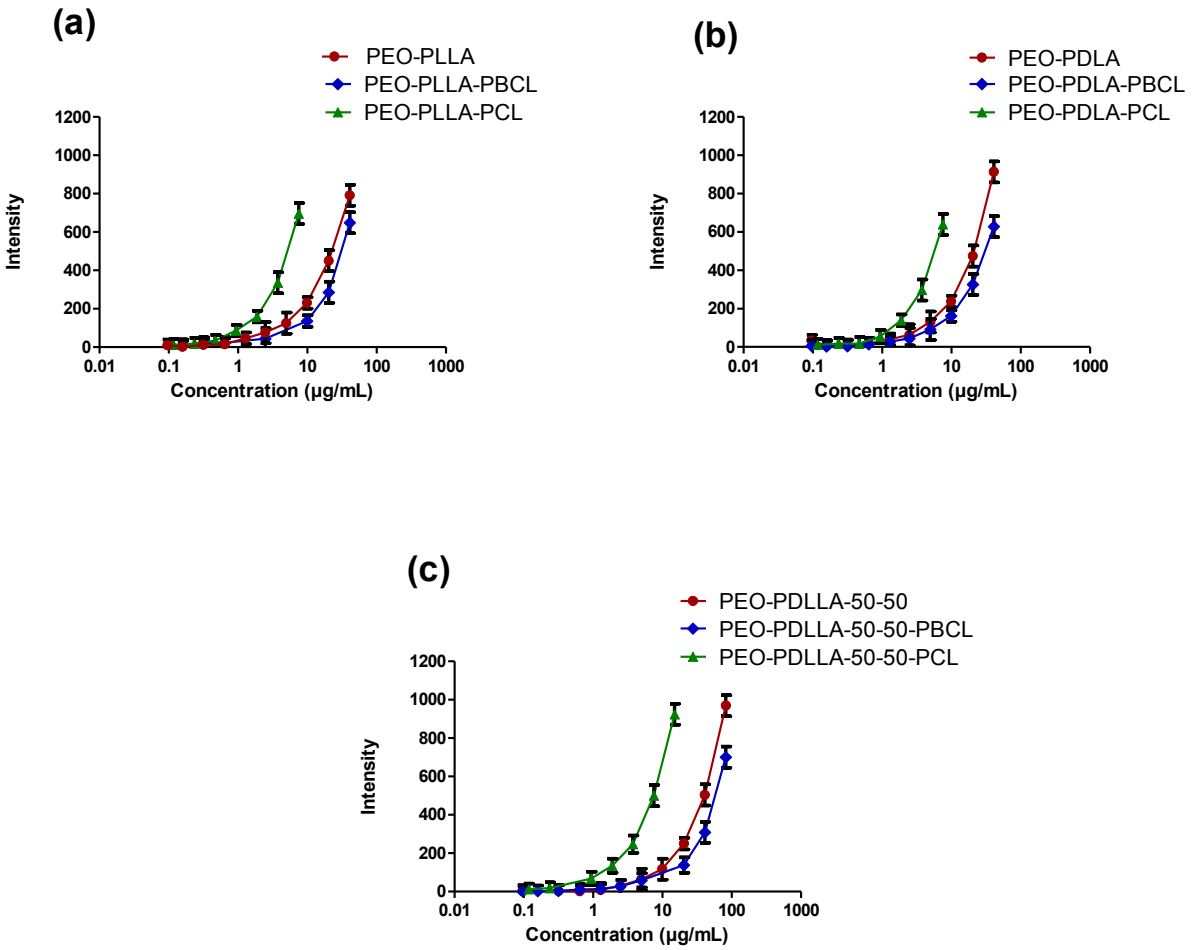

Figure 3.5 DLS signal as a function of log concentration of copolymers was used to measure the CMC of different block copolymers containing blocks of **(a)** poly(L-lactide), **(b)** poly(D-lactide), and **(c)** poly(D,L-lactide 50-50).Data are represented as mean ± SD (n=3).

3.3.2.5 Kinetic Stability of Polymeric Micelles

The results of our investigations on the micellar kinetic stability in the presence of sodium dodecyl sulfate (SDS), which acted as a micellar destabilizing agent (260), are illustrated in **Figure 3.6** The time dependence decrease in scattered light intensity of micelles is an indication of gradual micellar disassembly in the presence of SDS. The results indicated that the polymeric micelles prepared from diblock copolymers were kinetically more stable compared to those prepared from triblock copolymers, at least under current experimental conditions. This observation may be reflective of the formation of semicrystalline core structures of higher interaction strengths for these micelles and/or a higher aggregation number for di-versus triblock copolymer micelles. PEO-PLA-PCL micelles exhibited a drastic decrease in scattered light intensity right after adding the SDS irrespective of the stereoregularity of the

PLA block. The same trend but at a reduced extent was observed for the PEO-PLA-PBCL micelles. The better kinetic stability of PEO-PLA-PBCL micelles over their PCL containing counterparts may be due to π-π staking in PBCL containing cores and/or better interaction of SDS with PCL over PBCL containing structures (225).

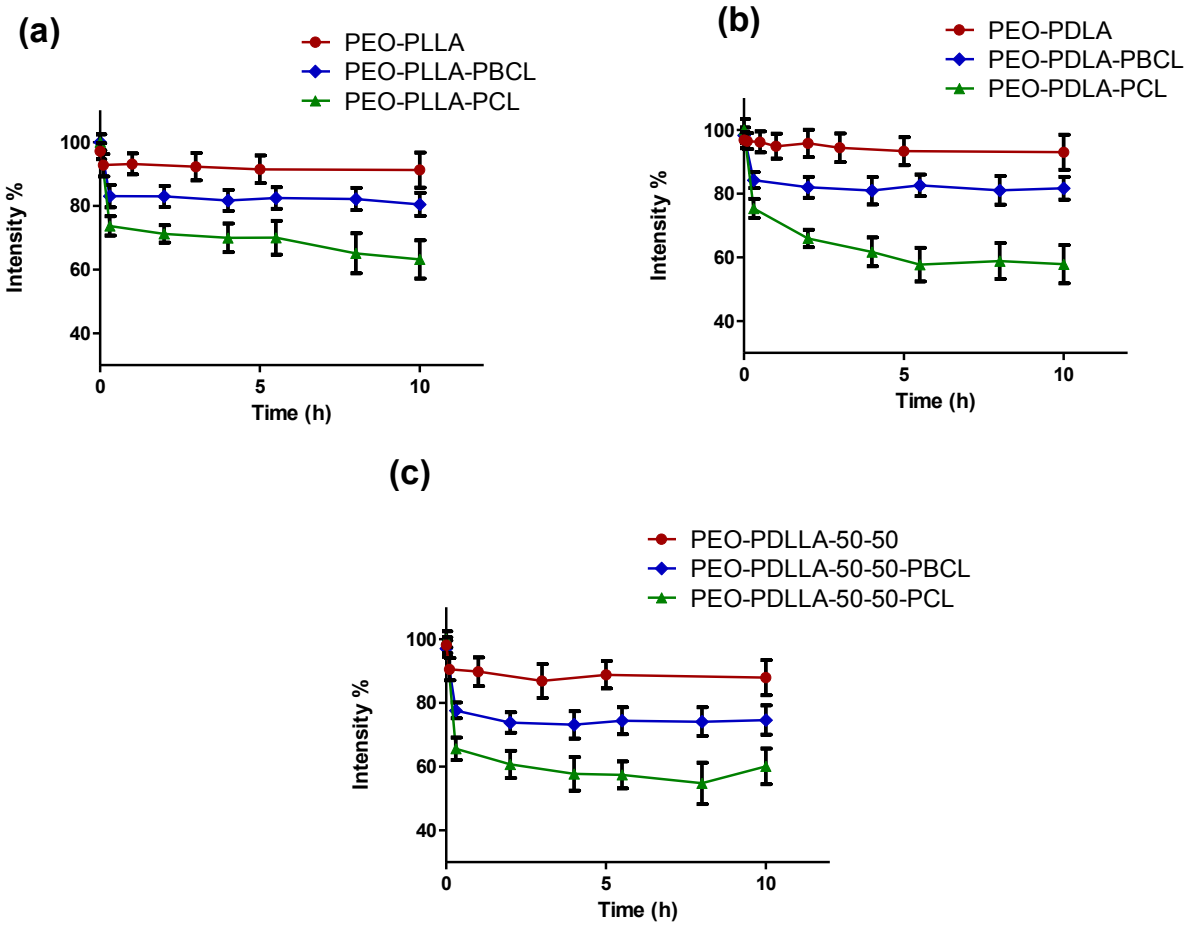

Figure 3.6 The time dependent changes in scattered light intensity of different copolymers containing **(a)** poly(L-lactide), **(b)** poly(D-lactide), and **(c)** poly(D,L-lactide-50-50) segments. The data was gathered after addition of SDS solution to micelles at different incubation time points. Data are represented as mean ± SD (n=3).

3.3.3 The effect of ABC Design and B Block Stereoregularity on the Loading and Release of a Model Drug from Polymeric Micelles

3.3.3.1 Nimodipine Loading in Polymeric Micelles

Overall, a significantly higher encapsulation efficiency and drug loading were obtained for micelles prepared from either PEO-PLA-PBCL and/or PEO-PLA-PCL triblock copolymers compared to PEO-PLA diblock copolymers for nimodipine (Student's t test, $p<0.05$) (**Table 3.3**). This observation is partly in concert with calculated Flory-Huggins interaction parameters (χ) determined using the group contribution method (GCM) for PBCL and PCL that show better compatibility than PLA with nimodipine (**Table 3.4**). Because of the lower Flory-Huggins interaction parameters (χ) between nimodipine and PCL as compared to PBCL one should expect better nimodipine solubility in PEO-PLA-PCL micelles than PEO-PLA-PBCL ones (at similar molecular weights for each block). This was not the case according to experimental data, which highlights the shortcomings of the GCM in predicting the solubility of drug polymer pairs as outlined in our previous publication (227).

The Z average diameter of nimodipine loaded micelles increased compared to empty micelles irrespective of the copolymer structure (Student's *t* test, $p<0.05$) (**Table 3.3**).

Table 3.3 Characteristics of nimodipine loaded micellar formulations of copolymers**.**

Polymer	Diameter ± SD[a] (nm)	PDI ± SD[b]	EE% ± SD[c]	DL% ± SD[d]	Drug/polymer (mol/mol) ± SD
PEO-PLLA	104 ± 4.93	0.15 ± 0.07	31.2 ± 2.03	3.12 ± 0.19	1.08 ± 0.07
PEO-PDLA	113 ± 3.26	0.10 ± 0.01	28.2 ± 2.06	2.82 ± 0.21	0.90 ± 0.01
PEO-PD/LLA	75.2 ± 1.68	0.15 ± 0.02	29.0 ± 2.51	2.90 ± 0.24	0.90 ± 0.02
PEO-PDLLA-50-50	72.5 ± 2.66	0.20 ± 0.09	26.3 ± 2.88	2.63 ± 0.29	0.85 ± 0.04
PEO-PLLA-PBCL	67.6 ± 2.54	0.18 ± 0.02	53.0 ± 2.75	5.30 ± 0.22	1.69 ± 0.15
PEO-PDLA-PBCL	64.0 ± 3.41	0.20 ± 0.06	49.6 ± 4.05	4.96 ± 0.40	1.59 ± 0.10
PEO-PD/LLA-PBCL	56.2 ± 2.43	0.21 ± 0.09	50.9 ± 4.67	5.09 ± 0.44	1.63 ± 0.11
PEO-PDLLA-50-50-PBCL	57.9 ± 3.48	0.12 ± 0.01	46.6 ± 3.02	4.66 ± 0.30	1.49 ± 0.06
PEO-PLLA-PCL	112 ± 5.20	0.08 ± 0.02	47.0 ± 3.52	4.70 ± 0.32	1.41 ± 0.08
PEO-PDLA-PCL	132 ± 4.56	0.06 ± 0.01	43.3 ± 2.36	4.33 ± 0.22	1.30 ± 0.05
PEO-PDLLA-50-50-PCL	143 ± 6.25	0.08 ± 0.03	48.2 ± 4.19	4.82 ± 0.38	1.43 ± 0.08

[a] Z average measured by DLS.

[b] Polydispersity index measured by DLS.

[c] Encapsulation efficiency $(\%) = \frac{the\ amount\ of\ encapsulated\ nimodipine}{the\ total\ feeding\ amount\ of\ nimodipine} \times 100.$

[d] Drug loading$(\%) = \frac{the\ amount\ of\ encapsulated\ nimodipine}{the\ total\ amount\ of\ polymer} \times 100.$

Table 3.4 The Solubility parameters and Flory-Huggins interaction parameters (χ) between nimodipine and PBCL, PCL and PLA blocks calculated by the GCM.

Drug	δ ($MPa^{1/2}$)	$\chi_{drug/polymer}$
PBCL	21.00	0.60
PCL	21.37	0.23
PLA	22.95	1.35
Nimodipine	21.60	-

3.3.3.2 Nimodipine Release from Polymeric Micelles

A comparison between the release profiles of nimodipine from di- versus triblock copolymer micelles provided interesting results. A burst release for micelles prepared from diblock copolymers, irrespective of the stereochemistry of the PLA block was observed (**Figure 3.7**). The burst release was, however, attenuated in micelles prepared from triblock copolymers. Nimodipine loaded in PEO-PLLA diblock copolymer micelles revealed a higher release compared to PEO-PLLA-PBCL and PEO-PLLA-PCL triblock copolymer micelles (similarity factor f_2 < 50 (270)) (**Figure 3.7**). There was no difference between drug release from PEO-PLLA-PBCL and PEO-PLLA-PCL triblock copolymer micelles (f_2 > 50) (**Figure 3.7a**). Similarly, the release of nimodipine from PEO-PDLA diblock copolymer micelles was higher from their triblock copolymer micelle counterparts (f_2 < 50) (**Figure 3.7b**). Similar results were observed for PDLLA-50-50 containing micelles (**Figure 3.7c**). Of note, the lower release of nimodipine from triblock copolymer micelles is achieved despite the higher loaded drug levels in these micelles compared to those prepared from diblock copolymers (**Table 3.3**).

To investigate the relative contribution of PLA versus PBCL block in our observation, we compared the release profile of nimodipine from PEO-PBCL diblock copolymer micelles to those of PEO-PLA-PBCL triblock copolymers. Similar to what was observed for the PEO-PLA diblock copolymer micelles, PEO-

PBCL micelles showed a burst drug release (**Figure 3.S5** and **Table 3.S1**). These data point to the effect of the PLA as an outer core in triblock copolymer micelles forming a barrier against drug release.

The relatively rapid release of nimodipine from PEO-PLA diblock copolymer micelles (**Figure 3.7**) was likely due to low drug-core compatibility evidenced by higher Flory-Huggins interaction parameters (χ) (**Table 3.4**). This may lead to nimodipine localization outside of the micellar core as described in our previous publication (242). The same behavior in terms of initial fast release was also observed for loaded micelles prepared from PEO-PBCL diblock copolymers. The inhibition of burst release in ABC triblock copolymer micelles compared to diblock copolymer micelles may be attributed to the presence of the middle PLA block (PLA) with poor solubility for the drug which acts as a physical barrier and prevents the initial fast drug release from the micellar core.

With respect to the effect of the stereochemistry of the B block in AB block copolymer micelles on the release rate of encapsulated nimodipine, there were no significant differences in the release profiles of nimodipine from micelles of PEO-PLLA, PEO-PDLA, PEO-PD/LLA and PEO-PDLLA-50-50 diblock copolymers (f_2 > 50). A similar release (~ 70 % nimodipine) within 24 h of study from these micelles was shown regardless of the stereochemistry and crystallinity of the PLA (**Figure 3.8a**). Comparing the release profiles of nimodipine from PEO-PLLA-PBCL, PEO-PDLA-PBCL, PEO-PD/LLA-PBCL and PEO-PDLLA-50-50-PBCL micelles also showed similar nimodipine release from different micelles irrespective of the stereochemistry of the PLA block (f_2 > 50). Similar (~ 64 %) level of nimodipine release within 24 h of study was achieved for all these block copolymer micelles (**Figure 3.8b**). Nimodipine loaded micelles of PEO-PLLA-PCL, PEO-PDLA-PCL and PEO-PDLLA-50-50-PCL triblock copolymers also showed similar rate of release irrespective of the stereochemistry of the block copolymer (f_2 > 50). Around ~ 55 % nimodipine release within 24 h of study, was seen for all the micelles (**Figure 3.8c**).

In spite of the presence of different stereoactive blocks in the poly(lactide block), no PLA crystallinity was detected in triblock copolymer micelles and they revealed an amorphous nature leading to no significant effect for the stereoregularity of the B block on the encapsulation and release profile of nimodipine from ABC triblock copolymer micelles of different stereoregularity in the B block.

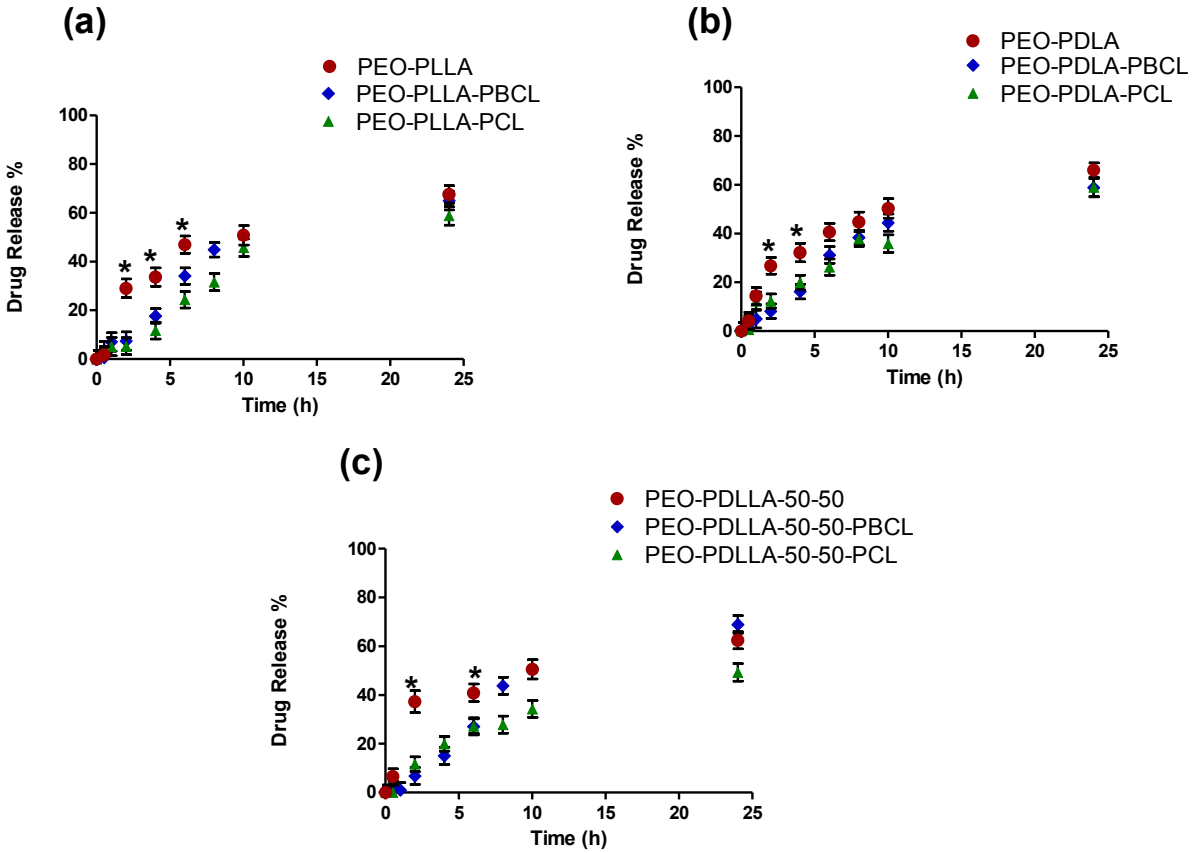

Figure 3.7 Release profiles of nimodipine from micelles of different copolymers featuring different stereochemistry of lactide, **(a)** poly(L-lactide), **(b)** poly(D-lactide), and **(c)** poly(D,L-lactide-50-50). (*) means, where the cumulative drug release appeared to be significantly different from other micelles in the group at the related time points (Student's *t* test, $p<0.05$). Data are represented as mean ± SD (n=3).

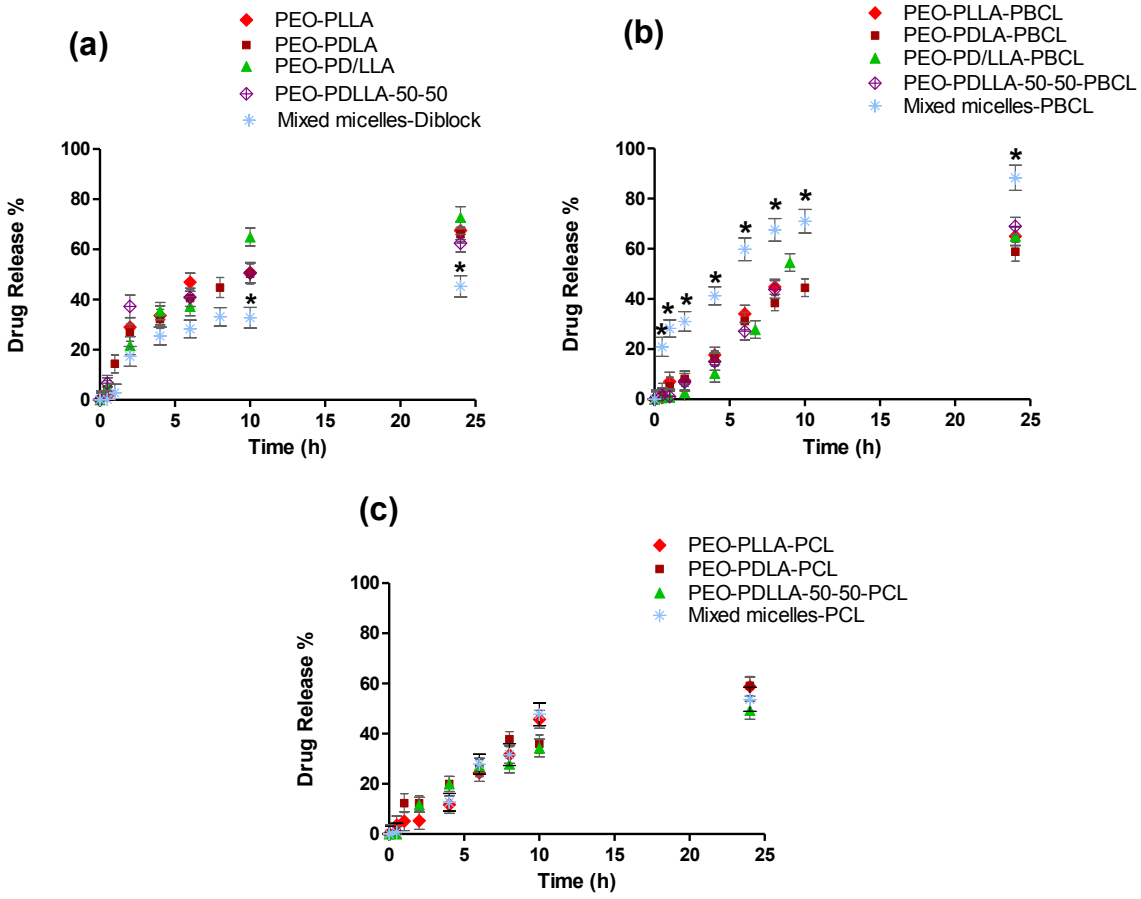

Figure 3.8 Release profiles of nimodipine from micelles of **(a)** PEO-PLA diblock, **(b)** PEO-PLA-PBCL triblock, and **(c)** PEO-PLA-PCL triblock. (*) indicates where drug release was significantly different from other micelles in the group at the related time point (Student's *t* test, $p<0.05$). Data are represented as mean ± SD (n=3).

3.3.4 Assessing the Stereocomplexation of Di- and Triblock Copolymers in Mixed Micelles from Block Copolymers with Opposite Stereochemistry in the B Block

During this study, mixed polymeric micelles were also prepared using 1:1 molar blends of PLLA: PDLA containing diblock as well as triblock copolymers. For mixed micelles formed from diblock copolymers, *i.e.*, the 1:1 blend of PEO-PLLA and PEO-PDLA, stereocomplexation was observed. This was evidenced by the presence of a melting peak at 211.2 °C in the DSC thermogram of mixed micelles described above (**Figure 3.9a**). By comparison, the melting peaks of PLA blocks diblock copolymer micelles of single stereoregular block copolymer, *i.e.*, PEO-PLLA or PEO-PDLA micelles, appeared at 167.2, 166.9 °C, respectively (**Figure3.4A**). This observation points to the occurrence of higher degree of crystallization

and stronger interaction in crystalline region in stereocomplex micellar core compared to single stereoregular micellar cores and was in line with the previous reports (225, 275). In contrast, for triblock copolymer mixtures, the 1:1 blend of PEO-PLLA-PBCL and PEO-PDLA-PBCL did not show any melting peak in the DSC thermograms (**Figure 3.9a**). This observation is likely due to the disruption of the attractive intermolecular interaction between opposite stereoactive PLA segments in the outer micellar cores by the PBCL segment. Based on the DSC results, stereocomplexation of opposite stereoactive segments in the triblock copolymer did not occur.

The diblock copolymer mixed micelles also showed reduced CMC compared to micelles from single PEO-PLLA or PEO-PDLA diblock copolymers (**Table 3.5**). These micelles also showed the highest kinetic stability among different block copolymer micelles under study (**Figure 3.9b**). Micelles formed from a mixture of PEO-PLLA-PBCL and PEO-PDLA-PBCL illustrated a significantly higher CMC compared to micelles formed from one kind of block copolymer (one way ANOVA with *Tukey* post-test, $p<0.05$) (**Table 3.5**). For the PEO-PLA-PCL triblock copolymers, no significant difference between the CMC of mixed micelles and micelles prepared from single polymers was observed (one way ANOVA with Tukey post-test, $p>0.05$) (**Table 3.5**). When comparing different mixed micelles for their CMC, the following trend was observed: PEO-PLA-PBCL>PEO-PLA>PEO-PLA-PCL (**Figure 3.9b**), which was similar to the trend observed for micelles from single chain block copolymers in the same categories (**Figure 3.5a-c**).

In terms of kinetic stability, mixed micelles formed from diblock copolymers, were the most stable ones (**Figure 3.9c**), perhaps owing to the stronger interactions between PLLA and PDLA blocks and subsequent higher crystallinity (**Figure 3.9a**). This was followed by mixed micelles prepared from PEO-PLA-PBCL and then PEO-PLA-PCL block copolymers. This trend was also similar to that observed for micelles from single chain block copolymers (**Figure 3.6**). The reason for higher kinetic stability of mixed micelles from PEO-PLA-PBCL blends compared to PEO-PLA-PCL blends is not clear, but may relate to possible π-π stacking in the core of PBCL containing micelles.

Similar to micelles prepared from single type of block copolymers, the encapsulation of nimodipine was higher in mixed micelles prepared from triblock copolymers compared to ones from diblock copolymers (**Table 3.5**). However, in terms of drug release the trend was as follows in mixed micelles: PEO-PLA-PBCL> PEO-PLA-PCL≥PEO-PLA. The lower drug release from PEO-PLA based mixed micelles is perhaps reflective of the stereocomplex formation within this core structure as opposed to PEO-PLA-PBCL mixed micelles that do not form stereocomplex cores. The slow release from PEO-PLA-PCL mixed micelles despite absence of stereocomplexation in the core is surprising and might be due to the semicrystalline, hydrophobic and drug miscible nature of PCL.

With respect to the comparison between release profile of nimodipine in mixed micelles, versus single chain micelles; for diblock copolymers, mixed micelles of PEO-PLLA and PEO-PDLA showed lower nimodipine release compared to micelles of single chain polymers (**Figure 3.9d**). Stereocomplexation of PDLA and PLLA segments (30, 276), and/or stronger interaction between the stereocomplexes and nimodipine (274), is likely the reason for the lower release rate of nimodipine from mixed diblock copolymer micelles. In contrast, micelles prepared from blends of PEO-PLLA-PBCL and PEO-PDLA-PBCL showed higher release compared to micelles prepared from single polymer chains (*i.e.,* either PEO-PLLA-PBCL or PEO-PDLA-PBCL micelles) (f_2 < 50) (**Figure 3.9d**). On the other hand, the release profile of nimodipine from micelles prepared from blends of PEO-PLLA-PCL and PEO-PDLA-PCL was similar to their counterparts from single polymer chains (f_2 > 50) (**Figure 3.9d**). This result is in line with the absence of stereocomplexation in mixed micelles formed from triblock copolymers.

In general, two different designs were shown to be successful in reducing drug release from polymeric micelles: a) ABC type polymeric micelles of PEO-PLA-PBCL or PEO-PLA-PCL; and b) stereocomplex mixed micelles from diblock copolymers. Stereocomplex mixed micelles of diblock copolymers reduced drug release at the later time points of the release (**Figure 3.8a**), whereas ABC polymeric micelles prepared from individual triblock copolymers of either PEO-PLA-PBCL or PEO-PLA-PCL reduced burst release at the early time points (**Figure 3.7**). ABC block copolymer micelle showed their superiority in reduction of the burst release of drug from micelles while providing higher encapsulation efficiency than micelles made from AB diblock copolymers. ABC triblock copolymer micelles were also shown to have improved thermodynamic stability compared to their diblock copolymer counterparts, but their stability in the presence of SDS was lower to that of diblock copolymer micelles.

The significance of this work lays in the rational design and development of three layered (ABC) block copolymer micelle with drug compatible blocks at the inner core (C block) and drug incompatible blocks (B block) at the outer core. So that drug compatible block at the inner core increased drug loading and encapsulation efficiency while drug incompatible block reduced the initial burst release of drug from the inner core. It is our expectation that this general design could be applied in case of other polymer/drug pairs to reduce the burst release of the drug of interest from micellar containers at nanoscale dimension.

Table 3.5 Characteristics of mixed micelles.

	Mixed micelles-diblocks[a]	Mixed micelles-PBCL[b]	Mixed micelles-PCL[c]
CMC ± SD[d] (μM)	0.31 ± 0.01	1.47 ± 0.02*	0.18 ± 0.01
Diameter ± SD[e] (nm)	89.8 ± 1.34	60.9 ± 2.46	85.6 ± 5.10
PDI ± SD[f]	0.06 ± 0.02	0.11 ± 0.01	0.11 ± 0.03
Diameter ± SD[g] (nm)	98.3 ± 3.15	134 ± 4.17	110 ± 2.89
PDI ± SD[h]	0.11 ± 0.01	0.16 ± 0.01	0.07 ± 0.02
EE% ± SD[i]	34.3 ± 3.00	49.2 ± 2.85	50.4 ± 3.27
DL% ± SD[j]	3.43 ± 0.29	4.92 ± 0.28	5.04 ± 0.22
Drug/polymer (mol/mol) ± SD	1.14 ± 0.10	1.57 ± 0.06	1.51 ± 0.07

[a] Equimolar blends of PEO-PLLA and PEO-PDLA.

[b] Equimolar blends of PEO-PLLA-PBCL and PEO-PDLA-PBCL.

[c] Equimolar blends of PEO-PLLA-PCL and PEO-PDLA-PCL.

[d] CMC measured by DLS.

[e] Z average of empty micelles measured by DLS.

[f] Polydispersity index measured by DLS for empty micelles.

[g] Z average of nimodipine loaded micelles measured by DLS.

[h] Polydispersity index measured by DLS for nimodipine loaded micelles.

[I] Encapsulation efficiency $(\%) = \frac{the\ amount\ of\ encapsulated\ nimodipine}{the\ total\ feeding\ amount\ of\ nimodipine} \times 100.$

[j] Drug loading$(\%) = \frac{the\ amount\ of\ encapsulated\ nimodipine}{the\ total\ amount\ of\ polymer} \times 100.$

(*) means prepared mixed micelles from equimolar blends of PEO-PLLA-PBCL and PEO-PDLA-PBCL copolymers showed a significantly higher CMC compared to those from PEO-PLA-PBCL triblock and PEO-PLA diblock copolymers (Student *t* test, $p<0.05$).

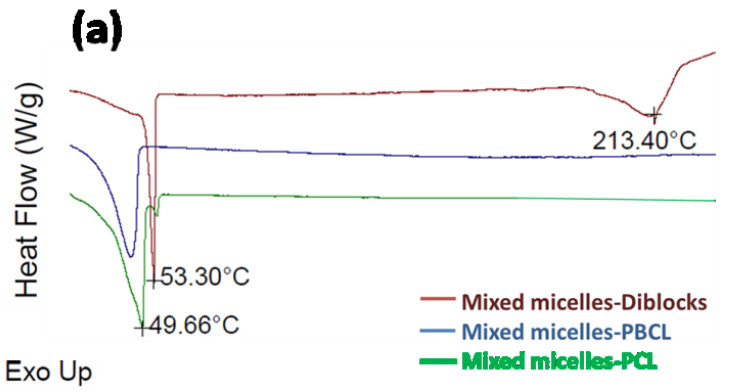
(a)
Heat Flow (W/g)
213.40°C
53.30°C
49.66°C
Exo Up
Mixed micelles-Diblocks
Mixed micelles-PBCL
Mixed micelles-PCL

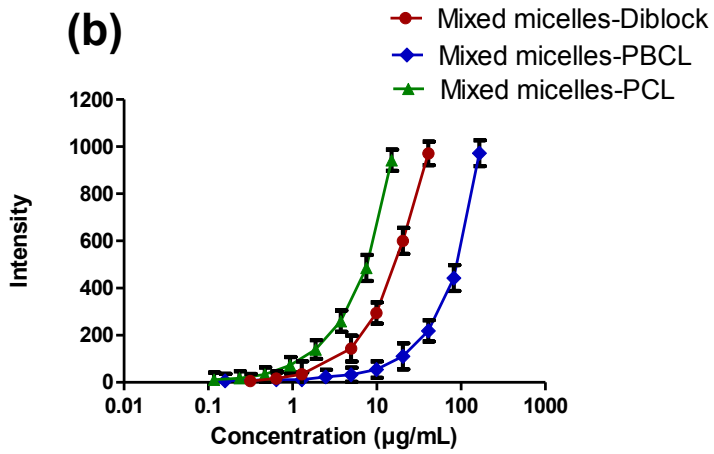
(b)
Mixed micelles-Diblock
Mixed micelles-PBCL
Mixed micelles-PCL
Intensity
1200
1000
800
600
400
200
0
0.01
0.1
1
10
100
1000
Concentration (µg/mL)

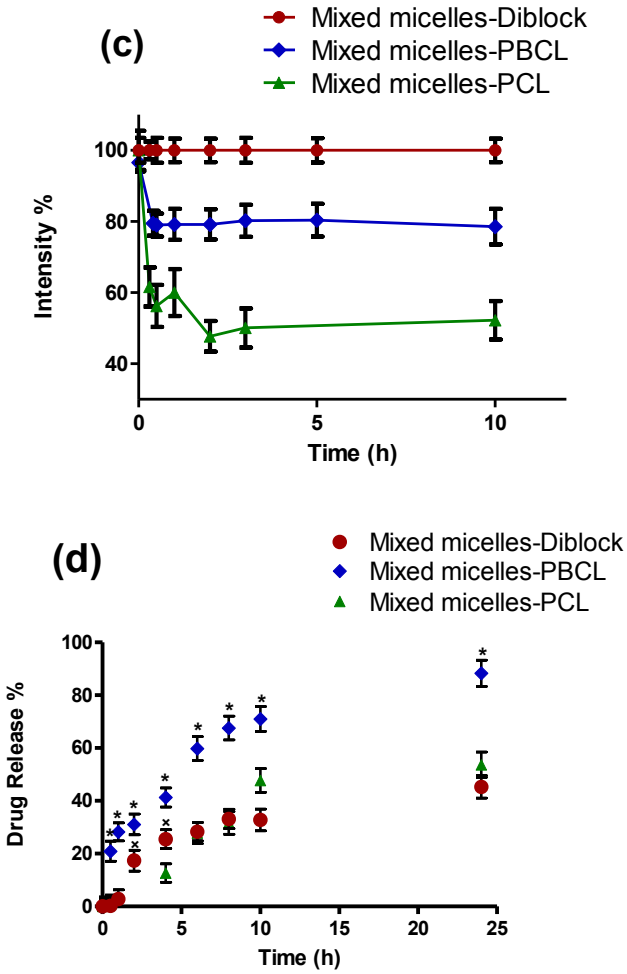

Figure 3.9 Characteristics of mixed micelles. **(a)** DSC thermograms of freeze-dried form of different mixed micelles. Melting temperatures were measured for the second heating ramp at a heating rate of 2 °C/min from 8 °C to 240 °C. **(b)** DLS signal as a function of log concentration of copolymers was used to measure the CMC of different mixed micelles. **(c)** The time dependent changes in scattered light intensity of different mixed micelles. The data was gathered after addition of SDS solution to micelles at different incubation time points. **(d)** Release profiles of nimodipine from different mixed micelles. Mixed micelles-diblocks denotes equimolar blends of the D and L isomers of PEO-PLA diblock copolymers. Mixed micelles-PBCL denotes equimolar blends of the D and L isomers of PEO-PLA-PBCL triblock copolymers and mixed micelles-PCL denotes equimolar blends of the D and L isomers of PEO-PLA-PCL triblock copolymers. (*) or (×) means where the cumulative drug release appeared to be significantly different from other micelles in the group at the related time points (p<0.05, student's t test). Data are represented as mean ± SD (n=3).

3.4 Conclusion

In conclusion, we have shown that a properly designed ABC block copolymer micelle with drug compatible blocks at the inner core and drug incompatible blocks at the outer core can be used to reduce the burst release of drug from micellar nano-carriers while providing higher encapsulation efficiency than micelles made from AB diblock copolymers. ABC triblock copolymer micelles were also shown to have improved thermodynamic stability compared to their diblock copolymer counterparts, but their stability in the presence of SDS was lower to that of diblock copolymer micelles. In this study, we were unable to preserve the stereoregularity of the outer core of ABC polymeric micelles perhaps because of the interaction of inner (C block) and outer core (B block) segments within the micellar structure. As a result, no notable effect for the stereochemistry of the B block on the micellar stability, drug loading level and release profile in ABC block copolymer micelles was observed. Stereocomplexation of the opposite stereochemistry of the B block in mixed ABC block copolymer micelles was not observed either. This resulted in inferior properties in terms of micellar stability and nimodipine release from mixed tri- versus mixed diblock copolymer micelles. It remains to be seen as to which of these factors (kinetic/thermodynamic stability and/or drug release rate and profile) play a more crucial role in defining the final pharmacokinetic of the carrier as well as the encapsulated drug in a biological system following *in vivo* administration.

3.5 Acknowledgments

This study was supported by grants from Natural Sciences and Engineering Research Council of Canada (NSERC). A.L. also acknowledges support from Canadian Foundation for Innovation (CFI) and Alberta Advanced Education and Technology (AAET) for the infrastructure used in the study. H.S.A. was awarded the Women and Children's Health Research Institute (WCHRI) Graduate Studentship through the generous support of the Royal Alexandra Hospital Foundation.

3.6 Supplementary Information

(a)

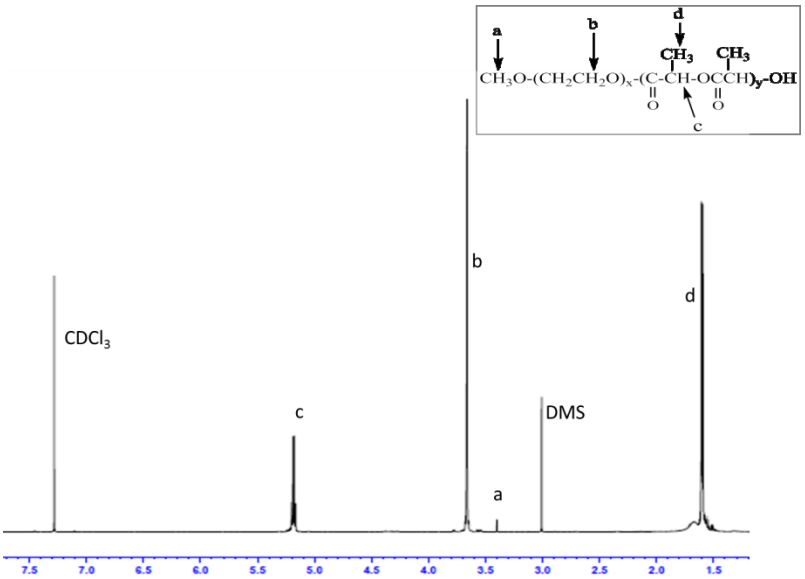

(b)

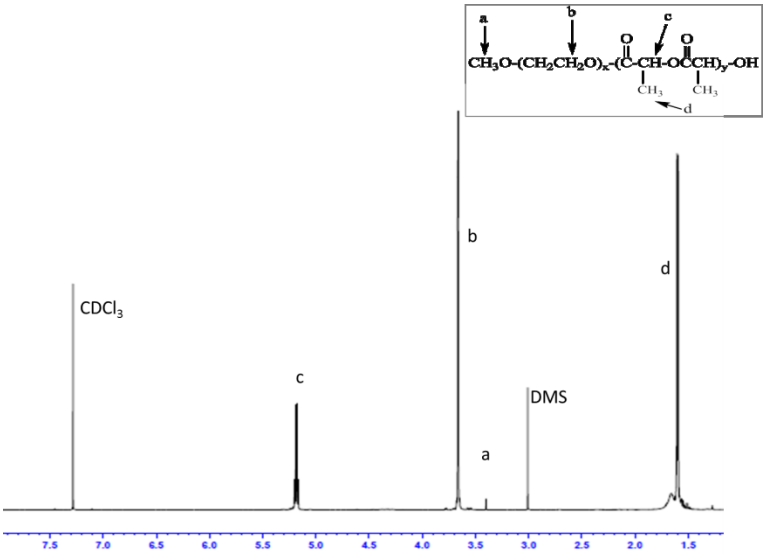

(c)

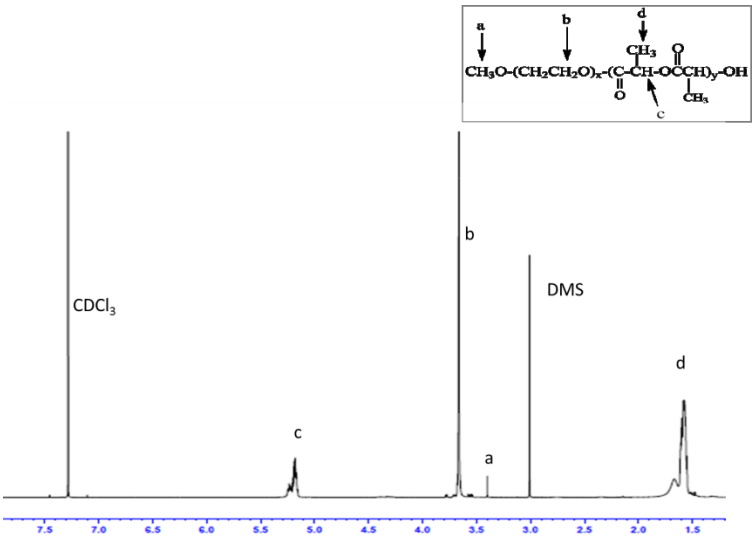

(d)

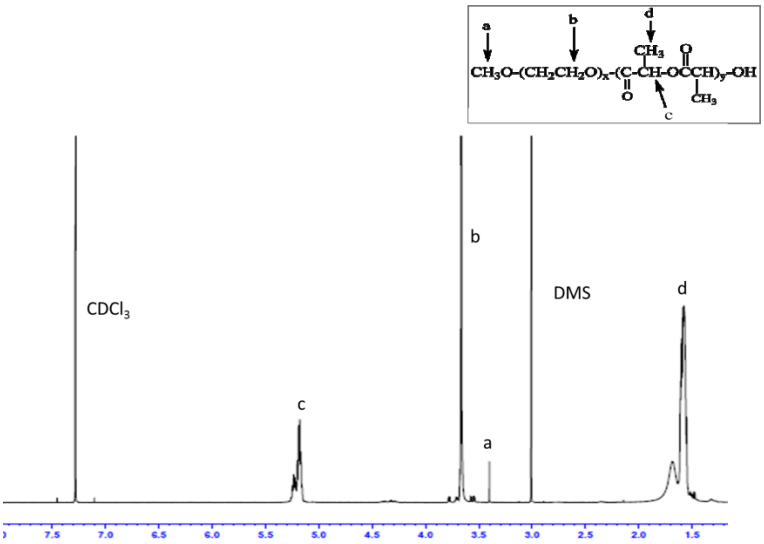

Figure 3.S1 ^{1}H NMR spectra and peak assignments for **(a)** PEO-PLLA; **(b)** PEO-PDLA; **(c)** PEO-PD/LLA and **(d)** PEO-PDLLA-50-50 block copolymers in $CDCl_3$ with dimethyl sulfone (DMS) as internal standard.

(a)

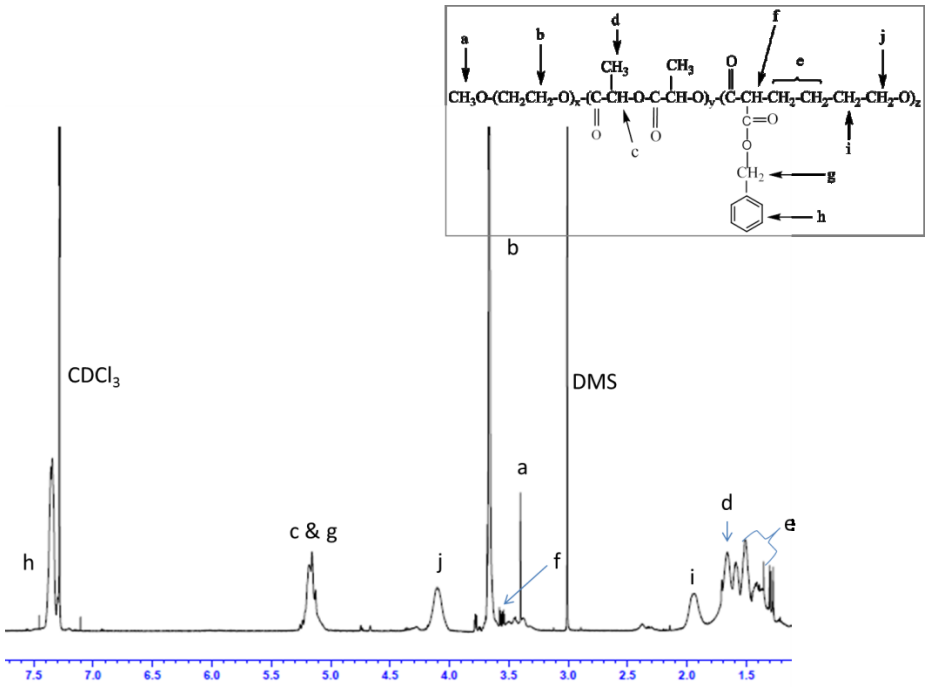
a
b
d
f
j
e
CH3
CH3
O
c
i
g
h
CDCl3
DMS
b
a
d
e
c & g
h
j
f
i
7.5
7.0
6.5
6.0
5.5
5.0
4.5
4.0
3.5
3.0
2.5
2.0
1.5

(b)

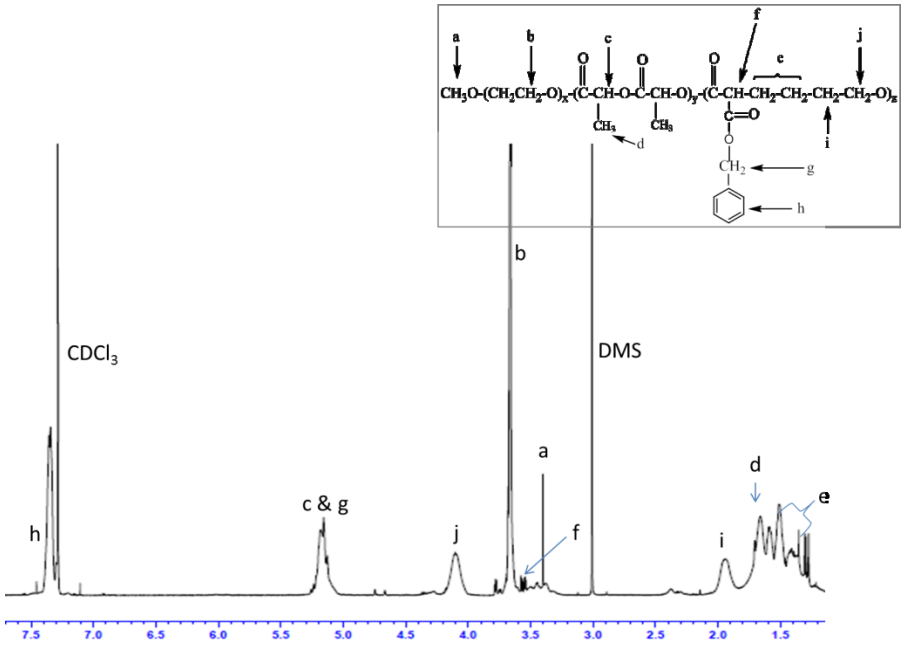
a
b
c
f
e
j
O
CH3
CH3
d
i
g
h
b
CDCl3
DMS
a
d
e
c & g
h
j
f
i
7.5
7.0
6.5
6.0
5.5
5.0
4.5
4.0
3.5
3.0
2.5
2.0
1.5

(c)

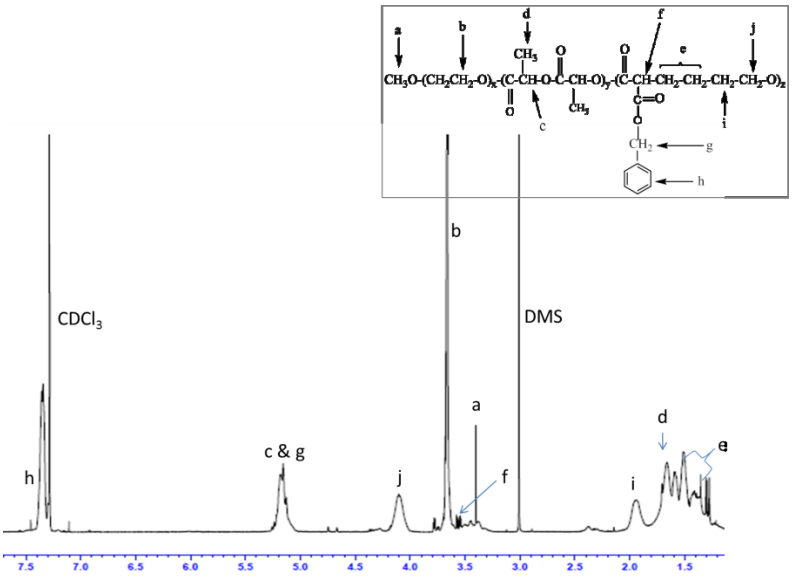

(d)

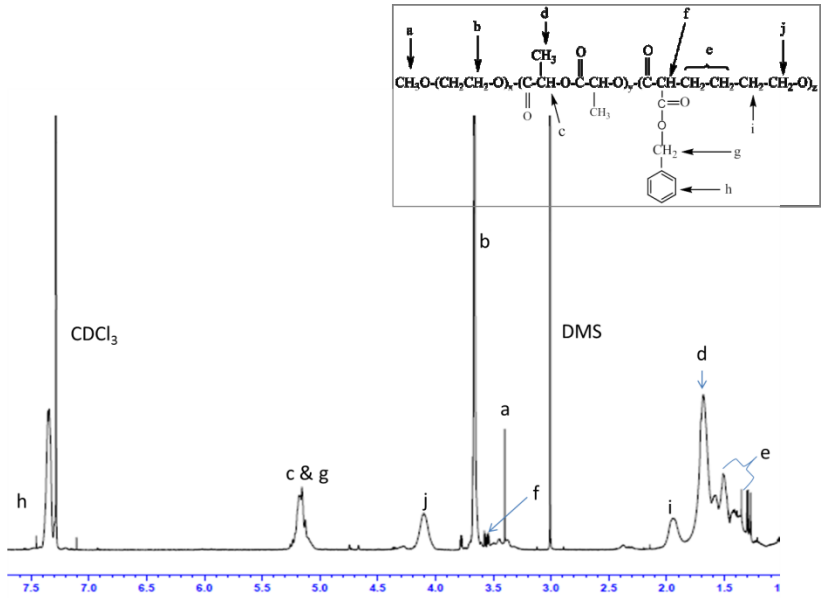

Figure 3.S2 ^{1}H NMR spectra and peak assignments for **(a)** PEO-PLLA-PBCL; **(b)** PEO-PDLA-PBCL; **(c)** PEO-PD/LLA -PBCL and **(d)** PEO-PDLLA-50-50-PBCL block copolymers in $CDCl_3$ with dimethyl sulfone (DMS) as internal standard.

(a)

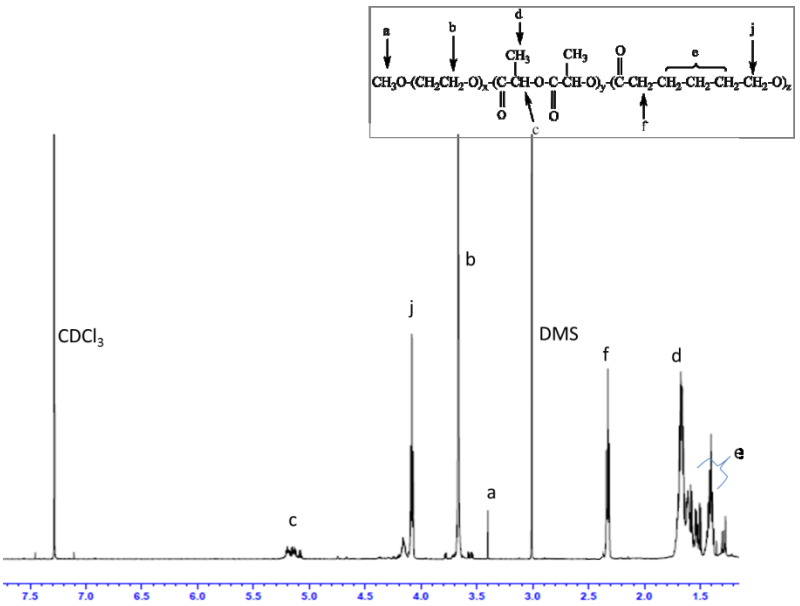
CDCl3
DMS
a
b
c
d
e
f
j
7.5
7.0
6.5
6.0
5.5
5.0
4.5
4.0
3.5
3.0
2.5
2.0
1.5

(b)

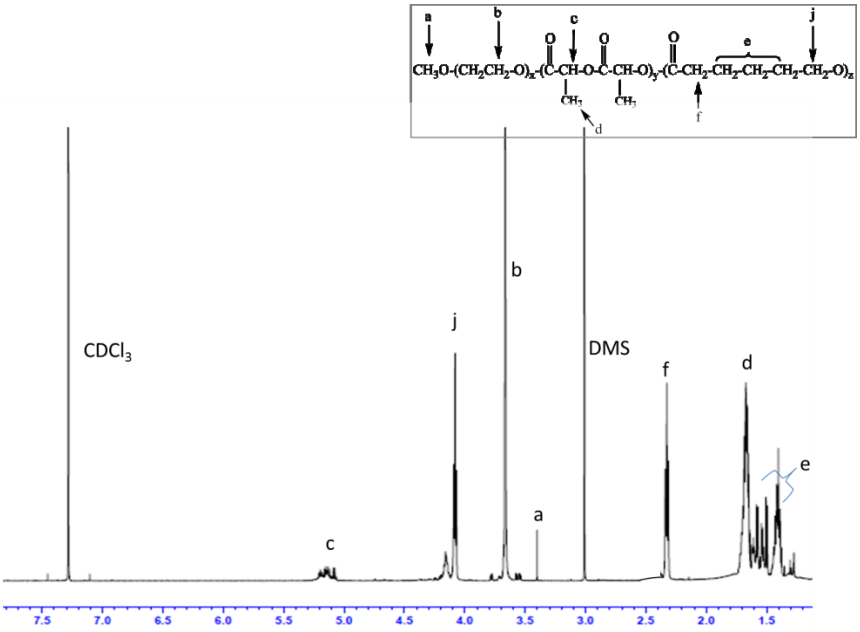
CDCl3
DMS
a
b
c
d
e
f
j
7.5
7.0
6.5
6.0
5.5
5.0
4.5
4.0
3.5
3.0
2.5
2.0
1.5

(c)

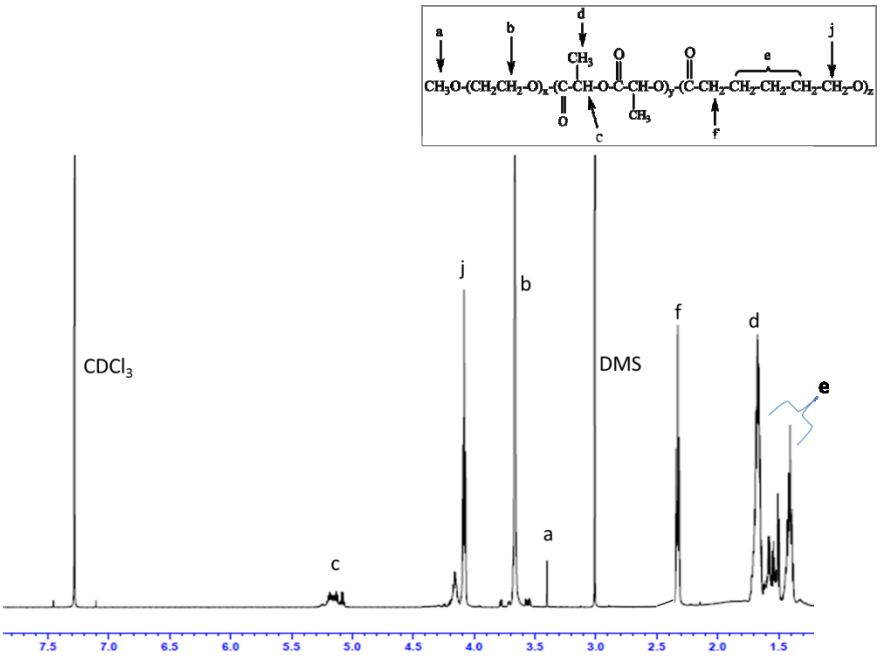

Figure 3.S3 ^{1}H NMR spectra and peak assignments for **(a)** PEO-PLLA-PCL; **(b)** PEO-PDLA-PCL and **(c)** PEO-PDLLA-50-50-PCL block copolymers in $CDCl_3$ with dimethyl sulfone (DMS) as internal standard.

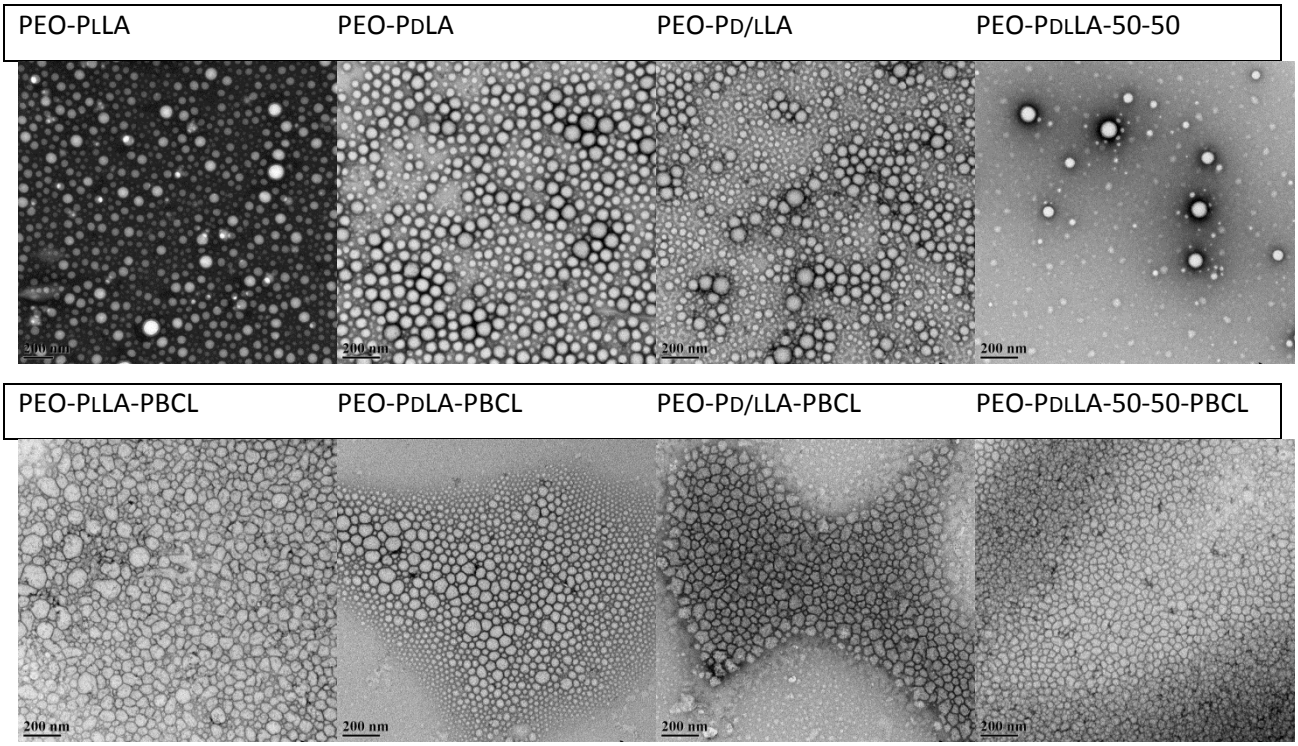

Figure 3.S4 TEM images of polymeric micelles from different di and triblock copolymers.

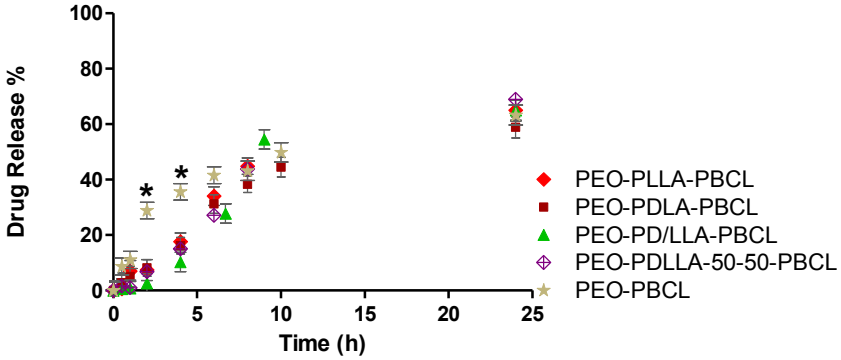

Figure 3.S5 Comparison between the release profiles of nimodipine from PEO-PLA-PBCL triblock and PEO-PBCL diblock micelles. (*) means where the cumulative drug release appeared to be significantly different from other micelles in the group (p<0.05, student's t test). Data are represented as mean ± SD (n=3).

Table 3.S1 Characteristics nimodipine loaded micellar formulations of PEO-PBCL block copolymer.

	PEO_{5000}-PBCL
Diameter ± SD[a]	55.33 ± 3.38
PDI ± SD[b]	0.21 ± 0.02
EE% ± SD[c]	29.61 ± 3.73
DL% ± SD[d]	2.96 ± 0.36
Drug/polymer (mol/mol) ± SD	0.81 ± 0.03

[a] Z average of nimodipine loaded micelles measured by DLS.

[b] Polydispersity index measured by DLS for nimodipine loaded micelles.

[c] Encapsulation efficiency $(\%) = \frac{the\ amount\ of\ encapsulated\ nimodipine}{the\ total\ feeding\ amount\ of\ nimodipine} \times 100.$

[d] Drug loading$(\%) = \frac{the\ amount\ of\ encapsulated\ nimodipine}{the\ total\ amount\ of\ polymer} \times 100.$

Chapter Four

STAT3 instead of HIF-1α is important in mediating hypoxia-induced chemoresistance in MDA-MB-231, a triple negative breast cancer cell line

4.1 Introduction

Hypoxia commonly occurs in solid tumors, as a result of their rapid proliferation that outpaces the oxygen supply (14). In response to hypoxia, cancer cells are known to upregulate a protein called Hypoxia Inducible Factor (HIF)(93). HIF is a heterodimeric transcription factor comprised of an oxygen regulated unit, HIF-1α, as well as a constitutionally expressed beta unit, HIF-1β. In the presence of oxygen, HIF-1α is degraded by prolyl hydroxylase via ubiquitination and proteolysis (92). Under hypoxia, HIF-1α is stabilized. After its dimerization with HIF-1β, the HIF heterodimer translocates to the nucleus where it activates the transcription of various downstream targets, many of which are known to be involved in cancer progression, survival, aggressiveness and chemoresistance (92, 93, 277). To induce drug resistance, HIF has been demonstrated to reduce drug-induced apoptosis and senescence (123, 163) and to induce autophagy (122, 278). In view of its significance as a master regulator of hypoxia-induced chemoresistance (HICR), HIF-1, especially its α subunit, is considered to be therapeutic target for cancer treatment (122-126, 163, 279).

While HIF has been shown to be the key mediator of HICR, a relatively small number of publications have implicated other molecular mechanisms in conferring HICR. For instance, p53 can be inactivated in cancer cells in hypoxia, inducing resistance to p53-mediated apoptosis (280-282). It also has been shown that hypoxia can induce the activation of a number of signalling pathways including those of phosphoinositol-3-kinase (PI3K), nuclear factor kappa-B (NFκB), cycloxygenase-2 (COX-2), activator protein-1 (AP-1), c-Jun, Pim-1, apoptosis inhibitory protein (IAP-2) and transducer and activator of transcription 3 (STAT3) protein, and these hypoxia-induced biochemical alterations may contribute to drug resistance in the setting of hypoxia (111, 229, 280, 283-289). However, in most of these studies, the role of HIF-1α relative to that of these signalling pathways was not directly assessed. Specifically, it is not clear if these pathways are key mediators of HICR that is independent of HIF-1α.

In this study, we aimed to understand the mechanism underlying HICR in triple negative breast cancer (TNBC), since TNBC tumors are known to frequently carry a hypoxic phenotype and HIF-1α is known to be frequently over-expressed in these tumors (231). Cisplatin, a platinum used as part of standard chemotherapy regimen for TNBC patients (231, 232), was used in this study. Our findings suggest that STAT3, instead of HIF-1α, is the key player of HICR in TNBC. This study has demonstrated that, while HIF-1α is recognized to be an important mediator for HICR, exceptions exist.

4.2 Methods and Materials

4.2.1 Cell Culture

TNBC cell line, MDA-MB-231 was obtained from ATCC (Manassas, VA) and maintained in RPMI 1640 medium supplemented with 10% fetal bovine serum (Invitrogen, Karlsruhe, Germany), 100 units/mL penicillin, and 100 mg/mL streptomycin in a humidified incubator under 95% air and 5% CO_2 at 37°C. For hypoxic condition, cells were cultured in a CO_2 incubator maintained at 94% N_2, 5% CO_2 and 1% O_2. MDA-MB-231 cells were plated at 25–30% confluence and cultured until they reached 60–70% confluence for different treatments. The chemotherapeutic agent cisplatin (cis-diamminedichloroplatinum(II) (CDDP) (purity 99%), #H878, AK Scientific Inc.) was freshly prepared in water as a stock solution (3.320 mM) and further diluted with the RPMI 1640 medium to reach the indicated concentrations.

4.2.2 Small Interfering RNAs (siRNAs) Complex Preparation

HIF-1α siRNAs (Hs_HIF1α_5 FlexiTube siRNA, #SI02664053, Qiagen), scrambled (Scr) siRNAs (Negative Control siRNA, #1027310, Qiagen), STAT3 siRNAs (Hs_STAT3_7 FlexiTube siRNA, #SI02662338, Qiagen) and Lipofectamine™ 2000 Transfection Reagent (Invitrogen), were used to make complexes (siRNA:polymer) ratio of 1:1 (weight/weight) in OptiMEM media (Life Technologies, Grand Island, NY, USA) according to the manufacturer's instructions. Complexes were added to the cells at 50 nM siRNA concentrations. Cells were transfected with siRNA complexes at 50–60% confluence.

4.2.3 Trypan Blue Assay

MDA-MB-231 cells (7 x 10^4 cells/well) were seeded in 24-well plates (1 mL in each well) overnight, then exposed to cisplatin at indicated concentrations and incubated under normoxia or hypoxia. Then the floating and adherent cells (harvested by trypsinization) were collected separately at different time points and resuspended in trypan blue solution (0.4%) (Sigma–Aldrich, Oakville, ON, Canada) and the number of viable and dead cells was counted in a hemocytometer under light microscope. At least 100 cells were counted for each sample. Percentage of viable cells is presented as the mean ± SD for three independently performed experiments.

4.2.4 MTT Assay

MDA-MB-231 cells (1 x 10^4 cells/well) were seeded in 96-well plates overnight and then exposed to increasing concentration of cisplatin (3.32-332 μM) for 24 and 48 h under hypoxia or normoxia. For siRNA transfection studies, cells (7 x 10^4 cells/well) were seeded in 24-well plates overnight. Then, cells

at 50-60 % confluence were transfected with siRNA complexes prior to cisplatin treatment for 24 h under normoxia. Cellular viability was assessed by the reduction of MTT (3-(4,5-dimethylthiazol-2-yl)-2,5-diphenyltetrazolim bromide, Sigma–Aldrich, Oakville, ON, Canada) to formazan crystals. Briefly, MTT solution (5 mg/mL) was added to incubated cells for 4 h at 37 °C prior to assessment. Then the medium was replaced by N,N, dimethyl sulfoxide (DMSO) to dissolve the crystals formed. Optical density was measured spectrophotometrically using a plate reader (Synergy H1 Hybrid Reader, Biotek) at 570 nm. The cellular activity ratio was represented relative to control.

4.2.5 Colony Formation Assay

MDA-MB-231 cells (35 x 10^4 cells/flask) were seeded in 25 cm^2 flasks overnight. The day after, culture medium was replaced with either drug free medium (for non-treated controls) or medium containing cisplatin. Drug exposure was performed either under normoxia or hypoxia for 24 h. Cells were then washed once in 1X phosphate buffered saline (PBS), harvested by trypsinization, counted using a hemocytometer, and then replated at three different densities of 500, 1000, and 2000 cells/well in duplicate in six-well plates under normoxia. After an additional 7 to 10 days of culture, cells were stained with a crystal violet solution (#HT90132, Sigma-Aldrich), and surviving colonies consisting of ~50 or more cells were counted with Protein Simple, AlphaImager HP. In another set of experiments cells were first transfected with siRNA complexes for 24 h under normoxia and then treated with cisplatin under hypoxia for another 24 h and then the above procedure was repeated.

4.2.6 Flow Cytometry Analyses for $CD44^+/CD24^-$ Expression

Single cell suspensions for flow cytometry are achieved by passing cells through 40 µm cell strainer (BD Falcon) and staining with CD44-APC (#559942) and CD24-PerCP-Cy5.5 (#561647) from BD Pharmingen in Hanks' buffer supplemented with 2% FBS according to the manufacturer's instructions. All stained cells were run in a BD FACS Canto II (BD Biosciences, San Jose, CA, USA), and data were analyzed using FCS Express 5.0 software (De Novo Software, Glendale, CA, USA).

4.2.7 RNA Extraction, cDNA Synthesis, Quantitative Reverse Transcription Polymerase Chain Reaction (qRT-PCR)

Total RNA extraction was performed with the Qiagen RNeasy Kit (#74104 Qiagen, Canada) according to the manufacturer's protocol. 1 µg of RNA was reverse transcribed using oligo-dT and superscript II (Life Technologies, Grand Island, NY, USA) according to the manufacturer's protocol. 1 µL of the resulting cDNA mixture was added to the Platinum SYBR Green qPCR SuperMix-UDG with Rox (Life Technologies, Grand Island, NY, USA) and amplified with target gene-specific primers on the Applied Biosystems

7900HT (Carsbad, CA; The Applied Genomics Centre, Edmonton, Alberta, Canada). All genes of interest were normalized to glyceraldehyde-3-phosphate dehydrogenase (GAPDH) transcript expression levels. For analysis of changes in gene expression under hypoxia, fold changes in gene expression were calculated using the $2^{-\Delta\Delta CT}$ method. Individual fold-changes for each of the hypoxic samples were calculated by subtracting the ΔCT (gene expression CT normalised to the endogenous control, GAPDH) for each sample from the average ΔCT for the normoxic group to obtain ΔΔCT and was entered into the formula $2^{-\Delta\Delta CT}$ to obtain the fold changes.

Table 4.1 Primer sequences

Gene	Forward Primers	Reverse Primers
ABCC1	5'-CTCTATCTCTCCCGACATGACC-3'	5'-AGCAGACGATCCACAGCAAAA-3'
ABCC2	5'-CCCTGCTGTTCGATATACCAATC-3'	5'-TCGAGAGAATCCAGAATAGGGAC-3'
ABCC4	5'-AGCTGAGAATGACGCACAGAA-3'	5'-ATATGGGCTGGATTACTTTGGC-3'
ABCC5	5'-AGTCCTGGGTATAGAAGTGTGAG-3'	5'-ATTCCAACGGTCGAGTTCTCC-3'
ABCC6	5'-AAGGAGGTACTAGGTGGGCTT-3	5'-CCAGTAGGACCCTTCGAGC-3'
ABCB1	5'-TTGCTGCTTACATTCAGGTTTCA-3	5'-AGCCTATCTCCTGTCGCATTA-3
GAPDH	5'- GGAGCGAGATCCCTCCAAAAT-3'	5'- GGCTGTTGTCATACTTCTCATGG-3'

4.2.8 Western Blot

To measure the expression level of different proteins, MDA-MB-231 cells (20 x 10^4 cells/well) were seeded in 6-well plates overnight. Then cells were transfected with siRNAs for 24 h under normoxia. Then after 48 h incubation under hypoxia, cells were washed with cold 1X PBS and lysed using RIPA lysis buffer that was supplemented with 0.1 mM phenylmethylsulfonyl fluoride (PMSF) (Sigma-Aldrich), a protease Inhibitor Cocktail Set III, Animal-Free - Calbiochem (#535140, Millipore), and a phosphatase Inhibitor Cocktail Set II (#524625, Millipore). The lysate was then incubated on ice for 30 min, which was followed by centrifugation at 17000 g for 20 min to remove genomic DNA. Protein quantification was determined by the BCA protein assay kit (Pierce, Rockford, IL, USA), and equal amounts of protein (35-40 μg) were loaded in 4−15% Tris-Glycine gradient gel (#456-1084, Biorad). After gel electrophoresis, proteins were transferred to a nitrocellulose membrane. Membranes were probed with antibodies

against HIF-1α (#3716s, Cell Signaling Technologies), Hypoxia Inducing Factor-1β (HIF-1β) (#sc-8076, Santa Cruz Biotechnologies), survivin (#2808s, Cell Signaling Technologies), and B-cell lymphoma 2 (BCL-2) (#sc-130308, Santa Cruz Biotechnologies), cleaved Poly (ADP-ribose) polymerase (c-PARP) (#9544s, Cell Signaling Technologies), PARP (#9542, Cell Signaling Technologies), phospho-STAT3 (Tyr705) (p-STAT3) (#9131, Cell Signaling Technologies), Total-STAT3 (T-STAT3) (#8768s, Cell Signaling Technologies), c-Myc (#5605s, Cell Signaling Technologies), cleaved caspase-3 (#9661s, Cell Signaling Technologies), caspase-3 (#9662s, Cell Signaling Technologies), BCL-2 homologous antagonist/killer (BAK) (#3814s, Cell Signaling Technologies), p53 (#554293, BD Pharmingen), GAPDH (# sc-47724, Santa Cruz Biotechnologies) and β-actin (#sc-47778, Santa Cruz Biotechnology). Proteins were then detected using peroxidase-conjugated anti-mouse IgG (#7076, Cell Signaling Technologies) or anti-rabbit IgG (#7074, Cell Signaling Technologies) and visualized by enhanced chemiluminescence (Pierce ECL Western Blotting Substrate, #32106, Thermo Scientific, Rockford, IL, USA).

4.2.9 Vascular Endothelial Growth Factor Enzyme-Linked Immunosorbent (VEGF Elisa) Assay

The level of secreted VEGF was determined by the Quantikine Human VEGF Immunoassay kit (#SVE00, R&D Systems). Briefly, cells were left untreated or transfected by siRNA under normoxia for 24 h and then kept under hypoxia for additional 48 h. The supernatant was then removed and analysed for VEGF levels in pg/mL according to the manufacturer's instructions.

4.2.10 HIF-1α DNA Binding Activity

HIF-1α DNA binding activity was measured in nuclear extract by HIF-1α transcription factor assay Abcam Kit (#ab133104, MA, USA). Briefly, cell lysates for samples incubated under normoxia or hypoxia for different incubation times were collected using RIPA lysis buffer that was supplemented with 0.1 mM phenylmethylsulfonyl fluoride (PMSF) (Sigma-Aldrich), a protease Inhibitor Cocktail Set III, Animal-Free - Calbiochem (#535140, Millipore), and a phosphatase Inhibitor Cocktail Set II (#524625, Millipore). The lysate was then incubated on ice for 30 min, which was followed by centrifugation at 17000 g for 20 min to remove genomic DNA. HIF transcription factor complex present in the nuclear extract was then detected according to the manufacturer's instructions.

4.2.11 Flow Cytometric Detection of Apoptosis using Annexin V-FITC and Propidium Iodide

Annexin V-FITC and propidium iodide (PI) from BD Biosciences (FITC Annexin V Apoptosis Detection Kit I, #556547, BD Pharmingen™) was used to measure apoptotic cells by flow cytometry according to the manufacturer's instructions. Briefly, both floating and adherent cells were harvested, adherent cells were collected by adding a warm solution of 10 mM ethylenediaminetetraacetic acid (EDTA) in PBS, the

cells were centrifuged at 500 g for 5 minute, washed with ice cold 1X PBS twice and resuspended in 400 µL 1x binding buffer containing 5 µL Annexin V-FITC and 5 µL PI for 15 minutes at room temperature in the dark. Fluorescence was induced on a Beckman Coulter Cytomics Quanta SC MPL flow cytometer (10,000 events per sample). Spectral compensation was performed using Cell Lab Quanta analysis software. Number of viable and apoptotic cells were quantified by events in the quadrants. Results were expressed as the percentage of apoptotic cells at early stage (PI negative and Annexin V positive, lower right quadrant), apoptotic cells at late stage (PI positive and Annexin V positive, upper right quadrant), necrotic cells (PI positive and Annexin V negative, upper left quadrant) and viable cells (PI negative and Annexin V negative, lower left quadrant).

4.2.12 Cell Uptake

Cellular uptake of cisplatin was quantified by using an ion coupled plasma mass spectrometer (ICP-MS, Agilent Technologies, Tokyo, Japan). MDA-MB-231 cells (50 x 10^4 cells/flask) were seeded in 25 cm^2 flasks overnight. Cells were exposed to cisplatin (166 µM) for 24 h under normoxia and hypoxia. On following day, medium was aspirated, cells were rinsed with cold PBS, detached using trypsin-EDTA, aliquoted in duplicate in 1.5 mL micro-centrifuge tubes and pelleted by centrifugation at 500 g for 5 minutes. One of each duplicate cell pellet was digested with 20% (v/v) HNO_3 over night at 60 °C and analyzed for Pt(II) content by ICP-MS. The other duplicate was lysed using RIPA lysis buffer that was supplemented with 0.1 mM phenylmethylsulfonyl fluoride (PMSF) (Sigma-Aldrich), a protease Inhibitor Cocktail Set III, Animal-Free - Calbiochem (#535140, Millipore), and a phosphatase Inhibitor Cocktail Set II (#524625, Millipore) and quantified for protein content using the BCA protein assay kit (Pierce, Rockford, IL, USA). The cell uptake is expressed as ng cisplatin/µg cell protein.

4.2.13 Statistical Analysis

The statistical analysis was performed by Graphpad Prism (version 5.00, Graphpad Software Inc., La Jolla, CA, USA). Statistical analysis was performed either using unpaired Student's *t* test or one way ANOVA with *Tukey* post-test analysis. Statistical significance is denoted by (p<0.05). All graphs represent the average of at least 3 independent experiments with triplicates, unless mentioned otherwise in the text, or Graphs. Results were represented as mean ± standard deviation (SD).

4.3 Results

4.3.1 Hypoxia Induces Resistance to Cisplatin in MDA-MB-231 Cells

Using the MTT assay to quantify the number of viable cells, we found that hypoxia significantly increased the resistance of MDA-MB-231 cells to cisplatin **(Figure 4.1a-b)**, increasing the inhibitory concentration at 50% (IC_{50}) from 17 µM (as seen under normal condition) to 330 µM at 48 hours after cisplatin treatment **(Figure 4.1b)**. Similar results were obtained when trypan blue assay was used to assess the number of viable cells (**Figure 4.1c-d**). As shown in **Figure 4.1e**, we performed clonogenic survival assays; with cisplatin treatment, we found that cells cultured under hypoxia had a significantly higher number of colonies than cells grown under the normal condition. Of note, without cisplatin treatment, there was no significant difference in the clonogenic potential between cells grown in hypoxia or normoxia (**Figure 4.S1**). Correlating with our observation that hypoxia induces chemoresistance in MDA-MB-231 cells, we found that the cell uptake of cisplatin under hypoxia was significantly less than that under the normal condition (**Figure 4.1f**). The intracellular cisplatin level was measured by using an ion coupled plasma mass spectrometer, as detailed in Materials and Methods.

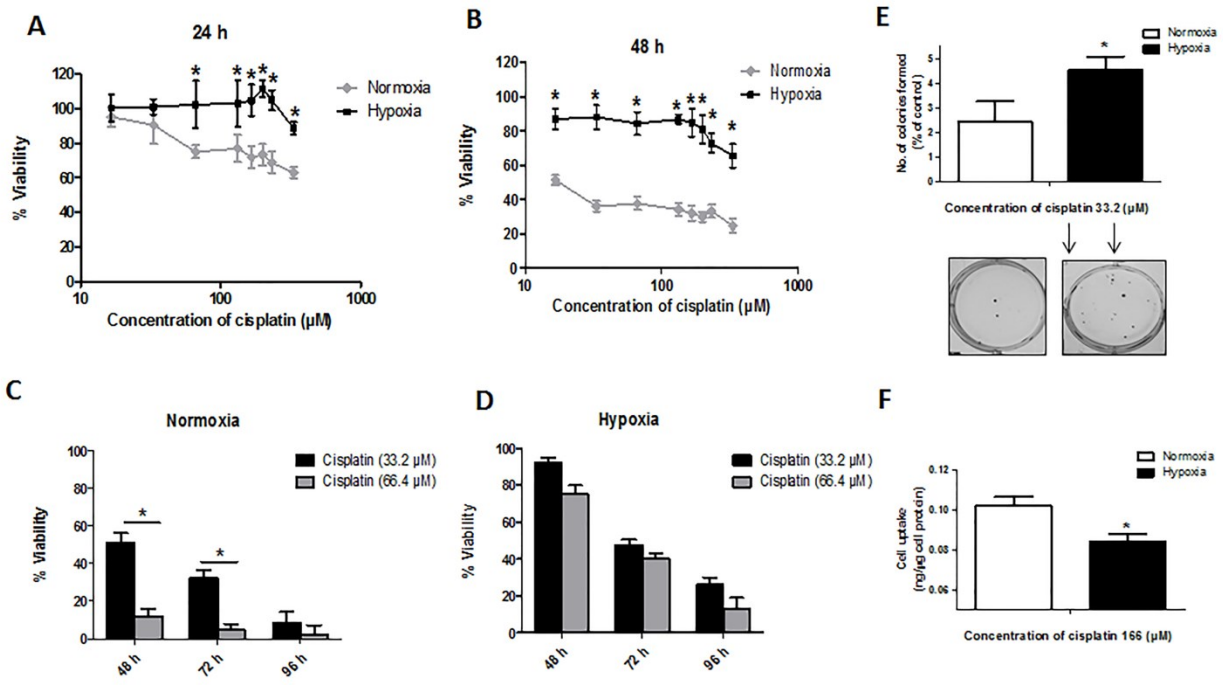

Figure 4.10 Hypoxia confers chemoresistance to cisplatin in MDA-MB-231 cells. Drug sensitivity of cells under normoxia or hypoxia was measured by MTT assay for **(a)** 24 h and **(b)** 48 h treatment with cisplatin. (*) denotes a significant difference compared to normoxic group at each individual cisplatin

concentration (Student's *t* test, $p<0.05$). Viability of MDA-MB-231 cells was measured by trypan blue assay for cells treated with cisplatin (33.2 and 66.4 μM) for 48, 72 and 96 h under **(c)** normoxia and **(d)** hypoxia. (*) denotes a significant difference compared to lower cisplatin concentration (33.2 μM) at each time point (Student's *t* test, $p<0.05$). **(e)** Clonogenic survival assay was conducted for cells treated with cisplatin (33.2 μM) under hypoxia or normoxia (24 h) in duplicate with plating of 500 cells. The number of colonies formed (% of control) from 500 cells was graphed. **(f)** Cisplatin cellular uptake was measured by ICP-MS for 24 h treatment with cisplatin. (*) denotes a significant difference between normoxic and hypoxic groups (Student's *t* test, $p<0.05$). Data are represented as mean ± SD (n=3).

4.3.2 Hypoxia Confers Stem-Like Features to Cells

It has been previously published that hypoxic challenge enriched the cancer stem cell (CSC) population in MDA-MB-231 (290). As shown in **Figure 4.2a**, we identified a significant increase in the percentage of $CD44^+/CD24^-$ cells, a well-documented CSC marker (291). In further support the concept hypoxia promotes cancer cell stemness, we also showed that hypoxic challenge resulted in significant increase in the mRNA levels of ATP-binding cassette (ABC) drug transporters (*i.e.*, ABCC1-6 as well as ABCB1) **(Figure 4.2b)**, previously published as CSC markers (292).

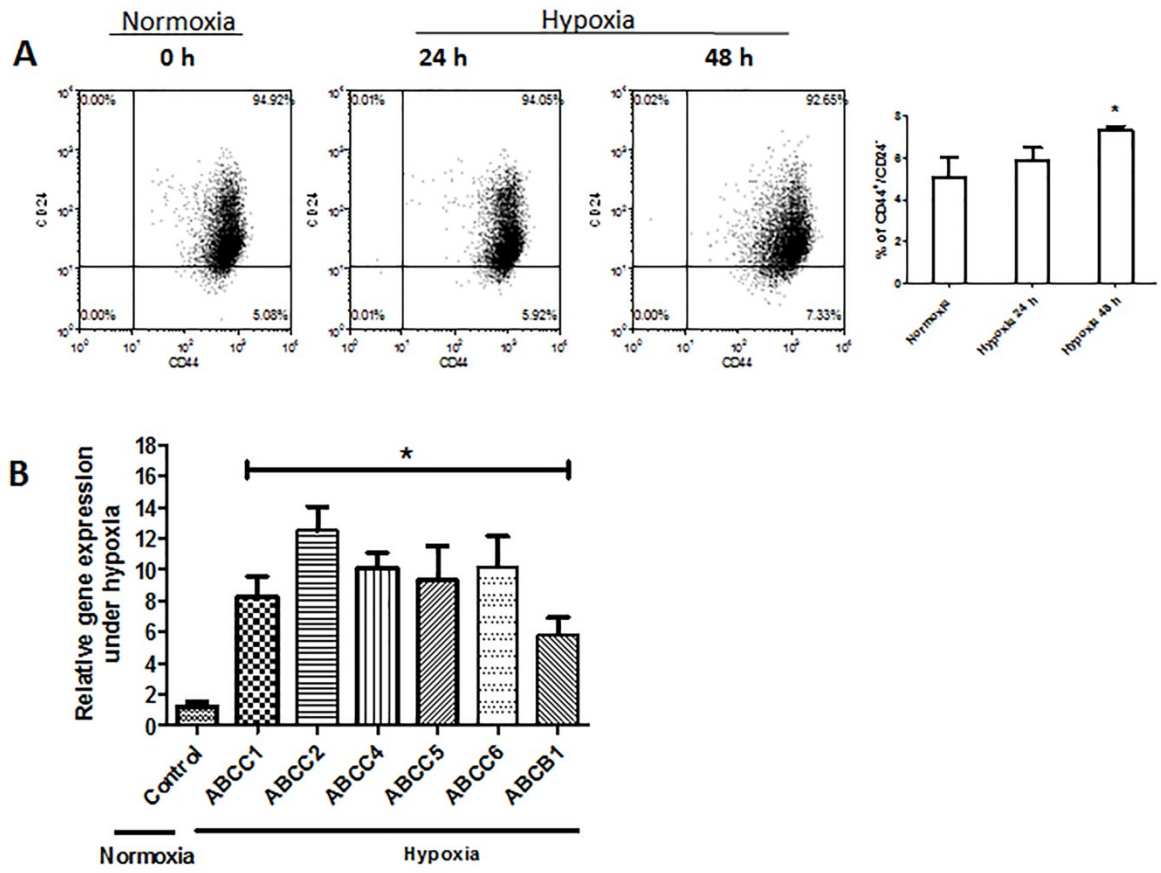

Figure 4.11 Hypoxia confers stem-like features to cells. The effect of hypoxia in the MDA-MB 231 cells on **(a)** enrichment of cells with $CD44^{+}/CD24^{-}$ subpopulation after 24 and 48 h incubation under hypoxia. (*) denotes a significant difference as compared to normoxic group (Student's *t* test, $p<0.05$) and **(b)** qRT-PCR results of ABC transporter genes expression after 48 h hypoxia normalized to GAPDH, and further normalized to normoxic group. (*) denotes a significant difference as compared to normoxic group (Student's *t* test, $p<0.05$). Data are represented as mean ± SD (n=3).

4.3.3 HIF-1α is Upregulated and Functionally Active in Response to Hypoxia

As expected, hypoxic challenge led to a substantial increase in the expression of HIF-1α protein **(Figure 4.3a)**. Moreover, the functional status of HIF-1α increased, as the DNA-binding of this protein showed a significant and time-dependent increase, detectable as early as 2 hours after the initiation of hypoxic challenge **(Figure 4.3b)**. In accordance with these observations, VEGF, a known downstream target of HIF-1α, also showed time-dependent increased secreted levels with 72 hours under hypoxic condition **(Figure 4.3c).** As shown in **Figure 4.3d**, hypoxia upregulated the expression of several downstream targets of HIF-1α that have known anti-apoptotic functions, such as survive and BCL-2. While we

identified increases in BAK, cleaved caspase3 and cleaved PARP, these changes were relatively subtle, suggesting a low degree of apoptosis induced by hypoxia (**Figure 4.3d**). Since STAT3 has been shown to stabilize HIF-1α upon hypoxia in Caki I human renal carcinoma cells (293) and MCF-7 breast cancer cells (294), we asked if STAT3 is activated in our experimental model. As shown in **Figure 4.3d**, hypoxic challenge induced a substantial upregulation of phospho-STAT3 (pSTAT3), the active form of STAT3. Of note, in contrast to HIF-1α, HIF-1β did not change in response to hypoxia. This finding is in keeping with the concept that it is the constitutively expressed subunit of HIF.

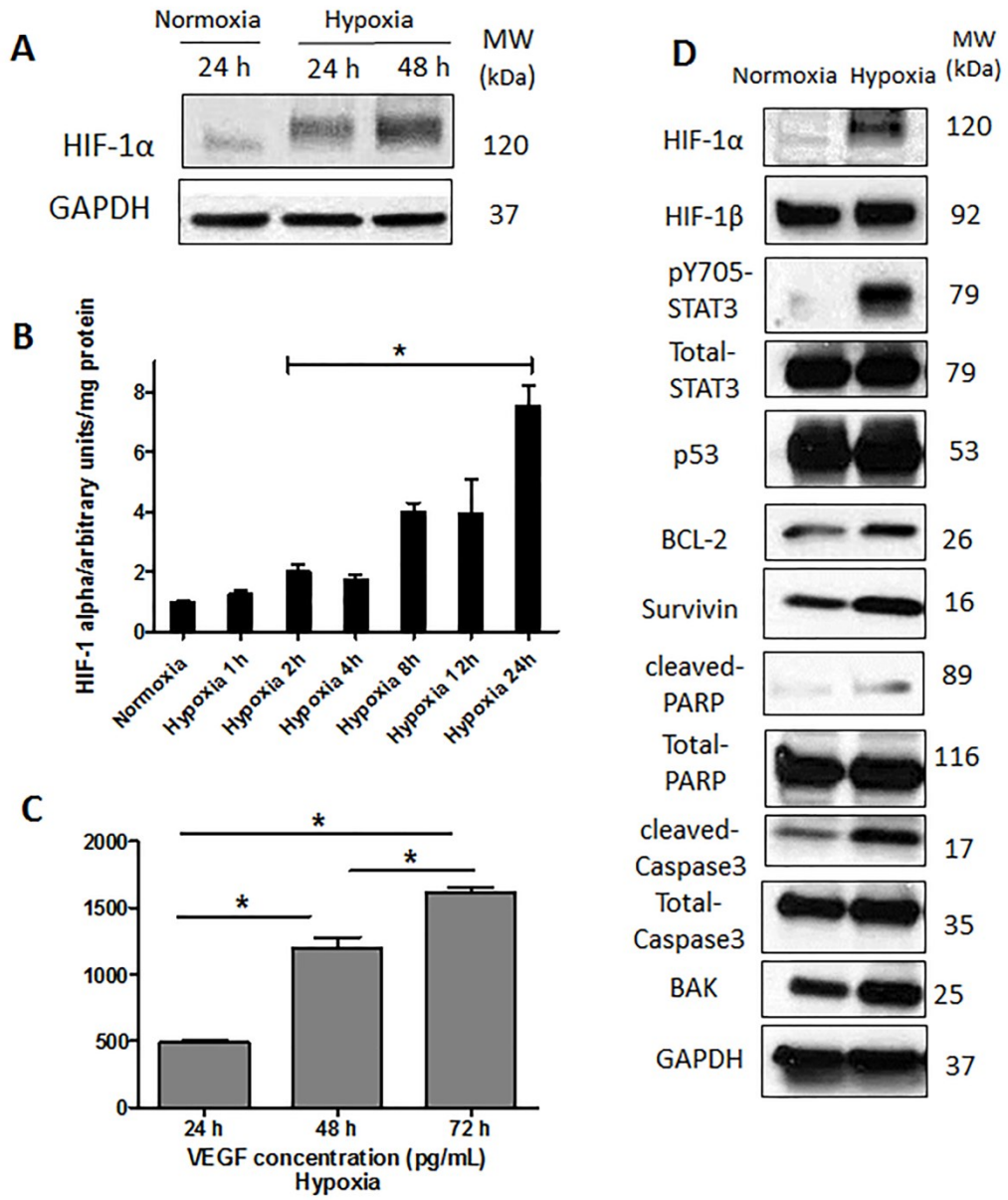

Figure 4.12 HIF-1α is upregulated and functionally active in response to hypoxia. The effect of hypoxia on **(a)** the expression of HIF-1α protein for different time periods, and **(b)** activation (DNA binding) of HIF1-α. (*) denotes a significant difference compared to normoxic group (Student's *t* test, $p<0.05$). **(c)** VEGF production. (*) denotes groups are significantly different from each other (one way ANOVA followed by a *post-hoc* Tukey test, $p<0.05$). **(d)** Expression of HIF-1α related proteins after 48 h incubation under hypoxia and normoxia. Data are represented as mean ± SD (n=3). Representative results of three independent Western blot analyses are shown.

4.3.4 Hypoxia-Induced STAT3 Activation is Independent of HIF-1α

To assess if HIF-1α plays a direct role in the observed biological changes induced by hypoxia, we knocked down the expression of HIF-1α using siRNA. As shown in **Figure 4.4a**, successful knockdown of HIF-1α was achieved. However, we did not observe appreciable changes in the levels of survivin, BCL-2, and BAK, all of which are downstream targets of HIF-1α. Accordingly, no detectable changes in the levels of cleaved caspase3 and cleaved PARP expression were identified. Importantly, pSTAT3 remained to be expressed at a relatively high level, indicating that the hypoxia-induced upregulation of pSTAT3 is not dependent on HIF-1α **(Figure 4.4a).**

Since it has been reported that cisplatin can exert inhibitory effect on HIF-1α (295), we will further address the question of whether STAT3 activation induced by hypoxia is dependent on HIF-1α. Thus, MDA-MB-231 cells were exposed to cisplatin at a relatively low concentration (32 μM) under hypoxia for different time duration (*i.e.*, 0-72 hours). As shown in **Figure 4.4b**, in the absence of cisplatin (*i.e.*, without HIF-1α inhibition), we observed upregulations of HIF-1α and pSTAT3 upon hypoxic challenge. In comparison, with cisplatin treatment (*i.e.*, with HIF-1α inhibition), the hypoxia-induced upregulation of pSTAT3 was sustained, despite the suppression of HIF-1α by cisplatin. Combination of both HIF-1α siRNA knockdown and cisplatin treatment revealed similar results under hypoxia (**Figure 4.4c**). Taken together, it appears that hypoxia-induced STAT3 activation is not dependent on HIF-1α.

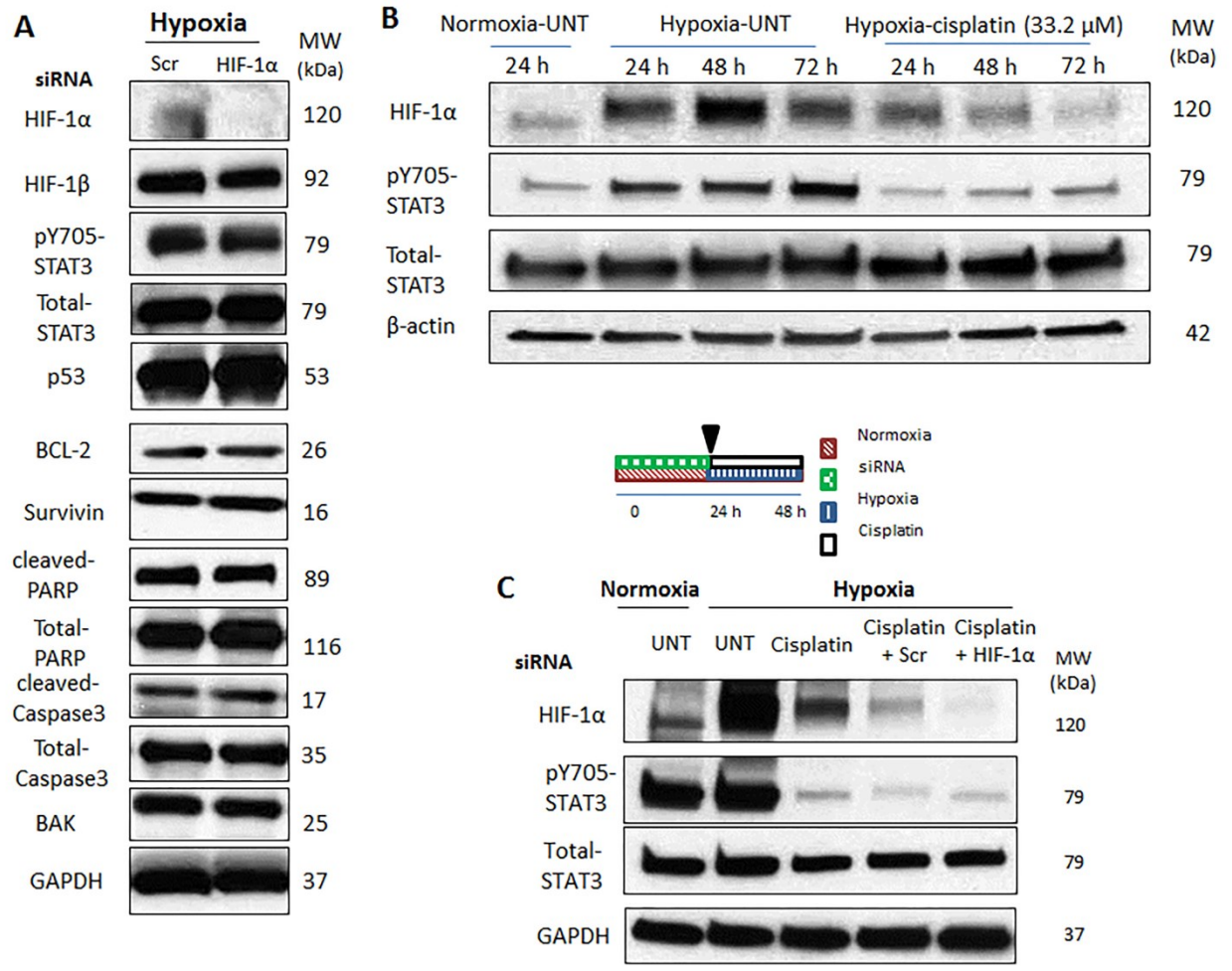

Figure 4.13 Hypoxia-induced STAT3 activation is independent of HIF-1α. Expression of HIF-1α related proteins was measured following **(a)** HIF-1α/scrambled (Scr) siRNAs treatment under hypoxia. Cells were transfected with HIF-1α/Scr siRNAs under normoxia (24 h) and then kept under hypoxia (48 h), **(b)** cisplatin treatment (33.2 μM) under hypoxia (24-72 h), and **(c)** HIF-1α/Scr siRNAs and cisplatin treatment under hypoxia. Cells were transfected with HIF-1α/Scr siRNAs under normoxia (24 h) and then treated with cisplatin (33.2 μM) under hypoxia (24 h). Representative results of three independent Western blot analyses are shown.

4.3.5 Simultaneous Inhibition of HIF-1α and STAT3 Proteins is More Efficient in Suppressing the Acquisition of Cancer Stemness Induced by Hypoxia

Since both HIF-1α and STAT3 are known to promote cell viability in face of adversity, our collected data suggests a model in which these two molecules work as two redundant systems in maintaining cell viability and tumorigenicity under hypoxia. To provide evidence to support this concept, we knocked

down HIF-1α and STAT3 simultaneously **(Figure 4.5b)**; if our model is correct, one expects to observe that simultaneous inhibition of these two proteins would be more efficient in suppressing the acquisition of cancer stemness induced by hypoxia, compared to inhibition with either protein alone. As shown in **Figure 4.5c**, simultaneous inhibition of both proteins resulted in a significant downregulation of VEGF expression, as compared to the inhibition of either protein alone. Later, the same treatment was run and in concert with our model, we found the simultaneous knockdown of both HIF-1α and STAT3 resulted in a significant decrease in the % of $CD44^{+}/CD24^{-}$ cell population, as compared to the inhibition of either protein alone **Figure 4.5d**.

As shown in **Figure 4.5e**, we also performed MTT assay to compare single knockdown as opposed to simultaneous knockdown of HIF-1α and STAT3, and found that the double knockdown was efficient in decreasing viable cells after cisplatin treatment, although it was not substantially different form STAT3 single knockdown. Of note, siRNA knockdown of HIF-1α under hypoxia did not substantially reverse the HICR to cisplatin **(Figure 4.S2-S4**). Also stabilization of HIF-1α in normoxia using cobalt chloride did not induce cisplatin resistance **(Figure 4.S5)**.

We postulated that HICR to cisplatin in MDA-MB-231 cells may be due to an upregulation of ABC transporters (i.e., ABCC1, ABCC2, ABCC5 and ABCC6), as these molecules have been implicated in cisplatin resistance in other cell types (296, 297). Thus, we investigated the effect of siRNA knockdown of HIF-1α or STAT3. As shown in Fig. 5f, only the knockdown of STAT3 resulted in a significant reduction in the mRNA expression levels of ABCC2 and ABCC6 under hypoxia; in contrast, knockdown of HIF-1α did not appreciably change the expression levels of these transporters. As for ABCC1 and ABCC5, we observed a decreased level of gene expression after STAT3 knockdown, although the levels of reduction are not statistically significant **(Figure 4.S6)**.

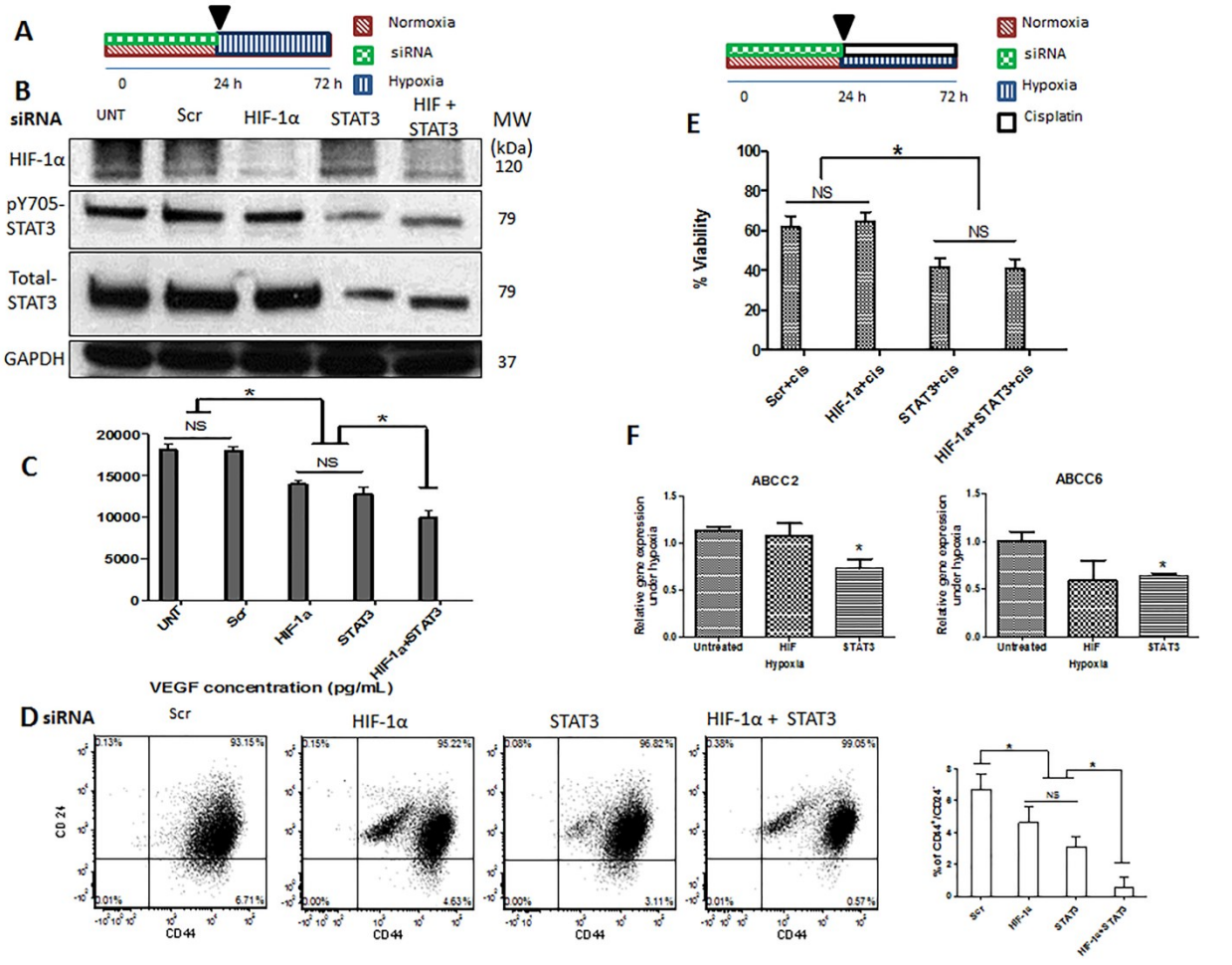

Figure 4.14 Simultaneous inhibition of HIF-1α and STAT3 proteins is more efficient in suppressing the acquisition of cancer stemness induced by hypoxia. **(a)** siRNA treatment diagram for Figures b-d. MDA-MB-231 cells were transfected with HIF-1α and STAT3 siRNAs individually or combined under normoxia (24 h) and then incubated under hypoxia (48 h), **(b)** Successful knockdown of HIF-1α and STAT3 as shown by immunoblotting, **(c)** VEGF production, **(d)** Expression of $CD44^{+}/CD24^{-}$ were measured for cells with flow cytometry. (e) Viability of cells was measured by MTT assay after cells were transfected with HIF-1α and STAT3 siRNA individually or combined under normoxia (24 h) and then treated with cisplatin (66.4 µM) under hypoxia (48 h). (*) denotes a significant difference between the groups (one way ANOVA followed by a *post-hoc* Tukey test, $p<0.05$). **(f)** qRT-PCR results of ABCC2 and ABCC6 expression in the MDA-MB 231 cells. Cells were treated with scrambled (Scr), HIF-1α, and STAT3 siRNAs under normoxia (24 h), and then incubated under hypoxia (48 h).The qRT-PCR results were normalized to GAPDH, and further normalized to untreated hypoxic sample. (*) denotes a significant difference as compared to untreated hypoxic group (Student's *t* test, $p<0.05$). Data are represented as mean ± SD (n=3).

4.4 Discussion

Hypoxia-induced chemoresistance (HICR) has been observed in a number of human cancer models (228-230) including TNBC (127, 135, 298). While the mechanism is not well understood, the role of HIF-1α has been highlighted (122-133, 163). To induce chemoresistance under hypoxia, it has been shown that HIF reduces drug-induced apoptosis and senescence (123, 163) and induces autophagy (122, 278). In this study, we aimed to expand on our understanding of HICR. We employed an experimental model in which a TNBC cell line, MDA-MB-231, was treated with cisplatin, which is a front-line chemotherapeutic agent used to treat TNBC patients (231, 232). Consistent with the published results of several studies using a variety of cancer cell lines and cisplatin under hypoxic condition (228, 287, 299-301), we found that hypoxia significantly induced cisplatin resistance in MDA-MB-231 cells. Importantly, this change correlated with reduced cellular uptake of cisplatin and increased stem-like features in these cells, as evidenced by the significant increase in the expression level of ABC transporters and the significantly higher proportions of cells expressing $CD44^{+}/CD24^{-}$. To our knowledge, this hypoxia-induced increase in stem-like features have been described in prior published studies of human cancer cells (302, 303). Overall, we believe that our experimental model is valid and appropriate to study HICR in cancer cells.

HIF-1α is considered to be a major factor in HICR (122-133, 163). In a wide range of different tumour types, HICR was shown to be reversed by HIF-1α inhibition (123-125, 127, 129-131, 133, 163). Our findings regarding the role of HIF-1α in HICR is however rather unexpected. Specifically, while we found that HIF-1α was effectively upregulated by hypoxia, siRNA knockdown of this protein did not significantly modulate the level of chemoresistance, nor the expression levels of a panel of apoptotic proteins. In agreement with published data, upregulation of HIF-1α was also was not sufficient to increase chemoresistance, since stabilization of HIF-1α in normoxic conditions (using cobalt chloride) did not induce chemoresistance (229, 282).

HIF-1α independent mechanisms of drug resistance in hypoxia are rarely reported. We have found similar observations published in only 4 studies (136, 229, 282, 285). In all of these studies, inhibition of HIF-1α either using siRNA, short hairpin RNA interference (shRNAi) or a dominant negative constructs did not lead to significant reduction in HICR. Instead of HIF-1α, a number of other mechanisms were highlighted as potential 'substitutes' for HIF-1α in conferring chemoresistance, including AP-1 induction, p53 suppression and mitochondrial inhibition(136, 229, 282, 285). None of these 4 studies employed TNBC in their experimental models and to our knowledge the role of HIF-1α in conferring HICR in TNBC

has not been previously studied in detail. In view of the fact that most published studies supporting the importance of HIF-1α in conferring HICR, we have considered two possible explanations for this apparent discrepancy. First, we have considered that the role of HIF-1α is variable depending cell types used in the study. Second, the exact chemotherapeutic agents used in the study are likely to be relevant. For instance, cisplatin is known to have inhibitory effect to HIF-1α function (295).

The high activation level of STAT3 under hypoxia, an oncoprotein strongly implicated in chemoresistance in cancer cells (297, 304-306), has led us to hypothesize that STAT3 sustained the chemoresistant phenotype despite the effective experimental abrogation of HIF-1α. STAT3 activation has been recognised as one of the mechanisms to confer chemoresistance in hypoxic condition (287). In another study using ovarian cancer cells treated with cisplatin under hypoxia, the authors also highlighted the role of STAT3 in this context (287), however whether HIF-1α is important was not examined. In support of the importance of STAT3 in this context, we found that treatment of cells with STAT3 siRNA to be highly effective in reversing hypoxia-induced chemoresistance to cisplatin, whereas HIF-1α siRNA was relatively ineffective. The importance of STAT3, relative to that of HIF-1α, was highlighted by the observation that simultaneous inhibition of these two proteins did not result in significant higher reversal of chemoresistance compared to STAT3 inhibition alone.

The inter-relationship between the expression of HIF-1α and STAT3 has been previously studied. Relatively extensive evidence has been published in support of the concept that STAT3 regulates the expression/function of HIF-1α (**Figure 4.S7**) (294). Furthermore, it has been shown that STAT3 works with HIF-1α; for instance, STAT3 is known to be part of the HIF-1α-DNA complex, which mediates the gene transcription functions of HIF-1α (307). Nonetheless, not much is known as to whether the expression and/or activation of STAT3 is regulated by HIF-1α. In our model, the observation that STAT3 remained to be highly activated after the siRNA knockdown of HIF-1α strongly suggests that STAT3 activation in response to hypoxia is not dependent on HIF-1α. This is in parallel with the results of a previous study, which has shown the same phenomenon in MDA-MB 231 cells (307). Nonetheless, this conclusion may be specific to cell types and/or experimental conditions, since pSTAT3 upregulation independent of HIF-1α has been previously reported in a human hepatoma cell line (308) while STAT3 down-regulation secondary to HIF-1α knockdown has also been found in human colon cancer cells (309).

Our data has led us to hypothesize that STAT3 activation may confer chemoresistance under hypoxia via its upregulation of selected number of ABC drug transporters, particularly those members that have been implicated in resistance to cisplatin (296). STAT3 knockdown resulted in significant lower level of expression of ABC drug transporters involved in cisplatin resistance (*i.e.*, ABCC2 and ABCC6); however knockdown of HIF-1α did not change the expression levels of these transporters under hypoxia. These results may explain why STAT3 knockdown is more effective in reversing hypoxia-induced cisplatin resistance as compared to HIF-1α.

How STAT3 confers hypoxia-induced chemoresistance in hypoxic condition may also be related to its ability to upregulate CD44, a marker of cancer stemness (310, 311). As previous studies have shown the STAT3 functions as a modulator for CD44 in aggressive breast cancer cells and promote a cancer stem cell phenotype(311). Notably, it was demonstrated that CD44 positive breast cancer stem cells had preferential activation of STAT3 (312). Furthermore, STAT3 mediated tamoxifen resistance has also been shown in the $CD44^{+}/CD24^{-/low}$ subpopulation of MCF-7 breast cancer stem cells with high mammosphere capacities(310).

4.5 Conclusions

While HIF-1α has been shown to be an important mediator for HICR, rare exceptions to this generalization exist. Our findings have shown that STAT3 activation, but not HIF-1α, appears to mediate HICR to cisplatin in TNBC, which often carries the hypoxic phenotype. Therefore, inhibition of STAT3 rather than HIF-1α should be the therapeutic targets in TNBC tumors to improve their chemosensitivity.

4.6 Acknowledgements

This work was financially supported by grants from Canadian Institutes of Health Research (CIHR) and Canadian Breast Cancer Foundation (CBCF) awarded to AL and RL. HSA was awarded the Women and Children's Health Research Institute (WCHRI) and Alberta Cancer Foundation (ACF) Graduate Studentships. NG was funded by CBCF. The authors would like to thank Dr. X. Chris Le, and Ms. Xiufen Lu, Department of Laboratory Medicine and Pathology, Dr. Keshav Gopal, Department of Laboratory Medicine and Pathology, and Dr. Victor Samokhvalov, Department of Pharmacy and Pharmaceutical Sciences, University of Alberta for their technical assistance.

4.7 Supplementary Information

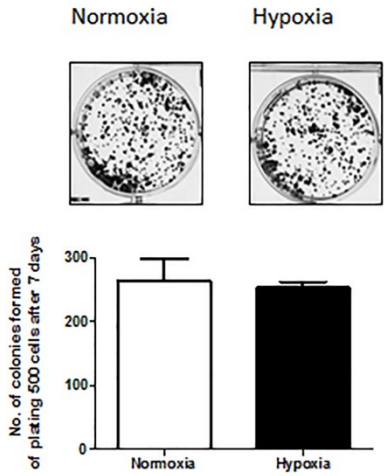

Figure 4.S1 There was no significant difference in clonogenic potential between cells grown in hypoxia or normoxia in the absence of cisplatin. Clonogenic survival assay was conducted for cells incubated under hypoxia or normoxia (24 h) in duplicate with plating of 500 cells. The number of colonies formed under normoxia from 500 cells was graphed after 7 days. Data are represented as mean ± SD (n=3), (Student's *t* test, $p>0.05$).

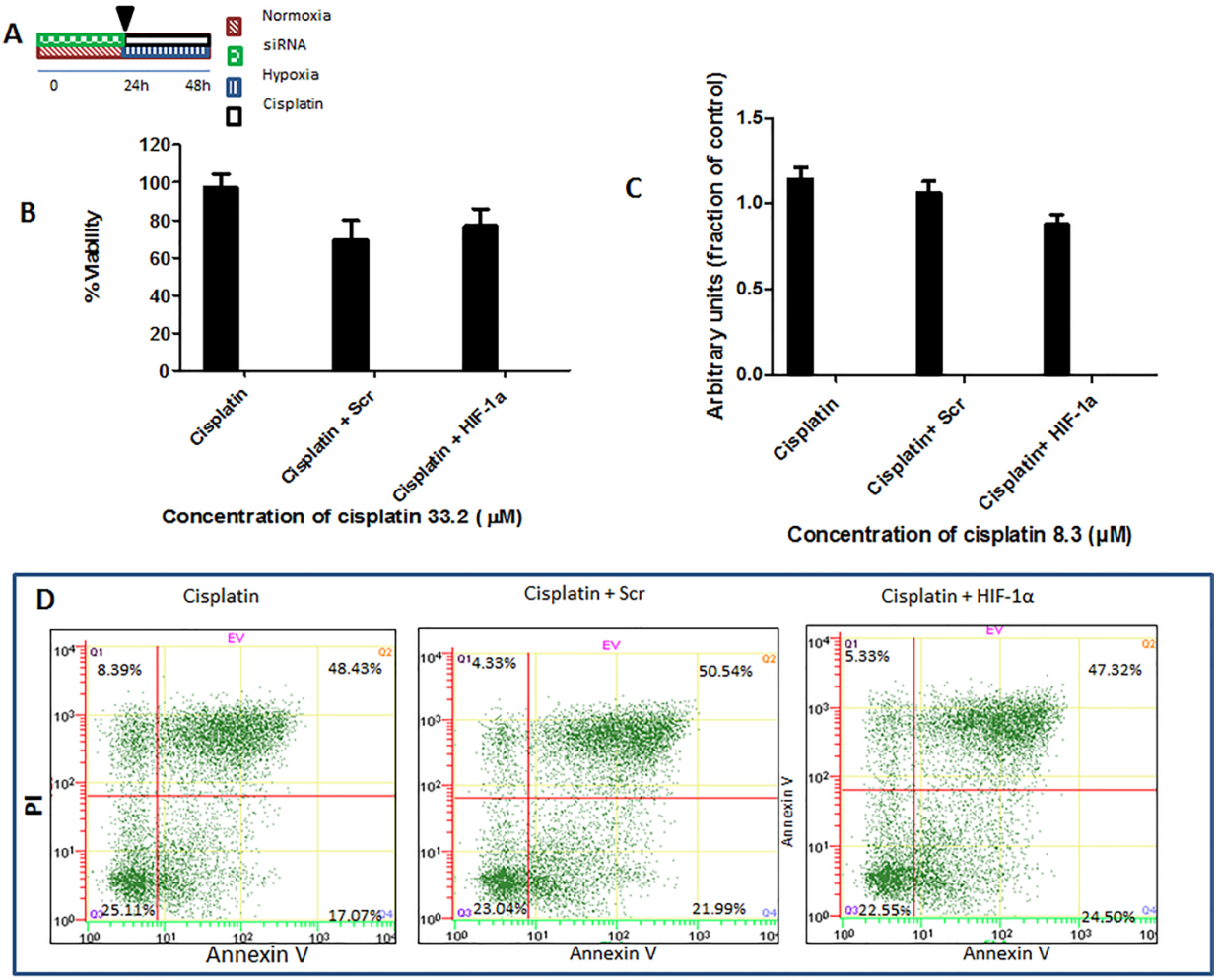

Figure 4.S2 Successful knockdown of HIF-1α is not effective in reversion of hypoxia-induced cisplatin resistance in the MDA-MB-231 cells. **(a)** Drug treatment diagram for Figures b-d, **(b)** Viability of cells was measured by MTT assay after cells were transfected with HIF-1α siRNA under normoxia (24 h) and then treated with cisplatin (33.2 µM) under hypoxia (24 h). **(c)** Clonogenic survival assay was conducted in duplicate with plating 500 cells after cells were transfected with HIF-1α siRNA under normoxia (24 h) and then treated with cisplatin (33.2 µM) under hypoxia (24 h). The number of colonies formed (% of control) from 500 cells was graphed after 10 days. Data are represented as mean ± SD (n=3). No significance difference was observed between the groups (one way ANOVA followed by a *post-hoc* Tukey test, $p>0.05$). **(d)** Apoptotic behaviour of cells was measured by Annexin V/PI assay for cells transfected with HIF-1α siRNA under normoxia (24 h) and then treated with cisplatin (33.2 µM) under hypoxia (24 h). Flow cytometry analysis showed different populations of (Q1) necrotic or already dead cells (PI positive), (Q2) cells in end stage apoptosis (FITC Annexin V and PI positive), (Q3) viable cells

(FITC Annexin V and PI negative), and (Q4) cells in early stage of apoptosis (FITC Annexin V positive and PI negative). No significance difference was observed between the groups treated with HIF-1α and scrambled siRNAs for different populations of the cells (Q1-Q4), (Student's *t* test, $p>0.05$) (n=3).

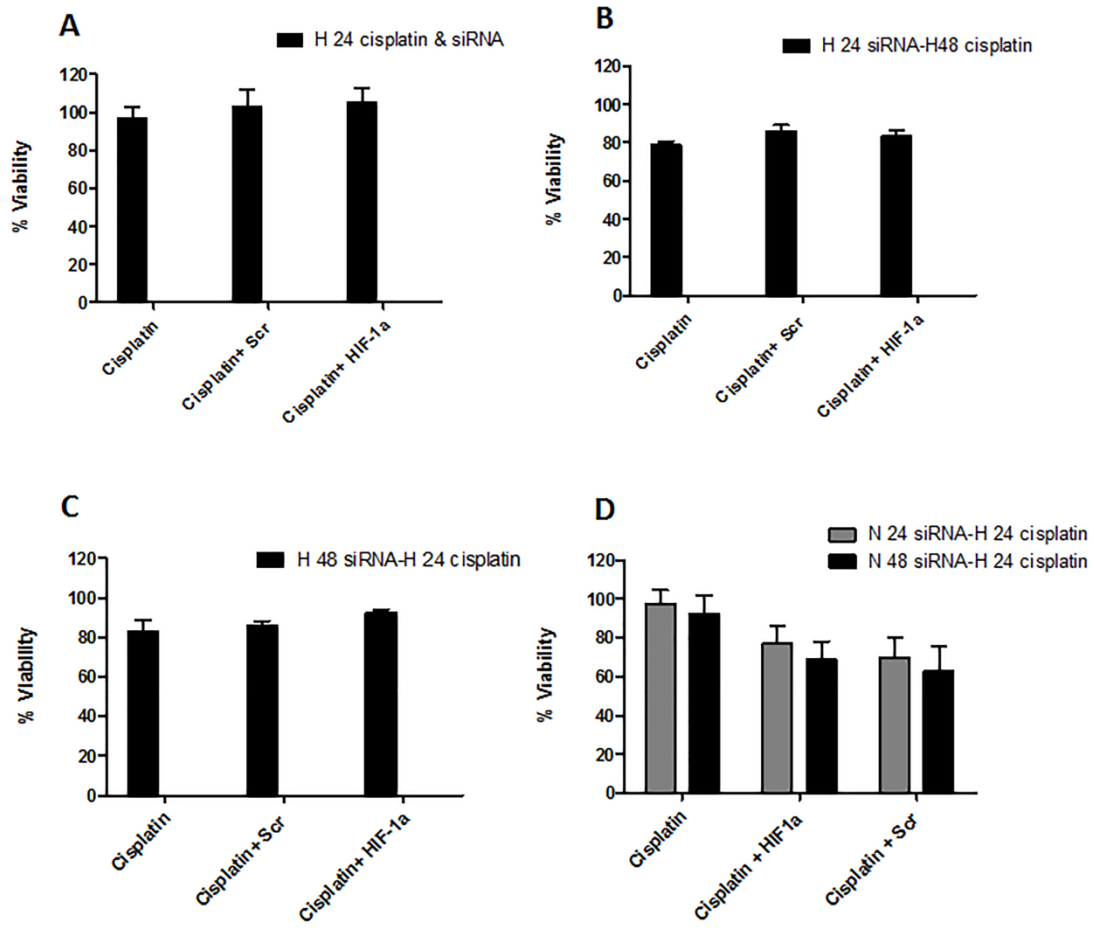

Figure 4.S3 Successful knockdown of HIF-1α is not effective in reversion of hypoxia-induced cisplatin resistance in the MDA-MB-231 cells regardless of scheduling. Viability of cells was measured by MTT assay after **(a)** cells were transfected with HIF-1α siRNA and concurrently treated with cisplatin (33.2 μM) for 24 h under hypoxia (H), **(b)** cells were transfected with HIF-1α siRNA under hypoxia (24 h) and then treated with cisplatin (33.2 μM) for 48 h under hypoxia, **(c)** cells were transfected with HIF-1α siRNA under hypoxia (48 h) and then treated with cisplatin (33.2 μM) for 24 h under hypoxia, and **(d)** cells were transfected with HIF-1α siRNA under normoxia (N) for 24 h and then treated with cisplatin (66.4 μM) for 24 or 48 h under hypoxia. No significance difference was observed between the groups (one way ANOVA followed by a *post-hoc* Tukey test, $p>0.05$) (n=3).

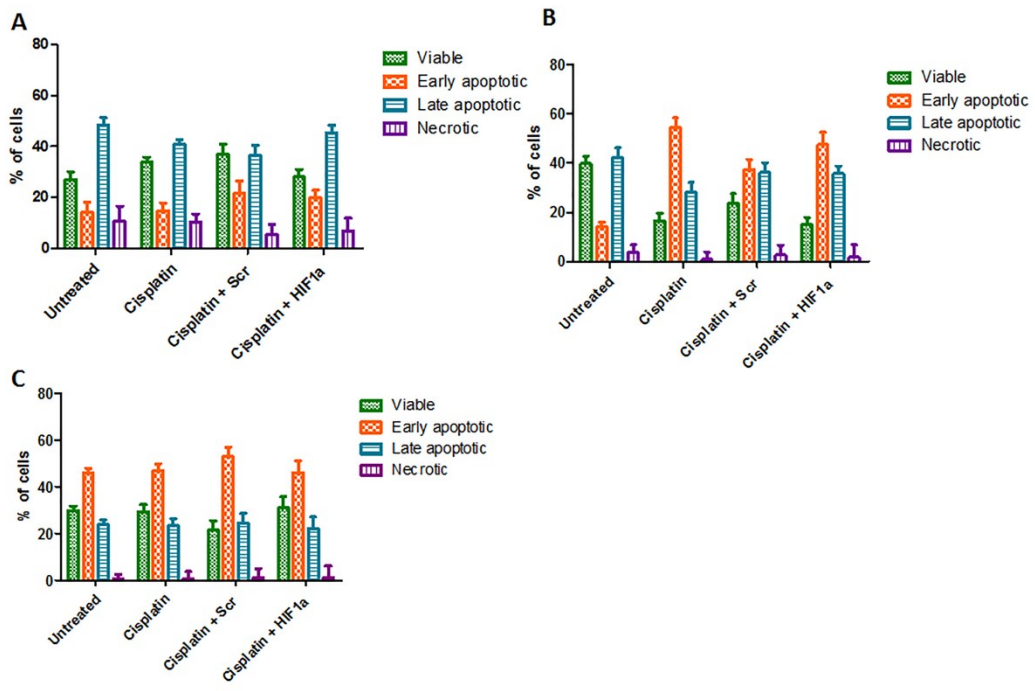

Figure 4.S4 Successful knockdown of HIF-1α with siRNA under hypoxia didn't enhance cisplatin-induced apoptosis regardless of scheduling in the MDA-MB-231 cells. Apoptotic behaviour of cells was measured by Annexin V/PI assay for cells **(a)** concurrently transfected with HIF-1α siRNA and treated with cisplatin (33.2 µM) for 48 h under hypoxia, **(b)** transfected with HIF-1α siRNA under hypoxia (24 h) and then treated with cisplatin (33.2 µM) for 48 h under hypoxia, **(c)** transfected with HIF-1α siRNA under hypoxia (48 h) and then treated with cisplatin (33.2 µM) for 24 h under hypoxia. Flow cytometry analysis showed different populations of necrotic or already dead cells (PI positive), cells in end stage apoptosis (FITC Annexin V and PI positive), viable cells (FITC Annexin V and PI negative), and cells in early stage of apoptosis (FITC Annexin V positive and PI negative). No significance difference was observed in the percentage of different populations (viable, early apoptotic, late apoptotic and necrotic) between cells transfected with HIF-1α and scrambled siRNAs, (Student's *t* test, $p>0.05$) (n=3).

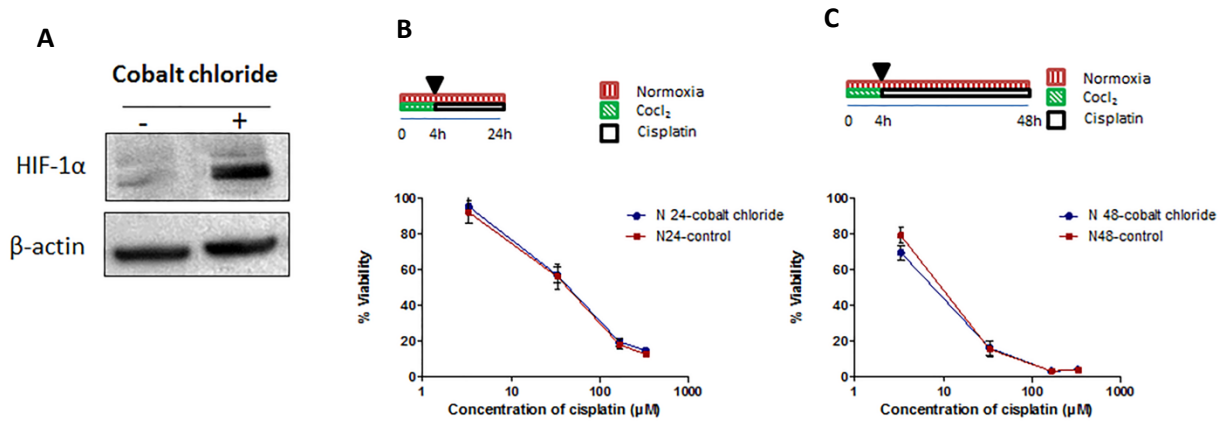

Figure 4.S5 Stabilization of HIF-1α in normoxia using cobalt chloride as hypoxia mimetic agent failed to induce cisplatin resistance. **(a)** Expression of HIF-1α was measured by immunoblotting after MDA-MB-231 cells were treated with $CoCl_2$ (100 μM) for 4 h under normoxia. **(b-c)** Viability of cells was measured by MTT assay for cells treated with cisplatin after using cobalt chloride as hypoxic mimicking agent. Cells first treated with cobalt chloride (100 μM) for 4 h. Then media was replaced and cells were exposed to increasing concentration of cisplatin for **(b)** 24 and **(c)** 48 h under normoxia (N). No significance difference was observed between groups (n=3).

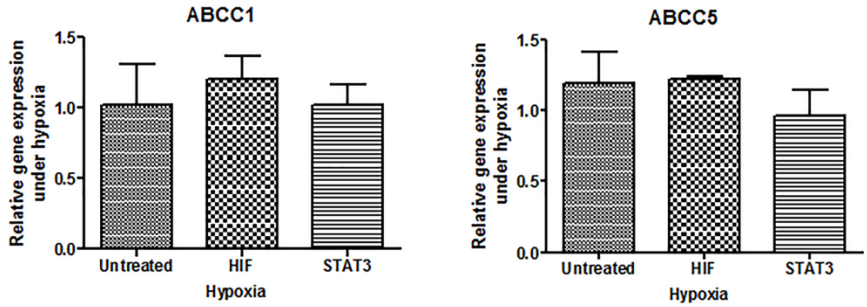

Figure 4.S6 qRT-PCR results of ABCC1 and ABCC5 expression in the MDA-MB 231 cells after HIF-1α, and STAT3 knockdown. Cells were treated with scrambled (Scr), HIF-1α, and STAT3 siRNAs under normoxia for 24 h, and then incubated under hypoxia for 48 h. The RT-PCR results were normalized to GAPDH, and further normalized to untreated hypoxic sample. No significance difference was observed as compared to untreated hypoxic group (Student's t test, $p>0.05$) (n=3).

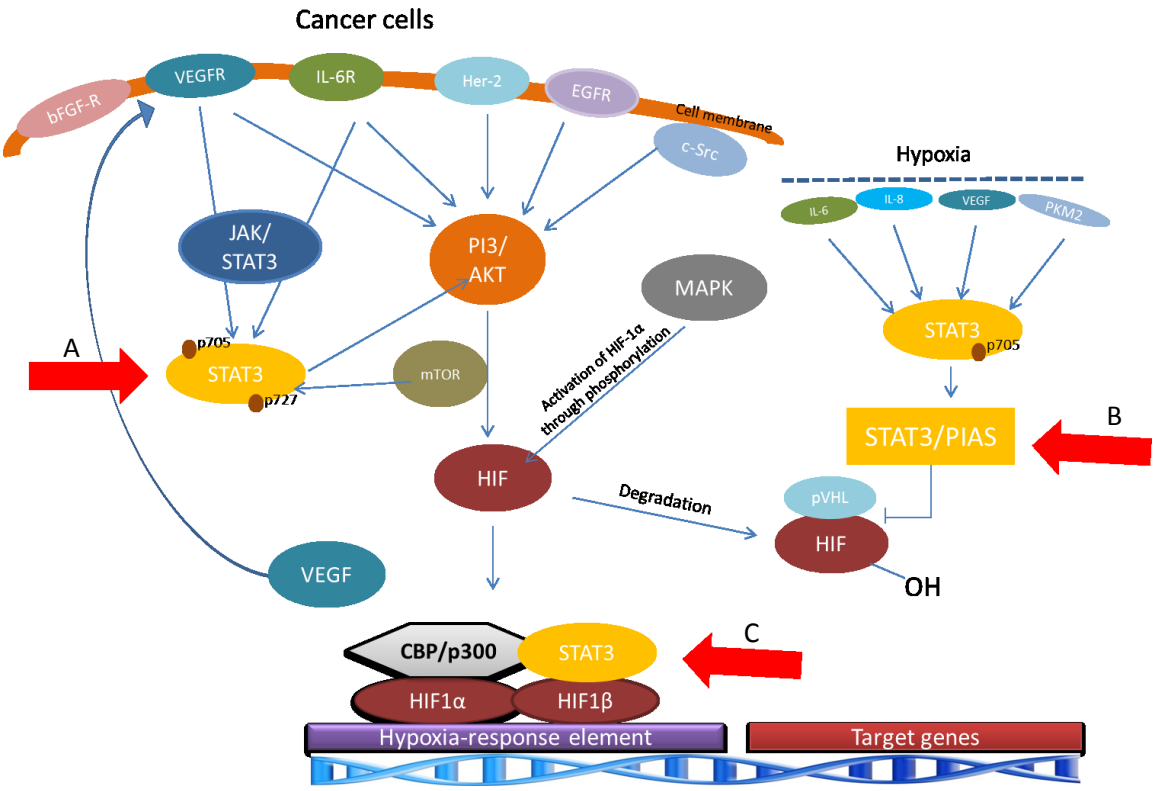

Figure 4.S7 Interplay exists between HIF-1α and STAT3 signalling at various levels. (A) STAT3 is obligatory for both basal and growth signal-induced HIF-1α expression (294). (B) Hypoxia-induced STAT3 can accelerate the activation of HIF-1α, an effect mediated through competition of STAT3 with HIF-1α for binding to the von Hippel Lindau (pVHL) protein. Protein inhibitor of activated STAT (PIAS), a negative regulator of STAT activation, also has the ability to interact with pVHL and thereby preventing pVHL from promoting the ubiquitylation and proteasomal degradation of HIF-1α (313). (C) HIF-1α and STAT3 exhibited functional cooperation in activating HIF-1α target genes (307).

Chapter five

Hypoxia induces the acquisition of cancer stem-like phenotype in triple-negative breast cancer by activation of signal transducer and activator of transcription 3 (STAT3)

5.1 Introduction

Triple negative breast cancer (TNBC) is an aggressive type of breast cancer with limited treatment options and a poor prognosis. It has a high incidence of reoccurrence, metastasis and a very short median of survival (314). This can be partly attributed to the fact that targeted therapies are not available for this disease due to lack of estrogen receptor, progesterone receptor and human epidermal growth factor receptor-2 (315-317). Its suboptimal therapeutic response also has been linked to the existence of cancer stem cells (CSCs). CSCs are a small subpopulation of cancer cells that are known to be responsible for cancer reoccurrence and resistance to therapy. Purified CSCs derived from TNBC cell lines and patient samples have been shown to be 100-fold more tumorigenic than the bulk tumor cell population (318, 319). Worse yet, the tumour microenvironment factors such as hypoxia actively induces bulk cancer cells to assume the CSC phenotype (320). TNBC tumors are known to carry a hypoxic phenotype (231). It has been postulated that eradication of CSCs is important in curing TNBC. Nonetheless, the molecular basis of acquisition of CSC like features in the setting of hypoxia has not been extensively studied.

Our group has previously identified a novel level of intratumoral heterogeneity in breast cancer cell lines as well as lymphoma cell lines and patient samples (235-237) by using a Sox2 regulatory region 2 (SRR2) reporter with GFP and luciferase as the readouts. Specifically, we identified a relatively small subset of cells that are reporter-responsive (RR), and they express GFP and luciferase; in contrast, the majority of the cells are reporter unresponsive, and they do not express GFP or luciferase (RU) (235-237). Importantly, we found that RR cells are more CSC-like than RU cells, and this observation can be made in both cell lines and primary patient samples (235, 236).

In this study, using the same SRR2 reporter, we aimed to gain insights into the molecular basis of acquisition of CSC-like features in TNBC in the setting of hypoxia. Using this study model, we reported that RU cells can be induced to convert into RR cells upon hypoxia challenge. Furthermore, our data suggests that STAT3 activation plays a key role in RU/RR conversion and conferring hypoxia-induced acquisition of cancer stemness in TNBC.

5.2 Methods and Materials

5.2.1 Cell Culture

TNBC cell line, MDA-MB-231 was obtained from ATCC (Manassas, VA) and maintained in RPMI 1640 medium supplemented with 10% fetal bovine serum (Invitrogen, Karlsruhe, Germany), 100 units/mL penicillin, and 100 mg/mL streptomycin in a humidified incubator under 95% air and 5% CO_2 at 37°C. For hypoxic condition, cells were cultured in a CO_2 incubator maintained at 94% N_2, 5% CO_2 and 1% O_2. MDA-MB-231 cells were virally infected twice with mCMV or SRR2 reporter as previously described (236). In brief, based on the GFP expression RU and RR cells have been purified and maintained in puromycin antibiotics. For stable cell lines overexpressing c-Myc, 10 million RU derived from MDA-MB-231 were initially transfected with 15 µg pcDNA-3.3-Myc (a gift from Derrick Rossi (Addgene plasmid #26818)) and pcDNA-3.3 plasmids Addgene (Cambridge, MA) and then cultured for 3-4 weeks in selection medium with increasing concentration of G418 up to 400ng/ml. Cells were plated at 25–30% confluence and cultured until they reached 60–70% confluence for different treatments. The chemotherapeutic agent cisplatin (cis-diamminedichloroplatinum(II) (CDDP) (purity 99%), #H878, AK Scientific Inc.) was freshly prepared in water as a stock solution (3.3 mM) and further diluted with the RPMI 1640 medium to reach the indicated concentrations.

5.2.2 Small Interfering RNAs (siRNAs) Complex Preparation

HIF-1α siRNAs (Hs_HIF1α_5 FlexiTube siRNA, #SI02664053, Qiagen), scrambled (Scr) siRNAs (Negative Control siRNA, #1027310, Qiagen), STAT3 siRNAs (Hs_STAT3_7 FlexiTube siRNA, #SI02662338, Qiagen), Myc siRNAs (SMARTpool: ON-TARGET plus Myc siRNA, Dharmacon, Fisher Scientific, ON, Canada) and Lipofectamine™ 2000 Transfection Reagent (Invitrogen), were used to make complexes (siRNA:polymer) ratio of 1:1 (weight/weight) in OptiMEM media (Life Technologies, Grand Island, NY, USA) according to the manufacturer's instructions. Complexes were added to the cells at 50 nM siRNA concentrations. Cells were transfected with siRNA complexes at 50–60% confluence.

5.2.3 SRR2 Luciferase Reporter Assay and Flow Cytometry

Luciferase reporter assay was performed using luciferase assay system kit (#E4530, Promega, Corporation, Madison, USA) according to the manufacturer's protocol, plated on Costar white polystyrene opaque 96-well plates (#3912, Corning, NY, USA) and analyzed on the FLUOstar Omega multi-mode microplate reader (BMG Labtech, Ortenburg, Germany). Flow cytometry analyses were performed as previously described (236).

5.2.4 MTT Assay

MDA-MB-231 cells (1 x 10^4 cells/well) were seeded in 96-well plates overnight and then exposed to increasing concentration of cisplatin (3.32-332 μM) for 24 and 48 h under hypoxia or normoxia. For siRNA transfection studies, cells (7 x 10^4 cells/well) were seeded in 24-well plates overnight. Then, cells at 50-60 % confluence were transfected with siRNA complexes prior to cisplatin treatment for 24 h under normoxia. Cellular viability was assessed by the reduction of MTT (3-(4,5-dimethylthiazol-2-yl)-2,5-diphenyltetrazolim bromide, Sigma–Aldrich, Oakville, ON, Canada) to formazan crystals. Briefly, MTT solution (5 mg/mL) was added to incubated cells for 4 h at 37 °C prior to assessment. Then the medium was replaced by N,N,dimethyl sulfoxide (DMSO) to dissolve the crystals formed. Optical density was measured spectrophotometrically using a plate reader (Synergy H1 Hybrid Reader, Biotek) at 570 nm. The cellular activity ratio was represented relative to control.

5.2.5 Colony Formation Assay

MDA-MB-231 cells (35 x 10^4 cells/flask) were seeded in 25 cm^2 flasks overnight. The day after, culture medium was replaced with either drug free medium (for non-treated controls) or medium containing cisplatin. Drug exposure was performed either under normoxia or hypoxia for 24 h. Cells were then washed once in 1X phosphate buffered saline (PBS), harvested by trypsinization, counted using a hemocytometer, and then re-plated at three different densities of 500, 1000, and 2000 cells/well in duplicate in six-well plates under normoxia. After an additional 7 to 10 days of culture, cells were stained with a crystal violet solution (#HT90132, Sigma-Aldrich), and surviving colonies consisting of ~50 or more cells were counted with Protein Simple, Alpha Imager HP. In another set of experiments cells were first transfected with siRNA complexes for 24 h under normoxia and then treated with cisplatin under hypoxia for another 24 h and then the above procedure was repeated.

5.2.6 Mammosphere Assay

In mammosphere assay cells were seeded and cultured as previously described **(236)**. Briefly, RU MDA-MB-231 cells were transfected with HIF-1α/Scr siRNAs under normoxia for 24 h and then kept under hypoxia for 48 h. In the next step, cells were trypsinized and passed through a 40 μm cell strainer (BD, Franklin Lakes, New Jersey, USA) and 10000 cells seeded into ultra-low adherent plates (Corning, NY, USA) in Mammocult media (StemCell Technologies, Vancouver, BC, Canada) as per manufacturer's instructions. Mammosphere larger than 60 μm were counted 5-7 days after seeding.

5.2.7 Flow Cytometry Analyses for $CD44^+/CD24^-$ Expression

Single cell suspensions for flow cytometry are achieved by passing cells through 40 µm cell strainer (BD Falcon) and staining with CD44-APC (#559942) and CD24-PerCP-Cy5.5 (#561647) from BD Pharmingen in Hanks' buffer supplemented with 2% FBS according to the manufacturer's instructions. All stained cells were run in a BD FACS Canto II (BD Biosciences, San Jose, CA, USA), and data were analyzed using FCS Express 5.0 software (De Novo Software, Glendale, CA, USA).

5.2.8 Western Blot

To measure the expression level of different proteins, MDA-MB-231 cells (20 x 10^4 cells/well) were seeded in 6-well plates overnight. Then cells either left untreated or were transfected with siRNAs for 24 h under normoxia. Then after 48 h incubation under hypoxia, cells were washed with cold 1X PBS and lysed using RIPA lysis buffer that was supplemented with 0.1 mM phenylmethylsulfonyl fluoride (PMSF) (Sigma-Aldrich), a protease Inhibitor Cocktail Set III, Animal-Free - Calbiochem (#535140, Millipore), and a phosphatase Inhibitor Cocktail Set II (#524625, Millipore). The lysate was then incubated on ice for 30 min, which was followed by centrifugation at 17000 g for 20 min to remove genomic DNA. Protein quantification was determined by the BCA protein assay kit (Pierce, Rockford, IL, USA), and equal amounts of protein (35-40 µg) were loaded in 4–15% Tris-Glycine gradient gel (#456-1084, Biorad). After gel electrophoresis, proteins were transferred to a nitrocellulose membrane. Membranes were probed with antibodies against HIF-1α (#3716s, Cell Signaling Technologies), survivin (#2808s, Cell Signaling Technologies), phospho-STAT3 (Tyr705) (p-STAT3) (#9131, Cell Signaling Technologies), Total-STAT3 (T-STAT3) (#8768s, Cell Signaling Technologies), c-Myc (#5605s, Cell Signaling Technologies), myeloid cell leukemia-1 (MCL-1) (#sc-819, Santa Cruz Biotechnology) and GAPDH (# sc-47724, Santa Cruz Biotechnologies). Proteins were then detected using peroxidase-conjugated anti-mouse IgG (#7076, Cell Signaling Technologies) or anti-rabbit IgG (#7074, Cell Signaling Technologies) and visualized by enhanced chemiluminescence (Pierce ECL Western Blotting Substrate, #32106, Thermo Scientific, Rockford, IL, USA).

5.2.9 Nuclear-Cytoplasmic Fractionation

Nuclear and cytoplasmic proteins of cells were extracted using the NE-PER Protein Extraction Kit (#78833, Thermo Scientific, USA) according to the manufacturer's protocol. For nuclear fraction, histone deacetylase 1 (HDAC-1, Santa Cruz biotechnology Inc. USA) was used as a marker for western blotting experiments.

5.2.10 SRR2-Probe Pull Down Assay

A Biotinylated SRR2 probes was synthesized from Integrated DNA Technologies, USA. SRR2 sequence is 5'-AAGAATTTCCCGGGCTCGGGCAGCCATTGTGATGCATATAGGATTATTCACGTGGTAATG-3'. 400µg nuclear protein was incubated with 3 pmole of either with or without biotin-labeled SRR2 probe for 30 min at room temperature. Then 75 µl streptavidin beads were added and the samples were incubated overnight by rotation at 4°C. The next day beads were washed 3 times with cold 1XPBS and protein was eluted at 100°C in 4Xprotein loading dye and loaded on SDS-PAGE gels and then processed for western blotting.

5.2.11 Statistical Analysis

The statistical analysis was performed by Graphpad Prism (version 5.00, Graphpad Software Inc., La Jolla, CA, USA). Statistical analysis was performed either using unpaired Student's *t* test or one way ANOVA with *Tukey* post-test analysis. Statistical significance is denoted by ($p<0.05$). All graphs represent the average of at least 3 independent experiments with triplicates, unless mentioned otherwise in the text, or Graphs. Results were represented as mean ± standard deviation (SD).

5.3 Results

5.3.1 Hypoxia Induced Acquisition of the RR Phenotype in RU Cells

Our previous studies have revealed a novel functional dichotomy in TNBC cells detectable based on their differential responsiveness to a Sox2 reporter (SRR2) with GFP and luciferase as the readouts, with reporter responsive (RR) cells being more stem-like than reporter unresponsive (RU) cells under normoxia (236). In this study, we tested the effect of hypoxic condition on assumption of stem-like features in RU cells. Thus, we performed flow cytometry to measure changes in the GFP expression in RU cells subjected to hypoxia (i.e. 1% O_2) at 48 hours. As shown in **Figure 5.1a**, there was an appreciable increase in GFP expression in hypoxic RU cells, with the median GFP expression being (120 ± 35), as compared to (72 ± 17) in native RU cells (p=0.01). Notably, the overall GFP expression level in hypoxic RU cells remained to be substantially lower than that of native RR cells (median GFP expression level, 509 ± 28). Since the Sox2 reporter also carries the luciferase reporter gene, we compared the luciferase activity between native RU and hypoxic RU cells. As shown in **Figure 5.1b**, RU cultured under hypoxia showed a significant increase in luciferase activity over native RU cells (1.6 fold, p=0.03); again, the

luciferase activity level of hypoxic RU cells was appreciably lower than that of native RR cells. Overall, our flow cytometric results were in parallel with the luciferase assay results.

5.3.2 Hypoxia Significantly Increased Tumorigenic and Stem-like Properties in RU Cells

Next, we asked if the hypoxia-induced RR conversion correlates with any phenotypic changes. As shown in **Figure 5.1c**, RU cells cultured under hypoxia showed a significant increase (1.7 ± 0.9% versus 4.8 ± 0.8%, p=0.03) in the percentage of cells expressing the $CD44^+/CD24^-$ immunophenotype, a widely used CSC marker (291). Interestingly, the median percentage of cells expressing the $CD44^+/CD24^-$ immunophenotype in native RR cells was 3.8 ± 0.6%. Furthermore, compared to native RU cells, hypoxic RU cells also showed a significant increase in colony formation (330 ± 10 to 414 ± 25, p=0.01). In the same assay, the median colonies formed were 545 ± 40 in native RR cells **(Figure 5.1d)**. Lastly, hypoxia significantly increased the resistance of RU cells to cisplatin, with the inhibitory concentration at 50% (IC_{50}) increased from 16 μM to 300 μM, p<0.001). Notably, hypoxic RU cells became significantly more chemoresistant than native RR cells (IC_{50}= 66.4 μM) **(Figure 5.1e)**.

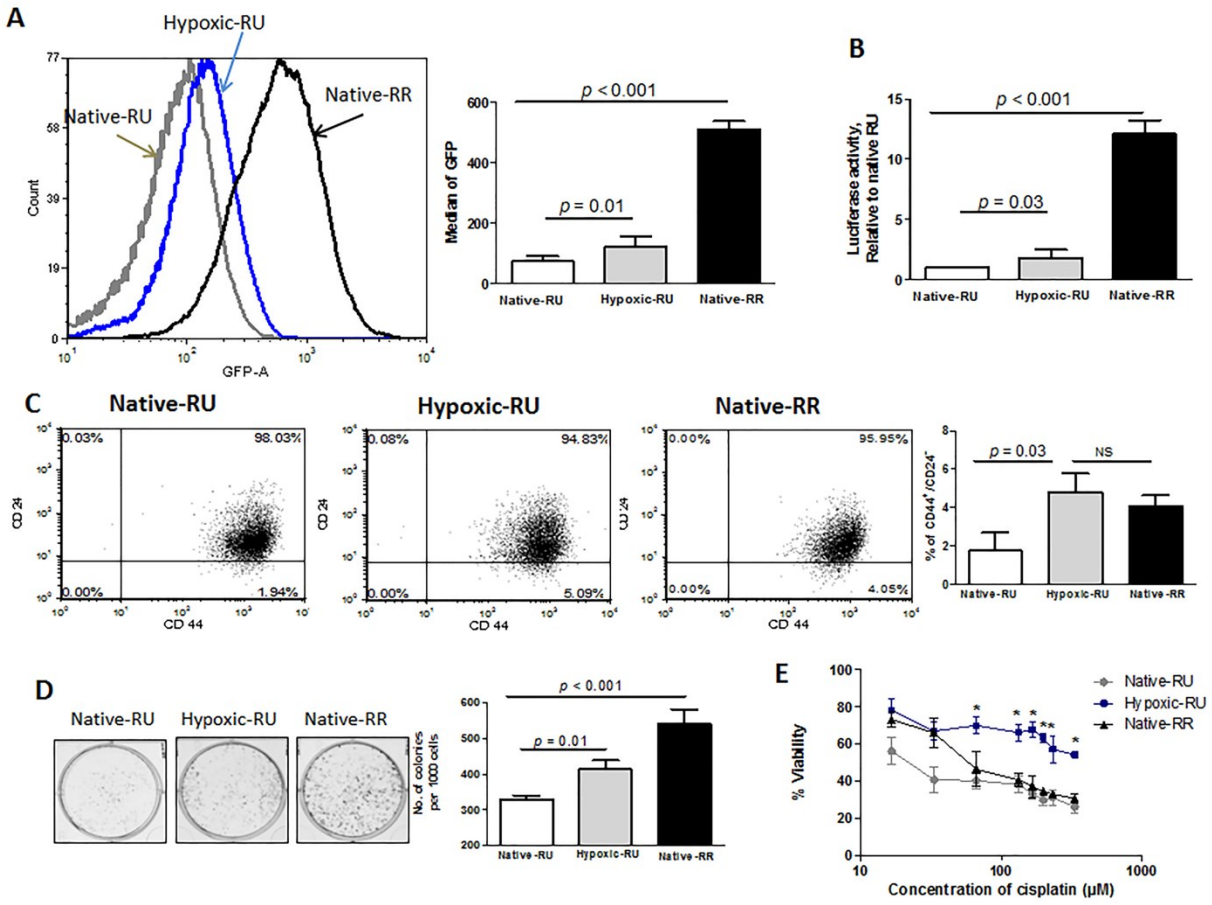

Figure 5.1 Hypoxia significantly increased tumorigenic and stem-like properties in RU cells. The effect of 48 hours hypoxia incubation in RU cells as compared to RU and RR cells incubated under normoxia on **(a)** GFP expression as illustrated by flow cytometry histogram plots, **(b)** SRR2 luciferase activity, **(c)** Proportion of $CD44^{+}/CD24^{-}$as illustrated by flow cytometry dot plots **(d)** Colony formation ability which was conducted by plating of 500 cells under normoxia or hypoxia. The number of colonies formed after 7 days was graphed. **(e)** Cellular viability to cisplatin as measured by MTT assay (*) denotes a significant difference between hypoxic RU cells and native RU or native RR cells (one way ANOVA followed by a post-hoc Tukey test, $p<0.05$). Data are represented as mean ± SD (n=3).

5.3.3 STAT3 Activation Drives Hypoxia-Induced RU/RR Conversion

As expected, hypoxic challenge led to a substantial increase in the expression of HIF-1α protein (**Figure 5.2a**). In accordance with this observation, VEGF, a known downstream target of HIF-1α, also showed a significant increase in its secreted level under hypoxia (**Figure 5.S1a**). To assess if HIF-1α plays a direct

role in the observed biological changes induced by hypoxia, we knocked down the expression of HIF-1α using siRNA. As shown in **Figure 5.S1b**, successful knockdown of HIF-1α was achieved and this finding correlated with a decrease in the level of secreted VEGF (**Figure 5.S1b**). However, HIF-1α knockdown did not inhibit the acquisition of hypoxia-induced stem-like features in RU cells and we did not observe any change in chemoresistance to cisplatin, proportion of $CD44^{+}/CD24^{-}$ cells or mammosphere formation ability (**Figure 5.S1c-e**).

We have also studied the role of c-Myc under hypoxia in conferring the stem-like features, since c-Myc is strongly implicated in cancer stemness in TNBC (321, 322). However, the expression of c-Myc is potently suppressed under hypoxia **(Figure 5.2a)**. Downregulation of HIF-1α using siRNA in RU cells under hypoxia resulted in regained expression of c-Myc (**Figure 5.S1b**), but as discussed previously, we did not observe any appreciable changes in the acquisition of stem-like features by cells after siRNA knockdown of HIF-1α (**Figure 5.S1c-e**).

We also enforced expression of c-Myc in RU cells to further investigate the role of c-Myc in hypoxia-induced stemness (**Figure 5.S2a**). Although the hypoxia-mediated suppression of c-Myc got abrogated in c-Myc-overexpressing cells (**Figure 5.S2a**), this approach was not effective in conferring stem-like features to RU cells under hypoxia as evidenced by the lack of enhancement in their colony formation ability (**Figure 5.S2b**). The lack of role for c-Myc in hypoxia-induced stemness is further shown when siRNA knockdown of Myc did not reverse the chemoresistance to cisplatin as well (**Figure 5.S2c**). Our DNA binding assay also showed a lower level of c-Myc protein pulled down with the SRR2 probe in RU cells under hypoxia as compared to normoxia (**Figure 5.S2d**), correlating with suppression of c-Myc expression under hypoxia. Overall, our collected data suggests a model in which c-Myc protein level may not be associated with RR phenotype under hypoxia. To provide more evidence, we sorted RU cells under hypoxia based on their level of conversion to GFP-positive and GFP-negative subsets (**Figure 5.2c)**; if our model is correct, one expects to observe GFP-positive subset (*i.e.*, with the highest degree of conversion) to show lower level of c-Myc expression as compared to GFP-negative subset (*i.e.*, with the lowest degree of conversion). In concert with this model, we couldn't detect any band for c-Myc in GFP-positive subset of RU cells sorted under hypoxia, in spite of detecting a band for c-Myc in GFP-negative subset (**Figure 5.S2e**).

In contrast to c-Myc, hypoxia induced a substantial upregulation of phospho-STAT3 (pSTAT3), the active form of STAT3 in converted RR cells (**Figure 5.2a**). Since native RR cells also show a higher expression of pSTAT3 than RU cells (**Figure 5.2a**), we suggest a model in which higher pSTAT3 protein level may be

associated with RR phenotype. In alliance with this concept, we substantially pulled down more STAT3 protein with the SRR2 probe under hypoxia as compared to normoxia (**Figure 5.2b)**. Of note, hypoxia has no effect on the level of expression of total STAT3 and only the level of pSTAT3 increases under hypoxia. To provide further support for the role of STAT3 in RU/RR conversion, we assessed the level of pSTAT3 in two subsets of RU cells sorted under hypoxia to GFP-positive and GFP-negative populations. As shown in (**Figure 5.2d**) GFP-positive subset (*i.e.,* with the highest degree of conversion) showed a higher expression of pSTAT3 as compared to GFP-negative subset (*i.e.,* with the lowest degree of conversion).

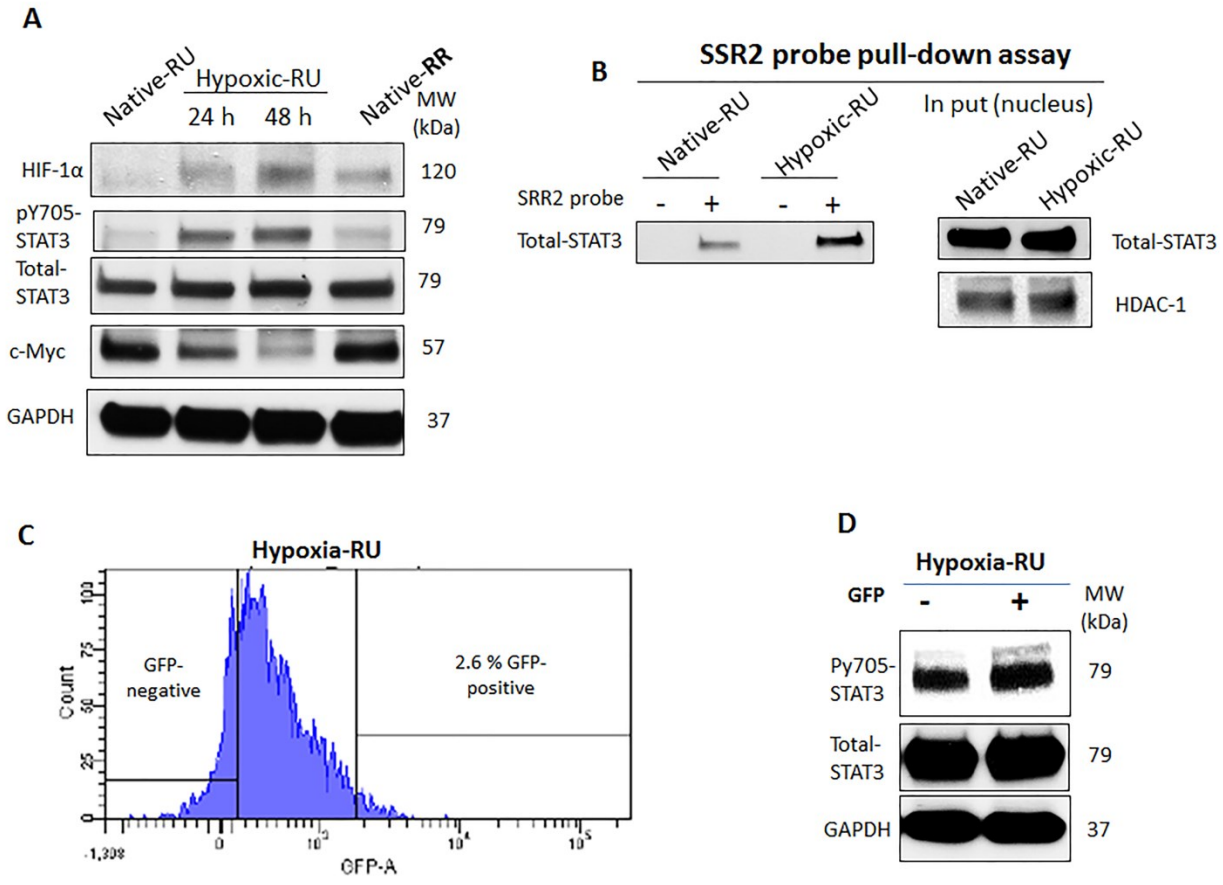

Figure 5.2 Hypoxia-induced activation of STAT3 is driving force for RU/RR conversion and assumption of stem-like features by converted RR cells. Western blot depicting **(a)** the effect of hypoxia on the protein expression profile of RU cells as compared to protein expression profile of native RR cells. **(b)** Higher amount of STAT3 pulled down with SSR2 probe in RU cells under hypoxia as compared to normoxia. **(c)** FACS histogram plot showing the sorting scheme of the RU GFP-positive and GFP-negative subsets incubated for 72 h under hypoxia. Percentages of gated populations from the live single cell population

are reported. Cells were subsequently collected for Western blot experiment. **(d)**Higher expression of pSTAT3 in GFP-positive subset of sorted RU cells under hypoxia as depicted by Western blot.

5.3.4 Suppression of STAT3 Effectively Inhibits RU/RR Conversion

To provide further evidence that STAT3 activation plays a direct role in the observed biological changes induced by hypoxia in RU cells, we knocked down the expression of STAT3 using siRNA. As shown in **Figure 5.3a**, successful knockdown of STAT3 and its downstream target genes (i.e*., survivin*, *Mcl-1* and *c-Myc*) was achieved. STAT3 silencing in hypoxic RU cells hindered the hypoxia-induced conversion of RU/RR cells as evidenced by lower median of GFP expression in hypoxic RU cells subjected to STAT3 siRNA (85 ± 13), as compared to (115 ± 13) in hypoxic RU cells subjected to scrambled siRNA (p=0.01), and brought back the level of GFP expression to the similar level in the native RU cells (median GFP expression level, 120 ± 35). Additionally, we compared the luciferase activity of hypoxic RU cells after the same siRNAs treatment. STAT3 silencing in hypoxic RU cells significantly decreased the luciferase activity of hypoxic RU cells subjected to STAT3 siRNA over hypoxic RU cells subjected to scrambled siRNA (1.3 fold, p=0.03) and brought back the level of luciferase activity to the similar level in the native RU cells (**Figure 5.3b**). Overall, our flow cytometric results were in parallel with the luciferase assay results.

Furthermore, we found that STAT3 knockdown was efficient in reversal of hypoxia-induced cisplatin chemoresistance and hypoxic RU cells subjected to STAT3 siRNA showed significant decrease in the level of chemoresistance (1.3 fold, p=0.03) as compared to hypoxic RU cells subjected to scrambled siRNA (**Figure 5.3d**). Hypoxic RU cells also showed a significant decrease in colony formation when subjected to STAT3 siRNA (124 ± 12 to 84 ± 24 p=0.03) as compared to hypoxic RU cells subjected to scrambled siRNA (**Figure 5.3e**). Lastly, we performed additional DNA pull-down experiments in the presence of STAT3 inhibitor (stattic) (323) to show the specificity of STAT3 binding to the SRR2 probe. As shown in **Figure 5.3f**, substantially less amount of STAT3 protein was pulled down with the SRR2 probe in hypoxic RU cells treated with 20 μM stattic as compared to untreated hypoxic RU cells.

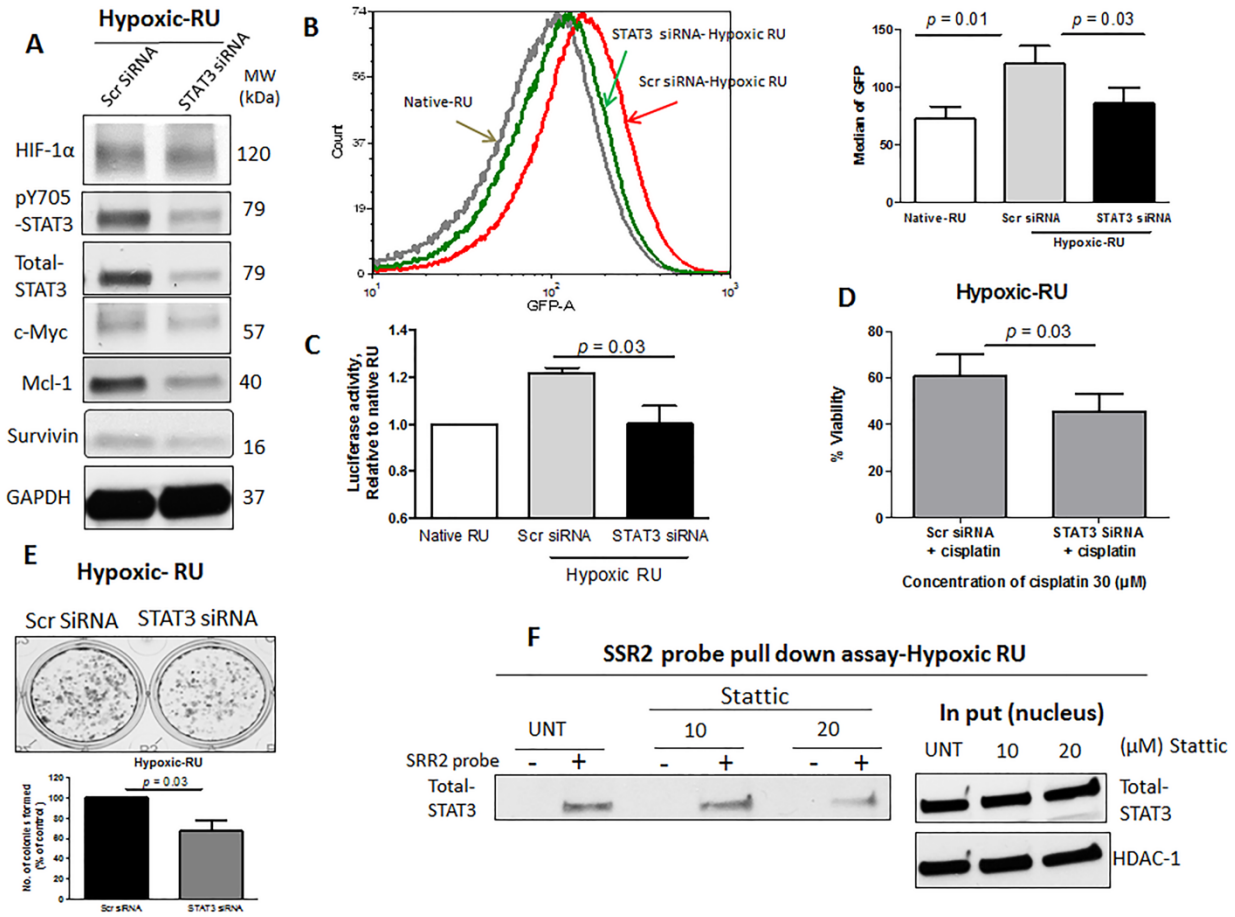

Figure 5.3 Suppression of STAT3 effectively inhibits RU/RR conversion. The effect of siRNA STAT3 knockdown in RU cells under hypoxia on; **(a)** the protein expression profile of RU cells as depicted by Western blot. **(b)** GFP expression as illustrated by flow cytometry histograms. **(c)** SRR2 luciferase activity, and **(d)** cellular viability after cisplatin exposure. **(e)** Clonogenic survival. **(f)** Lower amount of STAT3 was pulled down with SSR2 probe in RU cells in the presence of STAT3 inhibitor (20 μM stattic) under hypoxia.

5.4 Discussion

Tumors often contain heterogeneous populations of cancer cells with different tumor initiating potentials or cancer cell "stemness." Hypoxia as a common feature of tumor microenvironments has been implicated in the generation and sustainability of cancer stem cells in their undifferentiated stem cell state. In this regard, a number of recent studies have shown that hypoxic tumor cells seem to be poorly differentiated and express stem cell markers (324, 325) with increased clonogenic potential (326, 327). Exposure to hypoxia *in vitro* also results in enhanced tumorigenic potential *in vivo* (325). Although

the pro-tumorigenic role of hypoxia has been highlighted, the underlying mechanisms are not well understood. In this study, we aimed to expand on our understanding of how hypoxia mediates the induction of cancer stemness. For this purpose, we employed our previously described *in vitro* model of TNBC cell line, MDA-MB-231, in which a small subset of highly tumorigenic/stem-like cells can be differentiated from the bulk cell population based on their differential responsiveness to a Sox2 reporter (SSR2). Using the SRR2 reporter, we have previously identified intratumoral heterogeneity (*i.e.*, RU/RR dichotomy and their difference in stem-like features) in different types of cancer cell lines including estrogen receptor-positive breast cancer, estrogen receptor-negative breast cancer and ALK-positive anaplastic large cell lymphoma, as well as in patient samples of estrogen receptor-positive and estrogen receptor-negative breast cancers (235-237). In the current study, we showed that how hypoxia can mediate the generation of this dichotomy in TNBC cells.

Our results revealed that hypoxic challenge induced stem-like features in the cells, and consistently converted RU cells into RR cells. Using GFP and luciferase as the readouts, our study model has enabled us to readily track the acquisition of the RR phenotype, which is associated with stem-like features. When RU cells were subjected to hypoxia they showed a significantly higher expression of GFP and luciferase as compared to native RU cells. The association between the RR phenotype and stem-like features was evidenced by the observation that hypoxic RU cells exhibited significantly higher colony formation capacity, chemoresistance to cisplatin, and a higher proportion of cells carrying the $CD44^{+}/CD24^{-}$immunophenotype, a well-known marker to be associated with cancer stemness in TNBC (328). We believe that our observed hypoxia-induced RU/RR conversion is an example of development of intratumoral heterogeneity. To our knowledge, development of intratumoral heterogeneity has not been extensively studied in TNBC, let alone upon hypoxic challenge.

In general, events responsible for triggering phenotypic and functional heterogeneity are those that require significant metabolic adaptations for cells to survive, such as hypoxia and oxidative stress (329). It has been hypothesised that hypoxia induces a stem cell phenotype in non-stem cancer cells (330) and prolonged exposure to hypoxia can result in a phenotypic shift in the non-stem population towards a population enriched for cancer cells with more aggressive properties, in essence “reprogramming” of non-stem cells into a stem-like state which illustrates cancer cell plasticity (331). This dedifferentiation of differentiated cells has been reported to occur in hypoxic regions at higher frequencies compared to normoxic regions within the same tumours in different human cancer models (332). For instance, hypoxic conditions promote dedifferentiation in ductal breast carcinoma in situ (characterised by increased nuclear to cytoplasmic ratio, loss of polarity, downregulation of ERα and upregulation of the

epithelial breast stem cell marker CK19), suggesting the acquisition of cellular attributes reminiscent of a "stem-like" state (333). Consistent with these observations, highly tumorigenic fractions of cells are preferentially located within the hypoxic regions of neuroblastomas (324). Furthermore, upregulation of the CSC cell surface marker CD133 has also been reported in hypoxic regions of medulloblastomas (334).

The primary drivers of the hypoxic phenotype in different human cancer models are HIF-related transcription factors (*i.e.,* HIF-1α and HIF-2α) (233). Our findings regarding the role of HIF-1α under hypoxia in induction of cancer stemness in TNBC is however rather unexpected. Specifically, while we found that HIF-1α was effectively upregulated by hypoxia, siRNA knockdown of this protein did not inhibit the emergence of the RR phenotype, as we did not observe any changes in the level of chemoresistance to cisplatin, the proportion of $CD44^+/CD24^-$ cells and mammosphere formation ability.

The high activation level of STAT3, an oncoprotein strongly implicated in cancer stemness (335, 336), under hypoxia as well as its differential activation status in RU and RR cells have led us to hypothesize that STAT3 sustained the stem-like phenotype. HIF-independent drivers of the hypoxic phenotype in cancer cells are rarely reported and include chromatin remodeling histone demethylases (*i.e.*, JARID1B and MLL1) (233). To our knowledge the role of STAT3 under hypoxia in conferring stemness in TNBC has not been previously studied. To support the direct role of pSTAT3 in RU/RR conversion and acquisition of cancer stemness after hypoxic insult, we found that native RR cells had higher pSTAT3 than native RU cells, but their pSTAT3 level was substantially lower than that of hypoxic RU cells. Using a STAT3-DNA binding assay, we also found substantially more STAT3 pull-down in converted RR cells as compared to RU cells. The specificity of this binding was further confirmed in the presence of STAT3 inhibitor (stattic)(323), where less STAT3 protein pulled down with the SRR2 probe under hypoxia from converted RR cells. Furthermore, siRNA knockdown of STAT3 substantially blocked the RU/RR conversion, and this inhibition reversed the chemoresistance to cisplatin and reduced the clonogenic survival after cisplatin treatment.

In MDA-MB-231 cells, STAT3 activation in response to hypoxia is not HIF-dependent (307), although it has been shown that STAT3 and HIF-1α work together (294). This HIF-independent activation of STAT3 under hypoxia may explain why siRNA knockdown of HIF-1α did not prevent the emergence of RR phenotype and underscore the role of STAT3 as a key regulator of hypoxia-induced stemness. In contrast to STAT3, expression of c-Myc, an oncoprotein strongly implicated in cancer stemness in TNBC (321, 322), is HIF-dependant. As shown in previous studies, expression of c-Myc is potently supressed under hypoxia; however knockdown of HIF-1α abrogated the hypoxia-induced suppression of c-Myc and

restored its expression (337, 338). In our study, successful knockdown of HIF-1α restored c-Myc expression, but that did not change the acquisition of the RR phenotype. Similarly, either enforced expression of c-Myc or siRNA knockdown of c-Myc in hypoxic RU cells had no significant impact on stem-like features. This was an interesting finding, since under normoxia c-Myc was shown to be a major driver of RR phenotype in this cell line (321, 322). This finding emphasizes that driving forces of cancer stemness are context dependant, and different regulators may play a key role under hypoxic or normoxic conditions.

We think that our observation of hypoxia-induced RU/RR conversion illustrates cancer cell plasticity, a concept that has been nicely described in several recently published reviews (339-341). Given the biological and clinical significance of both cancer stemness and hypoxia, it is highly relevant and important to understand the molecular mechanisms that regulate cancer cell plasticity in the setting of hypoxia. To our knowledge, only few study models for cancer cell plasticity exists, with the epithelial-mesenchymal transition being the most frequently used (342-344). We also found a recently published paper in which cells responsive to a Wnt reporter are more stem-like than those unresponsive to the reporter, and stimulation with hepatocyte growth factor was found to convert unresponsive cells to responsive cells (345). Considering that the RR phenotype is readily detectable by flow cytometry and/or luciferase assay, and the fact that RU cells can be converted to RR cells upon hypoxia challenge, we believe that our study model is a powerful tool to examine the molecular basis of cancer cell plasticity under hypoxia.

In the current study, we not only confirmed the biological significance of hypoxia in conferring stem-like features in TNBC, we have also demonstrated that hypoxia exerts this specific biological function by up-regulating the expression of pSTAT3. Overall, we believe that our finding is in parallel with multiple previous studies, in which STAT3 was shown to promote cancer stemness in various cancer models (335, 336). Nonetheless, to our knowledge the role of STAT3 in promotion of cancer stemness in the setting of hypoxia in TNBC has not been previously studied.

5.5 Conclusion

To conclude, we have provided evidence to support that STAT3 plays an important role in conferring hypoxia-induced acquisition of cancer stemnss in TNBC. Targeting STAT3 may be a useful therapeutic approach to overcome treatment-induced cancer stemness, which is believed to be a contributory factor to cancer relapses.

5.6 Acknowledgements

This work was financially supported by grants from Canadian Institutes of Health Research (CIHR) and Canadian Breast Cancer Foundation (CBCF) awarded to AL and RL. HSA was awarded the Women and Children's Health Research Institute (WCHRI) and Alberta Cancer Foundation (ACF) Graduate Studentships. NG was funded by CBCF.

5.7 Supplementary Information

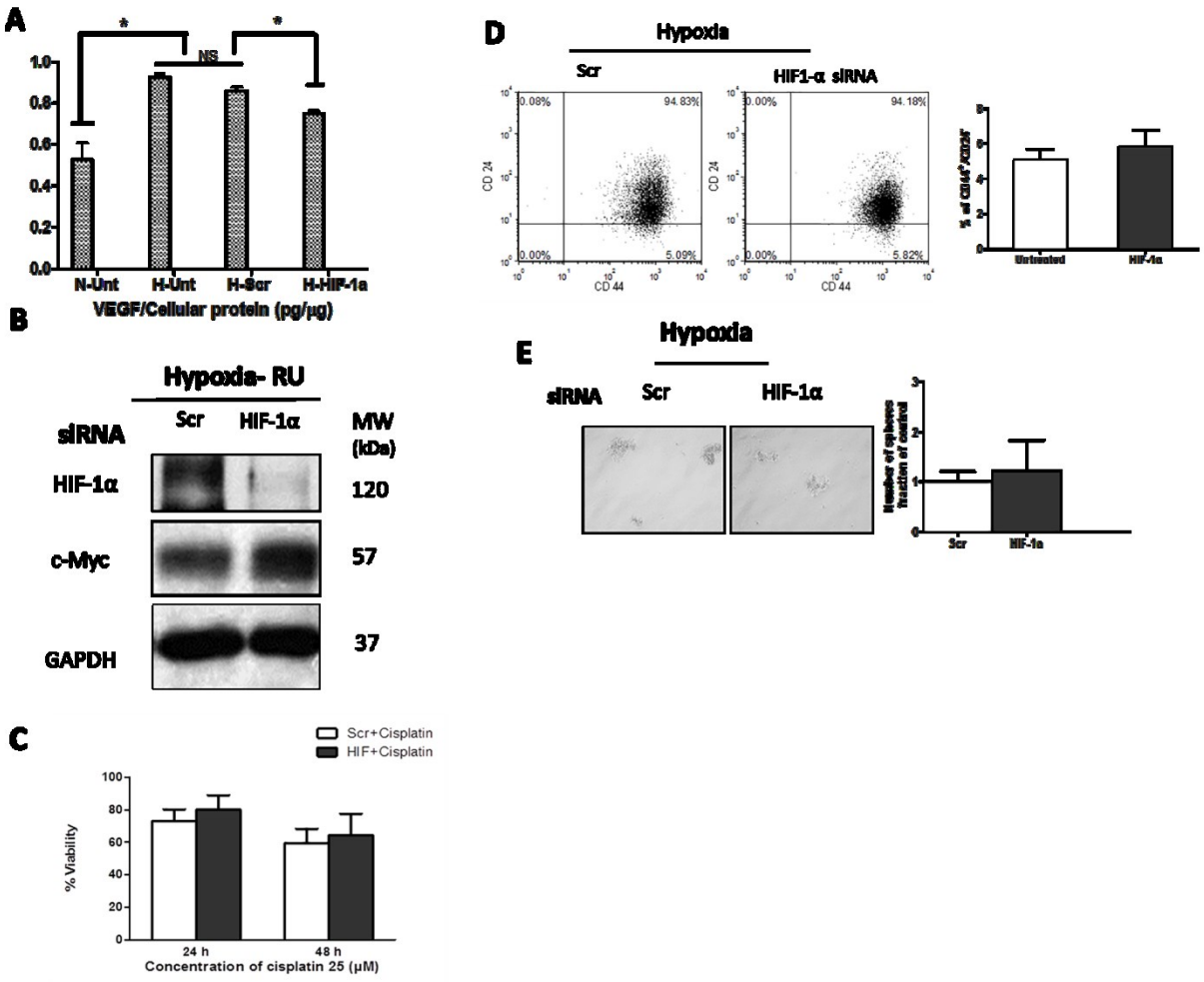

Figure 5.S1 Hypoxia-induced conversion of RU/RR cells is independent of HIF-1α. The effect of siRNA HIF-1 α knockdown in RU cell incubated for 48 h under hypoxia on **(a)** production of VEGF , **(b)** protein expression profile as depicted by Western blot , **(c)** cellular viability after cisplatin treatment as measured by MTT assay, **(d)** proportion of $CD44^{+}/CD24^{-}$ subpopulation as illustrated by flow cytometry dot plots, and **(e)** mammosphere formation. Representative micrographs of a 7-day mammosphere

culture are shown. (*) denotes a significant difference between the groups (Student's t test, $p<0.05$). Data are represented as mean ± SD (n=3).

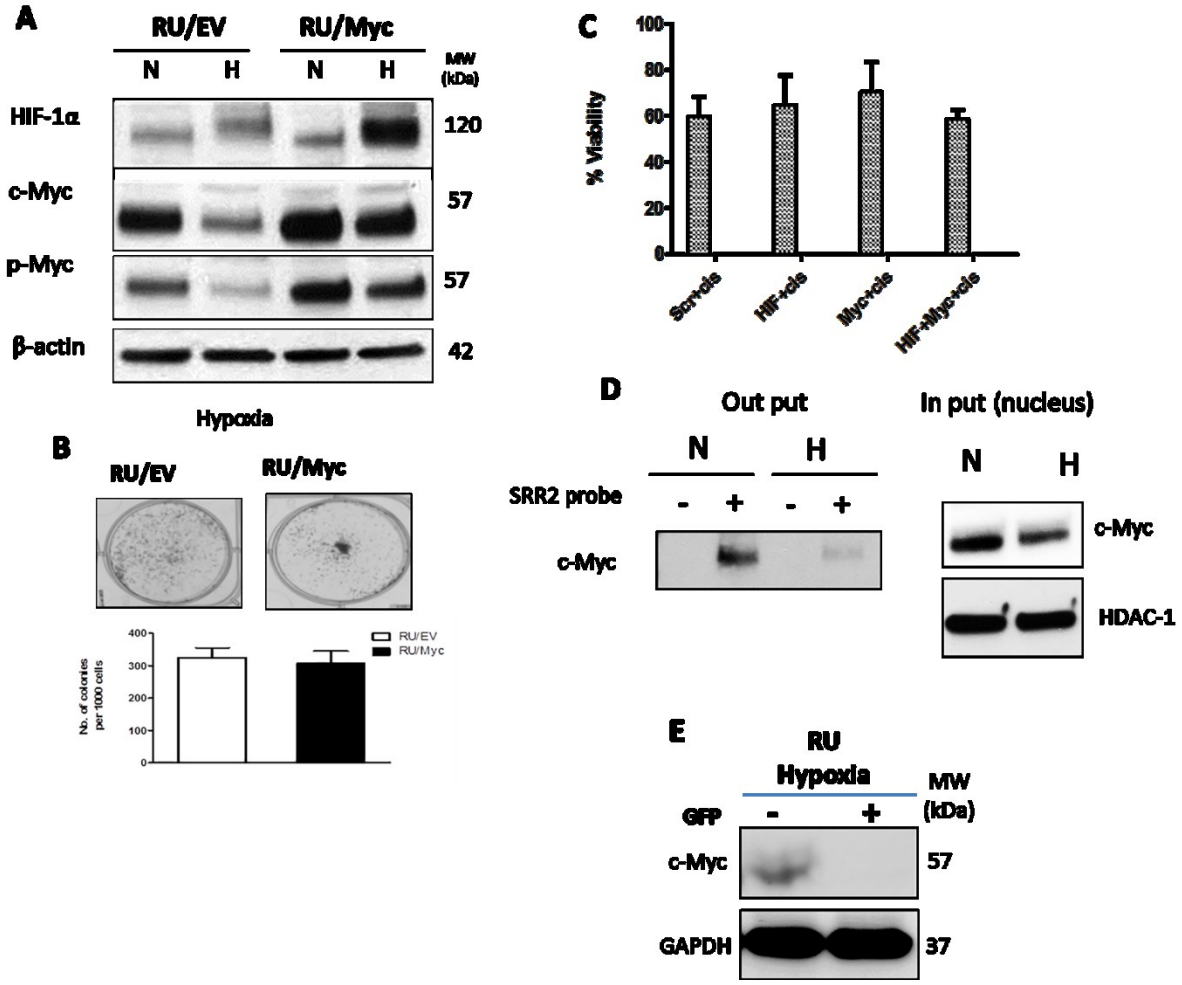

Figure 5.S2 Hypoxia-induced conversion of RU/RR cells is independent of c-Myc. **(a)** Hypoxia- mediated suppression of c-Myc was abrogated in c-Myc overexpressing RU cells (RU/Myc) as compared to empty vector (RU/EV) as depicted by Western blot. **(b)** Overexpression of c-Myc in RU/Myc cells did not enhance their clonogenic potential under hypoxia as compared to RU/EV. **(c)** siRNA knockdown of c-Myc alone or in combination withHIF-1 α did not reverse the chemoresistance in RU after 48 h cisplatin exposure under hypoxia . **(d)** Lower amount of c-Myc was pulled down with SSR2 probe in RU cells in normoxia as compared to hypoxia. **(e)** Lower expression of c-Myc in GFP-positive subset of sorted RU cells under hypoxia.

Chapter Six

Modulation of hypoxia-induced chemoresistance to polymeric micellar cisplatin in MDA-MB-231 cells: The effect of EGFR ligand modification of polymeric micelles and combination therapy with selected chemo-sensitizers

6.1 Introduction

The development of chemoresistance is a significant clinical obstacle which necessitates the development of new therapies to combat and overcome chemoresistance. Hypoxia is a common feature of solid tumors (14) and hypoxia-induced chemoresistance (HICR) has been observed in a number of human cancer models (123, 230, 287, 298). In chapter 3, we have reported on the development of a hypoxic cisplatin resistant model of triple negative breast cancer (TNBC) using MDA-MB-231 cells. In this chapter we explored two strategies for the modulation of hypoxia-induced cisplatin resistance in this cell line at the cellular lever: a) development of actively targeted nano-carriers of cisplatin capable of enhanced cisplatin delivery to MDA-MB-231 cells; and b) combination therapy with modulators of HICR which were selected based on the results of our studies in chapters 3 and 4.

Coexistence of hypoxia and high levels of epidermal growth factor receptor (EGFR) expression is a known feature of TNBC (239, 240), the most deadly and therapy resistant type of breast cancer. The high expression of EGFR on the hypoxic TNBC cells can be exploited to achieve enhanced delivery of cancer therapeutics to the cells (240, 346).

A substantial body of literature has demonstrated the ability of targeted nano-carriers to significantly improve drug pharmacokinetics by delivering a high payload of drug to tumor tissue while sparing healthy organs (78, 347-349). Once in the tumor tissue, the EGFR-targeted nano-carriers can potentially interact and preferentially deliver a high payload of cancer therapeutics to hypoxic TNBC cells. Previous studies have shown the use of EGFR monoclonal antibody for the development of ligand guided nano-carriers for the purpose of tumor imaging or targeted drug delivery (350-354). The high molecular weight of the full-length antibody, however, may compromise the penetration of antibody modified nano-carriers into tumor tissue further, and/or enhance the chance of nano-carrier removal by reticuloendotelial system following opsonization in the blood circulation (355). Furthermore, the high cost of the full-length antibody and limitations on the use of organic solvents for its incorporation in nano-formulations, prohibits its wide use as a ligand for tumor-targeted nano-carriers. In this context, use of EGFR-specific peptide, GE11, may be a better option. GE11 is a 12-residue peptide (YHWYGYTPQNVI) which was originally developed via the phage display technique (241). GE11 peptide shows a lower affinity for EGFR than the native ligand, EGF, however, it provides the advantage of lower mitogenic activity. Overall, due to its high EGFR affinity, minimum immunogenicity, and relatively cheap method of synthesis and scale-up, GE11 has been widely conjugated to a variety of nano-carriers,

including liposomes, polymeric micelles, and gold and gelatin nano-particles for therapeutic/diagnostic purposes (241, 355).

In this study, we first developed GE11 modified polymeric micellar complexes of cisplatin and assessed the success of this approach in overcoming hypoxia-induced cisplatin resistance in a TNBC associated cell line, i.e., MDA-MB-231 cells. TNBC tumors often carry a hypoxic phenotype (231) and cisplatin, is a platinum drug used as part of standard chemotherapy regimen for TNBC patients (231, 232). We then investigated the effect of adding pharmacological inhibitors of HIF-1α and STAT3, as the key molecules involved in chemoresistance under hypoxic conditions in this cell line, on anti-cancer activity of cisplatin. This was based on a hypothesis that the combination of cisplatin formulations (particularly its tumor targeted nano-formulation) with inhibitors of HIF-1α and/or STAT3 can potentiate the anti-cancer activity of this drug in hypoxic and resistant MDA-MB-231 cell line.

6.2 Materials and Methods

6.2.1 Synthesis of Block Copolymers with Functionalized PEO

Acetal-poly(ethylene oxide) (acetal-PEO) was synthesized based on the previous published method by Nagasaki *et. al.*(356). Briefly, potassium naphthalene, the catalyst, was freshly prepared before the synthesis of acetal-PEO. To prepare the catalyst, 1.65 g (12.9 mmol) naphthalene and 0.575 g (14.7 mmol) potassium was added into 50 mL anhydrous THF. The reaction was protected under dry argon gas and kept running for 24 hours, until the catalyst in THF solution with dark green color was obtained. To prepare acetal-PEO, 0.3 mL (2 mmol) 3,3-diethoxy propanol, the initiator, was first added into 40 mL anhydrous THF in a three-neck round bottom flask. The flask was purged with dry argon gas and maintained an argon atmosphere. The catalyst solution (7 mL, ~2 mmol) was added dropwise into the reaction solution to activate the initiator. After 10 minutes of stirring, the flask was transferred into an ice water bath. Ethylene oxide (11.4 mL, 228 mmol) was added into the reaction solution. After 48 hours, the reaction was quenched by acidified ethanol (2 mL). Acetal-PEO was recovered by precipitation in ethyl ether. The product was purified by dissolution in THF and precipitation in ethyl ether, and vacuum dried for further use.

Synthesis of acetal-PEO-poly-(ε-caprolactone) (acetal-PEO-PCL) and acetal-PEO-α-benzyl carboxylate-ε-caprolactone (acetal-PEO-PBCL) block copolymers has been described in our previous publications in detail (357). To synthesize acetal-PEO-poly-(α-carboxyl-ε-caprolactone) (acetal-PEO-PCCL), acetal-PEO-

PBCL was first prepared through bulk ring opening polymerization of BCL with acetal-PEO as an initiator. This was followed by hydrogen reduction of PBCL block catalyzed by Pd/charcoal. Briefly, 600 mg (0.1 mmol) acetal-PEO was reacted with 500 mg (2 mmol) BCL under vacuum at 145 °C for 6 hours using stannous octoate as a catalyst. Then the benzyl groups on acetal-PEO-PBCL were removed through hydrogen reduction in anhydrous tetrahydrofuran (THF) catalyzed by Pd/charcoal. The produced acetal-PEO-PCCL was recovered and purified by precipitation in hexane.

6.2.2 Synthesis of GE11 Peptide and GE11 Conjugation to PEO-PCCL Block Copolymers

The peptide GE11 (NH_2-YHWYGYTPQNVI-COOH) (Figure 6.S1a) was synthesized chemically using standard Fmoc solid phase peptide synthesis as described previously by the laboratory of Kaur *et. al.* (358). Briefly, the first amino acid, isoleucine, was coupled to a 2-chlorotrityl resin (0.1 mM) (NovaBiochem, San Diego, CA) at 5-fold excess using the N,N diisopropyl ethylamine (DIPEA) at room temperature for 5 hours. Further amino acids were added automatically using an automated peptide synthesizer (Tribute, Protein Technology, Inc., USA). The completed peptide was ultimately released from the resin with a mixture of 90% trifluoroacetic acid (TFA), 9% dichloromethane, and 1% triisopropylsilane (~10 mL) for 90 minutes at room temperature. The cleaved peptide combined with TFA was then concentrated, washed with diethyl either, dissolved in water and purified using reversed-phase HPLC. Purification was done using C18 semi-preparative (1 cm × 25 cm, 5 µm) reversed-phase HPLC (Varian Prostar, MD, USA) with a gradient of acetonitrile−H_2O (10−70% containing 0.05% TFA, 2 mL/min, 45 minutes run time). The peptide solution was freeze-dried to give pure peptide as a white powder. Analytical (0.46 cm × 25 cm, 5 µm) HPLC revealed a purity of 97% at 220 nm with Rt = 13 min, and the MALDITOF (Voyager spectrometer, Applied Biosystems, USA) mass analysis showed $[M + H]^+$ for the peptide as 1541.6 (calculated 1540.7) (Figure 6.S1b).

The GE11 peptide was conjugated to the micellar surface through a reaction with the functional acetal groups on the micellar shell (357). First, acetal-PEO_{5000}-$PCCL_{4000}$ (87% reduction of PBCL groups) was assembled into polymeric micelles. Briefly, diblock copolymer of acetal-PEO_{5000}-$PCCL_{4000}$ (20 mg) was dissolved in 1 mL acetone and added dropwise to 4 mL water while stirring. The solution was stirred for 24 hours under a fume hood to remove the acetone by evaporation. On the following day, the aqueous solution of polymeric micelles was then acidified to pH 2 with 0.5 M HCl and stirred for 1 hour at room temperature to produce aldehyde polymeric micelles. The resulting solution was then neutralized with 0.5 M NaOH. For conjugation of the peptide, the osmolarity of the micellar solution was adjusted by the addition of an appropriate volume of concentrated 10X PBS to obtain the final concentration of 1X PBS.

An aqueous solution of the peptide (1.3 mg peptide in 500 µL of 1% DMSO) (1 peptide : 2 polymer, mole:mole ratio) was added and incubated with the aldehyde bearing micelles at room temperature for 2 hours under moderate stirring. Subsequently, sodium cyanoborohydride ($NaBH_3CN$) (1 mg) was added to the polymer to reduce the Schiff's base. After 48 hours of reaction, the unreacted peptide and reducing agent were removed by extensive dialysis (Spectrapor, MWCO 3500) against distilled water (24 hours). The conjugation efficiency of the peptide to polymeric micelle was assessed by gradient reversed phase HPLC method. A µ Bondpack (Waters Corp., United States) C18 analytical column (10 µm 3.9× 300 mm) was used. Gradient elution was performed at a flow rate of 1 mL/min using a Varian Prostar 210 HPLC System. Detection was performed at 214 nm using a Varian 335 detector (Varian Inc., Australia). The mobile phase consisted of 0.1% TFA in H_2O (solution A) and acetonitrile (solution B). The mobile phase was programmed as follows: (1) 100% A for 1 min, (2) linear gradient from 100% A to 60% A in 20 min, (3) linear gradient from 60% A to 0% A in 4 min, (4) 0% A for 2 min, (5) linear gradient from 0% A to 100% A in 4 min, and (6) 100% A for 5 min. The concentration of unreacted peptide was calculated based on a calibration curve for the peak height of known concentrations of GE11-peptide in aqueous solution of 1% DMSO (Figure 6.S2). The amount of conjugated peptide was calculated by subtracting the amount of unreacted peptide from the initial peptide added to the reaction. The peptide conjugated polymer was then freeze-dried for micelle preparation.

Additionally ^1H NMR was performed on a Bruker, ASENDTM 600 MHz spectrometer to calculate the molar conjugation % for GE11-conjugated PEO-PCCL block polymer. Samples (GE11 peptide, acetal-PEO-PCCL, and GE11-PEO-PCCL) were dissolved in DMSO at a concentration range of 3-5 mg/mL and ^1H NMR spectra were generated. Signals from 6.5 to 8.5 ppm in ^1H NMR spectra of GE11 peptide corresponded to aromatic protons in its structure (n=20). To calculate the molar conjugation % for GE11-conjugated PEO-PCCL block polymer, first the summation of integration of peaks from 6.5 to 8.5 ppm in acetal-PEO-PCCL spectra was subtracted from the summation of integration of peaks from 6.5 to 8.5 ppm in GE11-PEO-PCCL spectra. The obtained value corresponded to integration of aromatic hydrogens of GE11 peptide (n=20). The degree of conjugation of GE11 then determined from spectra of GE11-PEO-PCCL by examining the peak intensity ratio of methylene protons of PCCL segment ($OC\underline{H_2}CH_2CH_2CH_2(COOH)CO$): δ = 4.1 ppm) and the value calculated for the integration of aromatic hydrogens of GE11 peptide of GE11-PEO-PCCL.

6.2.3 Preparation of Plain and GE11-Cisplatin Micelles

GE11-PEO-PCCL or PEO-PCCL block copolymers were assembled into cisplatin polymeric micelles as reported previously with slight modification (359). Briefly, either diblock copolymer (20 mg) was mixed with 4 mL aqueous solution of cisplatin (20 mg) and sodium bicarbonate (4-5 mg). The mixture was stirred for 24 hours at room temperature. Unbound cisplatin was removed by ultrafiltration (3600 g for 40 minutes) using Centricon® plus centrifugal filter units (MWCO 3 KDa, Millipore, Billerica, MA) and micelles were resuspend in 4 mL doubly distilled water.

6.2.4 Measurement of the Size and Zeta Potential of Micelles

The average hydrodynamic diameter and size distribution of the GE11-cisplatin micelles were estimated and compared to plain cisplatin micelles by dynamic light scattering (DLS) using Malvern Zetasizer (Nano ZEN3600, Malvern, UK). The zeta potential of polymeric micelles was also estimated using the same equipment.

6.2.5 Measuring the Critical Micellar Concentration (CMC) of Micelles

The CMC of the GE11-cisplatin micelles were estimated and compared to plain cisplatin micelles by dynamic light scattering (DLS) (360) using Malvern Zetasizer (Nano ZEN3600, Malvern, UK). Briefly, plain and GE11-cisplatin micelles having concentrations ranging from 1000 to 3 µg/mL were prepared. The intensity of scattered light was measured at scattering angle of 173° at 25 °C.

6.2.6 Measurement of Cisplatin Encapsulation

The Pt(II) content in the GE11-cisplatin micelles was determined by ion coupled plasma mass spectrometer (ICP-MS, Agilent Technologies, Tokyo, Japan). The ICP operated at a radiofrequency power of 1550 W, and the flow rate of argon carrier gas was 0.9–1.0 L/min. Pt(II) was monitored at m/z 195. Standard curve in the Pt(II) concentration range of 100, 50, 20, 10, 1 ppb was generated using atomic absorption standard. Appropriate dilutions of the test samples were prepared in 1% nitric acid (HNO_3). Data were acquired and processed by ICP-MS ChemStation (Agilent Technologies, Santa Clara, CA). The encapsulation efficiency and drug loading were calculated using the following equation:

$$EE\ (\%) = \frac{the\ amount\ of\ encapsulated\ cisplatin\ (mg)}{the\ total\ feeding\ amount\ of\ cisplatin\ (mg)} \times 100$$

$$DL\ (\%) = \frac{the\ amount\ of\ encapsulated\ cisplatin\ (mg)}{the\ total\ amount\ of\ polymer\ (mg)} \times 100$$

6.2.7 In vitro Release Studies

The release of free cisplatin and its micellar formulations (plain and GE11-cisplatin micelles) was measured using equilibrium dialysis method in PBS (pH=7) and acetate buffer saline (pH=5). Briefly, free cisplatin, plain or GE11-cisplatin micelles (4 mL) containing 30 µg/mL cisplatin were placed into a dialysis bag (Spectrapor, MWCO 3500) in a beaker containing 500 mL PBS or acetate buffer saline. The release study was performed at 37 °C in a Julabo SW 22 shaking water bath (Seelbach, Germany). At selected time intervals, 100 µL samples were withdrawn from the dialysis bag and replaced with fresh medium for ICP-MS analysis. The % cumulative amount of cisplatin released was calculated and plotted as a function of time. The release profiles of plain and GE11 cisplatin micelles were compared using similarity factor, f_2, and the profiles were considered significantly different if f_2 <50 (269). The similarity factor, f_2, was calculated based on Equation (1) (270).

$$f_2 = 50 \times \log\left(\left[1 + \left(\frac{1}{n}\right)\sum_{j=1}^{n}|Rj - Tj|^2\right]^{-0.5} \times 100\right) \quad (1)$$

where n is the sampling number, R_j and T_j are the percent released of the reference and test formulations at each time point j.

6.2.8 Cell Culture

TNBC cell line, MDA-MB-231 was obtained from ATCC (Manassas, VA) and maintained in RPMI 1640 medium supplemented with 10% fetal bovine serum (Invitrogen, Karlsruhe, Germany), 100 units/mL penicillin, and 100 mg/mL streptomycin in a humidified incubator under 95% air and 5% CO_2 at 37°C. For hypoxic condition, cells were cultured in a CO_2 incubator maintained at 94% N_2, 5% CO_2 and 1% O_2.

6.2.9 Flow Cytometric Detection of Apoptosis using Annexin V-FITC and Propidium Iodide

Annexin V-FITC and propidium iodide (PI) from BD Biosciences (FITC Annexin V Apoptosis Detection Kit I, #556547, BD Pharmingen™) was used to measure apoptotic cells by flow cytometry according to the manufacturer's instructions. Briefly, MDA-MB-231 cells (35 x 10^4 cells/well) were seeded in 25 cm^2 flask overnight, then exposed to increasing concentration of cisplatin under hypoxic and normoxic conditions for 24 and 48 hours. At each incubation time, both floating and adherent cells were harvested, (adherent cells were collected by adding a warm solution of 10 mM ethylenediaminetetraacetic acid (EDTA) in PBS), the cells were centrifuged at 500 g for 5 minutes, washed with ice cold 1X PBS twice and resuspended in 400 µL 1x binding buffer containing 5 µL Annexin V-FITC and 5 µL PI for 15 minutes at room temperature in the dark. Fluorescence was induced on a Beckman Coulter Cytomics Quanta SC MPL flow cytometer (10,000 events per sample). Spectral compensation was performed using Cell Lab

Quanta analysis software. The number of viable and apoptotic cells were quantified by events in the quadrants. Results were expressed as the percentage of apoptotic cells at the early stage (PI negative and Annexin V positive, lower right quadrant), apoptotic cells at the late stage (PI positive and Annexin V positive, upper right quadrant), necrotic cells (PI positive and Annexin V negative, upper left quadrant) and viable cells (PI negative and Annexin V negative, lower left quadrant).

6.2.10 MTT Assay

MDA-MB-231 cells (9 x 10^3 cells/well) were seeded in 96-well plates overnight. On following day, cells were treated with Tat-tagged form of cyclic peptide inhibitor of HIF-1α (*cyclo*-CLLFVY) (50 μM per well) (361) or combination of stattic (Sigma, St. Louis, MO) and *cyclo*-CLLFVY for 4 hours under normoxia, to give a final concentration of 2 μM and 50 μM per well, respectively. After 4 hours incubation, cells were treated with cisplatin (50 μM) (as free drug, plain cisplatin micelles or GE11 cisplatin micelles) and then incubated for additional 48 hours under hypoxic conditions. Cellular viability was assessed by the reduction of MTT (3-(4,5-dimethylthiazol-2-yl)-2,5-diphenyltetrazolim bromide, Sigma–Aldrich, Oakville, ON, Canada) to formazan crystals. Briefly, MTT solution (5 mg/mL) was added to incubated cells for 4 hours at 37 °C prior to assessment. Then the medium was replaced by N,N, dimethyl sulfoxide (DMSO) to dissolve the crystals. Optical density was measured spectrophotometrically using a plate reader (Synergy H1 Hybrid Reader, Biotek) at 570 nm. The cellular activity ratio was represented relative to control (untreated group, cells with media only).

6.2.11 Western Blot

To measure the expression level of different proteins, MDA-MB-231 cells (20 x 10^4 cells/well) were seeded in 6-well plates overnight. After treatment, cells were washed with cold 1X PBS and lysed using RIPA lysis buffer that was supplemented with 0.1 mM phenylmethylsulfonyl fluoride (PMSF) (Sigma-Aldrich), a protease Inhibitor Cocktail Set III, Animal-Free - Calbiochem (#535140, Millipore), and a phosphatase Inhibitor Cocktail Set II (#524625, Millipore). The lysate was then incubated on ice for 30 min, which was followed by centrifugation at 17000 g for 20 min to remove genomic DNA. Protein quantification was determined by the BCA protein assay kit (Pierce, Rockford, IL, USA), and equal amounts of protein (35-40 μg) were loaded in 4–15% Tris-Glycine gradient gel (#456-1084, Biorad). After gel electrophoresis, proteins were transferred to a nitrocellulose membrane. Membranes were probed with antibodies against HIF-1α (#3716s, Cell Signaling Technologies), phospho-STAT3 (Tyr705) (p-STAT3) (#9131, Cell Signaling Technologies), Total-STAT3 (T-STAT3) (#8768s, Cell Signaling Technologies), EGFR

(#2232, Cell Signaling Technologies), and GAPDH (# sc-47724, Santa Cruz Biotechnologies). Proteins were then detected using peroxidase-conjugated anti-mouse IgG (#7076, Cell Signaling Technologies) or anti-rabbit IgG (#7074, Cell Signaling Technologies) and visualized by enhanced chemiluminescence (Pierce ECL Western Blotting Substrate, #32106, Thermo Scientific, Rockford, IL, USA).

6.2.12 Cisplatin Cellular Uptake

Cellular uptake of cisplatin was quantified by ICP-MS, (Agilent Technologies, Tokyo, Japan). MDA-MB-231 cells (65 x 10^4 cells/flask) were seeded in 25 cm^2 flasks overnight. Cells were exposed to free cisplatin or its micellar formulations (plain and GE11-cisplatin micelles) (166 µM) for 24 hours under normoxia and hypoxia. On following day, the medium was aspirated, cells were rinsed with cold PBS, detached using trypsin-EDTA, aliquoted in duplicate in 1.5 mL micro-centrifuge tubes and pelleted by centrifugation at 500 g for 5 minutes. One of each duplicate cell pellet was digested with 20% (v/v) HNO_3 overnight at 60 °C and analyzed for Pt(II) content by ICP-MS. The other duplicate was lysed using RIPA lysis buffer that was supplemented with 0.1 mM phenylmethylsulfonyl fluoride (PMSF) (Sigma-Aldrich), a protease Inhibitor Cocktail Set III, Animal-Free - Calbiochem (#535140, Millipore), and a phosphatase Inhibitor Cocktail Set II (#524625, Millipore) and quantified for protein content using the BCA protein assay kit (Pierce, Rockford, IL, USA). The cell uptake was expressed as ng cisplatin/µg cell protein.

6.2.13 Statistical Analysis

The statistical analysis was performed by Graphpad Prism (version 5.00, Graphpad Software Inc., La Jolla, CA, USA). Statistical analysis was performed either using unpaired Student's *t* test or one way ANOVA with *Tukey* post-test analysis. Statistical significance is denoted by (p<0.05). All graphs represent the average of at least 3 independent experiments with triplicates, unless mentioned otherwise in the text, or Graphs. Results were represented as mean ± standard deviation (SD).

6.3 Results

6.3.1 Synthesis of GE11 Peptide Conjugated PEO-PCCL Block Copolymer

Under the reaction conditions described, the reaction mixture showed a conjugation efficiency reaching 70% quantified by reversed phase HPLC (Figure 6.S3). The molar conjugation % for GE11-conjugated PEO-PCCL block polymer was ~35%. This means there is around 35 mole peptide per 100 mole block copolymers. The calculated molar conjugation % for GE11-conjugated by ^{1}HNMR was 45 % which is in good agreement with HLPC data (**Figure 6.S4**).

6.3.2 Characterization of Plain and GE11 Cisplatin Micelles

Both plain and GE11-cisplatin micelles showed similar sizes around 80 nm with a low polydispersity index. CMC, encapsulation efficiency and drug loading of both micelles were also comparable as summarized in **Table 6.1.** Overall, both micellar formulations showed similar characteristics and it appeared as though the presence of the GE11 peptide did not alter their properties.

Table 6.1.Charecteristics of cisplatin and GE11- cisplatin micelles

Micelle [a]	Diameter ± SD (nm)[b]	PDI ± SD [c]	Zeta potential/mV ± SD	CMC (μg/mL) ± SD [d]	EE% ± SD [e]	DL% ± SD [f]	Drug/polymer (mol/mol) ± SD
Cisplatin micelle	84.4 ± 2.6	0.263 ± 0.11	-13.3 ± 1.2	65.1 ± 5.5	12.4 ± 0.99	12.0 ± 1.41	3.93 ± 0.31
GE11-Cisplatin micelle	84.1 ± 3.2	0.235 ±0.18	-13.6 ± 0.95	70.5 ± 7.2	13.0 ± 2.95	15.5 ± 3.53	4.01 ± 0.93

[a] Plain and GE111 cisplatin micelles consist of PEO_{113}-$PCCL_{20.6}$ block copolymers. The number shown in the subscript indicates the polymerization degree of each block determined by ^{1}H NMR spectroscopy.

[b] Z average measured by DLS.

[c] Average polydispersity index (PDI) of micellar size distribution measured by DLS.

[d] Measured from the onset of rise in the intensity values of scattered light as a function of concentration of micelles by DLS.

[e] Encapsulation efficiency $(\%) = \frac{the\ amount\ of\ encapsulated\ cisplatin}{the\ total\ feeding\ amount\ of\ cisplatin} \times 100.$

[f] Drug loading$(\%) = \frac{the\ amount\ of\ encapsulated\ cisplatin}{the\ total\ amount\ of\ polymer} \times 100.$

The *in vitro* release of cisplatin from both micelles was investigated in PBS (pH=7.4) and acetate buffer saline (pH=5.0) using dialysis method. Both micellar formulations showed burst release at the early time points (<1 hour), but the cumulative drug release appeared to be significantly slower at the later time points as compared to free drug release in these medias (Student's t test, $p<0.05$). As shown in **Figure 6.1a**, micellar formulations showed initial fast rate of release (~60% release of cisplatin from micellar formulation within 30 minutes as compared to ~80% release of free drug); however the drug release reduced after the first hour and micelles maintained slow rate of release and only ~85 % release

happened after 48 hours. No difference was observed between the release profile of plain and GE11 cisplatin micelles within the time frame of the study ($f_2 > 50$).

Similar results were obtained for micellar formulations of cisplatin in acetate buffer saline (pH=5.0) and significant reduced drug release was achieved at the later time points of the release (Student's t test, $p<0.05$). Of note, acid triggered release was seen for both micelles in acetate buffer (pH=5) with complete release of drug after 48 hours, whereas only 80% drug was released in PBS at the same time point (pH=7) (**Figure 6.1b**).

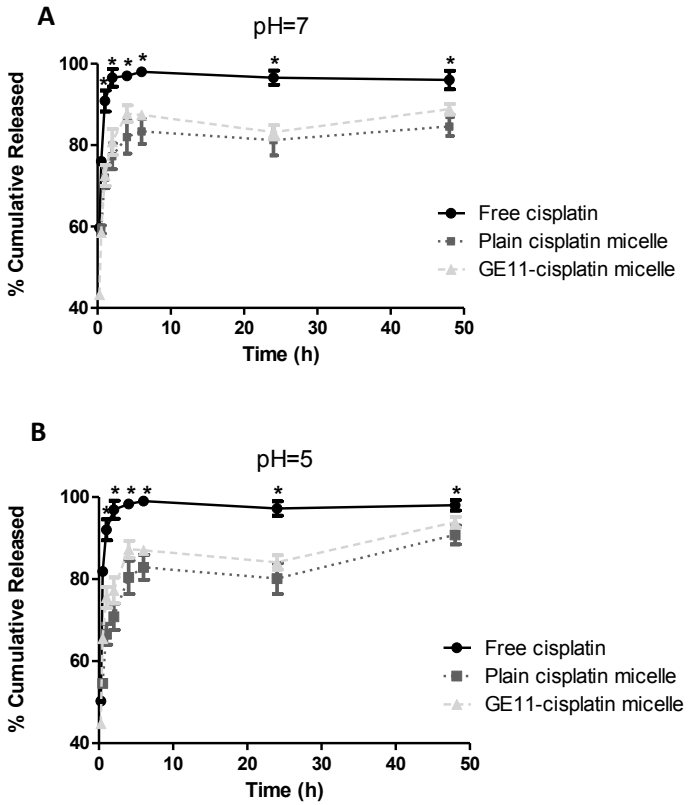

Figure 6.1 Percent cumulative release profile of cisplatin from plain and GE11 cisplatin micelles at different pHs in **(a)** PBS (pH=7.4) and **(b)** acetate buffer saline (pH=5.0).

6.3.3 Hypoxia Induces Chemoresistance to Cisplatin in MDA-MB-231 Cells

Hypoxia significantly increased the viability of MDA-MB-231 cells exposed to cisplatin as measured by MTT assay (**Figure 6.2a-b**). Correlating with this observation, cisplatin-induced apoptosis significantly reduced under hypoxia, as evidenced by significant increase in the proportion of the viable cells as well

as the significant decrease in the proportion of late apoptotic cells measured by FITC Annexin V/propodium iodide (PI) assay(**Figure 6.2c-d**). Similar results were obtained with plain cisplatin micelles, where clonogenic survival assays also showed resistance to cisplatin treatment (**Figure 6.S5**).

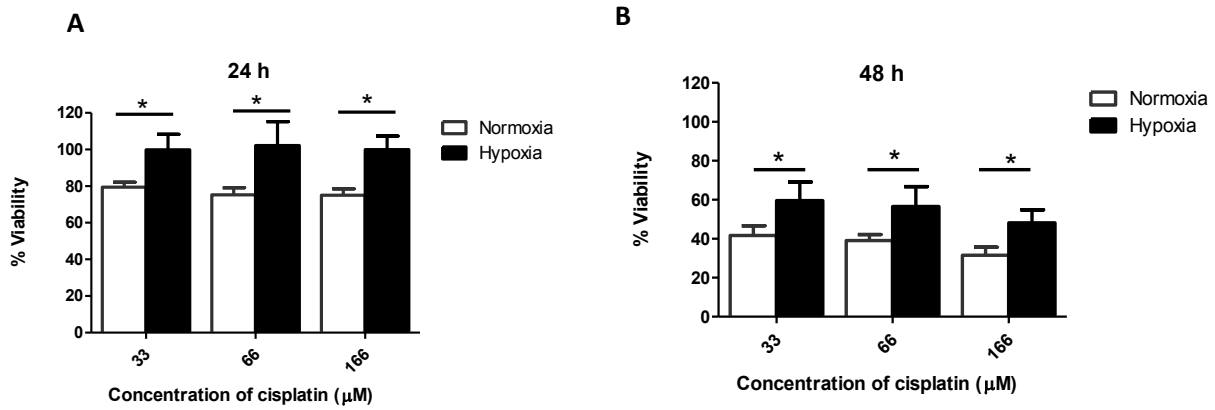

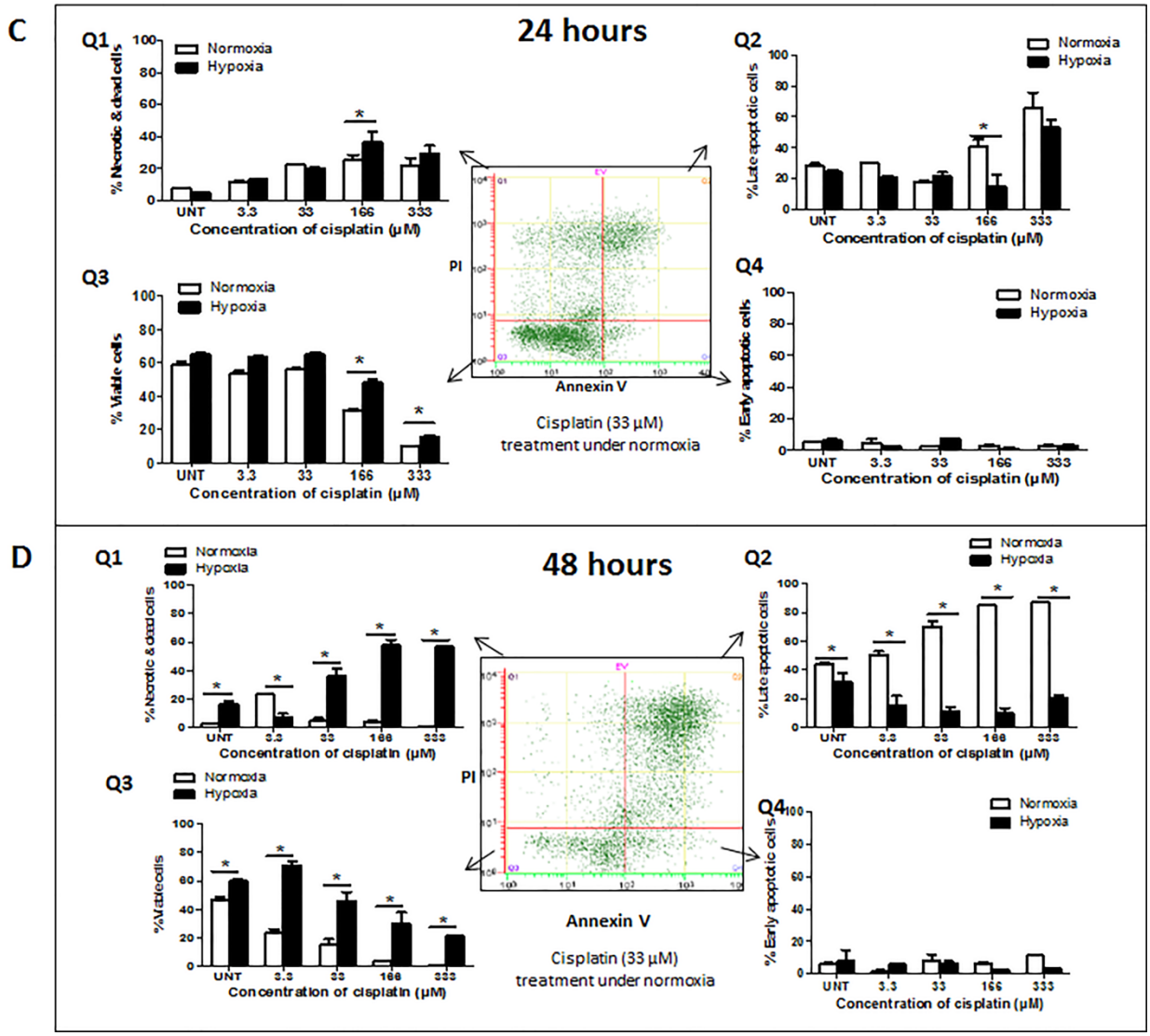

Figure 6.2 Hypoxia confers chemoresistance to cisplatin in MDA-MB-231 cells. Drug sensitivity of cells under normoxia or hypoxia was measured by MTT assay for **(a)** 24 hours and **(b)** 48 hours treatment with cisplatin. Cisplatin induced-apoptosis was measured under normoxia or hypoxia by flow cytometric analysis of FITC Annexin V staining in a buffer containing PI. MDA-MB 231 cells were left untreated or treated with increasing concentration of cisplatin for **(c)** 24 hours and **(d)** 48 hours. Flow cytometry analysis showed different populations of (Q1) necrotic or already dead cells (PI positive), (Q2) cells in end stage apoptosis (FITC Annexin V and PI positive), (Q3) viable cells (FITC Annexin V and PI negative), and (Q4) cells in early stage of apoptosis (FITC Annexin V positive and PI negative). 2D plots are representative of cells treated with cisplatin (33 µM) under normoxia for **(c)** 24 hours and **(d)** 48 hours.

6.3.4 Decoration of Cisplatin Micelle with GE11 Peptide Enhances the Cellular Uptake under Hypoxia

As expected, MDA-MB-231 cells showed high levels of EGFR expression under normoxia; importantly they maintained similarly high level of EGFR expression under hypoxia (**Figure 6.3**) (240). Of note, upon hypoxic challenge, a time-dependent increase in the level of HIF-1α, a well-known hypoxic marker, was shown which further validated the hypoxic model.

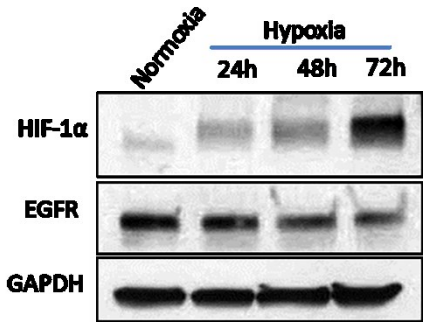

Figure 6.3 High levels of EGFR expression under normoxia and hypoxia in MDA-MB-231 cells.

In the next step, to assess if the decoration of micelles with the GE11 peptide enhances their uptake under hypoxia, intracellular concentration of cisplatin was measured after 24 hours incubation of free cisplatin and its micellar formulations. As shown in **Figure 6.4,** intracellular uptake of cisplatin was found to be significantly reduced under hypoxia for free drug (~20% decrease) as well as plain cisplatin micelles (~32% decrease) as compared to normoxia. Nonetheless, the presence of the GE11 peptide on micelles compensated for the hypoxia-mediated reduced cisplatin uptake, and GE11 micelles showed similar drug uptake under both hypoxic and normoxic conditions. GE11 micelles showed significantly higher cisplatin cellular uptake as compared to the plain cisplatin micelles under hypoxic conditions (~1.4 fold, Student's t test, $p<0.05$) **(Figure 6.4)**.

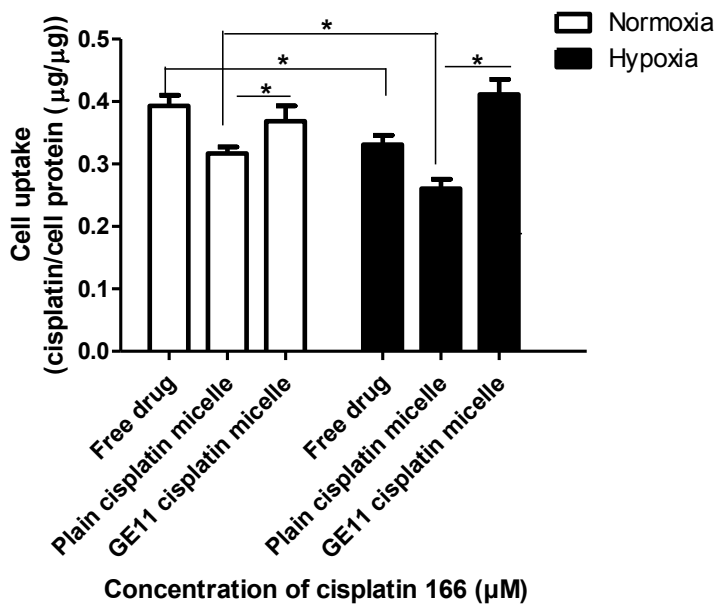

Figure 6.4 The GE11-peptide decoration of cisplatin micelles enhanced cellular uptake of cisplatin under hypoxia in MDA-MB-231 cells and bridged the gap of its cellular uptake under hypoxia and normoxia. Cisplatin content was measured by ICP-MS after 24 hours incubation.

6.3.5 Dual Pharmacological Inhibition of STAT3 and HIF-1α in Combination with Free/Cisplatin Micelles Successfully Reversed Hypoxia Induced Chemoresistance

To assess the chemo-sensitizing effect of STAT3 and/or HIF-1α inhibition on enhancing the efficacy of cisplatin treatment, pharmacological inhibitors of STAT3 (stattic) (323) and HIF-1α (cyclo-CLLFVY peptide) (361) were used in combination with free and cisplatin micelles and the toxicity of cisplatin against MDA-MB-231 cells was measured using MTT assay under hypoxic conditions.

Stattic is a small molecule shown to inhibit the dimerization and activation of STAT3 mainly through prevention of its phosphorylation (323). As shown in **Figure 6.5**, successful inhibition of phosphorylation of STAT3 was achieved using stattic under hypoxia.

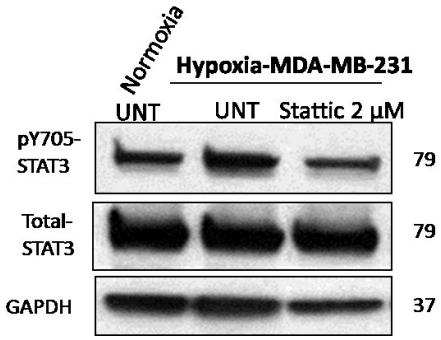

Figure 6.5 Lower expression of pSTAT3 in MDA-MB-231 cells after treatment with stattic. MDA-MB-231 cells were treated with STAT3 inhibitor (stattic (2 µM)) under normoxia (4 hours), and then incubated under hypoxia (48 hours). Phosphorylation of STAT3 Tyr705 was analyzed by western blot.

Tat-tagged form of *cyclo*-CLLFVY, a cyclic peptide which has shown to prevent the dimerization of HIF-1α/HIF-1β complex and subsequently to inhibit HIF-1α transcription activity (361), was used as a HIF-1α inhibitor. As shown in **Figure 6.6**, combination of cisplatin and HIF-1α inhibitor (cyclo-CLLFVY) significantly enhanced the toxicity of cisplatin under hypoxia (one way ANOVA with Tukey post-test, $p<0.05$).

In addition, dual inhibition of STAT3 and HIF-1α further enhanced the toxicity of the cisplatin in MDA-MB-231 cells when they were pre-incubated with both inhibitors and exposed to cisplatin formulations. As shown in **Figure 6.6**, dual inhibition of STAT3 and HIF-1α was the most effective approach in reversal of HICR with different formulations of cisplatin and significantly increased the toxicity of the cisplatin (one way ANOVA with Tukey post-test, $p<0.05$). Of note, in all the above experiments no significant difference observed between the toxicity of free drug and micellar formulations. In addition, GE11 micelles showed similar profile of toxicity as compared to plain cisplatin micelles.

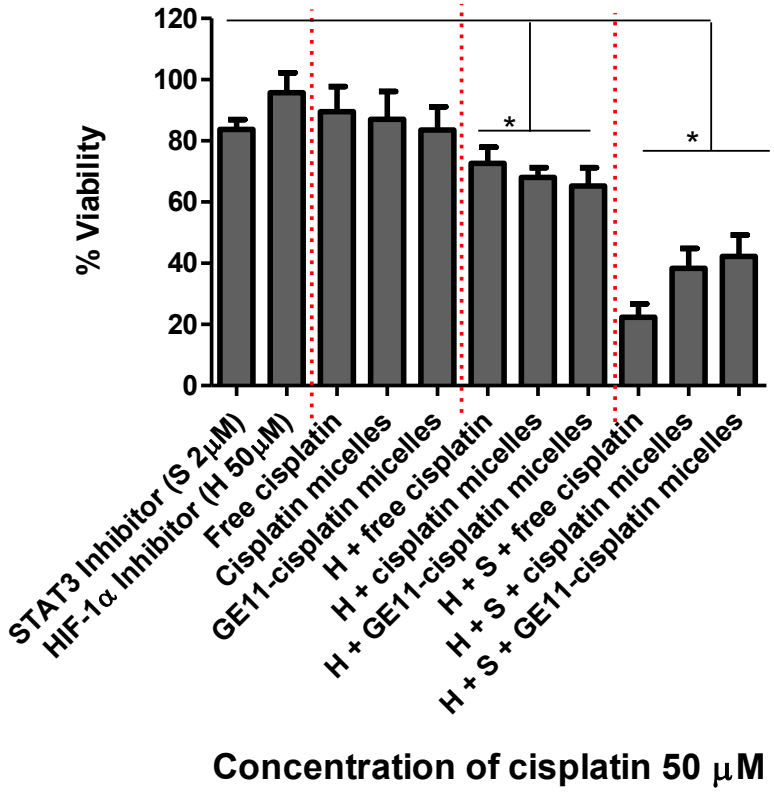

Figure 6.6 Dual pharmacological inhibition of STAT3 and HIF-1α in combination with free/cisplatin micelles successfully reversed HICR. MDA-MB-231 cells were pre-incubated with cyclic peptide inhibitor of HIF-1α (H) (50 μM), or combination of peptide inhibitor of HIF-1α (H) (50 μM) and STAT3 inhibitor (stattic (S)) (2 μM) under normoxia (4 hours). Then cells were treated with cisplatin (50 μM) under hypoxia (48 hours). Viability of cells was measured by MTT assay.

6.4 Discussion

Substantial evidence suggests that hypoxia, as a key tumor microenvironment factor, is widely associated with chemoresistance in different types of tumors (230, 287) including TNBC (123, 298). Overexpression of epidermal growth factor receptor (EGFR) and tumor hypoxia have been shown to correlate with worse outcomes in several types of cancers including breast cancer (238, 239). This coexistence of hypoxia and EGFR points to a survival advantage of hypoxic cells that are also able to express EGFR. In this study, we aimed to develop alternate mechanisms to overcome hypoxia-induced chemoresistance (HICR) by developing EGFR-targeted cisplatin micelles using EGFR-specific peptide, GE11, as well as investigating the effect of adding pharmacological inhibitors of HIF-1α and STAT3, as the

key molecules involved in chemoresistance under hypoxic conditions in this cell line, on anti-cancer activity of different formulations of cisplatin.

We employed an experimental model in which a TNBC cell line, MDA-MB-231, was treated with cisplatin, which is a front-line chemotherapeutic agent used to treat TNBC patients (231, 232). Consistent with the published results of several studies using a variety of cancer cell lines and cisplatin under hypoxic condition (299-301), we found that hypoxia significantly induced cisplatin resistance in MDA-MB-231 cells. To our knowledge, HICR have been described in prior published studies of human cancer cells (123, 230, 287, 298). Overall, we believe that our experimental model is valid and appropriate to study the applicability of our developed micellar formulations in the setting of hypoxia for overcoming HICR in cancer cells.

In concert with our previous study with plain cisplatin micelles (359), the GE11-cisplatin micelles were also pH sensitive and showed accelerated drug release in an acidic environment. The ability of acid triggered release of these micelles is of utmost importance, since in addition to hypoxic regions, tumors usually have lower extracellular pH (more acidic) than that of normal tissues (92). Thus, the acid triggered release of cisplatin from the micellar formulations is expected to be advantageous in the targeted delivery of cisplatin. In this case, premature release of cisplatin in the blood circulation (pH 7.4) is prevented by the cisplatin micelles, while accelerated cisplatin release will be achieved in the extracellular space in tumor tissue upon micellar accumulation. Hydrolytic and acid catalyzed degradability of the micellar core is a distinguishing factor of our system from NC-6004 micellar formulation of cisplatin which is currently in clinical trials phase III (74-76). It is of note that this feature, i.e., acid triggered release of cisplatin from polymeric micellar formulation, was not investigated in our cell cytotoxicity studies as the pH of the cell culture media was maintained at 7.4.

Non-targeted cisplatin micelles can accumulate in tumor tissues by passive targeting through the EPR (enhanced permeability and retention) effect (74, 362) and many different types of nano-carriers have already been studied for cisplatin delivery in this regard (76, 78, 363-369). However, passive targeting does not necessarily ensure delivery of the drug within the tumor cell. To facilitate tumor cell-specific internalization, one of the most promising strategies is the incorporation of additional mechanisms in the nano-carriers for receptor-mediated endocytosis. Surface modification of cisplatin micelles with the GE11 peptide as targeting moieties for EGFR-expressing cells in this study enhanced their uptake significantly under hypoxia. EGF receptors (EGFR) are ‘internalizing’ receptors; that is, following ligand binding, the ligand/receptor complex is actively endocytosed (370). For instance, in our model, the decoration of micellar core with the GE11 peptide expectedly directed the GE11-cisplatin micelles into

the EGFR-expressing cells under hypoxia. EGFR-targeted micelles have been constructed for the targeted delivery of different types of drugs (371, 372), but we only found one study which used an anti-EGFR antibody (ScFvEGFR) for enhancing cisplatin delivery in lung cancer (373).

Upregulation of ATP-binding cassette (ABC) drug transporters (responsible for active efflux of a wide range of anticancer agents including cisplatin (chapter 3)) under hypoxia is one of the proposed mechanisms for HICR (201, 374). Nano-carriers have a potential to divert ABC-transporter mediated drug efflux by altering drug internalization mechanisms and subcellular localization. The cellular uptake of GE11 cisplatin micelles, presumably through receptor-mediated rather than non-specific endocytosis in the case of plain cisplatin micelles or diffusion in the case of free drug, is an example of altering drug internalization mechanisms. Decoration of plain cisplatin micelles with GE11 peptide enhanced their cellular uptake under hypoxia, however this enhanced cellular uptake did not translate to a better toxicity for GE11-cisplatin micelles over plain cisplatin micelles and they both showed a similar profile of toxicity. The exact reason for this observation is not clear and can be attributed to the initial fast release of cisplatin (~60% release of cisplatin from micellar formulation within 30 minutes) from both plain and GE11 cisplatin micelles. Therefore, the higher cellular uptake of GE11 micelles which happens at the later time points will be less significant. Initial fast release of cisplatin from micelles can also contribute to the observed similar profile of toxicity between free drug and micellar formulations.

In the chapter 3, we showed that knockdown of HIF-1α using siRNA was unsuccessful in reversal of HICR to cisplatin. However, in this chapter our toxicity results showed that combination of *cyclo*-CLLFVY peptide, as a HIF-1α inhibitor, with cisplatin significantly enhanced the toxicity of cisplatin under hypoxia. *Cyclo-CLLFVY* peptide inhibits HIF-1α activity through inhibition of it is dimerization with HIF-1β and have no effect on the protein level of HIF-1α (361). However, HIF-1α siRNA treatment results in reduction at the protein level. It is worthy to note that HIF-1α protein level increases under hypoxia due to inhibition of its degradation and no change happens at the mRNA level under hypoxia. Additionally the siRNA treatment may not have long lasting effect due to long halftime of HIF-1α mRNA (12 to 19 hours in different cell lines (375, 376)). Lastly, the absence of a protein, or an extreme reduction in quantity, may alter cellular structures and pathway functions. That was the case shown in chapter 4 where downregulation of HIF-1α using siRNA under hypoxia resulted in regained expression of c-Myc. Although we have ruled out the role of c-Myc as a major player in HICR to cisplatin, other compensatory mechanisms could have happened in the absence of HIF-1α protein and altered the results.

In the chapter 3, we provided evidence for the significant role of STAT3 in HICR to cisplatin. Therefore, expectedly combined inhibition of STAT3 and HIF-1α using both inhibitors substantially enhanced the cisplatin toxicity, suggesting that STAT3 and HIF-1α contribute in HICR in parallel and not the same pathways, keeping with the concept that chemoresistance is a multifactorial phenomenon.

6.5 Conclusion

Chemoresistance is a multifactorial phenomenon with various underlying mechanisms. Rational therapeutic drug combination of sensitizing drugs with other therapies should be used to overcome drug resistance. Our results showed, the potency of conventional (i.e., cisplatin) and nano-chemotherapeutics (i.e., cisplatin micelles) can be enhanced under hypoxia once major cellular and molecular players of hypoxia-induced chemoresistance (i.e., HIF-1α and STAT3) were identified and appropriate inhibitors of these signaling pathways were used in combination with the different formulations of cisplatin. Additionally, the modification of cisplatin micelles with EGFR ligand (i.e. GE11 peptide) compensated for the hypoxia-mediated reduced cisplatin uptake, and GE11 micelles showed similar drug uptake under both hypoxic and normoxic conditions.

6.6 Acknowledgments

This study was supported by grants from Natural Sciences and Engineering Research Council of Canada (NSERC) and Canadian Institute of Health Research (CIHR). HSA acknowledges funding from Alberta Cancer Foundation (ACF) and Women and Children Health Research Institute (WCHRI). The authors would like to thank Dr. X. Chris Le, and Ms. Xiufen Lu, Department of Laboratory Medicine and Pathology for their technical assistance with ICP-MS.

6.7 Supplementary Information

A)

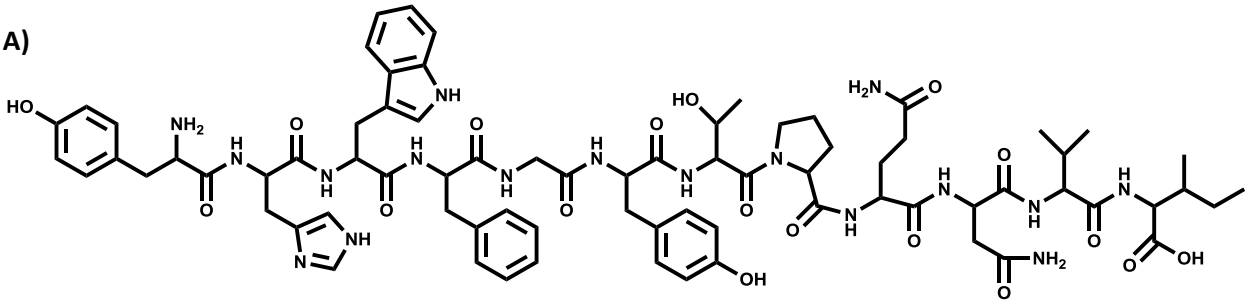

B)

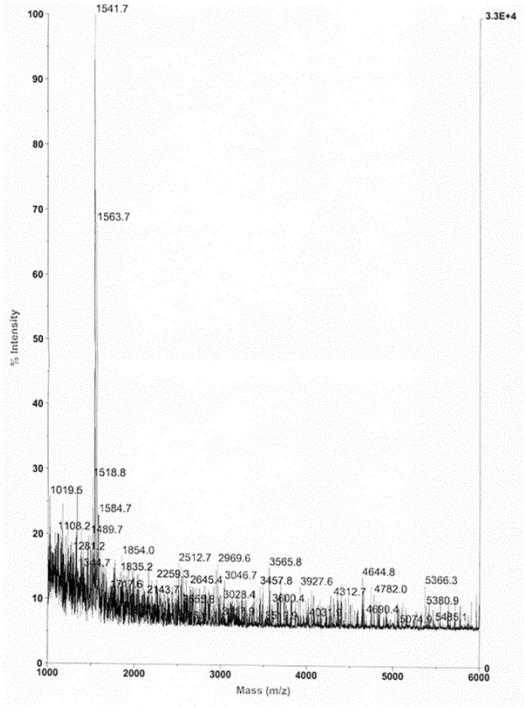

Figure 6.S1 (a) GE11 peptide structure. **(b)** MALDI-MS spectrum of GE11 peptide.

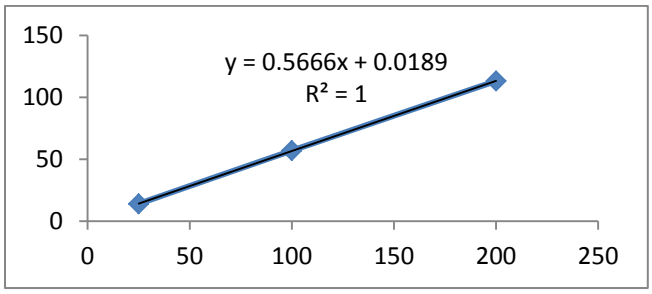

Figure 6.S2 Calibration curve for free GE11-amide (25-250) µg/mL.

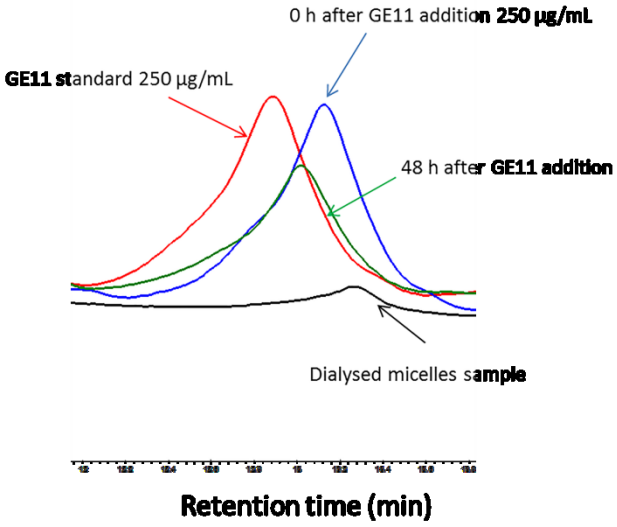

Figure 6.S3 Monitoring GE11-amide conjugation to acetal-PEO-PCCL polymers using HPLC-UV chromatography.

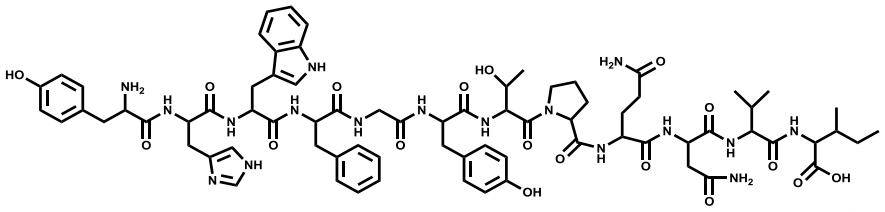

GE11 peptide

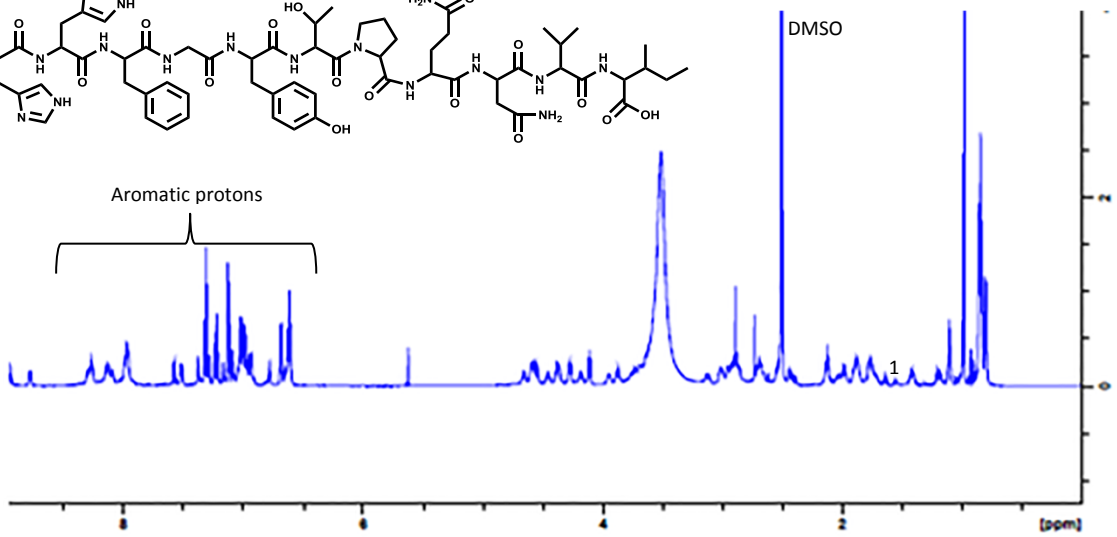

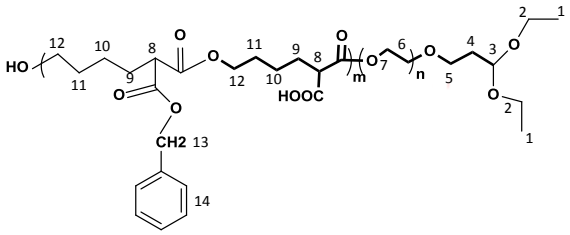

PCCL-PEO-acteal (with 87% reduction of PBCL groups)

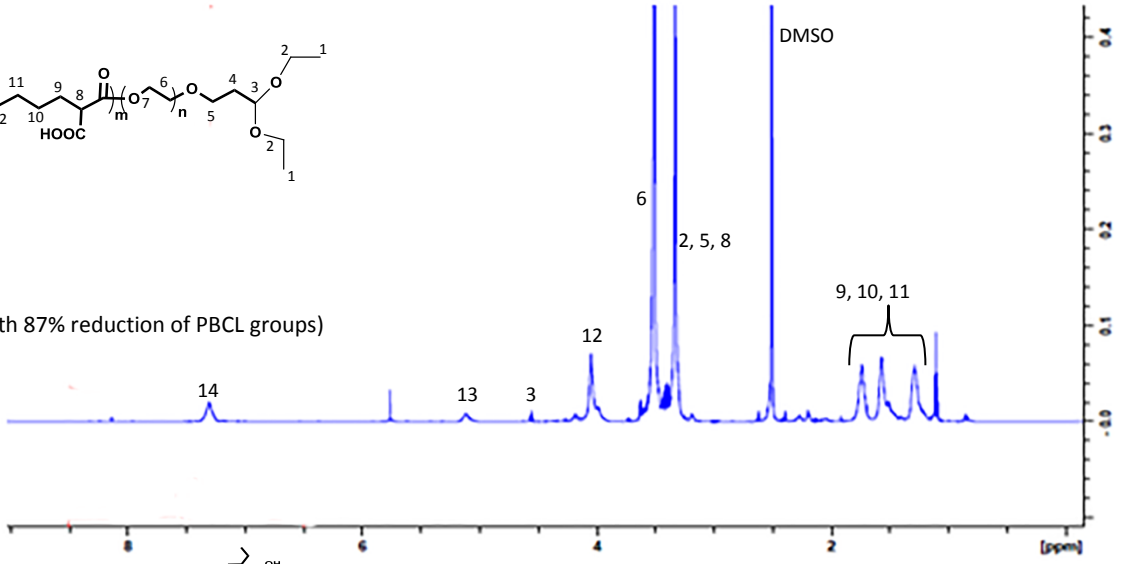

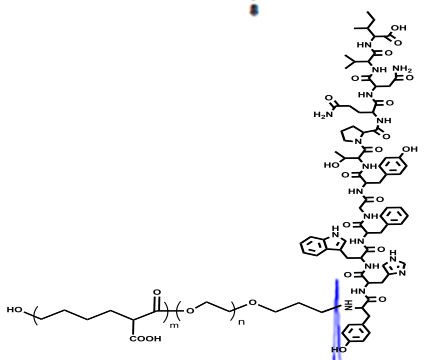

PCCL-PEO-GE11 amide

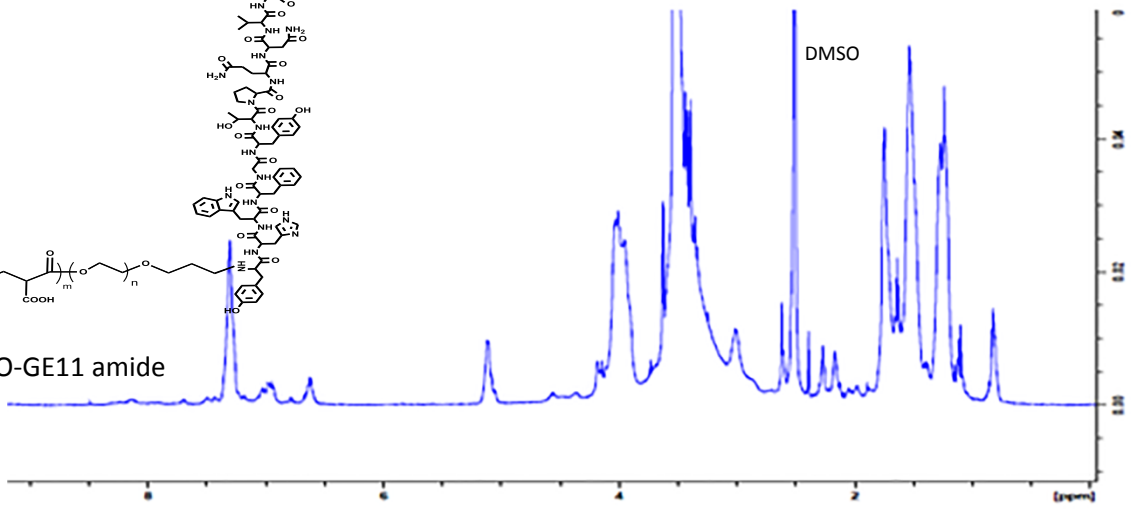

Figure 6.S4 The conjugation of GE11-amide onto acetal-PEO-PCCL was confirmed by ^{1}H-NMR spectra of block copolymer before and after peptide conjugation. Samples (3-5 mg/mL) of PCCL-PEO-acetal and PCCL- PEO-GE11-amide were prepared in DMSO for ^{1}H NMR analysis. Under these conditions, aromatic proton signals for GE11-amide (δ 6.5 to 8.5) were observed in addition to the phenyl proton (δ 7.5) which was shown in the PCCL-PEO-acetal spectrum as well.

Signals from 6.5 to 8.5 ppm in ^{1}H NMR spectra of GE11 peptide correspond to aromatic protons in its structure (n=20). To calculate the molar conjugation % for GE11-conjugated PEO-PCCL block polymer, first the summation of integration of peaks from 6.5 to 8.5 ppm in PCCL-PEO-acetal spectra was subtracted from the summation of integration of peaks from 6.5 to 8.5 ppm in PCCL-PEO-GE11-amide spectra. The obtained value corresponded to integration of aromatic hydrogens of GE11 peptide (n=20). The degree of conjugation of GE11 then determined from spectra of PCCL-PEO-GE11-amide by examining the peak intensity ratio of methylene protons of PCCL segment ($OC\underline{H_2}CH_2CH_2CH_2$ (COOH)CO): δ = 4.1 ppm) and the value calculated for the integration of aromatic hydrogens of GE11 peptide of PCCL-PEO-GE11-amide. The calculated degree of conjugation was 0.45 which corresponds to 45% conjugation efficiency. This means there is around 45 mole peptide per 100 mole block copolymers.

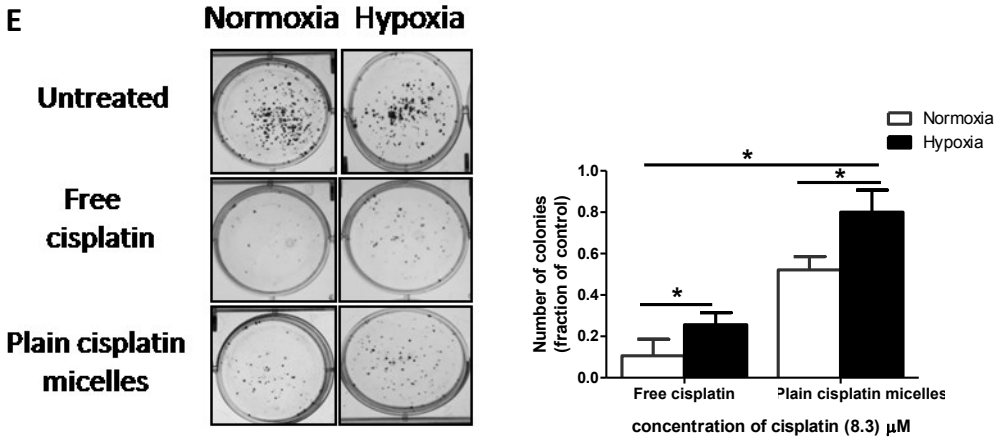

Figure 6.S5 Hypoxia confers chemoresistance to cisplatin in MDA-MB-231 cells. Clonogenic survival assay was conducted for cells treated with cisplatin as free drug or plain cisplatin micelles (8.3 μM) under hypoxia or normoxia (24 hours) in duplicate with plating of 500 cells. The number of colonies formed (% of control) from 500 cells was graphed. Data are represented as mean ± SD (n=3). (*) denotes a significant difference between hypoxic and normoxic groups (Student's t test, $p<0.05$).

Chapter Seven

General Discussion, Conclusion, and Future Directions

7.1 General Discussion

Treatment of many types of cancer has improved dramatically over the past two decades and the cancer death rate has been decreasing steadily. Still, many challenges remain in the pursuit of a cancer cure. One key issue concerns resistance towards chemotherapy. Chemoresistance is the development of a phenotype resistant to a variety of structurally and functionally distinct anticancer drugs which results in treatment failure. Broadly, the underlying reasons for most cases of chemotherapy failure can be classified into three categories: inadequate pharmacokinetic properties of the drug, tumor cell intrinsic resistance and tumor microenvironment related factors (2, 3). Evidence of many different mechanisms of chemoresistance have been reported in the literature, however it remains a great challenge to delineate the pathways involved, and subsequently develop therapies to combat and overcome chemoresistance. The purpose of this thesis was to develop alternate mechanisms to overcome chemoresistance.

In the first two chapters of this thesis (Chapter 2 and 3) we focused on a rational design and development of polymeric micelles with suitable physicochemical and functional properties to improve the pharmacokinetic of drugs. Polymeric micelles are core–shell nano-structures that are widely used for the delivery of hydrophobic drugs to tumors, while avoiding nonselective distribution of the drug to healthy tissues; however the low stability of these nano-carriers is a major barrier in their systemic administration. Often premature drug release occurs after systemic administration of these systems because micelles cannot retain their integrity upon introduction to infinite dilution in blood circulation(223). Modification of micellar core-forming block is a popular approach for enhancement of micellar stability, and mostly attempted through chemical modification of the core (224).

We intended to enhance the micellar stability by increasing the rigidity of core-forming block through induction of crystallinity. The stereoregularity of polymers as building blocks of micelles is believed to affect the arrangement and compactness of the polymer chains within the micellar structure, hence affecting properties like morphology, stability, drug loading, as well as drug release profile (28-32). Stereoregular polymers have a higher likelihood of crystallization in the polymer bulk. On the other hand, atactic polymers make polymeric materials with a higher percentage of amorphous structure. Previous studies have shown an effect of poly(lactide) (PLA) stereoregularity on the formation of semicrystalline regions (225). Thus, for our study polymeric micelles with a PLA segment were suitable candidates to assess the effect of polymerization method (bulk versus solution polymerization) on the crystalline structure of the core-forming block. Accordingly, AB diblock copolymers of poly(ethylene

oxide)-PLA (PEO-PLA) block copolymers containing L-, meso D/L and racemic lactide were synthesized and the effect of polymerization method on the crystallinity of core-forming and its eventual influence on the properties of resulted polymeric micelles was studied. To minimize the detrimental effect of high temperature on stereoregularity and gain more control over stereochemistry of polymer backbone, method of polymerization was changed from bulk to solution. Since solution polymerization employs lower temperatures during reaction, the stereoregularity of produced polymers preserved better. Application of solution polymerization instead of bulk polymerization favored the crystallization of the PLA segment in stereoregular core-forming block micelles, *i.e.*, PEO-PLLA micelles and a positive correlation between higher degree of crystallinity of the core-forming block and kinetic stability of these stereoregular micelles was shown. Nonetheless, the improved micellar stability did not translate to a reduced rate of drug release and we observed a more rapid release of our model drug (nimodipine) from polymeric micelles with semicrystalline cores (PLLA-based micelles) at high loaded drug levels. We attributed this observation to the fast formation of PEO-PLLA micelles due to presence of semicrystalline PLLA core-forming blocks which prevent the uniform dispersion of the drug in the micellar core. In this case, the drug may be squeezed out of the core and eventually accumulate in the surrounding regions (core/shell interface or the shell) and release with a rapid rate from micelles. In contrast, PEO-PDLLA copolymers that have less crystalline core-forming structure may allow for better drug loading within the micellar core and subsequently showed slower rate of drug release. As for the effect of polymerization method on rate of drug release, higher release of nimodipine from micelles was observed when polymers were prepared by solution polymerization compared to those prepared by the bulk method. This was also attributed to higher stereoregularity of core-forming blocks in polymers prepared in solution than bulk.

Although enhancing the stability of the micellar structure is a crucial step to ascertain that the encapsulated drug will be kept within the nano-carrier, it is not sufficient. Release of the drug from the micellar carrier must also be controlled to attain sustained drug release and/or insure the same fate for the incorporated drug and the micellar carrier for the purpose of targeted drug delivery. In an effort to achieve micelles with enhanced stability as well as sufficient drug encapsulation and appropriate drug release profile, we exploited the design and development of ABC triblock copolymer micelles by addition of a third block to our AB diblock copolymer. For development of this ABC three layered micelles, the C block was selected from a relatively drug compatible polymer for efficient solubilization of our drug nimodipine. The B block, on the other hand, was selected from a drug incompatible polymer segment to

provide a barrier against drug release. The A block was expected to make the micellar shell, interfacing the media.

Poly(α-benzyl-ε-caprolactone) (PBCL) and poly(ε-caprolactone) (PCL), were used as the "C" block to form the micellar inner core because of their excellent solubilization of nimodipine(227). PLA, was used as the "B" block to form the micellar outer core acting as a nano-membrane controlling the rate of drug release based on its non-miscibility with the drug (226). With this design in mind, we expected that drug miscible block at the inner core to increase drug loading and encapsulation efficiency while drug immiscible block to reduce the initial burst release of drug from the inner core. During this study, stereocomplex polymeric micelles were also prepared to sustain drug release using 1:1 molar blends of oppositely orientated stereoregular block copolymers (PLLA: PDLA containing diblock). Stereocomplexation of the opposite stereoregularity of the B block was only observed in mixed AB block copolymer micelles and was not evident in either of the ABC block copolymer micelles, perhaps because of the interaction of inner (C block) and outer core (B block) segments within the micellar structure. Overall, two different designs were shown to be successful in reducing drug release from polymeric micelles: a) ABC type polymeric micelles; and b) stereocomplex mixed micelles from diblock copolymers. Stereocomplex mixed micelles of diblock copolymers reduced drug release at the later time points of the release, whereas ABC polymeric micelles reduced burst release at the early time points.

In general, ABC block copolymer micelle showed their superiority in reduction of the burst release of drug from micelles while providing higher encapsulation efficiency than micelles made from AB diblock copolymers. ABC triblock copolymer micelles were also shown to have improved thermodynamic stability compared to their diblock copolymer counterparts, but their kinetic stability in the presence of sodium dodecyl sulfate (SDS) was lower to that of diblock copolymer micelles. It remains to be seen as to which of these factors (kinetic/thermodynamic stability and/or drug release rate and profile) play a more crucial role in defining the final pharmacokinetic of the carrier as well as the encapsulated drug in a biological system following *in vivo* administration. In this study, we were unable to preserve the stereoregularity of the outer core of ABC polymeric micelles perhaps because of the interaction of inner (C block) and outer core (B block) segments within the micellar structure. As a result, no notable effect for the stereoregularity of the B block on the micellar stability, drug loading level and release profile in the ABC block copolymer micelles was observed.

In chapters 4 and 5, we approached the problem of chemoresistance from a different angle and studied the effect of tumor microenvironment factors with special attention to hypoxia. The tumor niche or

microenvironment is a complex network of cells, signaling molecules, soluble factors, and the extracellular matrix that plays a crucial role in tumor development, metastasis, and response to therapy (377). Our aim was to understand the mechanism underlying hypoxia-induced chemoresistance (HICR) in triple negative breast cancer (TNBC), since TNBC tumors are known to frequently carry a hypoxic phenotype and Hypoxia Inducible Factor-1α (HIF-1α) is known to be frequently over-expressed in these tumors (231). We employed an experimental model in which a TNBC cell line, MDA-MB-231, was treated with cisplatin, which is a front-line chemotherapeutic agent used to treat TNBC patients (231, 232). Consistent with the published results of several studies using a variety of cancer cell lines and cisplatin under hypoxic condition (228, 287, 299-301), we found that hypoxia significantly induced cisplatin resistance in MDA-MB-231 cells. Importantly, these findings correlated with reduced cellular uptake of cisplatin and increased stem-like features in these cells, as evidenced by the significant increase in the expression level of ABC transporters and the significantly higher proportions of cells expressing $CD44^{+}/CD24^{-}$, a well-known marker to be associated with cancer stemness in TNBC (291). Hypoxia-induced increases in stem-like features have been described in previously published studies of human cancer cells (302, 303). Overall, we believe that our experimental model was valid and appropriate to study HICR in cancer cells.

In our next studies, involvement of activator of transcription 3 (STAT3) molecules in addition to HI-1α as mediators of HICR to cisplatin treatment was shown. HIF-1α is considered to be a major factor in HICR (122-133, 163). Our findings regarding the major role of HIF-1α in HICR was however rather unexpected. Specifically, while we found that HIF-1α was effectively upregulated by hypoxia, siRNA knockdown of this protein did not significantly modulate the level of chemoresistance. Our findings suggest that STAT3 (an oncoprotein strongly implicated in chemoresistance in cancer cells), instead of HIF-1α, is the key player of HICR in TNBC. High activation of STAT3 under hypoxia may confer HICR by upregulating ABC drug transporters, particularly ABCC2 and ABCC6, both of which have been implicated in cisplatin resistance in other cancer cell types (296, 297).

Importantly, we provided a biochemical basis for assumption of stem-like features by cancer cells under hypoxia and showed how hypoxia can exploit tumor cell plasticity and mediate the generation of intratumoral heterogeneity using our MDA-MB-231 *in vitro* model. In this model, a small subset of highly tumorigenic/stem-like cells can be differentiated from the bulk cell population based on their differential responsiveness to Sox2 reporter (SRR2) with GFP and luciferase as the readouts. Reporter

responsive (RR) cells are more tumorigenic/stem-like as compared to reporter unresponsive (RU) cells (235-237).

Tumors often contain heterogeneous populations of cancer cells. The origins of intratumoral heterogeneity have been highly debated and different cellular mechanisms have been hypothesized to account for the diversity within a tumor. The clonal evolution theory, proposed cancer to be an evolutionary process where most tumor tissues arise from a single cell of origin, and tumor progression results from a stepwise acquisition of mutations within the original clone allowing sequential selection of more aggressive sub-clones. According to this theory, cells in the dominant sub-clone populations would possess similar tumorigenic potential (378). The second theoretically opposing hypothesis is the cancer stem cell (CSC) paradigm. Unlike clonal evolution, where sub-clones possess tumorigenic potential, the CSC hypothesis postulates that only small subpopulations of the tumor, the CSCs, are capable of self-renewal and have the potential to give rise to a tumor and the rest of the tumor consists of cells with limited proliferation and tumorigenic potential (341). Adding to this multifaceted heterogeneity are the continuously changing extracellular influences which provides a niche for CSC plasticity. The concept of CSC plasticity in which cancer cells harbor the dynamic ability of shifting from a non-CSC state to a CSC state and vice versa may be modulated by specific microenvironmental signals such as hypoxia. Hypoxia as a common feature of tumor microenvironments has been implicated in the promotion of CSC plasticity and sustainability of CSC in their undifferentiated stem cell state (233). Our obtained results also showed that hypoxic challenge induced the assumption of stem-like features in the cells and consistently converted a small subset of RU cells (with low tumorigenic/stem-like potential) into RR cells (with high tumorigenic/stem-like potential). When RU cells were subjected to hypoxia, a subset of RU cells (*i.e.*, converted RR cells) emerged and became detectable based on the expression of GFP and luciferase. The association between the RR phenotype and stem-like features in this subset was evidenced by the observation that converted RR cells exhibited significantly higher colony formation capacity, chemoresistance to cisplatin, and a higher proportion of cells carrying the $CD44^{+}/CD24^{-}$ immunophenotype.

The primary drivers of the hypoxic phenotype in different human cancer models are HIF-related transcription factors (*i.e.*, HIF-1α and HIF-2α) (233). HIF-independent drivers of the hypoxic phenotype in cancer cells are rarely reported and include chromatin remodeling histone demethylases (*i.e.,* JARID1B and MLL1) (233). However, siRNA knockdown of HIF-1α in our model did not inhibit the emergence of hypoxic phenotype, as we observed the acquisition of stem-like features in converted RR cells. Our

findings suggested a model that STAT3 activation rather than HIF-1α played a key role in the acquisition of stem-like features. To support the direct role of pSTAT3 in RU/RR conversion under hypoxia, we found that converted RR cells and native RR cells had a similar level of pSTAT3, which is higher than that of RU cells. We also found substantially more STAT3 pulled down with SRR2 probe in converted RR cells as compared to RU cells. The specificity of this binding was further confirmed in the presence of STAT3 inhibitor (stattic) (323). Furthermore, siRNA knockdown of STAT3 substantially blocked the RU/RR conversion, and this inhibition reversed the chemoresistance to cisplatin. In summary, we showed that some cancer cells are not static, but rather have a transient nature and acquire stem-like properties under hypoxia.

The data reviewed herein described the complexities of TNBC cancer and highlighted the need for more comprehensive therapeutic strategies that address and target the multiple stages and branches of a single tumor. Therefore, in the last chapter, we investigated the potential of using targeted-polymeric micelles for enhancing a drug efficacy by overcoming chemoresistance in the setting of hypoxia. Since coexistence of hypoxia and high level of epidermal growth factor receptor (EGFR) expression has been shown in different type of cancers including TNBC (238-240), the EGFR-targeted cisplatin micelles for enhanced cisplatin delivery under hypoxia were developed. GE11 peptide (YHWYGYTPQNVI), an EGFR-targeting ligand (241), was conjugated to the benzyl carboxylate derivative of PEO-PCL (*i.e.*, PEO-PCCL) based micelles for selective cisplatin delivery to hypoxic MDA-MB-231 cells. Decoration of micelles with GE11-peptide increased the cisplatin cellular uptake under hypoxia. However, we did not find a better toxicity with GE11-cisplatin micelles over non-decorated micelles under hypoxias.

We then investigated the combination of free and micellar cisplatin with inhibitors of cellular pathways involved in hypoxia-induced tumorigenic conversion and chemoresistance against cisplatin in MDA-MB-231 cells (STAT3 and HIF-1α). Our results showed that combined inhibition of STAT3 and HIF-1α using both inhibitors substantially enhanced the cisplatin toxicity, suggesting that STAT3 and HIF-1α contribute in HICR in parallel and not the same pathways; keeping with the concept that chemoresistance is a multifactorial phenomenon.

Evidence of many different mechanisms of chemoresistance have been reported in the literature and there is significant support for the role of CSCs in therapeutic resistance and tumor recurrence (379, 380). CSC plasticity induced by microenvironmental signals may limit the effect of treatments even furtherer. Therapies targeting CSCs would also be only temporarily effective in eliminating this population since new CSCs may arise from non-CSCs left untargeted. Therefore, targeting each

subpopulation or sub-clone within the tumor should be considered for a successful clinical response to become achievable. It is possible that some compounds could be used to induce differentiation of CSCs in combination with drugs that would target the newly-differentiated cells. Novartis is currently testing a compound, LGK974, for its ability to inhibit Wnt signaling (one of the main CSC- inducing signaling pathways) (381). One caveat of these therapies is the fact that the pathways they target are not exclusive to CSCs but are shared with normal stem cells. Identifying a threshold of killing activity of normal cells will be necessary to prevent deleterious effects. Additionally, it is unlikely that a single pathway will be operative in all of the CSCs in a given tumor; therefore, concurrent use of drugs that can affect multiple pathways that are essential to CSCs-mediated plasticity are likely to be obligatory to achieve effective therapies.

7.2 Conclusion

Stereoregularity of polymers is known to influence their physicochemical and functional properties in the bulk form. In our studies, we have provided evidence for the effect of polymer stereoregularity on the physicochemical and functional properties of their self-assembled micelles such as size, morphology, thermodynamic and kinetic stability, drug loading and release. In this context, the results of our conducted studies appeared to point to a better kinetic stability for block copolymers of higher stereoregularity in the core-forming block (which can form cores of higher crystallinity) compared to those with atactic (or amorphous) cores. Studying the effect of core stereoregularity and crystallinity on the level of drug loading in polymer micelles, as well as a drug release profile, provided us with clues towards the design of optimized micellar carriers that simultaneously maintain high drug content and slow release properties. This was the foundation for the rational design and development of three layered ABC micelles with drug compatible blocks at the inner core and drug incompatible blocks at the outer core to sustain the rate of drug release while providing high amount of drug encapsulated in the core.

To test the applicability of our nano-carriers for overcoming drug resistance, we developed and validated an experimental hypoxia-induced-chemoresistant TNBC model. Importantly, we provided a biochemical basis for assumption of stem-like features including chemoresistance by cancer cells under hypoxia. We have provided evidence that STAT3 activation under hypoxia is an important mediator for HICR, and in assumption of stem-like phenotype by bulk of cancer cells. Furthermore, we exploited the coexistence of hypoxia and high level of EGFR expression and investigated the potential of using nano-carriers for overcoming HICR by developing the EGFR-targeted cisplatin micelles. Decoration of micelles

with GE11-peptide, an EGFR-targeting ligand, increased the cisplatin cellular uptake under hypoxia; however it did not enhance the profile of toxicity of the cisplatin micelles. Lastly, we investigated the effect of combination of free and micellar cisplatin with inhibitors of cellular pathways involved in hypoxia-induced tumorigenic conversion and chemoresistance against cisplatin in MDA-MB-231 cells (STAT3 and HIF-1α). Our results showed that combined inhibition of STAT3 and HIF-1α using both inhibitors substantially enhanced the cisplatin toxicity, suggesting that STAT3 and HIF-1α contribute in HICR in parallel and not the same pathways; keeping with the concept that many different mechanisms are involved in chemoresistance.

Chemoresistance is a multifactorial phenomenon with various underlying mechanisms, such as inadequate pharmacokinetic properties of the drug, tumor microenvironment related factors and tumor cell intrinsic resistance. Rational therapeutic drug combination of sensitizing drugs with other therapies should be used to overcome drug resistance by simultaneous sensitization of cancer cells to chemotherapeutics while delivering a high payload of drug.

7.3 Future Directions

In this thesis we provided a foundation for the rational design and selection of micellar core segments based on miscibility of drug/core (predicted by Flory Huggins interaction parameter) to sustain a drug release as well as increase the drug content. The feasibility of this design was supported in our developed three-layered ABC micelles with nimodipine as a model drug (226). Future studies on the development of similar models for the production of effective drug delivery systems for different drugs can also be investigated.

We are also interested to study the effect of stereoregularity of core-forming block on pharmacokinetic behaviors of drug-loaded micelles. As such, *in vivo* studies of micelles with different stereochemistry of core-forming block can be designed in mice-bearing tumors to investigate tissue distribution, tumor accumulation and antitumor activity of chemotherapeutic agent, similar to studies done by Kataoka *et. al.* (50).

Herein, using our MDA-MB-231 *in vitro* model which, a small subset of highly tumorigenic/stem-like cells can be differentiated from the bulk cell population based on their differential responsiveness to Sox2 reporter (SRR2) with GFP and luciferase as the readouts (236), we also provided an example of how hypoxia induced plasticity in TNBC. We showed that RU cells (non-stem-like cells) converted to RR cells (stem-like cells) under hypoxia and this conversion was mediated by STAT3 activation. Complementary

studies may be warranted to elucidate the molecular links between STAT3 and cancer stem cell (CSC) phenotype to show how STAT3 play a role in the development of the CSC state under hypoxia. For instance, which core stem cell genes in TNBC are regulated by activation of STAT3 under hypoxia, resulting in increased cancer stemness and tumorigenic potential. Previous studies have highlighted the role of cytokines and growth factors (*e.g.*, IL-4, IL-6, Oncostatin M, IL-10, TNFα , ILEI, IFNɣ and VEGF) on the pathways that govern CSC plasticity (339), therefore it remained to be seen whether activation of STAT3 regulates cytokine/growth factors-driven tumor cell plasticity and if so which cytokines/growth factors are involved. Another important area we are considering is to investigate the role of STAT3 signaling pathway in induction of a CSC phenotype in other TNBC models under hypoxia, investigating the universal role of STAT3 in TNBC under hypoxia.

Furthermore, in support of our hypothesis that cancer stem cell plasticity is driven by STAT3 in TNBC under hypoxia, we are planning to detect the expression and distribution of STAT3, as well as its co-localization with HIF-1α (or other hypoxia marker such as CA IX) in tumor samples from TNBC patients, using paraffin-embedded TNBC archival tumor samples immunohistochemistry. We anticipate that high STAT3 expression or co-localization of STAT3/HIF-1α correlates with worse clinical outcomes, such as poor overall survival rate.

Looking at the unsuccessful *in vitro* results of the GE11-ciplatin micelles in decreasing cisplatin toxicity, in spite of their enhanced cellular uptake under hypoxia we are now interested in investigating the underlying reasons for such discrepancy. Upon resolving this issue, we can further study the pharmacokinetic behaviors of GE11-cisplatin micelle in combination with inhibitors of STAT3 and HIF-1α. As such, *in vivo* studies of GE11-cisplatin micelles can be designed in mice-bearing EGFR-positive versus EGFR-negative tumors to investigate tissue distribution, tumor accumulation and antitumor activity of cisplatin.

References

1. H. Soleymani Abyaneh, M.R. Vakili, A. Shafaati, and A. Lavasanifar. Block Copolymer Stereoregularity and Its Impact on Polymeric Micellar Nanodrug Delivery. Mol Pharm (2017).
2. L. Gattiand F. Zunino. Overview of tumor cell chemoresistance mechanisms. Methods Mol Med. 111:127-148 (2005).
3. M.M. Gottesman. Mechanisms of cancer drug resistance. Annu Rev Med. 53:615-627 (2002).
4. H.R. Mellorand R. Callaghan. Resistance to chemotherapy in cancer: a complex and integrated cellular response. Pharmacology. 81:275-300 (2008).
5. J. Lankelma. Tissue transport of anti-cancer drugs. Curr Pharm Des. 8:1987-1993 (2002).
6. L. Milane, S. Ganesh, S. Shah, Z.F. Duan, and M. Amiji. Multi-modal strategies for overcoming tumor drug resistance: hypoxia, the Warburg effect, stem cells, and multifunctional nanotechnology. J Control Release. 155:237-247 (2011).
7. S. Hedeand N. Huilgol. "Nano": the new nemesis of cancer. J Cancer Res Ther. 2:186-195 (2006).
8. V.V. Pokropivnyand V.V. Skorokhod. New dimensionality classifications of nanostructures. Physica E: Low-dimensional Systems and Nanostructures. 40:2521-2525 (2008).
9. S.M. Moghimi, A.C. Hunter, and J.C. Murray. Nanomedicine: current status and future prospects. FASEB J. 19:311-330 (2005).
10. S.H. Jang, M.G. Wientjes, D. Lu, and J.L. Au. Drug delivery and transport to solid tumors. Pharm Res. 20:1337-1350 (2003).
11. Y. Matsumuraand H. Maeda. A new concept for macromolecular therapeutics in cancer chemotherapy: mechanism of tumoritropic accumulation of proteins and the antitumor agent smancs. Cancer Res. 46:6387-6392 (1986).
12. H. Maeda, J. Wu, T. Sawa, Y. Matsumura, and K. Hori. Tumor vascular permeability and the EPR effect in macromolecular therapeutics: a review. Journal of Controlled Release. 65:271-284 (2000).
13. H. Maeda, K. Greish, and J. Fang. The EPR Effect and Polymeric Drugs: A Paradigm Shift for Cancer Chemotherapy in the 21st Century. In R. Satchi-Fainaroand R. Duncan (eds.), Polymer Therapeutics II, Springer Berlin Heidelberg, Berlin, Heidelberg, 2006, pp. 103-121.
14. O. Tredan, C.M. Galmarini, K. Patel, and I.F. Tannock. Drug resistance and the solid tumor microenvironment. J Natl Cancer Inst. 99:1441-1454 (2007).
15. A. Vermaand F. Stellacci. Effect of surface properties on nanoparticle-cell interactions. Small. 6:12-21 (2010).
16. U. Cavallaroand G. Christofori. Multitasking in tumor progression: signaling functions of cell adhesion molecules. Ann N Y Acad Sci. 1014:58-66 (2004).
17. L.E. van Vlerken, T.K. Vyas, and M.M. Amiji. Poly(ethylene glycol)-modified nanocarriers for tumor-targeted and intracellular delivery. Pharm Res. 24:1405-1414 (2007).
18. J.H. Lee, H.B. Lee, and J.D. Andrade. Blood compatibility of polyethylene oxide surfaces. Progress in Polymer Science. 20:1043-1079 (1995).
19. V.P. Torchilinland M.I. Papisov. Why do Polyethylene Glycol-Coated Liposomes Circulate So Long?: Molecular Mechanism of Liposome Steric Protection with Polyethylene Glycol: Role of Polymer Chain Flexibility. Journal of Liposome Research. 4:725-739 (1994).
20. S. Kommareddy, S.B. Tiwari, and M.M. Amiji. Long-circulating polymeric nanovectors for tumor-selective gene delivery. Technol Cancer Res Treat. 4:615-625 (2005).
21. A. Jhaveri, P. Deshpande, and V. Torchilin. Stimuli-sensitive nanopreparations for combination cancer therapy. Journal of Controlled Release. 190:352-370 (2014).
22. S. Ganta, H. Devalapally, A. Shahiwala, and M. Amiji. A review of stimuli-responsive nanocarriers for drug and gene delivery. J Control Release. 126:187-204 (2008).

23. A.C. Anselmoand S. Mitragotri. Nanoparticles in the clinic. Bioengineering & Translational Medicine. 1:10-29 (2016).
24. H.S. Abyaneh, M.R. Vakili, F. Zhang, P. Choi, and A. Lavasanifar. Rational design of block copolymer micelles to control burst drug release at a nanoscale dimension. Acta biomaterialia. 24:127-139 (2015).
25. E. Oledzka, P. Horeglad, Z. Gruszczyńska, A. Plichta, G. Nałęcz-Jawecki, and M. Sobczak. Polylactide conjugates of camptothecin with different drug release abilities. Molecules. 19:19460-19470 (2014).
26. G. Odian. Principles of polymerization, John Wiley & Sons, 2004.
27. R.H. Platel, L.M. Hodgson, and C.K. Williams. Biocompatible initiators for lactide polymerization. Polymer Reviews. 48:11-63 (2008).
28. L. Izzo, P.C. Griffiths, R. Nilmini, S.M. King, K.-L. Wallom, E.L. Ferguson, and R. Duncan. Impact of polymer tacticity on the physico-chemical behaviour of polymers proposed as therapeutics. International journal of pharmaceutics. 408:213-222 (2011).
29. T. Akagi, Y. Zhu, F. Shima, and M. Akashi. Biodegradable nanoparticles composed of enantiomeric poly (γ-glutamic acid)-graft-poly (lactide) copolymers as vaccine carriers for dominant induction of cellular immunity. Biomaterials Science. 2:530-537 (2014).
30. L. Chen, Z. Xie, J. Hu, X. Chen, and X. Jing. Enantiomeric PLA–PEG block copolymers and their stereocomplex micelles used as rifampin delivery. J Nanopart Res. 9:777-785 (2007).
31. H.S. Abyaneh, M.R. Vakili, and A. Lavasanifar. The effect of polymerization method in stereo-active block copolymers on the stability of polymeric micelles and their drug release profile. Pharmaceutical research. 31:1485-1500 (2014).
32. L.-E. Chile, P. Mehrkhodavandi, and S.G. Hatzikiriakos. A Comparison of the Rheological and Mechanical Properties of Isotactic, Syndiotactic, and Heterotactic Poly (lactide). Macromolecules. 49:909-919 (2016).
33. C. Agatemorand M.P. Shaver. Tacticity-Induced Changes in the Micellization and Degradation Properties of Poly (lactic acid)-block-poly (ethylene glycol) Copolymers. Biomacromolecules. 14:699-708 (2013).
34. J. Zhang, L.-Q. Wang, H. Wang, and K. Tu. Micellization phenomena of amphiphilic block copolymers based on methoxy poly (ethylene glycol) and either crystalline or amorphous poly (caprolactone-b-lactide). Biomacromolecules. 7:2492-2500 (2006).
35. C. Garofalo, G. Capuano, R. Sottile, R. Tallerico, R. Adami, E. Reverchon, E. Carbone, L. Izzo, and D. Pappalardo. Different insight into amphiphilic PEG-PLA copolymers: influence of macromolecular architecture on the micelle formation and cellular uptake. Biomacromolecules. 15:403-415 (2014).
36. J. Ding, C. Li, Y. Zhang, W. Xu, J. Wang, and X. Chen. Chirality-mediated polypeptide micelles for regulated drug delivery. Acta Biomater. 11:346-355 (2015).
37. M. Barz, A. Armiñán, F. Canal, F. Wolf, K. Koynov, H. Frey, R. Zentel, and M.J. Vicent. P (HPMA)-block-P (LA) copolymers in paclitaxel formulations: polylactide stereochemistry controls micellization, cellular uptake kinetics, intracellular localization and drug efficiency. Journal of controlled release. 163:63-74 (2012).
38. L. Glavas, P. Olsen, K. Odelius, and A.C. Albertsson. Achieving micelle control through core crystallinity. Biomacromolecules. 14:4150-4156 (2013).
39. K. Fukushima, R.C. Pratt, F. Nederberg, J.P. Tan, Y.Y. Yang, R.M. Waymouth, and J.L. Hedrick. Organocatalytic approach to amphiphilic comb-block copolymers capable of stereocomplexation and self-assembly. Biomacromolecules. 9:3051-3056 (2008).
40. F. Nederberg, E. Appel, J.P. Tan, S.H. Kim, K. Fukushima, J. Sly, R.D. Miller, R.M. Waymouth, Y.Y. Yang, and J.L. Hedrick. Simple approach to stabilized micelles employing miktoarm terpolymers

and stereocomplexes with application in paclitaxel delivery. Biomacromolecules. 10:1460-1468 (2009).
41. L. Yang, Z. Zhao, J. Wei, A. El Ghzaoui, and S. Li. Micelles formed by self-assembling of polylactide/poly (ethylene glycol) block copolymers in aqueous solutions. Journal of colloid and interface science. 314:470-477 (2007).
42. S. Zhao, X. Fan, X. Li, X. Lv, W. Zhang, and Z. Hu. Stable micelles formed through a stereocomplex of amphiphilic copolymers zwitterionic-(PLLA)2 and MPEG-(PDLA)2 for controlled drug delivery. RSC Advances. 6:63597-63606 (2016).
43. M. Nakajima, H. Nakajima, T. Fujiwara, Y. Kimura, and S. Sasaki. Nano-structured micelle particles of polylactide-poly(oxyethylene) block copolymers with different block sequences: Specific influence of stereocomplex formation of the polylactide blocks. Polymer. 66:160-166 (2015).
44. C. Ma, P. Pan, G. Shan, Y. Bao, M. Fujita, and M. Maeda. Core-shell structure, biodegradation, and drug release behavior of poly(lactic acid)/poly(ethylene glycol) block copolymer micelles tuned by macromolecular stereostructure. Langmuir. 31:1527-1536 (2015).
45. Z. Zhao, Z. Zhang, L. Chen, Y. Cao, C. He, and X. Chen. Biodegradable stereocomplex micelles based on dextran-block-polylactide as efficient drug deliveries. Langmuir. 29:13072-13080 (2013).
46. L. Yang, X. Wu, F. Liu, Y. Duan, and S. Li. Novel biodegradable polylactide/poly (ethylene glycol) micelles prepared by direct dissolution method for controlled delivery of anticancer drugs. Pharmaceutical research. 26:2332-2342 (2009).
47. S.H. Kim, J.P. Tan, F. Nederberg, K. Fukushima, Y.Y. Yang, R.M. Waymouth, and J.L. Hedrick. Mixed micelle formation through stereocomplexation between enantiomeric poly (lactide) block copolymers. Macromolecules. 42:25-29 (2008).
48. N. Kang, M.-È. Perron, R.E. Prud'Homme, Y. Zhang, G. Gaucher, and J.-C. Leroux. Stereocomplex block copolymer micelles: core-shell nanostructures with enhanced stability. Nano letters. 5:315-319 (2005).
49. K. Jelonek, S. Li, X. Wu, J. Kasperczyk, and A. Marcinkowski. Self-assembled filomicelles prepared from polylactide/poly(ethylene glycol) block copolymers for anticancer drug delivery. Int J Pharm. 485:357-364 (2015).
50. Y. Mochida, H. Cabral, Y. Miura, F. Albertini, S. Fukushima, K. Osada, N. Nishiyama, and K. Kataoka. Bundled assembly of helical nanostructures in polymeric micelles loaded with platinum drugs enhancing therapeutic efficiency against pancreatic tumor. ACS nano. 8:6724-6738 (2014).
51. W. Zhang, D. Zhang, X. Fan, G. Bai, g. Yuming, and Z. Hu. Stable stereocomplex micelles from Y-shaped amphiphilic copolymers MPEG-(scPLA)2: preparation and characteristics. RSC Advances. 6:20761-20771 (2016).
52. L. Sun, A. Pitto-Barry, N. Kirby, T.L. Schiller, A.M. Sanchez, M.A. Dyson, J. Sloan, N.R. Wilson, R.K. O'Reilly, and A.P. Dove. Structural reorganization of cylindrical nanoparticles triggered by polylactide stereocomplexation. Nature Communications. 5:5746 (2014).
53. S.K. Agrawal, N. Sanabria-DeLong, J.M. Coburn, G.N. Tew, and S.R. Bhatia. Novel drug release profiles from micellar solutions of PLA–PEO–PLA triblock copolymers. Journal of controlled release. 112:64-71 (2006).
54. J. Skey, C.F. Hansell, and R.K. O'Reilly. Stabilization of amino acid derived diblock copolymer micelles through favorable D: L side chain interactions. Macromolecules. 43:1309-1318 (2010).
55. A. Makino, E. Hara, I. Hara, R. Yamahara, K. Kurihara, E. Ozeki, F. Yamamoto, and S. Kimura. Control of in vivo blood clearance time of polymeric micelle by stereochemistry of amphiphilic polydepsipeptides. Journal of controlled release. 161:821-825 (2012).

56. G. Yang, L. Hui, C. Xiujun, J. Hongliang, T. Kehua, and W. Liqun. EFFECT OF DRUG INCORPORATION ON THE MORPHOLOGY OF AMPHIPHILIC BLOCK COPOLYMER MICELLES. Acta Polymerica Sinica. 1:390-394 (2010).
57. J. Gou, S. Feng, H. Xu, G. Fang, Y. Chao, Y. Zhang, H. Xu, and X. Tang. Decreased Core Crystallinity Facilitated Drug Loading in Polymeric Micelles without Affecting Their Biological Performances. Biomacromolecules. 16:2920-2929 (2015).
58. K. Feng, S. Wang, H. Ma, and Y. Chen. Chirality plays critical roles in enhancing the aqueous solubility of nocathiacin I by block copolymer micelles. Journal of Pharmacy and Pharmacology. 65:64-71 (2013).
59. J. Wang, W. Xu, J. Ding, S. Lu, X. Wang, C. Wang, and X. Chen. Cholesterol-Enhanced Polylactide-Based Stereocomplex Micelle for Effective Delivery of Doxorubicin. Materials. 8:216 (2015).
60. A. Makino, E. Hara, I. Hara, R. Yamahara, K. Kurihara, E. Ozeki, F. Yamamoto, and S. Kimura. Control of in vivo blood clearance time of polymeric micelle by stereochemistry of amphiphilic polydepsipeptides. J Control Release. 161:821-825 (2012).
61. L. Kelland. The resurgence of platinum-based cancer chemotherapy. Nat Rev Cancer. 7:573-584 (2007).
62. N.J. Wheate, S. Walker, G.E. Craig, and R. Oun. The status of platinum anticancer drugs in the clinic and in clinical trials. Dalton Trans. 39:8113-8127 (2010).
63. I. Ali, W.A. Wani, K. Saleem, and A. Haque. Platinum compounds: a hope for future cancer chemotherapy. Anticancer Agents Med Chem. 13:296-306 (2013).
64. S. Dasariand P.B. Tchounwou. Cisplatin in cancer therapy: molecular mechanisms of action. Eur J Pharmacol. 740:364-378 (2014).
65. M. Jennerweinand P.A. Andrews. Effect of intracellular chloride on the cellular pharmacodynamics of cis-diamminedichloroplatinum(II). Drug Metab Dispos. 23:178-184 (1995).
66. L.R. Kelland. Preclinical perspectives on platinum resistance. Drugs. 59 Suppl 4:1-8; discussion 37-38 (2000).
67. A. Eastman. The formation, isolation and characterization of DNA adducts produced by anticancer platinum complexes. Pharmacology & Therapeutics. 34:155-166 (1987).
68. S.F. Bellon, J.H. Coleman, and S.J. Lippard. DNA unwinding produced by site-specific intrastrand cross-links of the antitumor drug cis-diamminedichloroplatinum(II). Biochemistry. 30:8026-8035 (1991).
69. Z.H. Siddik. Cisplatin: mode of cytotoxic action and molecular basis of resistance. Oncogene. 22:7265-7279 (2003).
70. Z. Hang, M.A. Cooper, and Z.M. Ziora. Platinum-based anticancer drugs encapsulated liposome and polymeric micelle formulation in clinical trials. Biochemical Compounds. 4:1 (2016).
71. M.G. Ormerod, C. O'Neill, D. Robertson, L.R. Kelland, and K.R. Harrap. cis-Diamminedichloroplatinum(II)-induced cell death through apoptosis in sensitive and resistant human ovarian carcinoma cell lines. Cancer Chemother Pharmacol. 37:463-471 (1996).
72. L. Galluzzi, L. Senovilla, I. Vitale, J. Michels, I. Martins, O. Kepp, M. Castedo, and G. Kroemer. Molecular mechanisms of cisplatin resistance. Oncogene. 31:1869-1883 (2012).
73. L. Amable. Cisplatin resistance and opportunities for precision medicine. Pharmacol Res. 106:27-36 (2016).
74. Y. Matsumuraand K. Kataoka. Preclinical and clinical studies of anticancer agent-incorporating polymer micelles. Cancer Sci. 100:572-579 (2009).
75. H. Cabraland K. Kataoka. Progress of drug-loaded polymeric micelles into clinical studies. J Control Release. 190:465-476 (2014).

76. H. Uchino, Y. Matsumura, T. Negishi, F. Koizumi, T. Hayashi, T. Honda, N. Nishiyama, K. Kataoka, S. Naito, and T. Kakizoe. Cisplatin-incorporating polymeric micelles (NC-6004) can reduce nephrotoxicity and neurotoxicity of cisplatin in rats. Br J Cancer. 93:678-687 (2005).
77. M. Baba, Y. Matsumoto, A. Kashio, H. Cabral, N. Nishiyama, K. Kataoka, and T. Yamasoba. Micellization of cisplatin (NC-6004) reduces its ototoxicity in guinea pigs. J Control Release. 157:112-117 (2012).
78. N. Nishiyama, S. Okazaki, H. Cabral, M. Miyamoto, Y. Kato, Y. Sugiyama, K. Nishio, Y. Matsumura, and K. Kataoka. Novel cisplatin-incorporated polymeric micelles can eradicate solid tumors in mice. Cancer Res. 63:8977-8983 (2003).
79. J.M. Brownand W.R. Wilson. Exploiting tumour hypoxia in cancer treatment. Nat Rev Cancer. 4:437-447 (2004).
80. P. Vaupel. Tumor oxygenation: an appraisal of past and present concepts and a look into the future : Arisztid G. B. Kovach Lecture. Adv Exp Med Biol. 789:229-236 (2013).
81. R.K. Jain. Normalization of tumor vasculature: an emerging concept in antiangiogenic therapy. Science. 307:58-62 (2005).
82. J.C. Walsh, A. Lebedev, E. Aten, K. Madsen, L. Marciano, and H.C. Kolb. The clinical importance of assessing tumor hypoxia: relationship of tumor hypoxia to prognosis and therapeutic opportunities. Antioxid Redox Signal. 21:1516-1554 (2014).
83. P. Vaupeland A. Mayer. Hypoxia in cancer: significance and impact on clinical outcome. Cancer Metastasis Rev. 26:225-239 (2007).
84. R. Sullivanand C.H. Graham. Hypoxia-driven selection of the metastatic phenotype. Cancer Metastasis Rev. 26:319-331 (2007).
85. J. Changand J. Erler. Hypoxia-mediated metastasis. Adv Exp Med Biol. 772:55-81 (2014).
86. P. Friedland S. Alexander. Cancer invasion and the microenvironment: plasticity and reciprocity. Cell. 147:992-1009 (2011).
87. K. Ghattass, R. Assah, M. El-Sabban, and H. Gali-Muhtasib. Targeting hypoxia for sensitization of tumors to radio- and chemotherapy. Curr Cancer Drug Targets. 13:670-685 (2013).
88. B.J. Moeller, R.A. Richardson, and M.W. Dewhirst. Hypoxia and radiotherapy: opportunities for improved outcomes in cancer treatment. Cancer Metastasis Rev. 26:241-248 (2007).
89. R.F. Thompsonand A. Maity. Radiotherapy and the tumor microenvironment: mutual influence and clinical implications. Adv Exp Med Biol. 772:147-165 (2014).
90. M.R. Horsmanand J. Overgaard. The impact of hypoxia and its modification of the outcome of radiotherapy. J Radiat Res (2016).
91. A.J. Majmundar, W.J. Wong, and M.C. Simon. Hypoxia-inducible factors and the response to hypoxic stress. Mol Cell. 40:294-309 (2010).
92. C. Brahimi-Hornand J. Pouyssegur. The role of the hypoxia-inducible factor in tumor metabolism growth and invasion. Bull Cancer. 93:E73-80 (2006).
93. G.L. Semenza. Defining the role of hypoxia-inducible factor 1 in cancer biology and therapeutics. Oncogene. 29:625-634 (2010).
94. G.L. Wang, B.H. Jiang, E.A. Rue, and G.L. Semenza. Hypoxia-inducible factor 1 is a basic-helix-loop-helix-PAS heterodimer regulated by cellular O2 tension. Proceedings of the National Academy of Sciences. 92:5510-5514 (1995).
95. B.H. Jiang, E. Rue, G.L. Wang, R. Roe, and G.L. Semenza. Dimerization, DNA binding, and transactivation properties of hypoxia-inducible factor 1. J Biol Chem. 271:17771-17778 (1996).
96. G.L. Wangand G.L. Semenza. Purification and characterization of hypoxia-inducible factor 1. J Biol Chem. 270:1230-1237 (1995).
97. H. Li, H.P. Ko, and J.P. Whitlock. Induction of phosphoglycerate kinase 1 gene expression by hypoxia. Roles of Arnt and HIF1alpha. J Biol Chem. 271:21262-21267 (1996).

98. K. Yamashita, D.J. Discher, J. Hu, N.H. Bishopric, and K.A. Webster. Molecular regulation of the endothelin-1 gene by hypoxia. Contributions of hypoxia-inducible factor-1, activator protein-1, GATA-2, AND p300/CBP. J Biol Chem. 276:12645-12653 (2001).
99. R.K. Bruickand S.L. McKnight. A Conserved Family of Prolyl-4-Hydroxylases That Modify HIF. Science. 294:1337-1340 (2001).
100. M.S. Wiesener, J.S. Jurgensen, C. Rosenberger, C.K. Scholze, J.H. Horstrup, C. Warnecke, S. Mandriota, I. Bechmann, U.A. Frei, C.W. Pugh, P.J. Ratcliffe, S. Bachmann, P.H. Maxwell, and K.U. Eckardt. Widespread hypoxia-inducible expression of HIF-2alpha in distinct cell populations of different organs. FASEB J. 17:271-273 (2003).
101. A. Pasanen, M. Heikkila, K. Rautavuoma, M. Hirsila, K.I. Kivirikko, and J. Myllyharju. Hypoxia-inducible factor (HIF)-3alpha is subject to extensive alternative splicing in human tissues and cancer cells and is regulated by HIF-1 but not HIF-2. Int J Biochem Cell Biol. 42:1189-1200 (2010).
102. P. Zhang, Q. Yao, L. Lu, Y. Li, P.J. Chen, and C. Duan. Hypoxia-inducible factor 3 is an oxygen-dependent transcription activator and regulates a distinct transcriptional response to hypoxia. Cell Rep. 6:1110-1121 (2014).
103. G.N. Masoudand W. Li. HIF-1alpha pathway: role, regulation and intervention for cancer therapy. Acta Pharm Sin B. 5:378-389 (2015).
104. G.L. Semenza. Regulation of oxygen homeostasis by hypoxia-inducible factor 1. Physiology (Bethesda). 24:97-106 (2009).
105. J.-W. Jeong, M.-K. Bae, M.-Y. Ahn, S.-H. Kim, T.-K. Sohn, M.-H. Bae, M.-A. Yoo, E.J. Song, K.-J. Lee, and K.-W. Kim. Regulation and Destabilization of HIF-1α by ARD1-Mediated Acetylation. Cell. 111:709-720.
106. A. Weidemannand R.S. Johnson. Biology of HIF-1alpha. Cell Death Differ. 15:621-627 (2008).
107. G.L. Semenza. HIF-1: upstream and downstream of cancer metabolism. Curr Opin Genet Dev. 20:51-56 (2010).
108. S. Frede, U. Berchner-Pfannschmidt, and J. Fandrey. Regulation of hypoxia-inducible factors during inflammation. Methods Enzymol. 435:405-419 (2007).
109. R. Ravi, B. Mookerjee, Z.M. Bhujwalla, C.H. Sutter, D. Artemov, Q. Zeng, L.E. Dillehay, A. Madan, G.L. Semenza, and A. Bedi. Regulation of tumor angiogenesis by p53-induced degradation of hypoxia-inducible factor 1alpha. Genes Dev. 14:34-44 (2000).
110. J.S. Isaacs, Y.J. Jung, E.G. Mimnaugh, A. Martinez, F. Cuttitta, and L.M. Neckers. Hsp90 regulates a von Hippel Lindau-independent hypoxia-inducible factor-1 alpha-degradative pathway. J Biol Chem. 277:29936-29944 (2002).
111. N. Rohwer, C. Dame, A. Haugstetter, B. Wiedenmann, K. Detjen, C.A. Schmitt, and T. Cramer. Hypoxia-inducible factor 1alpha determines gastric cancer chemosensitivity via modulation of p53 and NF-kappaB. PLoS One. 5:e12038 (2010).
112. F. Aganiand B.H. Jiang. Oxygen-independent regulation of HIF-1: novel involvement of PI3K/AKT/mTOR pathway in cancer. Curr Cancer Drug Targets. 13:245-251 (2013).
113. G.L. Semenza. Targeting HIF-1 for cancer therapy. Nat Rev Cancer. 3:721-732 (2003).
114. A.J. Primeau, A. Rendon, D. Hedley, L. Lilge, and I.F. Tannock. The distribution of the anticancer drug Doxorubicin in relation to blood vessels in solid tumors. Clin Cancer Res. 11:8782-8788 (2005).
115. R.H. Grantaband I.F. Tannock. Penetration of anticancer drugs through tumour tissue as a function of cellular packing density and interstitial fluid pressure and its modification by bortezomib. BMC Cancer. 12:214 (2012).
116. R. Grantab, S. Sivananthan, and I.F. Tannock. The penetration of anticancer drugs through tumor tissue as a function of cellular adhesion and packing density of tumor cells. Cancer Res. 66:1033-1039 (2006).

117. P. Kovacicand J.A. Osuna, Jr. Mechanisms of anti-cancer agents: emphasis on oxidative stress and electron transfer. Curr Pharm Des. 6:277-309 (2000).
118. P. Wardman. Electron transfer and oxidative stress as key factors in the design of drugs selectively active in hypoxia. Curr Med Chem. 8:739-761 (2001).
119. B.A. Teicher. Hypoxia and drug resistance. Cancer Metastasis Rev. 13:139-168 (1994).
120. B.A. Teicher, J.S. Lazo, and A.C. Sartorelli. Classification of antineoplastic agents by their selective toxicities toward oxygenated and hypoxic tumor cells. Cancer Res. 41:73-81 (1981).
121. K.A. Kennedy. Hypoxic cells as specific drug targets for chemotherapy. Anticancer Drug Des. 2:181-194 (1987).
122. X.W. Liu, Y. Su, H. Zhu, J. Cao, W.J. Ding, Y.C. Zhao, Q.J. He, and B. Yang. HIF-1alpha-dependent autophagy protects HeLa cells from fenretinide (4-HPR)-induced apoptosis in hypoxia. Pharmacol Res. 62:416-425 (2010).
123. R. Sullivan, G.C. Pare, L.J. Frederiksen, G.L. Semenza, and C.H. Graham. Hypoxia-induced resistance to anticancer drugs is associated with decreased senescence and requires hypoxia-inducible factor-1 activity. Mol Cancer Ther. 7:1961-1973 (2008).
124. L.M. Brown, R.L. Cowen, C. Debray, A. Eustace, J.T. Erler, F.C. Sheppard, C.A. Parker, I.J. Stratford, and K.J. Williams. Reversing hypoxic cell chemoresistance in vitro using genetic and small molecule approaches targeting hypoxia inducible factor-1. Mol Pharmacol. 69:411-418 (2006).
125. D. Hussein, E.J. Estlin, C. Dive, and G.W. Makin. Chronic hypoxia promotes hypoxia-inducible factor-1alpha-dependent resistance to etoposide and vincristine in neuroblastoma cells. Mol Cancer Ther. 5:2241-2250 (2006).
126. L. Huang, Q. Ao, Q. Zhang, X. Yang, H. Xing, F. Li, G. Chen, J. Zhou, S. Wang, G. Xu, L. Meng, Y. Lu, and D. Ma. Hypoxia induced paclitaxel resistance in human ovarian cancers via hypoxia-inducible factor 1alpha. J Cancer Res Clin Oncol. 136:447-456 (2010).
127. R. Sullivanand C.H. Graham. Hypoxia prevents etoposide-induced DNA damage in cancer cells through a mechanism involving hypoxia-inducible factor 1. Mol Cancer Ther. 8:1702-1713 (2009).
128. R. Ravizza, R. Molteni, M.B. Gariboldi, E. Marras, G. Perletti, and E. Monti. Effect of HIF-1 modulation on the response of two- and three-dimensional cultures of human colon cancer cells to 5-fluorouracil. Eur J Cancer. 45:890-898 (2009).
129. X. Song, X. Liu, W. Chi, Y. Liu, L. Wei, X. Wang, and J. Yu. Hypoxia-induced resistance to cisplatin and doxorubicin in non-small cell lung cancer is inhibited by silencing of HIF-1alpha gene. Cancer Chemother Pharmacol. 58:776-784 (2006).
130. M. Kilic, H. Kasperczyk, S. Fulda, and K.M. Debatin. Role of hypoxia inducible factor-1 alpha in modulation of apoptosis resistance. Oncogene. 26:2027-2038 (2007).
131. L. Liu, X. Ning, L. Sun, H. Zhang, Y. Shi, C. Guo, S. Han, J. Liu, S. Sun, Z. Han, K. Wu, and D. Fan. Hypoxia-inducible factor-1 alpha contributes to hypoxia-induced chemoresistance in gastric cancer. Cancer Sci. 99:121-128 (2008).
132. D.L. Roberts, K.J. Williams, R.L. Cowen, M. Barathova, A.J. Eustace, S. Brittain-Dissont, M.J. Tilby, D.G. Pearson, C.J. Ottley, I.J. Stratford, and C. Dive. Contribution of HIF-1 and drug penetrance to oxaliplatin resistance in hypoxic colorectal cancer cells. Br J Cancer. 101:1290-1297 (2009).
133. A. Sermeus, J.P. Cosse, M. Crespin, V. Mainfroid, F. de Longueville, N. Ninane, M. Raes, J. Remacle, and C. Michiels. Hypoxia induces protection against etoposide-induced apoptosis: molecular profiling of changes in gene expression and transcription factor activity. Mol Cancer. 7:27 (2008).
134. G.L. Semenza. Hypoxia-inducible factor 1 (HIF-1) pathway. Sci STKE. 2007:cm8 (2007).

135. L. Flamant, A. Notte, N. Ninane, M. Raes, and C. Michiels. Anti-apoptotic role of HIF-1 and AP-1 in paclitaxel exposed breast cancer cells under hypoxia. Mol Cancer. 9:191 (2010).
136. J. Hao, X. Song, B. Song, Y. Liu, L. Wei, X. Wang, and J. Yu. Effects of lentivirus-mediated HIF-1alpha knockdown on hypoxia-related cisplatin resistance and their dependence on p53 status in fibrosarcoma cells. Cancer Gene Ther. 15:449-455 (2008).
137. X.H. Peng, P. Karna, Z. Cao, B.H. Jiang, M. Zhou, and L. Yang. Cross-talk between epidermal growth factor receptor and hypoxia-inducible factor-1alpha signal pathways increases resistance to apoptosis by up-regulating survivin gene expression. J Biol Chem. 281:25903-25914 (2006).
138. A. Sermeusand C. Michiels. Reciprocal influence of the p53 and the hypoxic pathways. Cell Death Dis. 2:e164 (2011).
139. T.G. Graeber, C. Osmanian, T. Jacks, D.E. Housman, C.J. Koch, S.W. Lowe, and A.J. Giaccia. Hypoxia-mediated selection of cells with diminished apoptotic potential in solid tumours. Nature. 379:88-91 (1996).
140. I. Amelioand G. Melino. The p53 family and the hypoxia-inducible factors (HIFs): determinants of cancer progression. Trends Biochem Sci. 40:425-434 (2015).
141. A. Sendoel, I. Kohler, C. Fellmann, S.W. Lowe, and M.O. Hengartner. HIF-1 antagonizes p53-mediated apoptosis through a secreted neuronal tyrosinase. Nature. 465:577-583 (2010).
142. A. Fekiand I. Irminger-Finger. Mutational spectrum of p53 mutations in primary breast and ovarian tumors. Crit Rev Oncol Hematol. 52:103-116 (2004).
143. N. Mizushima, B. Levine, A.M. Cuervo, and D.J. Klionsky. Autophagy fights disease through cellular self-digestion. Nature. 451:1069-1075 (2008).
144. J.J. Lum, R.J. DeBerardinis, and C.B. Thompson. Autophagy in metazoans: cell survival in the land of plenty. Nat Rev Mol Cell Biol. 6:439-448 (2005).
145. H. Zhang, M. Bosch-Marce, L.A. Shimoda, Y.S. Tan, J.H. Baek, J.B. Wesley, F.J. Gonzalez, and G.L. Semenza. Mitochondrial autophagy is an HIF-1-dependent adaptive metabolic response to hypoxia. J Biol Chem. 283:10892-10903 (2008).
146. I. Papandreou, A.L. Lim, K. Laderoute, and N.C. Denko. Hypoxia signals autophagy in tumor cells via AMPK activity, independent of HIF-1, BNIP3, and BNIP3L. Cell Death Differ. 15:1572-1581 (2008).
147. S. Chen, S.K. Rehman, W. Zhang, A. Wen, L. Yao, and J. Zhang. Autophagy is a therapeutic target in anticancer drug resistance. Biochim Biophys Acta. 1806:220-229 (2010).
148. J. Li, N. Hou, A. Faried, S. Tsutsumi, and H. Kuwano. Inhibition of autophagy augments 5-fluorouracil chemotherapy in human colon cancer in vitro and in vivo model. Eur J Cancer. 46:1900-1909 (2010).
149. S.M. Schleicher, L. Moretti, V. Varki, and B. Lu. Progress in the unraveling of the endoplasmic reticulum stress/autophagy pathway and cancer: implications for future therapeutic approaches. Drug Resist Updat. 13:79-86 (2010).
150. I.F. Tannock. The relation between cell proliferation and the vascular system in a transplanted mouse mammary tumour. Br J Cancer. 22:258-273 (1968).
151. D.G. Hirstand J. Denekamp. Tumour cell proliferation in relation to the vasculature. Cell Tissue Kinet. 12:31-42 (1979).
152. A.S. Ljungkvist, J. Bussink, P.F. Rijken, J.H. Kaanders, A.J. van der Kogel, and J. Denekamp. Vascular architecture, hypoxia, and proliferation in first-generation xenografts of human head-and-neck squamous cell carcinomas. Int J Radiat Oncol Biol Phys. 54:215-228 (2002).
153. L.B. Gardner, Q. Li, M.S. Park, W.M. Flanagan, G.L. Semenza, and C.V. Dang. Hypoxia inhibits G1/S transition through regulation of p27 expression. J Biol Chem. 276:7919-7926 (2001).

154. B. St Croix, V.A. Florenes, J.W. Rak, M. Flanagan, N. Bhattacharya, J.M. Slingerland, and R.S. Kerbel. Impact of the cyclin-dependent kinase inhibitor p27Kip1 on resistance of tumor cells to anticancer agents. Nat Med. 2:1204-1210 (1996).
155. J. Campisi. Senescent cells, tumor suppression, and organismal aging: good citizens, bad neighbors. Cell. 120:513-522 (2005).
156. F. d'Adda di Fagagna. Living on a break: cellular senescence as a DNA-damage response. Nat Rev Cancer. 8:512-522 (2008).
157. R.H. te Poele, A.L. Okorokov, L. Jardine, J. Cummings, and S.P. Joel. DNA damage is able to induce senescence in tumor cells in vitro and in vivo. Cancer Res. 62:1876-1883 (2002).
158. B.D. Chang, E.V. Broude, M. Dokmanovic, H. Zhu, A. Ruth, Y. Xuan, E.S. Kandel, E. Lausch, K. Christov, and I.B. Roninson. A senescence-like phenotype distinguishes tumor cells that undergo terminal proliferation arrest after exposure to anticancer agents. Cancer Res. 59:3761-3767 (1999).
159. A.E. Greijerand E. van der Wall. The role of hypoxia inducible factor 1 (HIF-1) in hypoxia induced apoptosis. J Clin Pathol. 57:1009-1014 (2004).
160. S.R. Walmsley, C. Print, N. Farahi, C. Peyssonnaux, R.S. Johnson, T. Cramer, A. Sobolewski, A.M. Condliffe, A.S. Cowburn, N. Johnson, and E.R. Chilvers. Hypoxia-induced neutrophil survival is mediated by HIF-1alpha-dependent NF-kappaB activity. J Exp Med. 201:105-115 (2005).
161. R.K. Bruick. Expression of the gene encoding the proapoptotic Nip3 protein is induced by hypoxia. Proc Natl Acad Sci U S A. 97:9082-9087 (2000).
162. N. Chen, X. Chen, R. Huang, H. Zeng, J. Gong, W. Meng, Y. Lu, F. Zhao, L. Wang, and Q. Zhou. BCL-xL is a target gene regulated by hypoxia-inducible factor-1{alpha}. J Biol Chem. 284:10004-10012 (2009).
163. J.T. Erler, C.J. Cawthorne, K.J. Williams, M. Koritzinsky, B.G. Wouters, C. Wilson, C. Miller, C. Demonacos, I.J. Stratford, and C. Dive. Hypoxia-mediated down-regulation of Bid and Bax in tumors occurs via hypoxia-inducible factor 1-dependent and -independent mechanisms and contributes to drug resistance. Mol Cell Biol. 24:2875-2889 (2004).
164. J.Y. Kim, H.J. Ahn, J.H. Ryu, K. Suk, and J.H. Park. BH3-only protein Noxa is a mediator of hypoxic cell death induced by hypoxia-inducible factor 1alpha. J Exp Med. 199:113-124 (2004).
165. H.M. Sowter, P.J. Ratcliffe, P. Watson, A.H. Greenberg, and A.L. Harris. HIF-1-dependent regulation of hypoxic induction of the cell death factors BNIP3 and NIX in human tumors. Cancer Res. 61:6669-6673 (2001).
166. X. Feng, X. Liu, W. Zhang, and W. Xiao. p53 directly suppresses BNIP3 expression to protect against hypoxia-induced cell death. EMBO J. 30:3397-3415 (2011).
167. D. Hanahanand R.A. Weinberg. Hallmarks of cancer: the next generation. Cell. 144:646-674 (2011).
168. C.J. Lordand A. Ashworth. The DNA damage response and cancer therapy. Nature. 481:287-294 (2012).
169. L.E. Huang, R.S. Bindra, P.M. Glazer, and A.L. Harris. Hypoxia-induced genetic instability--a calculated mechanism underlying tumor progression. J Mol Med (Berl). 85:139-148 (2007).
170. R.G. Bristowand R.P. Hill. Hypoxia and metabolism. Hypoxia, DNA repair and genetic instability. Nat Rev Cancer. 8:180-192 (2008).
171. E. Bolderson, D.J. Richard, B.B. Zhou, and K.K. Khanna. Recent advances in cancer therapy targeting proteins involved in DNA double-strand break repair. Clin Cancer Res. 15:6314-6320 (2009).
172. M.S. Huen, S.M. Sy, and J. Chen. BRCA1 and its toolbox for the maintenance of genome integrity. Nat Rev Mol Cell Biol. 11:138-148 (2010).

173. M. Koshiji, Y. Kageyama, E.A. Pete, I. Horikawa, J.C. Barrett, and L.E. Huang. HIF-1alpha induces cell cycle arrest by functionally counteracting Myc. EMBO J. 23:1949-1956 (2004).
174. R. Wirthner, S. Wrann, K. Balamurugan, R.H. Wenger, and D.P. Stiehl. Impaired DNA double-strand break repair contributes to chemoresistance in HIF-1 alpha-deficient mouse embryonic fibroblasts. Carcinogenesis. 29:2306-2316 (2008).
175. R.H. Medemaand L. Macurek. Checkpoint control and cancer. Oncogene. 31:2601-2613 (2012).
176. H. Cam, J.B. Easton, A. High, and P.J. Houghton. mTORC1 signaling under hypoxic conditions is controlled by ATM-dependent phosphorylation of HIF-1alpha. Mol Cell. 40:509-520 (2010).
177. T.A. Yap, S.K. Sandhu, C.P. Carden, and J.S. de Bono. Poly(ADP-ribose) polymerase (PARP) inhibitors: Exploiting a synthetic lethal strategy in the clinic. CA Cancer J Clin. 61:31-49 (2011).
178. M. Elser, L. Borsig, P.O. Hassa, S. Erener, S. Messner, T. Valovka, S. Keller, M. Gassmann, and M.O. Hottiger. Poly(ADP-ribose) polymerase 1 promotes tumor cell survival by coactivating hypoxia-inducible factor-1-dependent gene expression. Mol Cancer Res. 6:282-290 (2008).
179. J.W. Kim, I. Tchernyshyov, G.L. Semenza, and C.V. Dang. HIF-1-mediated expression of pyruvate dehydrogenase kinase: a metabolic switch required for cellular adaptation to hypoxia. Cell Metab. 3:177-185 (2006).
180. I. Papandreou, R.A. Cairns, L. Fontana, A.L. Lim, and N.C. Denko. HIF-1 mediates adaptation to hypoxia by actively downregulating mitochondrial oxygen consumption. Cell Metab. 3:187-197 (2006).
181. R.A. Cardone, V. Casavola, and S.J. Reshkin. The role of disturbed pH dynamics and the Na+/H+ exchanger in metastasis. Nat Rev Cancer. 5:786-795 (2005).
182. M.S. Ullah, A.J. Davies, and A.P. Halestrap. The plasma membrane lactate transporter MCT4, but not MCT1, is up-regulated by hypoxia through a HIF-1alpha-dependent mechanism. J Biol Chem. 281:9030-9037 (2006).
183. A.P. Halestrapand M.C. Wilson. The monocarboxylate transporter family--role and regulation. IUBMB Life. 64:109-119 (2012).
184. L. Counillonand J. Pouyssegur. The expanding family of eucaryotic Na(+)/H(+) exchangers. J Biol Chem. 275:1-4 (2000).
185. N.K. Tafreshi, M.C. Lloyd, M.M. Bui, R.J. Gillies, and D.L. Morse. Carbonic anhydrase IX as an imaging and therapeutic target for tumors and metastases. Subcell Biochem. 75:221-254 (2014).
186. I.F. Tannockand D. Rotin. Acid pH in tumors and its potential for therapeutic exploitation. Cancer Res. 49:4373-4384 (1989).
187. L.E. Gerweck, S. Vijayappa, and S. Kozin. Tumor pH controls the in vivo efficacy of weak acid and base chemotherapeutics. Mol Cancer Ther. 5:1275-1279 (2006).
188. D.S. Cowanand I.F. Tannock. Factors that influence the penetration of methotrexate through solid tissue. Int J Cancer. 91:120-125 (2001).
189. H.F. Dvorak, J.A. Nagy, D. Feng, L.F. Brown, and A.M. Dvorak. Vascular permeability factor/vascular endothelial growth factor and the significance of microvascular hyperpermeability in angiogenesis. Curr Top Microbiol Immunol. 237:97-132 (1999).
190. E.K. Rofstad, S.H. Tunheim, B. Mathiesen, B.A. Graff, E.F. Halsor, K. Nilsen, and K. Galappathi. Pulmonary and lymph node metastasis is associated with primary tumor interstitial fluid pressure in human melanoma xenografts. Cancer Res. 62:661-664 (2002).
191. A.J. Leu, D.A. Berk, A. Lymboussaki, K. Alitalo, and R.K. Jain. Absence of functional lymphatics within a murine sarcoma: a molecular and functional evaluation. Cancer Res. 60:4324-4327 (2000).
192. C.H. Heldin, K. Rubin, K. Pietras, and A. Ostman. High interstitial fluid pressure - an obstacle in cancer therapy. Nat Rev Cancer. 4:806-813 (2004).

193. M. Stohrer, Y. Boucher, M. Stangassinger, and R.K. Jain. Oncotic pressure in solid tumors is elevated. Cancer Res. 60:4251-4255 (2000).
194. M.F. Milosevic, A.W. Fyles, R. Wong, M. Pintilie, M.C. Kavanagh, W. Levin, L.A. Manchul, T.J. Keane, and R.P. Hill. Interstitial fluid pressure in cervical carcinoma: within tumor heterogeneity, and relation to oxygen tension. Cancer. 82:2418-2426 (1998).
195. P.A. Netti, L.M. Hamberg, J.W. Babich, D. Kierstead, W. Graham, G.J. Hunter, G.L. Wolf, A. Fischman, Y. Boucher, and R.K. Jain. Enhancement of fluid filtration across tumor vessels: implication for delivery of macromolecules. Proc Natl Acad Sci U S A. 96:3137-3142 (1999).
196. A.V. Salnikov, V.V. Iversen, M. Koisti, C. Sundberg, L. Johansson, L.B. Stuhr, M. Sjoquist, H. Ahlstrom, R.K. Reed, and K. Rubin. Lowering of tumor interstitial fluid pressure specifically augments efficacy of chemotherapy. FASEB J. 17:1756-1758 (2003).
197. Y. Boucher, L.T. Baxter, and R.K. Jain. Interstitial pressure gradients in tissue-isolated and subcutaneous tumors: implications for therapy. Cancer Res. 50:4478-4484 (1990).
198. A.I. Minchintonand I.F. Tannock. Drug penetration in solid tumours. Nat Rev Cancer. 6:583-592 (2006).
199. A. Di Paoloand G. Bocci. Drug distribution in tumors: mechanisms, role in drug resistance, and methods for modification. Curr Oncol Rep. 9:109-114 (2007).
200. G. Szakacs, J.K. Paterson, J.A. Ludwig, C. Booth-Genthe, and M.M. Gottesman. Targeting multidrug resistance in cancer. Nat Rev Drug Discov. 5:219-234 (2006).
201. T. Arnasonand T. Harkness. Development, Maintenance, and Reversal of Multiple Drug Resistance: At the Crossroads of TFPI1, ABC Transporters, and HIF1. Cancers (Basel). 7:2063-2082 (2015).
202. K.M. Comerford, T.J. Wallace, J. Karhausen, N.A. Louis, M.C. Montalto, and S.P. Colgan. Hypoxia-inducible factor-1-dependent regulation of the multidrug resistance (MDR1) gene. Cancer Res. 62:3387-3394 (2002).
203. J. Li, M. Shi, Y. Cao, W. Yuan, T. Pang, B. Li, Z. Sun, L. Chen, and R.C. Zhao. Knockdown of hypoxia-inducible factor-1alpha in breast carcinoma MCF-7 cells results in reduced tumor growth and increased sensitivity to methotrexate. Biochem Biophys Res Commun. 342:1341-1351 (2006).
204. H. Zhu, X.P. Chen, S.F. Luo, J. Guan, W.G. Zhang, and B.X. Zhang. Involvement of hypoxia-inducible factor-1-alpha in multidrug resistance induced by hypoxia in HepG2 cells. J Exp Clin Cancer Res. 24:565-574 (2005).
205. P. Krishnamurthy, D.D. Ross, T. Nakanishi, K. Bailey-Dell, S. Zhou, K.E. Mercer, B. Sarkadi, B.P. Sorrentino, and J.D. Schuetz. The stem cell marker Bcrp/ABCG2 enhances hypoxic cell survival through interactions with heme. J Biol Chem. 279:24218-24225 (2004).
206. F. Bohm, R. Edge, S. Foley, L. Lange, and T.G. Truscott. Antioxidant inhibition of porphyrin-induced cellular phototoxicity. J Photochem Photobiol B. 65:177-183 (2001).
207. H.J. Broxterman, J. Lankelma, and H.M. Pinedo. How to probe clinical tumour samples for P-glycoprotein and multidrug resistance-associated protein. Eur J Cancer. 32A:1024-1033 (1996).
208. L. Chen, P. Feng, S. Li, D. Long, J. Cheng, Y. Lu, and D. Zhou. Effect of hypoxia-inducible factor-1alpha silencing on the sensitivity of human brain glioma cells to doxorubicin and etoposide. Neurochem Res. 34:984-990 (2009).
209. E.M. Leslie, R.G. Deeley, and S.P. Cole. Multidrug resistance proteins: role of P-glycoprotein, MRP1, MRP2, and BCRP (ABCG2) in tissue defense. Toxicol Appl Pharmacol. 204:216-237 (2005).
210. D.M. Townsendand K.D. Tew. The role of glutathione-S-transferase in anti-cancer drug resistance. Oncogene. 22:7369-7375 (2003).

211. A. Troyano, C. Fernandez, P. Sancho, E. de Blas, and P. Aller. Effect of glutathione depletion on antitumor drug toxicity (apoptosis and necrosis) in U-937 human promonocytic cells. The role of intracellular oxidation. J Biol Chem. 276:47107-47115 (2001).
212. N.A. Phamand D.W. Hedley. Respiratory chain-generated oxidative stress following treatment of leukemic blasts with DNA-damaging agents. Exp Cell Res. 264:345-352 (2001).
213. H. Pelicano, D. Carney, and P. Huang. ROS stress in cancer cells and therapeutic implications. Drug Resist Updat. 7:97-110 (2004).
214. G.L. Semenza. Oxygen sensing, homeostasis, and disease. N Engl J Med. 365:537-547 (2011).
215. G.L. Semenza. HIF-1: mediator of physiological and pathophysiological responses to hypoxia. J Appl Physiol (1985). 88:1474-1480 (2000).
216. B. Krishnamachary, S. Berg-Dixon, B. Kelly, F. Agani, D. Feldser, G. Ferreira, N. Iyer, J. LaRusch, B. Pak, P. Taghavi, and G.L. Semenza. Regulation of colon carcinoma cell invasion by hypoxia-inducible factor 1. Cancer Res. 63:1138-1143 (2003).
217. N.C. Denko, L.A. Fontana, K.M. Hudson, P.D. Sutphin, S. Raychaudhuri, R. Altman, and A.J. Giaccia. Investigating hypoxic tumor physiology through gene expression patterns. Oncogene. 22:5907-5914 (2003).
218. Q. Zhang, Z.F. Zhang, J.Y. Rao, J.D. Sato, J. Brown, D.V. Messadi, and A.D. Le. Treatment with siRNA and antisense oligonucleotides targeted to HIF-1alpha induced apoptosis in human tongue squamous cell carcinomas. Int J Cancer. 111:849-857 (2004).
219. T. Fojoand D.R. Parkinson. Biologically targeted cancer therapy and marginal benefits: are we making too much of too little or are we achieving too little by giving too much? Clin Cancer Res. 16:5972-5980 (2010).
220. T.W. Jacobs, J.E. Prioleau, I.E. Stillman, and S.J. Schnitt. Loss of tumor marker-immunostaining intensity on stored paraffin slides of breast cancer. J Natl Cancer Inst. 88:1054-1059 (1996).
221. N. Rohwer, S. Lobitz, K. Daskalow, T. Jons, M. Vieth, P.M. Schlag, W. Kemmner, B. Wiedenmann, T. Cramer, and M. Hocker. HIF-1alpha determines the metastatic potential of gastric cancer cells. Br J Cancer. 100:772-781 (2009).
222. K. Daskalow, N. Rohwer, E. Raskopf, E. Dupuy, A. Kuhl, C. Loddenkemper, B. Wiedenmann, V. Schmitz, and T. Cramer. Role of hypoxia-inducible transcription factor 1alpha for progression and chemosensitivity of murine hepatocellular carcinoma. J Mol Med (Berl). 88:817-827 (2010).
223. T. Miller, S. Breyer, G. van Colen, W. Mier, U. Haberkorn, S. Geissler, S. Voss, M. Weigandt, and A. Goepferich. Premature drug release of polymeric micelles and its effects on tumor targeting. Int J Pharm. 445:117-124 (2013).
224. X.-B. Xiong, A. Falamarzian, S.M. Garg, and A. Lavasanifar. Engineering of amphiphilic block copolymers for polymeric micellar drug and gene delivery. Journal of Controlled Release. 155:248-261 (2011).
225. N. Kang, M.E. Perron, R.E. Prud'homme, Y. Zhang, G. Gaucher, and J.C. Leroux. Stereocomplex block copolymer micelles: core-shell nanostructures with enhanced stability. Nano Lett. 5:315-319 (2005).
226. H. Soleymani Abyaneh, M.R. Vakili, F. Zhang, P. Choi, and A. Lavasanifar. Rational design of block copolymer micelles to control burst drug release at a nanoscale dimension. Acta Biomater. 24:127-139 (2015).
227. S. Patel, A. Lavasanifar, and P. Choi. Application of molecular dynamics simulation to predict the compatability between water-insoluble drugs and self-associating poly(ethylene oxide)-b-poly(epsilon-caprolactone) block copolymers. Biomacromolecules. 9:3014-3023 (2008).
228. X.P. Sun, X. Dong, L. Lin, X. Jiang, Z. Wei, B. Zhai, B. Sun, Q. Zhang, X. Wang, H. Jiang, G.W. Krissansen, H. Qiao, and X. Sun. Up-regulation of survivin by AKT and hypoxia-inducible factor 1alpha contributes to cisplatin resistance in gastric cancer. FEBS J. 281:115-128 (2014).

229. J. Adamski, A. Price, C. Dive, and G. Makin. Hypoxia-induced cytotoxic drug resistance in osteosarcoma is independent of HIF-1Alpha. PLoS One. 8:e65304 (2013).
230. A.C. Mamede, A.M. Abrantes, L. Pedrosa, J.E. Casalta-Lopes, A.S. Pires, R.J. Teixo, A.C. Goncalves, A.B. Sarmento-Ribeiro, C.J. Maia, and M.F. Botelho. Beyond the limits of oxygen: effects of hypoxia in a hormone-independent prostate cancer cell line. ISRN Oncol. 2013:918207 (2013).
231. E.A. O'Reilly, L. Gubbins, S. Sharma, R. Tully, M.H. Guang, K. Weiner-Gorzel, J. McCaffrey, M. Harrison, F. Furlong, M. Kell, and A. McCann. The fate of chemoresistance in triple negative breast cancer (TNBC). BBA Clin. 3:257-275 (2015).
232. S.R. Parkand A. Chen. Poly(Adenosine diphosphate-ribose) polymerase inhibitors in cancer treatment. Hematol Oncol Clin North Am. 26:649-670, ix (2012).
233. Z. Yunand Q. Lin. Hypoxia and regulation of cancer cell stemness. Adv Exp Med Biol. 772:41-53 (2014).
234. L.N. Abdullahand E.K. Chow. Mechanisms of chemoresistance in cancer stem cells. Clin Transl Med. 2:3 (2013).
235. F. Wu, J. Zhang, P. Wang, X. Ye, K. Jung, K.M. Bone, J.D. Pearson, R.J. Ingham, T.P. McMullen, Y. Ma, and R. Lai. Identification of two novel phenotypically distinct breast cancer cell subsets based on Sox2 transcription activity. Cell Signal. 24:1989-1998 (2012).
236. K. Jung, N. Gupta, P. Wang, J.T. Lewis, K. Gopal, F. Wu, X. Ye, A. Alshareef, B.S. Abdulkarim, D.N. Douglas, N.M. Kneteman, and R. Lai. Triple negative breast cancers comprise a highly tumorigenic cell subpopulation detectable by its high responsiveness to a Sox2 regulatory region 2 (SRR2) reporter. Oncotarget. 6:10366-10373 (2015).
237. P. Gelebart, S.A. Hegazy, P. Wang, K.M. Bone, M. Anand, D. Sharon, M. Hitt, J.D. Pearson, R.J. Ingham, Y. Ma, and R. Lai. Aberrant expression and biological significance of Sox2, an embryonic stem cell transcriptional factor, in ALK-positive anaplastic large cell lymphoma. Blood Cancer J. 2:e82 (2012).
238. I.J. Hoogsteen, H.A. Marres, F.J. van den Hoogen, P.F. Rijken, J. Lok, J. Bussink, and J.H. Kaanders. Expression of EGFR under tumor hypoxia: identification of a subpopulation of tumor cells responsible for aggressiveness and treatment resistance. Int J Radiat Oncol Biol Phys. 84:807-814 (2012).
239. A. Franovic, L. Gunaratnam, K. Smith, I. Robert, D. Patten, and S. Lee. Translational up-regulation of the EGFR by tumor hypoxia provides a nonmutational explanation for its overexpression in human cancer. Proc Natl Acad Sci U S A. 104:13092-13097 (2007).
240. L. Milane, Z. Duan, and M. Amiji. Development of EGFR-targeted polymer blend nanocarriers for combination paclitaxel/lonidamine delivery to treat multi-drug resistance in human breast and ovarian tumor cells. Mol Pharm. 8:185-203 (2011).
241. Z. Li, R. Zhao, X. Wu, Y. Sun, M. Yao, J. Li, Y. Xu, and J. Gu. Identification and characterization of a novel peptide ligand of epidermal growth factor receptor for targeted delivery of therapeutics. FASEB J. 19:1978-1985 (2005).
242. H. Soleymani Abyaneh, M.R. Vakili, and A. Lavasanifar. The effect of polymerization method in stereo-active block copolymers on the stability of polymeric micelles and their drug release profile. Pharm Res. 31:1485-1500 (2014).
243. X.B. Xiong, A. Falamarzian, S.M. Garg, and A. Lavasanifar. Engineering of amphiphilic block copolymers for polymeric micellar drug and gene delivery. J Control Release. 155:248-261 (2011).
244. N. Nishiyamaand K. Kataoka. Current state, achievements, and future prospects of polymeric micelles as nanocarriers for drug and gene delivery. Pharmacol Ther. 112:630-648 (2006).

245. X.B. Xiong, Z. Binkhathlan, O. Molavi, and A. Lavasanifar. Amphiphilic block co-polymers: preparation and application in nanodrug and gene delivery. Acta Biomater. 8:2017-2033 (2012).
246. K. Kazunori, K. Glenn S, Y. Masayuki, O. Teruo, and S. Yasuhisa. Block copolymer micelles as vehicles for drug delivery. Journal of Controlled Release. 24:119-132 (1993).
247. H.M. Aliabadi, M. Shahin, D.R. Brocks, and A. Lavasanifar. Disposition of drugs in block copolymer micelle delivery systems: from discovery to recovery. Clin Pharmacokinet. 47:619-634 (2008).
248. T. Inoue, G. Chen, K. Nakamae, and A.S. Hoffman. An AB block copolymer of oligo(methyl methacrylate) and poly(acrylic acid) for micellar delivery of hydrophobic drugs. J Control Release. 51:221-229 (1998).
249. S. Inkinen, M. Hakkarainen, A.C. Albertsson, and A. Sodergard. From lactic acid to poly(lactic acid) (PLA): characterization and analysis of PLA and its precursors. Biomacromolecules. 12:523-532 (2011).
250. S.K. Agrawal, N. Sanabria-DeLong, J.M. Coburn, G.N. Tew, and S.R. Bhatia. Novel drug release profiles from micellar solutions of PLA-PEO-PLA triblock copolymers. J Control Release. 112:64-71 (2006).
251. J. Zhang, L.Q. Wang, H. Wang, and K. Tu. Micellization phenomena of amphiphilic block copolymers based on methoxy poly(ethylene glycol) and either crystalline or amorphous poly(caprolactone-b-lactide). Biomacromolecules. 7:2492-2500 (2006).
252. D. Hanggi, J. Perrin, S. Eicker, K. Beseoglu, N. Etminan, M.A. Kamp, H.J. Heiroth, N. Bege, S. Macht, K. Frauenknecht, C. Sommer, T. Kissel, and H.J. Steiger. Local delivery of nimodipine by prolonged-release microparticles-feasibility, effectiveness and dose-finding in experimental subarachnoid hemorrhage. PLoS One. 7:e42597 (2012).
253. R.F. Storeyand J.W. Sherman. Kinetics and Mechanism of the Stannous Octoate-Catalyzed Bulk Polymerization of ε-Caprolactone. Macromolecules. 35:1504-1512 (2002).
254. C.M. Thomas. Stereocontrolled ring-opening polymerization of cyclic esters: synthesis of new polyester microstructures. Chem Soc Rev. 39:165-173 (2010).
255. H. Tsujiand Y. Ikada. Crystallization from the melt of poly(lactide)s with different optical purities and their blends. Macromolecular Chemistry and Physics. 197:3483-3499 (1996).
256. R. Slivniakand A.J. Domb. Stereocomplexes of enantiomeric lactic acid and sebacic acid ester-anhydride triblock copolymers. Biomacromolecules. 3:754-760 (2002).
257. H. Tsujiand Y. Ikada. Stereocomplex formation between enantiomeric poly(lactic acid)s. 6. Binary blends from copolymers. Macromolecules. 25:5719-5723 (1992).
258. H.M. Burt, X. Zhang, P. Toleikis, L. Embree, and W.L. Hunter. Development of copolymers of poly(d,l-lactide) and methoxypolyethylene glycol as micellar carriers of paclitaxel. Colloids and Surfaces B: Biointerfaces. 16:161-171 (1999).
259. N. Petzetakis, A.P. Dove, and R.K. O'Reilly. Cylindrical micelles from the living crystallization-driven self-assembly of poly(lactide)-containing block copolymers. Chemical Science. 2:955-960 (2011).
260. A. Kelarakis, C. Chaibundit, M.J. Krysmann, V. Havredaki, K. Viras, and I.W. Hamley. Interactions of an anionic surfactant with poly(oxyalkylene) copolymers in aqueous solution. J Colloid Interface Sci. 330:67-72 (2009).
261. H.M. Aliabadi, S. Elhasi, A. Mahmud, R. Gulamhusein, P. Mahdipoor, and A. Lavasanifar. Encapsulation of hydrophobic drugs in polymeric micelles through co-solvent evaporation: the effect of solvent composition on micellar properties and drug loading. Int J Pharm. 329:158-165 (2007).
262. C.M. Thomas. Stereocontrolled ring-opening polymerization of cyclic esters: synthesis of new polyester microstructures. Chemical Society Reviews. 39:165-173 (2010).

263. C. Agatemorand M.P. Shaver. Tacticity-induced changes in the micellization and degradation properties of poly(lactic acid)-block-poly(ethylene glycol) copolymers. Biomacromolecules. 14:699-708 (2013).
264. T.M. Ovittand G.W. Coates. Stereoselective ring-opening polymerization of meso-lactide: Synthesis of syndiotactic poly(lactic acid). Journal of the American Chemical Society. 121:4072-4073 (1999).
265. X.D. Guo, Y. Qian, C.Y. Zhang, S.Y. Nie, and L.J. Zhang. Can drug molecules diffuse into the core of micelles? Soft Matter. 8:9989-9995 (2012).
266. A. Mahmud, X.-B. Xiong, and A. Lavasanifar. Novel Self-Associating Poly(ethylene oxide)-block-poly(ε-caprolactone) Block Copolymers with Functional Side Groups on the Polyester Block for Drug Delivery. Macromolecules. 39:9419-9428 (2006).
267. Y. Liand G.S. Kwon. Methotrexate esters of poly(ethylene oxide)-block-poly(2-hydroxyethyl-L-aspartamide). Part I: Effects of the level of methotrexate conjugation on the stability of micelles and on drug release. Pharm Res. 17:607-611 (2000).
268. Y. Hu, X. Jiang, Y. Ding, L. Zhang, C. Yang, J. Zhang, J. Chen, and Y. Yang. Preparation and drug release behaviors of nimodipine-loaded poly(caprolactone)–poly(ethylene oxide)–polylactide amphiphilic copolymer nanoparticles. Biomaterials. 24:2395-2404 (2003).
269. M. Shahinand A. Lavasanifar. Novel self-associating poly(ethylene oxide)-b-poly(epsilon-caprolactone) based drug conjugates and nano-containers for paclitaxel delivery. Int J Pharm. 389:213-222 (2010).
270. P. Costaand J.M. Sousa Lobo. Modeling and comparison of dissolution profiles. European Journal of Pharmaceutical Sciences. 13:123-133 (2001).
271. X. Guo, Z. Rong, and X. Ying. Calculation of hydrophile–lipophile balance for polyethoxylated surfactants by group contribution method. Journal of Colloid and Interface Science. 298:441-450 (2006).
272. K. Fukushima, R.C. Pratt, F. Nederberg, J.P. Tan, Y.Y. Yang, R.M. Waymouth, and J.L. Hedrick. Organocatalytic approach to amphiphilic comb-block copolymers capable of stereocomplexation and self-assembly. Biomacromolecules. 9:3051-3056 (2008).
273. L. Yang, Z. Zhao, J. Wei, A. El Ghzaoui, and S. Li. Micelles formed by self-assembling of polylactide/poly(ethylene glycol) block copolymers in aqueous solutions. J Colloid Interface Sci. 314:470-477 (2007).
274. F. Nederberg, E. Appel, J.P.K. Tan, S.H. Kim, K. Fukushima, J. Sly, R.D. Miller, R.M. Waymouth, Y.Y. Yang, and J.L. Hedrick. Simple Approach to Stabilized Micelles Employing Miktoarm Terpolymers and Stereocomplexes with Application in Paclitaxel Delivery. Biomacromolecules. 10:1460-1468 (2009).
275. J.R. Sarasua, A.L. Arraiza, P. Balerdi, and I. Maiza. Crystallinity and mechanical properties of optically pure polylactides and their blends. Polymer Engineering & Science. 45:745-753 (2005).
276. L. Yang, X. Wu, F. Liu, Y. Duan, and S. Li. Novel biodegradable polylactide/poly(ethylene glycol) micelles prepared by direct dissolution method for controlled delivery of anticancer drugs. Pharm Res. 26:2332-2342 (2009).
277. N. Rohwerand T. Cramer. Hypoxia-mediated drug resistance: novel insights on the functional interaction of HIFs and cell death pathways. Drug Resist Updat. 14:191-201 (2011).
278. H.M. Wu, Z.F. Jiang, P.S. Ding, L.J. Shao, and R.Y. Liu. Hypoxia-induced autophagy mediates cisplatin resistance in lung cancer cells. Sci Rep. 5:12291 (2015).
279. P. Fu, F. Du, W. Chen, M. Yao, K. Lv, and Y. Liu. Tanshinone IIA blocks epithelial-mesenchymal transition through HIF-1alpha downregulation, reversing hypoxia-induced chemotherapy resistance in breast cancer cell lines. Oncol Rep. 31:2561-2568 (2014).

280. J.P. Cosse, M. Ronvaux, N. Ninane, M.J. Raes, and C. Michiels. Hypoxia-induced decrease in p53 protein level and increase in c-jun DNA binding activity results in cancer cell resistance to etoposide. Neoplasia. 11:976-986 (2009).
281. M. Achisonand T.R. Hupp. Hypoxia attenuates the p53 response to cellular damage. Oncogene. 22:3431-3440 (2003).
282. J. Wang, M.P. Biju, M.H. Wang, V.H. Haase, and Z. Dong. Cytoprotective effects of hypoxia against cisplatin-induced tubular cell apoptosis: involvement of mitochondrial inhibition and p53 suppression. J Am Soc Nephrol. 17:1875-1885 (2006).
283. K. Yokoiand I.J. Fidler. Hypoxia increases resistance of human pancreatic cancer cells to apoptosis induced by gemcitabine. Clin Cancer Res. 10:2299-2306 (2004).
284. J. Chen, M. Kobayashi, S. Darmanin, Y. Qiao, C. Gully, R. Zhao, S.C. Yeung, and M.H. Lee. Pim-1 plays a pivotal role in hypoxia-induced chemoresistance. Oncogene. 28:2581-2592 (2009).
285. J.P. Piret, J.P. Cosse, N. Ninane, M. Raes, and C. Michiels. Hypoxia protects HepG2 cells against etoposide-induced apoptosis via a HIF-1-independent pathway. Exp Cell Res. 312:2908-2920 (2006).
286. S.E. Schnitzer, T. Schmid, J. Zhou, and B. Brune. Hypoxia and HIF-1alpha protect A549 cells from drug-induced apoptosis. Cell Death Differ. 13:1611-1613 (2006).
287. K. Selvendiran, A. Bratasz, M.L. Kuppusamy, M.F. Tazi, B.K. Rivera, and P. Kuppusamy. Hypoxia induces chemoresistance in ovarian cancer cells by activation of signal transducer and activator of transcription 3. Int J Cancer. 125:2198-2204 (2009).
288. Z. Dong, M.A. Venkatachalam, J. Wang, Y. Patel, P. Saikumar, G.L. Semenza, T. Force, and J. Nishiyama. Up-regulation of apoptosis inhibitory protein IAP-2 by hypoxia. Hif-1-independent mechanisms. J Biol Chem. 276:18702-18709 (2001).
289. Y.C. Boller, L.M. Brandes, R.L. Russell, Z.P. Lin, S.R. Patierno, and K.A. Kennedy. Prostaglandin A1 inhibits stress-induced NF-kappaB activation and reverses resistance to topoisomerase II inhibitors. Oncol Res. 12:383-395 (2000).
290. J. Xie, Y. Xiao, X.Y. Zhu, Z.Y. Ning, H.F. Xu, and H.M. Wu. Hypoxia regulates stemness of breast cancer MDA-MB-231 cells. Med Oncol. 33:42 (2016).
291. Significance of CD44 and CD24 as Cancer Stem Cell Markers: An Enduring Ambiguity. Clinical and Developmental Immunology. 2012:11 (2012).
292. M. Dean. ABC transporters, drug resistance, and cancer stem cells. J Mammary Gland Biol Neoplasia. 14:3-9 (2009).
293. J.E. Jung, H.G. Lee, I.H. Cho, D.H. Chung, S.H. Yoon, Y.M. Yang, J.W. Lee, S. Choi, J.W. Park, S.K. Ye, and M.H. Chung. STAT3 is a potential modulator of HIF-1-mediated VEGF expression in human renal carcinoma cells. FASEB J. 19:1296-1298 (2005).
294. Q. Xu, J. Briggs, S. Park, G. Niu, M. Kortylewski, S. Zhang, T. Gritsko, J. Turkson, H. Kay, G.L. Semenza, J.Q. Cheng, R. Jove, and H. Yu. Targeting Stat3 blocks both HIF-1 and VEGF expression induced by multiple oncogenic growth signaling pathways. Oncogene. 24:5552-5560 (2005).
295. M.C. Duyndam, M.P. van Berkel, J.C. Dorsman, D.A. Rockx, H.M. Pinedo, and E. Boven. Cisplatin and doxorubicin repress Vascular Endothelial Growth Factor expression and differentially down-regulate Hypoxia-inducible Factor I activity in human ovarian cancer cells. Biochem Pharmacol. 74:191-201 (2007).
296. J.I. Fletcher, M. Haber, M.J. Henderson, and M.D. Norris. ABC transporters in cancer: more than just drug efflux pumps. Nat Rev Cancer. 10:147-156 (2010).
297. W.H. Liu, M.T. Chen, M.L. Wang, Y.Y. Lee, G.Y. Chiou, C.S. Chien, P.I. Huang, Y.W. Chen, M.C. Huang, S.H. Chiou, Y.H. Shih, and H.I. Ma. Cisplatin-selected resistance is associated with increased motility and stem-like properties via activation of STAT3/Snail axis in atypical teratoid/rhabdoid tumor cells. Oncotarget. 6:1750-1768 (2015).

298. A. Notte, N. Ninane, T. Arnould, and C. Michiels. Hypoxia counteracts taxol-induced apoptosis in MDA-MB-231 breast cancer cells: role of autophagy and JNK activation. Cell Death Dis. 4:e638 (2013).
299. Y. Liu, A.M. Bernauer, C.M. Yingling, and S.A. Belinsky. HIF1alpha regulated expression of XPA contributes to cisplatin resistance in lung cancer. Carcinogenesis. 33:1187-1192 (2012).
300. J. Song, Z. Qu, X. Guo, Q. Zhao, X. Zhao, L. Gao, K. Sun, F. Shen, M. Wu, and L. Wei. Hypoxia-induced autophagy contributes to the chemoresistance of hepatocellular carcinoma cells. Autophagy. 5:1131-1144 (2009).
301. S. Koch, F. Mayer, F. Honecker, M. Schittenhelm, and C. Bokemeyer. Efficacy of cytotoxic agents used in the treatment of testicular germ cell tumours under normoxic and hypoxic conditions in vitro. Br J Cancer. 89:2133-2139 (2003).
302. E. Louie, S. Nik, J.S. Chen, M. Schmidt, B. Song, C. Pacson, X.F. Chen, S. Park, J. Ju, and E.I. Chen. Identification of a stem-like cell population by exposing metastatic breast cancer cell lines to repetitive cycles of hypoxia and reoxygenation. Breast Cancer Res. 12:R94 (2010).
303. A.L. Ribeiroand V. Ribeiro. Drug metabolism and transport under hypoxia. Curr Drug Metab. 14:969-975 (2013).
304. F. Gu, Y. Ma, Z. Zhang, J. Zhao, H. Kobayashi, L. Zhang, and L. Fu. Expression of Stat3 and Notch1 is associated with cisplatin resistance in head and neck squamous cell carcinoma. Oncol Rep. 23:671-676 (2010).
305. W.J. Sheng, H. Jiang, D.L. Wu, and J.H. Zheng. Early responses of the STAT3 pathway to platinum drugs are associated with cisplatin resistance in epithelial ovarian cancer. Braz J Med Biol Res. 46:650-658 (2013).
306. N. Eckstein. Platinum resistance in breast and ovarian cancer cell lines. J Exp Clin Cancer Res. 30:91 (2011).
307. M.R. Pawlus, L. Wang, and C.J. Hu. STAT3 and HIF1alpha cooperatively activate HIF1 target genes in MDA-MB-231 and RCC4 cells. Oncogene. 33:1670-1679 (2014).
308. M.K. Oh, H.J. Park, N.H. Kim, S.J. Park, I.Y. Park, and I.S. Kim. Hypoxia-inducible factor-1alpha enhances haptoglobin gene expression by improving binding of STAT3 to the promoter. J Biol Chem. 286:8857-8865 (2011).
309. A. Nishimoto, N. Kugimiya, T. Hosoyama, T. Enoki, T.S. Li, and K. Hamano. HIF-1alpha activation under glucose deprivation plays a central role in the acquisition of anti-apoptosis in human colon cancer cells. Int J Oncol. 44:2077-2084 (2014).
310. X. Wang, G. Wang, Y. Zhao, X. Liu, Q. Ding, J. Shi, Y. Ding, and S. Wang. STAT3 mediates resistance of CD44(+)CD24(-/low) breast cancer stem cells to tamoxifen in vitro. J Biomed Res. 26:325-335 (2012).
311. S.S. Chung, C. Aroh, and J.V. Vadgama. Constitutive activation of STAT3 signaling regulates hTERT and promotes stem cell-like traits in human breast cancer cells. PLoS One. 8:e83971 (2013).
312. L.L. Marotta, V. Almendro, A. Marusyk, M. Shipitsin, J. Schemme, S.R. Walker, N. Bloushtain-Qimron, J.J. Kim, S.A. Choudhury, R. Maruyama, Z. Wu, M. Gonen, L.A. Mulvey, M.O. Bessarabova, S.J. Huh, S.J. Silver, S.Y. Kim, S.Y. Park, H.E. Lee, K.S. Anderson, A.L. Richardson, T. Nikolskaya, Y. Nikolsky, X.S. Liu, D.E. Root, W.C. Hahn, D.A. Frank, and K. Polyak. The JAK2/STAT3 signaling pathway is required for growth of CD44(+)CD24(-) stem cell-like breast cancer cells in human tumors. J Clin Invest. 121:2723-2735 (2011).
313. U. Fearon, M. Canavan, M. Biniecka, and D.J. Veale. Hypoxia, mitochondrial dysfunction and synovial invasiveness in rheumatoid arthritis. Nat Rev Rheumatol. 12:385-397 (2016).
314. W.D. Foulkes, I.E. Smith, and J.S. Reis-Filho. Triple-negative breast cancer. N Engl J Med. 363:1938-1948 (2010).

315. B.D. Lehmann, J.A. Bauer, X. Chen, M.E. Sanders, A.B. Chakravarthy, Y. Shyr, and J.A. Pietenpol. Identification of human triple-negative breast cancer subtypes and preclinical models for selection of targeted therapies. J Clin Invest. 121:2750-2767 (2011).
316. C.M. Perou, T. Sorlie, M.B. Eisen, M. van de Rijn, S.S. Jeffrey, C.A. Rees, J.R. Pollack, D.T. Ross, H. Johnsen, L.A. Akslen, O. Fluge, A. Pergamenschikov, C. Williams, S.X. Zhu, P.E. Lonning, A.L. Borresen-Dale, P.O. Brown, and D. Botstein. Molecular portraits of human breast tumours. Nature. 406:747-752 (2000).
317. M. Smid, Y. Wang, Y. Zhang, A.M. Sieuwerts, J. Yu, J.G. Klijn, J.A. Foekens, and J.W. Martens. Subtypes of breast cancer show preferential site of relapse. Cancer Res. 68:3108-3114 (2008).
318. M. Al-Hajj, M.S. Wicha, A. Benito-Hernandez, S.J. Morrison, and M.F. Clarke. Prospective identification of tumorigenic breast cancer cells. Proc Natl Acad Sci U S A. 100:3983-3988 (2003).
319. C.M. Fillmoreand C. Kuperwasser. Human breast cancer cell lines contain stem-like cells that self-renew, give rise to phenotypically diverse progeny and survive chemotherapy. Breast Cancer Res. 10:R25 (2008).
320. J.M. Heddleston, Z. Li, J.D. Lathia, S. Bao, A.B. Hjelmeland, and J.N. Rich. Hypoxia inducible factors in cancer stem cells. Br J Cancer. 102:789-795 (2010).
321. M. Moumen, A. Chiche, C. Decraene, V. Petit, A. Gandarillas, M.A. Deugnier, M.A. Glukhova, and M.M. Faraldo. Myc is required for beta-catenin-mediated mammary stem cell amplification and tumorigenesis. Mol Cancer. 12:132 (2013).
322. M. Moumen, A. Chiche, M.A. Deugnier, V. Petit, A. Gandarillas, M.A. Glukhova, and M.M. Faraldo. The proto-oncogene Myc is essential for mammary stem cell function. Stem Cells. 30:1246-1254 (2012).
323. J. Schust, B. Sperl, A. Hollis, T.U. Mayer, and T. Berg. Stattic: a small-molecule inhibitor of STAT3 activation and dimerization. Chem Biol. 13:1235-1242 (2006).
324. B. Das, R. Tsuchida, D. Malkin, G. Koren, S. Baruchel, and H. Yeger. Hypoxia enhances tumor stemness by increasing the invasive and tumorigenic side population fraction. Stem Cells. 26:1818-1830 (2008).
325. A. Jogi, I. Ora, H. Nilsson, A. Lindeheim, Y. Makino, L. Poellinger, H. Axelson, and S. Pahlman. Hypoxia alters gene expression in human neuroblastoma cells toward an immature and neural crest-like phenotype. Proc Natl Acad Sci U S A. 99:7021-7026 (2002).
326. V. Desplat, J.L. Faucher, F.X. Mahon, P. Dello Sbarba, V. Praloran, and Z. Ivanovic. Hypoxia modifies proliferation and differentiation of CD34(+) CML cells. Stem Cells. 20:347-354 (2002).
327. Y. Kim, Q. Lin, D. Zelterman, and Z. Yun. Hypoxia-regulated delta-like 1 homologue enhances cancer cell stemness and tumorigenicity. Cancer Res. 69:9271-9280 (2009).
328. A. Jaggupilliand E. Elkord. Significance of CD44 and CD24 as cancer stem cell markers: an enduring ambiguity. Clin Dev Immunol. 2012:708036 (2012).
329. J.A. Bertout, S.A. Patel, and M.C. Simon. The impact of O2 availability on human cancer. Nat Rev Cancer. 8:967-975 (2008).
330. J.M. Heddleston, Z. Li, R.E. McLendon, A.B. Hjelmeland, and J.N. Rich. The hypoxic microenvironment maintains glioblastoma stem cells and promotes reprogramming towards a cancer stem cell phenotype. Cell Cycle. 8:3274-3284 (2009).
331. T. van den Beucken, E. Koch, K. Chu, R. Rupaimoole, P. Prickaerts, M. Adriaens, J.W. Voncken, A.L. Harris, F.M. Buffa, S. Haider, M.H. Starmans, C.Q. Yao, M. Ivan, C. Ivan, C.V. Pecot, P.C. Boutros, A.K. Sood, M. Koritzinsky, and B.G. Wouters. Hypoxia promotes stem cell phenotypes and poor prognosis through epigenetic regulation of DICER. Nat Commun. 5:5203 (2014).
332. R.P. Hill, D.T. Marie-Egyptienne, and D.W. Hedley. Cancer stem cells, hypoxia and metastasis. Semin Radiat Oncol. 19:106-111 (2009).

333. K. Helczynska, A. Kronblad, A. Jogi, E. Nilsson, S. Beckman, G. Landberg, and S. Pahlman. Hypoxia promotes a dedifferentiated phenotype in ductal breast carcinoma in situ. Cancer Res. 63:1441-1444 (2003).
334. N. Platet, S.Y. Liu, M.E. Atifi, L. Oliver, F.M. Vallette, F. Berger, and D. Wion. Influence of oxygen tension on CD133 phenotype in human glioma cell cultures. Cancer Lett. 258:286-290 (2007).
335. I. Kryczek, Y. Lin, N. Nagarsheth, D. Peng, L. Zhao, E. Zhao, L. Vatan, W. Szeliga, Y. Dou, S. Owens, W. Zgodzinski, M. Majewski, G. Wallner, J. Fang, E. Huang, and W. Zou. IL-22(+)CD4(+) T cells promote colorectal cancer stemness via STAT3 transcription factor activation and induction of the methyltransferase DOT1L. Immunity. 40:772-784 (2014).
336. J. Wei, J. Barr, L.Y. Kong, Y. Wang, A. Wu, A.K. Sharma, J. Gumin, V. Henry, H. Colman, W. Priebe, R. Sawaya, F.F. Lang, and A.B. Heimberger. Glioblastoma cancer-initiating cells inhibit T-cell proliferation and effector responses by the signal transducers and activators of transcription 3 pathway. Mol Cancer Ther. 9:67-78 (2010).
337. W.J. Wong, B. Qiu, M.S. Nakazawa, G. Qing, and M.C. Simon. MYC degradation under low O2 tension promotes survival by evading hypoxia-induced cell death. Mol Cell Biol. 33:3494-3504 (2013).
338. C.V. Dang, J.W. Kim, P. Gao, and J. Yustein. The interplay between MYC and HIF in cancer. Nat Rev Cancer. 8:51-56 (2008).
339. M.R. Doherty, J.M. Smigiel, D.J. Junk, and M.W. Jackson. Cancer Stem Cell Plasticity Drives Therapeutic Resistance. Cancers (Basel). 8: (2016).
340. G. Lee, R.R. Hall, 3rd, and A.U. Ahmed. Cancer Stem Cells: Cellular Plasticity, Niche, and its Clinical Relevance. J Stem Cell Res Ther. 6: (2016).
341. M.C. Cabrera, R.E. Hollingsworth, and E.M. Hurt. Cancer stem cell plasticity and tumor hierarchy. World J Stem Cells. 7:27-36 (2015).
342. C.L. Chaffer, I. Brueckmann, C. Scheel, A.J. Kaestli, P.A. Wiggins, L.O. Rodrigues, M. Brooks, F. Reinhardt, Y. Su, K. Polyak, L.M. Arendt, C. Kuperwasser, B. Bierie, and R.A. Weinberg. Normal and neoplastic nonstem cells can spontaneously convert to a stem-like state. Proc Natl Acad Sci U S A. 108:7950-7955 (2011).
343. S.A. Mani, W. Guo, M.J. Liao, E.N. Eaton, A. Ayyanan, A.Y. Zhou, M. Brooks, F. Reinhard, C.C. Zhang, M. Shipitsin, L.L. Campbell, K. Polyak, C. Brisken, J. Yang, and R.A. Weinberg. The epithelial-mesenchymal transition generates cells with properties of stem cells. Cell. 133:704-715 (2008).
344. C. Scheeland R.A. Weinberg. Phenotypic plasticity and epithelial-mesenchymal transitions in cancer and normal stem cells? Int J Cancer. 129:2310-2314 (2011).
345. L. Vermeulen, E.M.F. De Sousa, M. van der Heijden, K. Cameron, J.H. de Jong, T. Borovski, J.B. Tuynman, M. Todaro, C. Merz, H. Rodermond, M.R. Sprick, K. Kemper, D.J. Richel, G. Stassi, and J.P. Medema. Wnt activity defines colon cancer stem cells and is regulated by the microenvironment. Nat Cell Biol. 12:468-476 (2010).
346. F. Rojo, J. Albanell, A. Rovira, J.M. Corominas, and F. Manzarbeitia. Targeted therapies in breast cancer. Semin Diagn Pathol. 25:245-261 (2008).
347. S. Nie, Y. Xing, G.J. Kim, and J.W. Simons. Nanotechnology applications in cancer. Annu Rev Biomed Eng. 9:257-288 (2007).
348. M.E. Davis, Z.G. Chen, and D.M. Shin. Nanoparticle therapeutics: an emerging treatment modality for cancer. Nat Rev Drug Discov. 7:771-782 (2008).
349. M.D. Wang, D.M. Shin, J.W. Simons, and S. Nie. Nanotechnology for targeted cancer therapy. Expert Rev Anticancer Ther. 7:833-837 (2007).
350. D.L. Nida, M.S. Rahman, K.D. Carlson, R. Richards-Kortum, and M. Follen. Fluorescent nanocrystals for use in early cervical cancer detection. Gynecol Oncol. 99:S89-94 (2005).

351. J. Yang, K. Eom, E.K. Lim, J. Park, Y. Kang, D.S. Yoon, S. Na, E.K. Koh, J.S. Suh, Y.M. Huh, T.Y. Kwon, and S. Haam. In situ detection of live cancer cells by using bioprobes based on Au nanoparticles. Langmuir. 24:12112-12115 (2008).
352. M.P. Melancon, W. Lu, Z. Yang, R. Zhang, Z. Cheng, A.M. Elliot, J. Stafford, T. Olson, J.Z. Zhang, and C. Li. In vitro and in vivo targeting of hollow gold nanoshells directed at epidermal growth factor receptor for photothermal ablation therapy. Mol Cancer Ther. 7:1730-1739 (2008).
353. C.R. Patra, R. Bhattacharya, E. Wang, A. Katarya, J.S. Lau, S. Dutta, M. Muders, S. Wang, S.A. Buhrow, S.L. Safgren, M.J. Yaszemski, J.M. Reid, M.M. Ames, P. Mukherjee, and D. Mukhopadhyay. Targeted delivery of gemcitabine to pancreatic adenocarcinoma using cetuximab as a targeting agent. Cancer Res. 68:1970-1978 (2008).
354. G. Wu, R.F. Barth, W. Yang, S. Kawabata, L. Zhang, and K. Green-Church. Targeted delivery of methotrexate to epidermal growth factor receptor-positive brain tumors by means of cetuximab (IMC-C225) dendrimer bioconjugates. Mol Cancer Ther. 5:52-59 (2006).
355. A.M. Masterand A. Sen Gupta. EGF receptor-targeted nanocarriers for enhanced cancer treatment. Nanomedicine (Lond). 7:1895-1906 (2012).
356. Y. Nagasaki, T. Kutsuna, M. Iijima, M. Kato, K. Kataoka, S. Kitano, and Y. Kadoma. Formyl-ended heterobifunctional poly(ethylene oxide): synthesis of poly(ethylene oxide) with a formyl group at one end and a hydroxyl group at the other end. Bioconjug Chem. 6:231-233 (1995).
357. X.B. Xiong, A. Mahmud, H. Uludag, and A. Lavasanifar. Conjugation of arginine-glycine-aspartic acid peptides to poly(ethylene oxide)-b-poly(epsilon-caprolactone) micelles for enhanced intracellular drug delivery to metastatic tumor cells. Biomacromolecules. 8:874-884 (2007).
358. R. Soudy, A. Gill, T. Sprules, A. Lavasanifar, and K. Kaur. Proteolytically stable cancer targeting peptides with high affinity for breast cancer cells. J Med Chem. 54:7523-7534 (2011).
359. M. Shahin, N. Safaei-Nikouei, and A. Lavasanifar. Polymeric micelles for pH-responsive delivery of cisplatin. J Drug Target. 22:629-637 (2014).
360. Ö. Topel, B.A. Çakır, L. Budama, and N. Hoda. Determination of critical micelle concentration of polybutadiene-block-poly(ethyleneoxide) diblock copolymer by fluorescence spectroscopy and dynamic light scattering. Journal of Molecular Liquids. 177:40-43 (2013).
361. E. Miranda, I.K. Nordgren, A.L. Male, C.E. Lawrence, F. Hoakwie, F. Cuda, W. Court, K.R. Fox, P.A. Townsend, G.K. Packham, S.A. Eccles, and A. Tavassoli. A cyclic peptide inhibitor of HIF-1 heterodimerization that inhibits hypoxia signaling in cancer cells. J Am Chem Soc. 135:10418-10425 (2013).
362. H. Maeda, J. Wu, T. Sawa, Y. Matsumura, and K. Hori. Tumor vascular permeability and the EPR effect in macromolecular therapeutics: a review. J Control Release. 65:271-284 (2000).
363. Y.I. Jeong, S.T. Kim, S.G. Jin, H.H. Ryu, Y.H. Jin, T.Y. Jung, I.Y. Kim, and S. Jung. Cisplatin-incorporated hyaluronic acid nanoparticles based on ion-complex formation. J Pharm Sci. 97:1268-1276 (2008).
364. Y. Mizumura, Y. Matsumura, T. Hamaguchi, N. Nishiyama, K. Kataoka, T. Kawaguchi, W.J. Hrushesky, F. Moriyasu, and T. Kakizoe. Cisplatin-incorporated polymeric micelles eliminate nephrotoxicity, while maintaining antitumor activity. Jpn J Cancer Res. 92:328-336 (2001).
365. E.C. Gryparis, M. Hatziapostolou, E. Papadimitriou, and K. Avgoustakis. Anticancer activity of cisplatin-loaded PLGA-mPEG nanoparticles on LNCaP prostate cancer cells. Eur J Pharm Biopharm. 67:1-8 (2007).
366. P. Xu, E.A. Van Kirk, W.J. Murdoch, Y. Zhan, D.D. Isaak, M. Radosz, and Y. Shen. Anticancer efficacies of cisplatin-releasing pH-responsive nanoparticles. Biomacromolecules. 7:829-835 (2006).

367. R.W. Staffhorst, K. van der Born, C.A. Erkelens, I.H. Hamelers, G.J. Peters, E. Boven, and A.I. de Kroon. Antitumor activity and biodistribution of cisplatin nanocapsules in nude mice bearing human ovarian carcinoma xenografts. Anticancer Drugs. 19:721-727 (2008).
368. J.H. Kim, Y.S. Kim, K. Park, S. Lee, H.Y. Nam, K.H. Min, H.G. Jo, J.H. Park, K. Choi, S.Y. Jeong, R.W. Park, I.S. Kim, K. Kim, and I.C. Kwon. Antitumor efficacy of cisplatin-loaded glycol chitosan nanoparticles in tumor-bearing mice. J Control Release. 127:41-49 (2008).
369. M. Kettering, H. Zorn, S. Bremer-Streck, H. Oehring, M. Zeisberger, C. Bergemann, R. Hergt, K.J. Halbhuber, W.A. Kaiser, and I. Hilger. Characterization of iron oxide nanoparticles adsorbed with cisplatin for biomedical applications. Phys Med Biol. 54:5109-5121 (2009).
370. M. Onoand M. Kuwano. Molecular mechanisms of epidermal growth factor receptor (EGFR) activation and response to gefitinib and other EGFR-targeting drugs. Clin Cancer Res. 12:7242-7251 (2006).
371. V.P. Torchilin, A.N. Lukyanov, Z. Gao, and B. Papahadjopoulos-Sternberg. Immunomicelles: targeted pharmaceutical carriers for poorly soluble drugs. Proc Natl Acad Sci U S A. 100:6039-6044 (2003).
372. W.J. Linand L.T. Kao. Cytotoxic enhancement of hexapeptide-conjugated micelles in EGFR high-expressed cancer cells. Expert Opin Drug Deliv. 11:1537-1550 (2014).
373. X.H. Peng, Y. Wang, D. Huang, H.J. Shin, Z. Chen, M.B. Spewak, H. Mao, X. Wang, Z.G. Chen, S. Nie, and D.M. Shin. Targeted delivery of cisplatin to lung cancer using ScFvEGFR-heparin-cisplatin nanoparticles. ACS Nano. 5:9480-9493 (2011).
374. G. Szakacs, J.K. Paterson, J.A. Ludwig, C. Booth-Genthe, and M.M. Gottesman. Targeting multidrug resistance in cancer. Nat Rev Drug Discov. 5:219-234 (2006).
375. T. Uchida, F. Rossignol, M.A. Matthay, R. Mounier, S. Couette, E. Clottes, and C. Clerici. Prolonged hypoxia differentially regulates hypoxia-inducible factor (HIF)-1alpha and HIF-2alpha expression in lung epithelial cells: implication of natural antisense HIF-1alpha. J Biol Chem. 279:14871-14878 (2004).
376. S. Chamboredon, D. Ciais, A. Desroches-Castan, P. Savi, F. Bono, J.J. Feige, and N. Cherradi. Hypoxia-inducible factor-1alpha mRNA: a new target for destabilization by tristetraprolin in endothelial cells. Mol Biol Cell. 22:3366-3378 (2011).
377. M.A. Swartz, N. Iida, E.W. Roberts, S. Sangaletti, M.H. Wong, F.E. Yull, L.M. Coussens, and Y.A. DeClerck. Tumor microenvironment complexity: emerging roles in cancer therapy. Cancer Res. 72:2473-2480 (2012).
378. P.C. Nowell. The clonal evolution of tumor cell populations. Science. 194:23-28 (1976).
379. J.E. Visvaderand G.J. Lindeman. Cancer stem cells: current status and evolving complexities. Cell Stem Cell. 10:717-728 (2012).
380. A. Mitra, L. Mishra, and S. Li. EMT, CTCs and CSCs in tumor relapse and drug-resistance. Oncotarget. 6:10697-10711 (2015).
381. Q. Li, J. Zhu, F. Sun, L. Liu, X. Liu, and Y. Yue. Oncostatin M promotes proliferation of ovarian cancer cells through signal transducer and activator of transcription 3. Int J Mol Med. 28:101-108 (2011).
382. S. Heptinstall, W.A. Groenewegen, P. Spangenberg, and W. Losche. Inhibition of platelet behaviour by feverfew: a mechanism of action involving sulphydryl groups. Folia Haematol Int Mag Klin Morphol Blutforsch. 115:447-449 (1988).
383. I.H. Hall, K.H. Lee, C.O. Starnes, Y. Sumida, R.Y. Wu, T.G. Waddell, J.W. Cochran, and K.G. Gerhart. Anti-inflammatory activity of sesquiterpene lactones and related compounds. J Pharm Sci. 68:537-542 (1979).
384. V. Pfaffenrath, H.C. Diener, M. Fischer, M. Friede, and H.H. Henneicke-von Zepelin. The efficacy and safety of Tanacetum parthenium (feverfew) in migraine prophylaxis--a double-blind,

multicentre, randomized placebo-controlled dose-response study. Cephalalgia. 22:523-532 (2002).
385. B. Pajak, B. Gajkowska, and A. Orzechowski. Molecular basis of parthenolide-dependent proapoptotic activity in cancer cells. Folia Histochem Cytobiol. 46:129-135 (2008).
386. J.M. Song, X. Qian, P. Upadhyayya, K.H. Hong, and F. Kassie. Dimethylaminoparthenolide, a water soluble parthenolide, suppresses lung tumorigenesis through down-regulating the STAT3 signaling pathway. Curr Cancer Drug Targets. 14:59-69 (2014).
387. R. Shanmugam, P. Kusumanchi, H. Appaiah, L. Cheng, P. Crooks, S. Neelakantan, T. Peat, J. Klaunig, W. Matthews, H. Nakshatri, and C.J. Sweeney. A water soluble parthenolide analog suppresses in vivo tumor growth of two tobacco-associated cancers, lung and bladder cancer, by targeting NF-kappaB and generating reactive oxygen species. Int J Cancer. 128:2481-2494 (2011).
388. P.M. Bork, M.L. Schmitz, M. Kuhnt, C. Escher, and M. Heinrich. Sesquiterpene lactone containing Mexican Indian medicinal plants and pure sesquiterpene lactones as potent inhibitors of transcription factor NF-kappaB. FEBS Lett. 402:85-90 (1997).
389. J. Wen, K.R. You, S.Y. Lee, C.H. Song, and D.G. Kim. Oxidative stress-mediated apoptosis. The anticancer effect of the sesquiterpene lactone parthenolide. J Biol Chem. 277:38954-38964 (2002).
390. E.A. Curry, 3rd, D.J. Murry, C. Yoder, K. Fife, V. Armstrong, H. Nakshatri, M. O'Connell, and C.J. Sweeney. Phase I dose escalation trial of feverfew with standardized doses of parthenolide in patients with cancer. Invest New Drugs. 22:299-305 (2004).
391. R. Shanmugam, V. Jayaprakasan, Y. Gokmen-Polar, S. Kelich, K.D. Miller, M. Yip-Schneider, L. Cheng, P. Bhat-Nakshatri, G.W. Sledge, Jr., H. Nakshatri, Q.H. Zheng, M.A. Miller, T. DeGrado, G.D. Hutchins, and C.J. Sweeney. Restoring chemotherapy and hormone therapy sensitivity by parthenolide in a xenograft hormone refractory prostate cancer model. Prostate. 66:1498-1511 (2006).
392. M.B. Lutz, N. Kukutsch, A.L. Ogilvie, S. Rossner, F. Koch, N. Romani, and G. Schuler. An advanced culture method for generating large quantities of highly pure dendritic cells from mouse bone marrow. J Immunol Methods. 223:77-92 (1999).
393. O. Molavi, A. Mahmud, S. Hamdy, R.W. Hung, R. Lai, J. Samuel, and A. Lavasanifar. Development of a poly(d,l-lactic-co-glycolic acid) nanoparticle formulation of STAT3 inhibitor JSI-124: implication for cancer immunotherapy. Mol Pharm. 7:364-374 (2010).
394. C.J. Henry, D.A. Ornelles, L.M. Mitchell, K.L. Brzoza-Lewis, and E.M. Hiltbold. IL-12 produced by dendritic cells augments CD8+ T cell activation through the production of the chemokines CCL1 and CCL17. J Immunol. 181:8576-8584 (2008).
395. R.D. Dabholkar, R.M. Sawant, D.A. Mongayt, P.V. Devarajan, and V.P. Torchilin. Polyethylene glycol-phosphatidylethanolamine conjugate (PEG-PE)-based mixed micelles: some properties, loading with paclitaxel, and modulation of P-glycoprotein-mediated efflux. Int J Pharm. 315:148-157 (2006).
396. L. Mu, T.A. Elbayoumi, and V.P. Torchilin. Mixed micelles made of poly(ethylene glycol)-phosphatidylethanolamine conjugate and d-alpha-tocopheryl polyethylene glycol 1000 succinate as pharmaceutical nanocarriers for camptothecin. Int J Pharm. 306:142-149 (2005).
397. R.R. Sawant, R.M. Sawant, and V.P. Torchilin. Mixed PEG-PE/vitamin E tumor-targeted immunomicelles as carriers for poorly soluble anti-cancer drugs: improved drug solubilization and enhanced in vitro cytotoxicity. Eur J Pharm Biopharm. 70:51-57 (2008).
398. J.C. Chen, M.H. Chiu, R.L. Nie, G.A. Cordell, and S.X. Qiu. Cucurbitacins and cucurbitane glycosides: structures and biological activities. Nat Prod Rep. 22:386-399 (2005).

399. Y. Nefedova, P. Cheng, D. Gilkes, M. Blaskovich, A.A. Beg, S.M. Sebti, and D.I. Gabrilovich. Activation of dendritic cells via inhibition of Jak2/STAT3 signaling. J Immunol. 175:4338-4346 (2005).
400. M.A. Blaskovich, J. Sun, A. Cantor, J. Turkson, R. Jove, and S.M. Sebti. Discovery of JSI-124 (cucurbitacin I), a selective Janus kinase/signal transducer and activator of transcription 3 signaling pathway inhibitor with potent antitumor activity against human and murine cancer cells in mice. Cancer Res. 63:1270-1279 (2003).
401. O. Molavi, Z. Ma, S. Hamdy, R. Lai, A. Lavasanifar, and J. Samuel. Synergistic antitumor effects of CpG oligodeoxynucleotide and STAT3 inhibitory agent JSI-124 in a mouse melanoma tumor model. Immunol Cell Biol. 86:506-514 (2008).
402. O. Molavi, Z. Ma, S. Hamdy, A. Lavasanifar, and J. Samuel. Immunomodulatory and anticancer effects of intra-tumoral co-delivery of synthetic lipid A adjuvant and STAT3 inhibitor, JSI-124. Immunopharmacol Immunotoxicol. 31:214-221 (2009).
403. X. Shi, B. Franko, C. Frantz, H.M. Amin, and R. Lai. JSI-124 (cucurbitacin I) inhibits Janus kinase-3/signal transducer and activator of transcription-3 signalling, downregulates nucleophosmin-anaplastic lymphoma kinase (ALK), and induces apoptosis in ALK-positive anaplastic large cell lymphoma cells. Br J Haematol. 135:26-32 (2006).
404. O. Molavi, Z. Ma, A. Mahmud, A. Alshamsan, J. Samuel, R. Lai, G.S. Kwon, and A. Lavasanifar. Polymeric micelles for the solubilization and delivery of STAT3 inhibitor cucurbitacins in solid tumors. Int J Pharm. 347:118-127 (2008).
405. A. Mahmud, S. Patel, O. Molavi, P. Choi, J. Samuel, and A. Lavasanifar. Self-associating poly(ethylene oxide)-b-poly(alpha-cholesteryl carboxylate-epsilon-caprolactone) block copolymer for the solubilization of STAT-3 inhibitor cucurbitacin I. Biomacromolecules. 10:471-478 (2009).
406. O. Molavi, A. Shayeganpour, V. Somayaji, S. Hamdy, D.R. Brocks, A. Lavasanifar, G.S. Kwon, and J. Samuel. Development of a sensitive and specific liquid chromatography/mass spectrometry method for the quantification of cucurbitacin I (JSI-124) in rat plasma. J Pharm Pharm Sci. 9:158-164 (2006).
407. P. Costaand J.M. Sousa Lobo. Modeling and comparison of dissolution profiles. Eur J Pharm Sci. 13:123-133 (2001).
408. A. Schulz, S. Jaksch, R. Schubel, E. Wegener, Z. Di, Y. Han, A. Meister, J. Kressler, A.V. Kabanov, R. Luxenhofer, C.M. Papadakis, and R. Jordan. Drug-induced morphology switch in drug delivery systems based on poly(2-oxazoline)s. ACS Nano. 8:2686-2696 (2014).

Appendix A

Development of Other Drug Loaded Micellar Formulation for Inhibitors of STAT3

A.1 Development of STAT3 Targeting Parthenolide Nano-carriers for Cancer Immunotherapy

A.1.1 Introduction

Parthenolide (PTL) isolated from Tanacetum parthenium (commonly referred as feverfew), is a naturally occurring sesquiterpene lactone used in the treatment of fever, migraine headaches, rheumatoid arthritis, and also as an anti-inflammatory agent (382-384). The PTL molecule and its analogs have shown to promotes apoptosis in cancer cells by inducing oxidative stress while inhibiting the cancer promoting transcription factor, nuclear factor kappa B (NFκB) and signal transducer and activator of transcription 3 (STAT3) (385-387). These unique properties are due to its α-methylene-γ-lactone ring and epoxide interacting with nucleophilic sites of biological molecules (388). PTL also generates reactive oxygen species (ROS) by depleting glutathione and other thiols and activates caspases and induces apoptosis (389).However, despite its promising *in vitro* activity, this potent natural product has a major limitation which prevents its further development as a therapeutic agent, that is, its poor water-solubility (0.169 µM maximum solubility in serum) (390). As shown in a study by *Curry et. al.*, parthenolide could not be detected in plasma when it is administered in humans as part of the herbal supplement, "feverfew" due to PTL's low bioavailability as a result of its poor solubility (390). Parthenolide limited *in vivo* activity was also correlated to its poor bioavailability in a separate study (391). Hence, in our study we opted to; a) investigate the STAT3 inhibitory effect of PTL in B16.F10 melanoma cells; b) study the direct anti-cancer activity of PTL by assessing its cytotoxicity against B16.F10; c) investigate the functional activity of PTL on tolerogenic dendritic cells (DC)s by pre-exposure of DCs to the supernatant of PTL-treated B16.F10 cells and measuring the level of expression of CD86 and CD40 on DCs and IL-12 production upon lipopolysaccharide (LPS) stimulation; d) increase the aqueous solubility of PTL by developing the PTL-loaded polymeric nano-carriers; and assess the potential of developed delivery systems for tumor targeted delivery of PTL.

A.1.2 Materials and Methods

A.1.2.1 Materials

Parthenolide, lipopolysaccharide (LPS) and bovine serum albumin (BSA) powder were purchased from Sigma (St. Louis, MO). Cell culture media RPMI 1640, fetal bovine serum (FBS), and penicillin-

streptomycin-L-glutamine were purchased from GIBCO, Life Technologies Inc. (Carlsbad, CA). Murine interleukin-12 (IL-12) p70 ELISA (enzyme-linked immunosorbent assay) Ready-SET-Go® kits, Fluorescein isothiocyanate (FITC) conjugated anti-mouse CD86 (B7-2) (GL7) mAb, Phycoerythrin-Cy5 (PE-Cy5) conjugated anti-mouse CD40 mAb, and purified anti-mouse CD16/CD32 (Fcχ-III/II receptor) were purchased from e-Biosciences (San Diego, CA). Recombinant murine granulocyte-macrophage colony-stimulating factor (GM-CSF) was purchased from Peprotech (Rocky Hill, NJ).

A.1.2.2 Cell Line

The murine melanoma cancer cell line B16.F10 of C57BL/6 origin was obtained from American Type Culture Collection (ATCC) (Manassas, VA). The B16.F10 cells were grown in RPMI-1640 supplemented with 10% FBS, 2 mM L-glutamine and 100 IU/mL penicillin/streptomycin at 37 °C in 5% CO_2 atmosphere.

A.1.2.3 Generation of Bone marrow Derived Dendritic Cells (BMDCs)

DC primary cultures were generated from murine bone marrow precursors from femurs of C57Bl/6 mice in complete media in the presence of GM-CSF as described previously with minor modifications (392). Briefly, femurs were removed and purified from surrounding tissue. Both ends of the intact bone were cut with scissors and the bone marrow was flushed with sterile PBS using an insulin syringe. Leukocytes were triturated and filtered through a nylon screen (40 μm cell strainer) to obtain a single cell suspension. Bone marrow leukocytes were washed and 2×10^6 cells were seeded in 100 mm non-treated cell culture dishes with 10 mL DC complete medium (RPMI-1640 with penicillin-streptomycin-L-glutamine, 10 % heat-inactivated FBS supplemented with 20 ng/mL of GM-CSF). At day 3, another 10 mL complete medium was added to the plates. At day 6, 10 mL of culture media was replaced with 10 mL fresh complete medium. At day 7, the cells were ready for use.

A.1.2.4 Generation of Tumor-Induced Immunosuppressed DCs

Tumor-induced immunosuppressed DCs were generated according to a method described previously with some modifications (393). Bone marrow leukocytes were obtained from C57BL/6 mice according to the method described in Section A.1.2.3. above. 2×10^6 cells were seeded in 100 mm non-treated cell culture dishes with 10 mL DC complete medium (RPMI-1640 with penicillin-streptomycin-L-glutamine, 10 % heat-inactivated FBS supplemented with 20 ng/mL of GM-CSF). At day 3, another 10 mL of DC complete medium (RPMI-1640 with penicillin-streptomycin-L-glutamine, 10 % heat-inactivated FBS supplemented with 20 ng/mL of GM-CSF) was added to the plates. At day 6, 10 mL of culture media was

replaced with 10 mL of conditioned media. To compensate for the serum free conditioned media, 1 ml FBS was added to 20 mL mixture to reach 10% FBS concentration. At day 7, the cells were ready for use.

A.1.2.5 Generation of Conditioned Media for B16.F10 Cells

To make B16.F10 conditioned media, 4×10^5 B16 cells were seeded in 6-well treated plate containing RPMI-1640 supplemented with 10% FBS, 2 mM L-glutamine and 100 IU/mL penicillin/streptomycin at 37 °C in 5% CO_2 overnight. At day 1 the media was replaced with serum free RPMI-1640 supplemented with 2 mM L-glutamine and 100 IU/mL penicillin/streptomycin containing different concentration of parthenolide (4, 0.4, and 0.04 μM). B16 cells grown in serum free RPMI-1640 supplemented with 2 mM L-glutamine and 100 IU/mL penicillin/streptomycin without parthenolide treatment were used as control for a drug. At day 2, the media was replaced with fresh one supplemented with 10% FBS, 2 mM L-glutamine and 100 IU/mL penicillin/streptomycin for all the control and treatment groups. At day 3, the supernatants were then collected, centrifuged (5 min, 500 × g) and stored at -20 °C and used later in the experiments.

A.1.2.6 Assessment of the Functional Characteristics of DCs by Flow Cytometry and ELISA

Tumor-induced immunosuppressed DCs were obtained according to the method described in Section A.1.2.4 above. They were treated with conditioned B16.F10 medium containing different concentration of parthenolide (4, 0.4, and 0.04 μM) or drug free medium on day 6 of their culture for 24 h. After 12 h incubation (on day 7), cells were treated with 100 ng/mL of lipopolysaccharide (LPS). BMDCs grown in DC complete medium without conditioned media and treated on day 7 with 100 ng/mL of LPS was used as control. After 24 h parthenolide treatment, cells were harvested and the supernatant was collected and stored in -20 °C until further use. The cells were then washed twice with sterile PBS. Cell suspensions consisting of 5×10^5 cells/100 μL were prepared in FACS buffer (PBS containing 2% FBS) and incubated with anti-mouse CD16/CD32 mAb to block Fcγ receptors for 15 min before incubating with anti-CD86 with FITC-conjugated secondary antibody, or anti-CD40 with PE-Cy5-conjugated secondary antibody for 30 min. The cells were then washed twice with FACS buffer. The samples were acquired on a BD FACSCalibur flow cytometer and the data was analyzed with FCS Express software.

The previously collected supernatants were analyzed for the level of IL-12 by ELISA using the commercially available ELISA kits in a 96-well microplate according to the manufacturer's instructions. The samples were analyzed using a microplate reader Powerwave with KC Junior Software (BioTek, Winooski, VT) at OD of 450 nm. The minimum detection level of the IL-12 cytokines was 15 pg/mL.

A.1.2.7 Preparation of Polymeric Micelles

A.1.2.7.1 Co-solvent Evaporation (Adding Organic Solvent to Water)

Preparation of colloidal dispersions from synthesized block copolymers was tried by co-solvent evaporation method adding organic solvent to water. Briefly, the block copolymer (20 mg) was dissolved in tetrahydrofuran (THF) (2.5 mL). After sonication for 10 min, this solution was added in a drop wise manner to 5 mL deionized water while stirring. The solution was stirred for 24 h under a fume hood to remove the organic solvent by evaporation. Drug-loaded polymeric micelles were prepared using the same procedure, except PTL (1 mg) was dissolved along with the block copolymers in THF. After the evaporation of THF, the micelle solution was centrifuged to remove the precipitated drug.

A.1.2.7.2 Co-Solvent Evaporation (Adding Water to Organic Solvent)

Preparation of colloidal dispersions from synthesized block copolymers was tried by co-solvent evaporation method adding water to organic solvent. Briefly, the block copolymer (20 mg) was dissolved in tetrahydrofuran (THF) (2.5 mL). After sonication for 10 min, 5 mL deionized water was added to this solution in a drop wise manner while stirring. The solution was stirred for 24 h under a fume hood to remove the organic solvent by evaporation. Drug-loaded polymeric micelles were prepared using the same procedure, except PTL (1 mg) was dissolved along with the block copolymers in THF. After the evaporation of THF, the micelle solution was centrifuged to remove the precipitated drug.

A.1.2.7.3 Film Formation

Preparation of colloidal dispersions from synthesized block copolymers was tried by film method. Briefly, the block copolymer (20 mg) was dissolved in the mixture of $CHCl_3$ (14 mL) and dichloromethane (0.5 mL). After sonication for 30 min, this solution was transferred to a round bottom flask. To remove the organic solvents, vacuum was applied overnight using a rotary evaporator. After complete organic solvent evaporation, 50 °C deionized water (10 mL) was added to the round bottom flask and vortexed for 10 min following by centrifugation (30 min, 2000× rmp). Drug-loaded polymeric micelles were prepared using the same procedure, except PTL (1 mg) was dissolved along with the block copolymers in the mixture of $CHCl_3$ and dichloromethane.

A.1.2.7.4 Preparation of PTL-Loaded Micelles by Addition of Vitamin E to Micellar Formulation

Drug-loaded polymeric micelles were prepared according to the method described in section A.1.2.7.1 above, except vitamin E-D-alpha tocopheryl polyethyleneglycol succinate; E-TPGS (2 mg) was dissolved

along with the block copolymers (20 mg) and PTL (1 mg) in THF. After the evaporation of THF, the micelle solution was centrifuged to remove the precipitated drug.

A.1.2.8 Release of Parthenolide from Block Copolymer Micelles

Release of free PTL (2% THF solution) and PTL–loaded micelles was assessed in deionized water at 37 °C. PTL-loaded micelle (5 mL micellar formulation containing 1 mg PTL) was transferred to a dialysis bag (MWCO - 3.5 kDa). The dialysis bag was placed in 500 mL of deionized water and release study was performed in a shaking water bath at 37 °C. At selected time intervals, the release media was replaced, and aliquots of 200 µL were withdrawn from the inside of the dialysis bag and analyzed by LC-MS.

A 2795 LC analytical (Waters Corp., United States) equipped with Xterra MS C18 3.5 µm column (2.1 × 50 mm) was used. Gradient elution was performed at a flow rate of 0.2 mL/min. The mobile phase consisted of methanol (solution A) and 0.2% TFA in H_2O (solution B). The mobile phase was programmed as follows: (1) 60% A for 0 min, (2) linear gradient from 60% A to 90% A in 8 min, (3) 90% A for 2 min, (4) linear gradient from 90% A to 60% A in 1 min. The standard free parthenolide eluted at retention time ~3 min and its presence was later confirmed with the electrospray positive (ESI^+) (ZQ 4000 MS spectrometer, Waters Corp., United States). Mass analysis showed $[M-17]^+$ for the parthenolide as 231 (calculated 248.37 g/mol). Mefnamic acid was used as an internal standard eluted at retention time ~8 min. Mass analysis showed $[M + H]^+$ for the mefnamic acid as 242 (calculated 241 g/mol).

A.1.3. Results and Discussion

A.1.3.1 Cell Viability Studies

The anti-cancer activity of parthenolide against murine B16.F10 melanoma cell line was investigated using MTT assay. As shown in **Figure A.1.1a**, treatment of B16.F10 cells with increasing concentrations of drug resulted in a significant loss of cell viability at both 24 h (IC_{50} 19.00 ± 0.13 µM) and 48 h (IC_{50} 10.95 ± 0.38 µM).

A.1.3.2 STAT3 Inhibitory Activity of Parthenolide

The STAT3 inhibitory activity of parthenolide against murine B16.F10 melanoma cell line is shown in **Figure A.1.1b**. Interestingly, treatment of B16.F10 cells with lower concentrations of parthenolide (0.04 µM) resulted in a significant suppression of pSTAT3 level after 24 h treatment. However, no reduction in pSTAT3 expression was observed with higher concentration of the drug (4 µM). This can point to the potential benefit of a sustained release formulation for PTL activity as a STAT3 inhibitor.

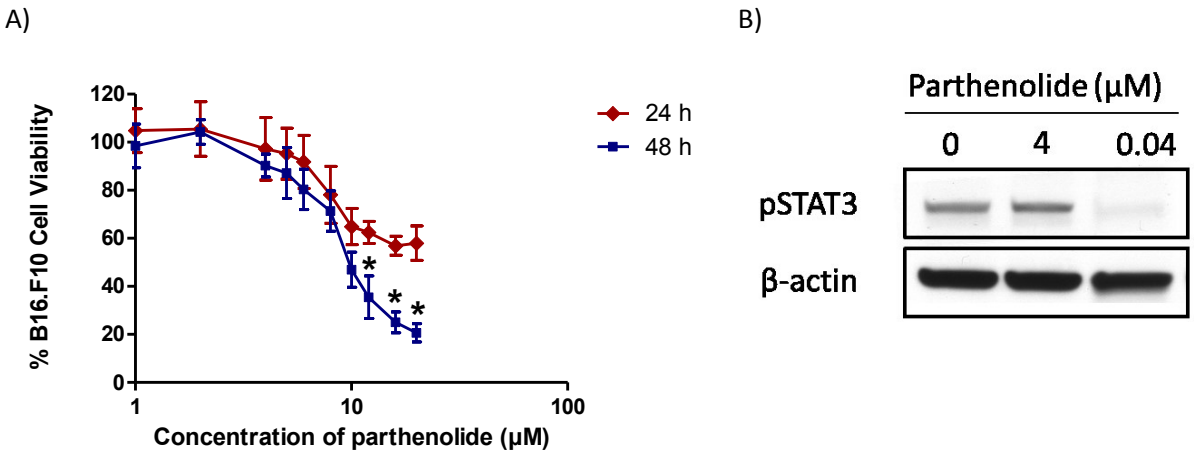

Figure A.1.1 Assessment of the anticancer activity of parthenolide against B16.F10 melanoma. **(a)** Drug sensitivity of cells was measured by MTT assay for 24 h and 48 h treatment with parthenolide. (*) denotes a significant difference compared to 24 h group at each individual parthenolide concentration (Student's *t* test, $p<0.05$). **(b)** pSTAT3 inhibitory effect of parthenolide. B16.F10 cells were treated with two concentrations of parthenolide for 24 h. Then cells were lysed and level of pSTAT3 expression was analyzed by immunoblotting.

A.1.3.3 Immunomodulatory Effects of Parthenolide on B16.F10 Tumor Induced Immune-Suppressed BMDCs

In contrast to untreated BMDCs, the BMDCs pretreated with B16.F10 tumor supernatant, showed decrease in the expression of maturation markers, i.e., CD40 and CD86, and secretion of IL-12 following LPS exposure ($p<0.05$, one way ANOVA; *post-hoc* Dunnett T3) (**Figure A.1.2 a-c**). Parthenolide was able to reverse the suppressive effects of tumor on CD86 expression in LPS exposed BMDCs ($p<0.05$, one-way ANOVA; *post-hoc* Dunnett T3). No significant difference in CD40 expression was observed for the same treatment groups, however ($p>0.05$, one-way ANOVA; *post-hoc* Dunnett T3).

IL-12 is produced by mature DCs and plays an important role in Th1 immune responses by augmenting IFN-γ production (394). Although, treatment with parthenolide increased the secretion of IL-12 from tumor suppressed BDMCs in the presence of LPS, the difference wasn't significant ($p>0.05$, one-way ANOVA; *post-hoc* Dunnett T3 test, $p>0.05$).

A

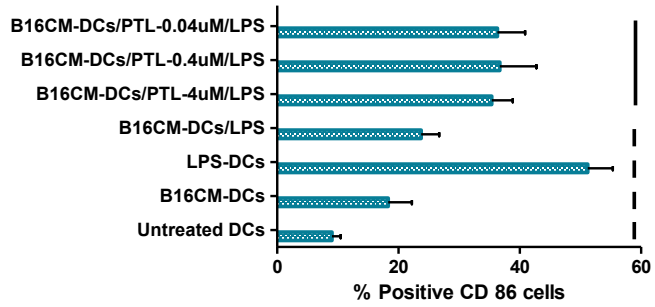

B

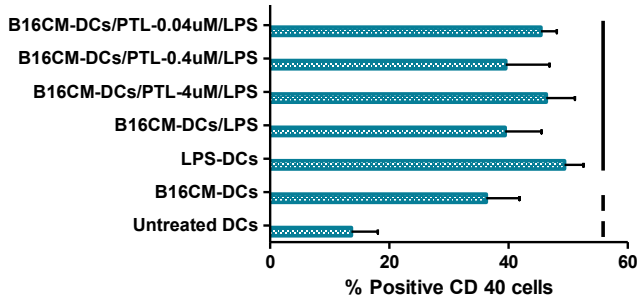

C

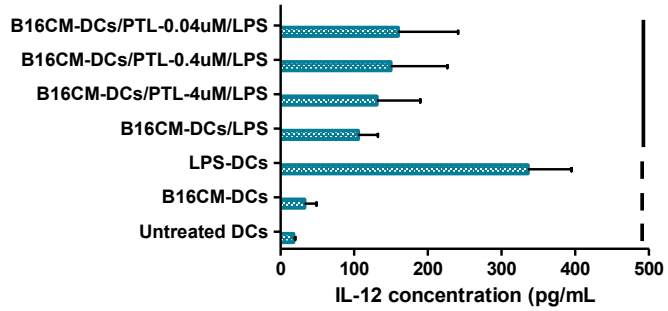

Figure A.1.2 The effects of parthenolide on the maturation and activation of B16.F10 tumor induced immune-suppressed BMDCs. BMDCs treated with B16.F10 tumor supernatant were analyzed by flow cytometry for upregulation of **(a)** CD86 and **(b)** CD40, and by ELISA for secretion of **(c)** IL-12. Each bar represents mean ± SD (n=3). For **(a)**, **(b)**, and **(c)**, Continuous lines over the data bars indicate lack of significance between groups encompassed by the lines; groups not encompassed within lines are significantly different from those encompassed by the lines (one way ANOVA followed by a *post-hoc* Dunnett T3 test, $p<0.05$).

A.1.3.4 Characterization of PTL-Loaded Polymeric Micelles

Polymeric micellar formulations of parthenolide based on different di and triblock block copolymers were developed. First the effect of micellar preparation method on size for empty and PTL-loaded micelles was investigated (**Table A.1.1**). Micelles of different di and triblock block copolymers were prepared by co-solvent evaporation (adding water to organic solvent), co-solvent evaporation (adding organic solvent to water) and film methods. Co-solvent evaporation method (adding water to organic solvent) resulted in micelles with the smallest size compared to the other two methods for both empty

and PTL-loaded micelles. The obtained sizes for micelles prepared by co-solvent evaporation (adding organic solvent to water) and film methods were similar for empty and PTL-loaded micelles (**Table A.1.1**).

Table A.1.1 Effect of method of micellar preparation on the size of empty and PTL loaded micelles (Diameter ± SD (nm))[a].

Polymer	PTL	Co-solvent evaporation (adding organic solvent to water)	Co-solvent evaporation (adding water to organic solvent)	Film
PEO-PLLA	Empty	33.39 ± 1.48	14.97 ± 1.03	34.75 ± 1.56
PEO-PD/LLA		34.38 ± 0.25	16.11 ± 1.15	36.40 ± 2.20
PEO-PLLA-PBCL		26.82 ± 2.09	23.13 ± 2.09	36.95 ± 3.37
PEO-PD/LLA-PBCL		25.36 ± 1.31	23.37 ± 1.53	37.22 ± 2.63
PEO-PLLA	Loaded	53.28 ± 1.06	30.52 ± 1.25	43.55 ± 3.28
PEO-PD/LLA		50.40 ± 2.55	28.28 ± 2.09	39.83 ± 2.24
PEO-PLLA-PBCL		39.29 ± 3.66	45.66 ± 1.41	44.24 ± 2.30
PEO-PD/LLA-PBCL		46.41 ± 4.41	33.74 ± 3.11	46.14 ± 3.30

[a]Z average measured by DLS.

In the next step, encapsulation efficiency (%EE) and drug loading (%DL) for PTL-loaded micelles prepared by co-solvent evaporation method (adding organic solvent to water) was measured (**Table A.1.2**) and drug release behaviour was studied (**Figure A.1.3**). In spite of having high EE and DL for different micellar formulations, the release of parthenolide was fast and micelles were unable to significantly sustain the release of drug in vitro under sink condition (**Figure A.1.3**). This observation may imply the localization of parthenolide in the core/shell interface rather than the micellar core.

Table A.1.2 Characterization of PTL loaded micelles.

Polymer	EE% ± SD[a]	DL% ± SD[b]
PEO-PCL	75.03 ± 3.91	3.75 ± 0.19
PEO-PLLA	92.24 ± 10.27	4.61 ± 1.16
PEO-PD/LLA	91.98 ± 8.26	4.59 ± 0.41
PEO-PDLLA50-50-PBCL	76.50 ± 2.12	3.82 ± 0.20
PEO-PDLLA20-80-PBCL	77.53 ± 3.53	3.87 ± 0.17

[a] Encapsulation efficiency $(\%) = \frac{the\ amount\ of\ encapsulated\ parthenolide}{the\ total\ feeding\ amount\ of\ parthenolide} \times 100.$

[b] Drug loading$(\%) = \frac{the\ amount\ of\ encapsulated\ parthenolide}{the\ total\ amount\ of\ polymer} \times 100.$

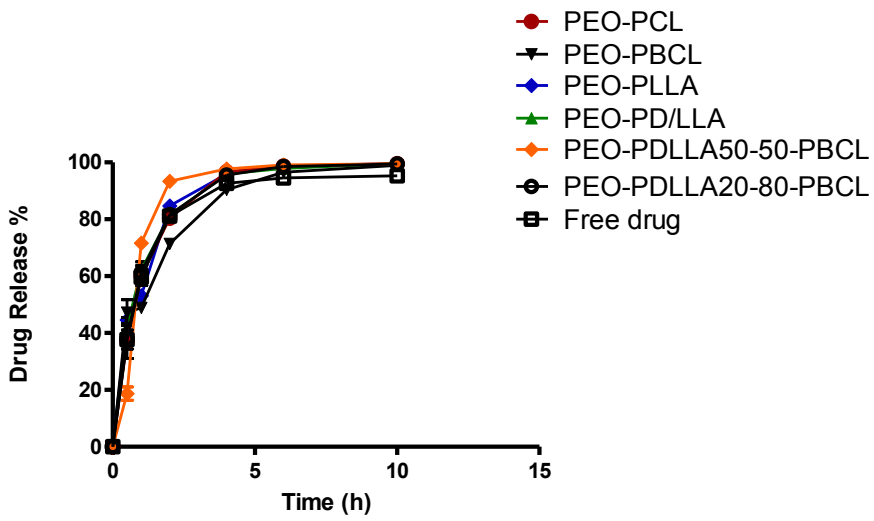

Figure A.1.3 Release profiles of parthenolide from micelles of different di and triblock copolymers. Data are represented as mean ± SD (n = 3). Parthenolide loaded micelles of different copolymers showed similar rate of release as a free drug (f_2 > 50).

Lastly to sustain the release of drug from micelles, we attempted to modulate the solubilization capacity of micelles by using vitamin E-D-alpha tocopheryl polyethyleneglycol succinate; E-TPGS (395). Vitamin E-TPGS has been used as a solubilizer, absorption enhancer, and a vehicle for lipid-based drug delivery formulations (396, 397). However, addition of vitamin E-TPGS to our formulation did not improve the encapsulation efficiency (**Table A.1.3**) or drug release profile as compared to micelles without vitamin E-TPGS or free drug (**Figure A.1.4**). The release of parthenolide was fast and micelles were unable to significantly sustain the release of drug *in vitro* under sink condition (**Figure A.1.4**). This observation may imply the localization of parthenolide in the core/shell interface rather than the micellar core.

Table A.1.3 Effect of addition of vitamin E-TPGS on encapsulation efficiency of PTL loaded micelles prepared by co-solvent evaporation method (adding organic solvent to water).

Polymer		% EE[a]
PEO-PBCL	W/O vit-E	96.80 ± 7.15
PEO-PCL		75.27 ± 5.40
PEO-PBCL	With vit-E	97.29 ± 4.66
PEO-PCL		84.31 ± 5.15

[a] Encapsulation efficiency $(\%) = \frac{the\ amount\ of\ encapsulated\ parthenolide}{the\ total\ feeding\ amount\ of\ parthenolide} \times 100.$

A)

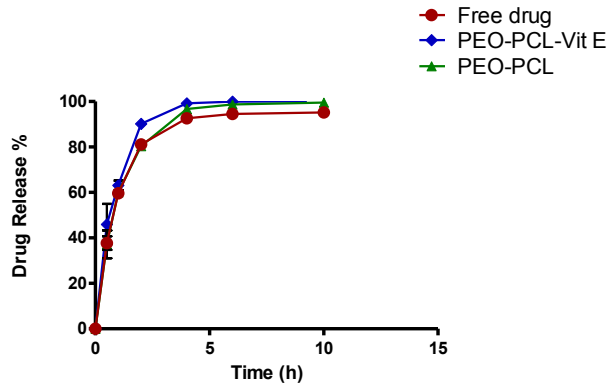

B)

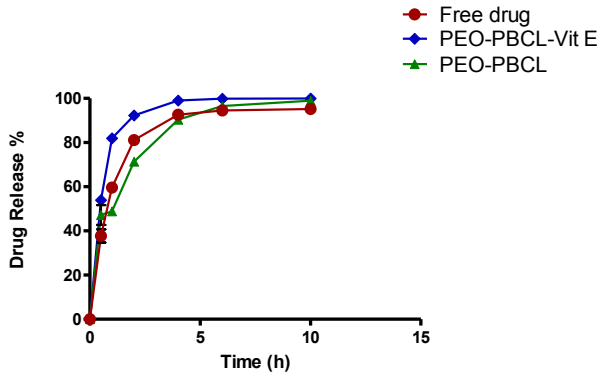

Figure A.1.4 Assessing the effect of vitamin E addition to micellar formulation on the release profile of parthenolide from **(a)** PEO-PBCL and **(b)** PEO-PCL micelles as compared to free drug. Data are represented as mean ± SD (n = 3).

A.1.4 Conclusion

Release of the drug from the micellar carrier must be controlled to attain sustained drug release and/or insure the same fate for the incorporated drug and the micellar carrier for the purpose of targeted drug delivery. Since the release of parthenolide was fast and micelles were unable to significantly sustain the release of drug in vitro under sink condition as well as we did not observe a significant immunomodulatory effects of parthenolide we decided to not continue with this project.

A.2 Development of STAT-3 Targeting JSI-124 Nano-Carriers for Cancer Therapy

A.2.1. Introduction

JSI-124 (cucrbitacin I) belongs to a group of natural products called cucurbitacins, which have been isolated from various plant families such as Cucurbitaceae (398). JSI-124 has been identified as a potent inhibitor of the JAK/STAT3 pathway and has been studied extensively for its direct anti-tumor effect and role in enhancing cancer immunotherapy in several human and murine models (393, 399-402). Previous studies suggested the role of JSI-124 in activation of phosphatases or in activation of certain physiological inhibitors that can directly or indirectly regulate STAT3 activation (400, 403). Our research group has previously reported on the development of polymeric micellar formulations that were successful in increasing the solubility of JSI-124 and maintaining its cytotoxicity towards B16 melanoma cells, but were unable to significantly hold on their encapsulated JSI-124 for a long time, *in vitro* (404,

405). Thus, here development of new polymeric micellar formulation for JSI-124 using different di and triblock copolymers was investigated.

A.2.2 Materials and Methods

A.2.2.1 Materials

JSI-124 was purchased from ABCR GmbH and Co. KG (Karlsruhe, Germany). L-lactide (98%) and meso D/L-lactide (99%) were purchased from Alfa Aesar, Lancashire, UK. D-lactide (98%) was a generous gift from Purac, Schiedam, Netherlands. Methoxy-PEO 5000 (MePEO), and tin(II) bis(2-ethylhexanoate) (stannous octoate) were obtained from Sigma, St Louis, MO, USA. Stannous octoate was dried and purified using anhydrous magnesium sulfate, dry toluene and vacuum distillation (253). α-benzylcarboxylate-ε-caprolactone (BCL) was synthesized by Alberta Research Chemicals Inc. (ARCI, Edmonton, AB, Canada) based on methods published previously by our group (266). All other chemicals and reagents used were of analytical grade.

A.2.2.2 Preparation of Polymeric Micelles

A.2.2.2.1 Co-Solvent Evaporation (Adding Organic Solvent to Water)

Preparation of colloidal dispersions from synthesized block copolymers was tried by co-solvent evaporation method adding organic solvent to water. Briefly, the block copolymer (20 mg) was dissolved in tetrahydrofuran (THF) (2.5 mL). After sonication for 10 min, this solution was added in a drop wise manner to 5 mL deionized water while stirring. The solution was stirred for 24 h under a fume hood to remove the organic solvent by evaporation. Drug-loaded polymeric micelles were prepared using the same procedure, except JSI-124 (1 mg) was dissolved along with the block copolymers in THF. After the evaporation of THF, the micelle solution was centrifuged to remove the precipitated drug.

A.2.2.2.2 Co-Solvent Evaporation (Adding Water to Organic Solvent)

Preparation of colloidal dispersions from synthesized block copolymers was tried by co-solvent evaporation method adding water to organic solvent. Briefly, the block copolymer (20 mg) was dissolved in tetrahydrofuran (THF) (2.5 mL). After sonication for 10 min, 5 mL deionized water was added to this solution in a drop wise manner while stirring. The solution was stirred for 24 h under a fume hood to remove the organic solvent by evaporation. Drug-loaded polymeric micelles were prepared using the same procedure, except JSI-124 (1 mg) was dissolved along with the block copolymers in THF. After the evaporation of THF, the micelle solution was centrifuged to remove the precipitated drug.

A.2.2.2.3 Film Formation

Preparation of colloidal dispersions from synthesized block copolymers was tried by film method. Briefly, the block copolymer (20 mg) was dissolved in the mixture of $CHCl_3$ (14 mL) and dichloromethane (0.5 mL). After sonication for 30 min, this solution was transferred to a round bottom flask. To remove the organic solvents, vacuum was applied overnight using a rotary evaporator. After complete organic solvent evaporation, 50 °C deionized water (10 mL) was added to the round bottom flask and vortexed for 10 min following by centrifugation (30 min, 2000× rmp). Drug-loaded polymeric micelles were prepared using the same procedure, except JSI-124 (1 mg) was dissolved along with the block copolymers in the mixture of $CHCl_3$ and dichloromethane.

A.2.2.3 Release of JSI-124 from Block Copolymer Micelles

Release of free JSI-124 or JSI-124 loaded micelles was assessed in deionized water at 37 °C. Free JSI-124 (2% THF) or micellar JSI-124 (5 mL micelle formulation containing 1 mg JSI-124) was prepared and transferred to a dialysis bag (MWCO - 3.5 kDa). The dialysis bag was placed in 500 mL of deionized water and release study was performed in a shaking water bath at 37 °C. At selected time intervals, the release media was replaced, and aliquots of 200 uL were withdrawn from the inside of the dialysis bag and analyzed by LC-MS (406). The release profiles were compared using similarity factor, f_2, and the profiles were considered significantly different if $f_2 < 50$ (407).

A.2.2.4 Determination of the Morphology of Micelles

Transmission electron microscopy (TEM) (FEI Morgagni^{TM} 268, North America NanoPort, Oregon, USA) was used to observe the morphology of micelles. For TEM measurements, the block copolymer concentration in micellar solutions was 1 mg/mL. Samples were placed onto copper grid, dried at room temperature, and examined using TEM by negative staining with 4% uranyl acetate.

A.2.3. Results

Polymeric micellar formulations of JSI-124 based on different di and triblock block copolymers have been developed. First the effect of micellar preparation methods on micelle size and morphology was investigated. Micelles of different di and triblock block copolymers were prepared by co-solvent evaporation (adding water to organic solvent), co-solvent evaporation (adding organic solvent to water) and film methods. Co-solvent evaporation (adding water to organic solvent) method resulted in micelles with the smallest size compared to the other two methods (**Table**

A.2.1). The obtained sizes for micelles prepared by solvent evaporation (adding organic solvent to water) and film methods were similar (**Table A.2.1**). TEM images showed that empty polymeric micelles of different di and triblock block copolymers prepared by co-solvent evaporation methods adopted a spherical and uniform shape in most cases. However, micelles prepared by film method were more irregular in shape (**Figure A.2.1**). As it can be clearly seen from the TEM images (**Figure A.2.1**), and in agreement with DLS results (**Table A.2.1**), co-solvent evaporation (adding water to organic solvent) method resulted in micelles with the smallest size as compared to other methods of micellar preparation.

Table A.2.1 Effect of method of micellar preparation on the size of empty micelles (Diameter ± SD (nm))[a].

Polymer	Co-solvent evaporation (adding organic solvent to water)	Co-solvent evaporation (adding water to organic solvent)	Film
PEO-PLLA	66.39 ± 4.48	34.52 ± 1.25	71.11 ± 5.30
PEO-PD/LLA	69.38 ± 3.25	36.23 ± 2.02	96.15 ± 3.40
PEO-PLLA-PBCL	73.82 ± 2.09	39.41 ± 3.11	75.23 ± 2.50
PEO-PD/LLA-PBCL	61.36 ± 3.31	37.36 ± 2.23	76.32 ± 3.36

[a]Z average measured by DLS.

JSI-124-loaded micelles were also prepared by solvent evaporation (adding organic solvent to water) and film methods. Drug loaded micelles prepared by solvent evaporation method increased in size as compared to their empty counterparts (**Table A.2.2**), however JSI-124-loaded micelles prepared by film method didn't show a significant increase in size as compare to empty micelles (**Table A.2.2**).

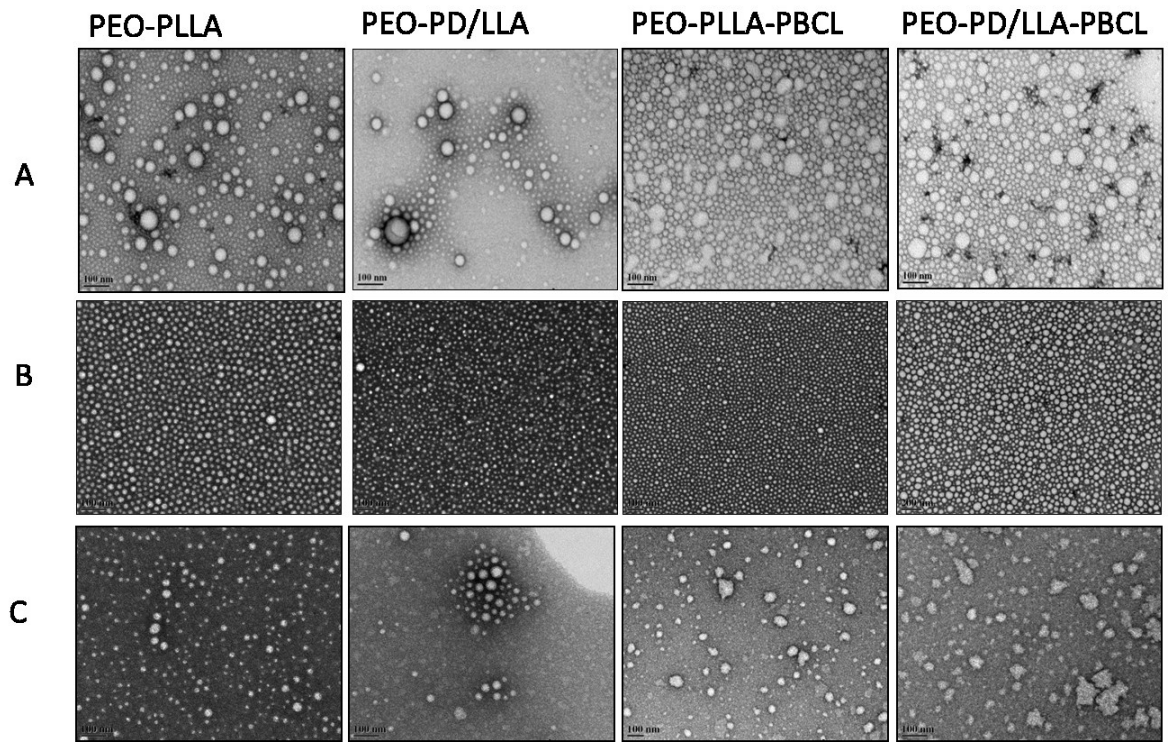

Figure A.2.1 Effect of micelle preparation method on morphology of micelles prepared from different di and tri block copolymers. TEM images of micelles prepared by **(a)** co-solvent evaporation (adding organic solvent to water), **(b)** co-solvent evaporation (adding water to organic solvent), and **(c)** film methods.

TEM images showed that JSI-124-loaded polymeric micelles of PEO-PLLA and PEO-PD/LLA diblock copolymers prepared by co-solvent evaporation method (adding organic solvent to water) adopted a spherical and uniform shape in most cases **(Figure A.2.2**), similar to their empty counterparts (**Figure A.2.1**). Interestingly, for JSI-124-loaded micelles from PEO-PLLA-PBCL and PEO-PD/LLA-PBCL triblock copolymers prepared with the same method of micellar preparation, in addition to spherical particles, rod and worm-like micelles were also observed especially with PEO-PLLA-PBCL triblock copolymer (**Figure A.2.2a**), suggesting the effect of drug incorporation on the micellar morphology (408). JSI-124-loaded micelles from PEO-PLLA-PBCL and PEO-PD/LLA-PBCL triblock copolymers prepared by co-solvent evaporation method (adding water to organic solvent) adopted a spherical and uniform shape, however (Figure A.2.2B).

Table A.2.2 Characteristics of JSI-124 self-assembled structures prepared by co-solvent evaporation (CSE) method adding organic solvent to water and film methods.

Polymer		Diameter ± SD (nm)[a]	PDI ± SD[b]	% EE ± SD [c]	% DL ± SD [d]
PEO-PLLA	CSE	106.28 ± 1.06	0.24 ± 0.25	83.64 ± 3.28	4.19 ± 0.21
PEO-PD/LLA		105.40 ± 2.55	0.25 ± 0.09	28.30 ± 2.24	1.41 ± 0.30
PEO-PLLA-PBCL		121.29 ± 3.66	0.28 ± 0.41	90.24 ± 2.30	4.52 ± 0.13
PEO-PD/LLA-PBCL		111.41 ± 4.41	0.19 ± 0.11	92.80 ± 3.30	4.64 ± 0.16
PEO-PLLA-PBCL	Film	88.29 ± 3.66	0.29 ± 0.41	93.24 ± 2.30	4.66 ± 0.13
PEO-PD/LLA-PBCL		80.41 ± 4.41	0.30 ± 0.11	91.80 ± 3.30	4.59 ± 0.16

[a] Z average measured by DLS.
[b] Polydispersity index measured by DLS.
[c] Encapsulation efficiency $(\%) = \frac{the\ amount\ of\ encapsulated\ JSI-124}{the\ total\ feeding\ amount\ of\ JSI-124} \times 100.$
[d] Drug loading$(\%) = \frac{the\ amount\ of\ encapsulated\ JSI-124}{the\ total\ amount\ of\ polymer} \times 100.$

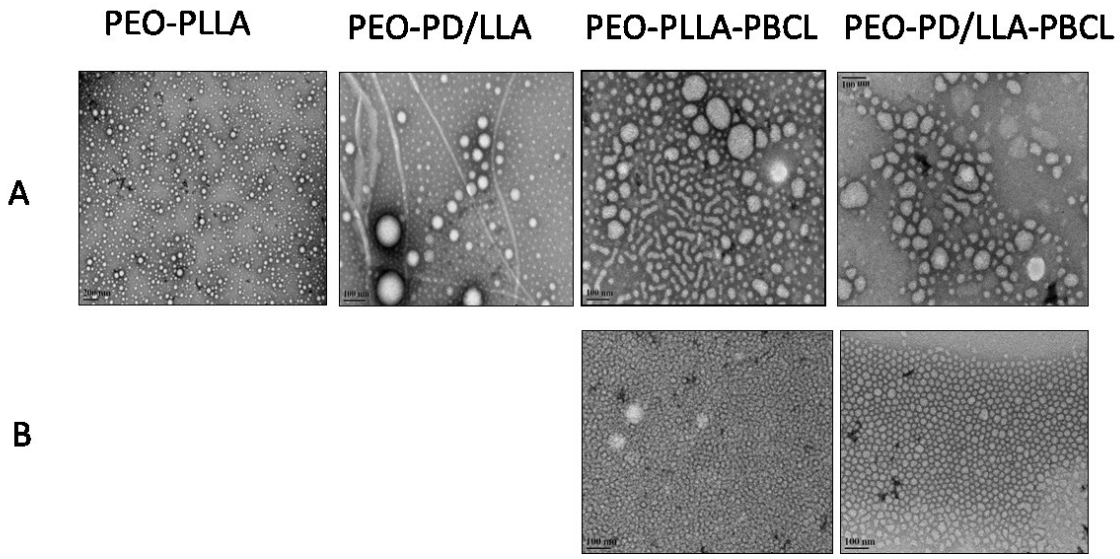

Figure A.2.2 TEM images of JSI-124 loaded polymeric micelles from different di and tri block copolymers prepared by **(a)** co-solvent evaporation method (adding organic solvent to water) and **(b)** co-solvent evaporation method (adding water to organic solvent)

Lastly, release of drug from JSI-124-loaded micelles prepared by different method of preparations (co-solvent evaporation and film) was studied. In all the studied formulations, the release of JSI-124 was fast and micelles were unable to significantly sustain the release of drug *in vitro* under sink

condition (**Figure A.2.3**). This observation may imply the localization of JSI-124 in the core/shell interface rather than the micellar core.

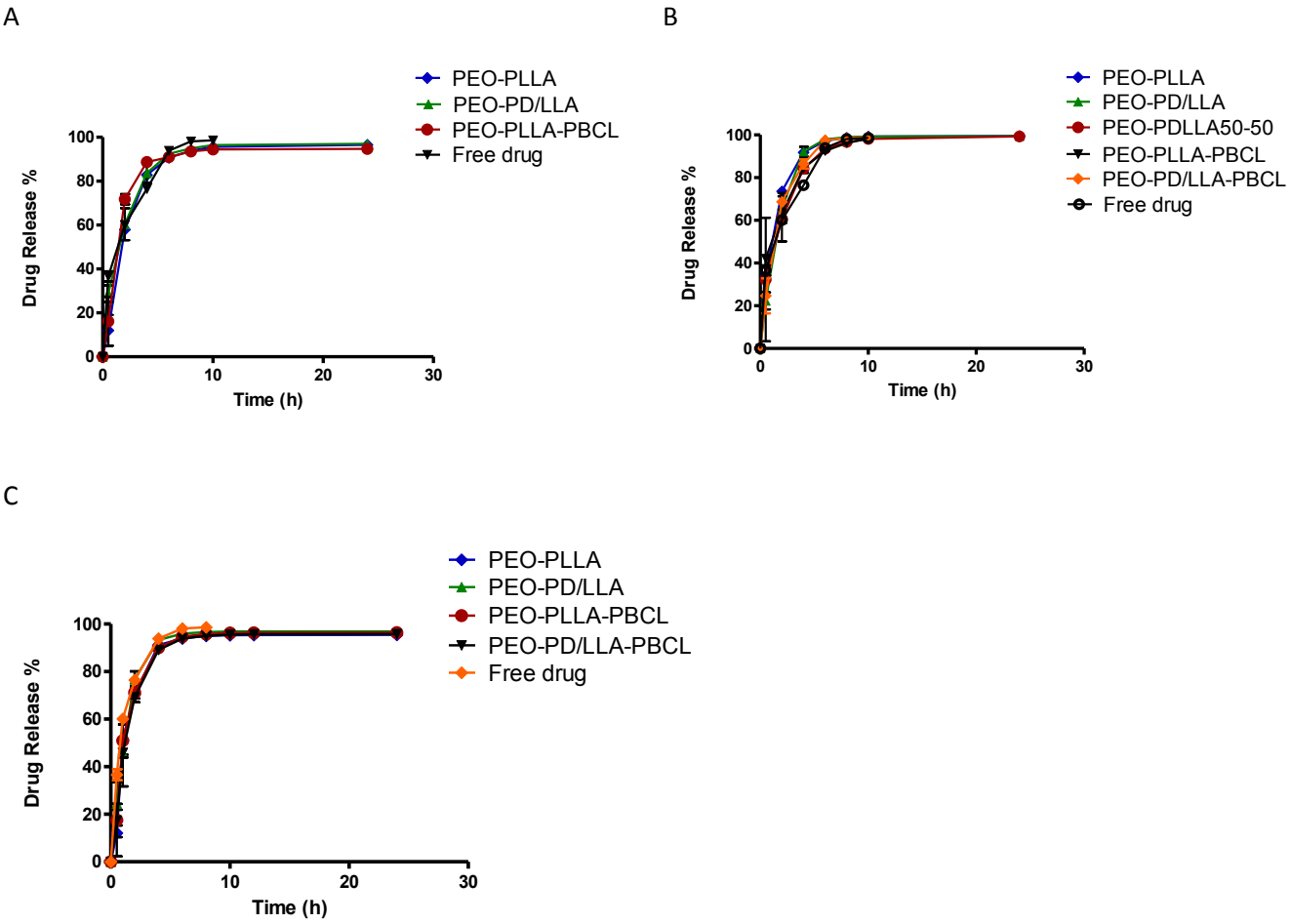

Figure A.2.3 Release profiles of JSI-124 from di and triblock block copolymers micelles prepared by **(a)** Film method, **(b)** co-solvent evaporation (adding water to organic solvent) and **(c)** co-solvent evaporation (adding organic solvent to water). Data are represented as mean ± SD (n = 3). JSI-124-loaded micelles of different copolymers showed similar rate of release as a free drug ($f_2 > 50$).

A.2.4 Conclusion

Release of the drug from the micellar carrier must be controlled to obtain a sustained drug release, and insure the same fate for the incorporated drug and the micellar carrier for the purpose of targeted drug delivery. Since the release of JSI-124 was fast and micelles were unable to significantly sustain the release of drug in vitro under sink condition, we decided to not continue with this project.